Geochemical characterization, petrogenetic modelling and engineering behaviour of granitic rocks and basic dykes from the northern Indian plate in north-western Pakistan

Muhammad Sajid

Submitted to the University of Exeter as a thesis for the degree of Doctor of Philosophy in Geology in September 2016

This thesis is available for Library use on the understanding that it is copyright material and that no quotation from the thesis may be published without proper acknowledgement. I certify that all material in this thesis which is not my own work has been identified and that no material has previously been submitted and approved for the award of a degree by this or any other University.

Signature: ……………………………………………………………..

September 2016

UNIVERSITY OF EXETER

COMMONWEALTH SCHOLARSHIPS

Abstract

The pre-Himalayan magmatic events along the northern margin of Indian plate in north-western Pakistan have been investigated and correlated with analogous magmatism in other Himalayan and northern Gondwana regions. The samples from Utla and Mansehra regions of NW Pakistan are dominantly megacrystic two mica granites, strongly peraluminous (A/CNK > 1.1) and intruded by aplite dykes and quartz-rich veins. The high precision zircon U-Pb ages (471-479 Ma) show their emplacement in early Paleozoic. These granites are enriched in light rare-earth elements (LREEs) and show similar chondrite normalized REE patterns with negative Eu anomalies (Eu/Eu* = 0.07–0.73). The geochemical signature and REE based modelling indicate that the granites are derived mainly from the partial melting of pelitic source followed by the evolution of melt via fractional crystallization resulting in the formation of aplites. Tourmaline occurrences in distinct modes show post-magmatic alteration of these granites triggered by hydrothermal fluids from different sources. Enrichment of Sn in certain alteration zones and trace elements ratios suggests a strong mineralization potential for these granites. The analogous composition, source rock characteristics and geochronology represent their regional association with other Cambro-Ordovician granitoids from northern Gondwana. Due to these similarities, an early Paleozoic orogenic event has been anticipated for these granitoids initiated due to subduction of Proto-Tethys oceanic lithosphere beneath the northern Gondwana supercontinent.

Dykes of basic composition that intrude these granites and other lithologies are divided into dolerites and amphibolites on the basis of their distinct mineralogical and geochemical composition. Major elements composition suggests alkaline to sub alkaline character of both dykes with intraplate tectonic setting, however, amphibolites (>3%) are markedly enriched in TiO_2 relative to dolerites (<3%). Trace element ratios designates the origination of dolerites from subcontinental lithosphere with significant crustal contamination. They show analogous geochemical character to Panjal traps which represent a regional scale rift related basic magmatism in Himalayan terrane during Permian. The geochemical signature of amphibolites, however, show similarities to high-Ti Qiangtang dykes which originates from asthenospheric source via deep mantle plume. The sporadic distribution of both dykes in similar aged host rocks represent their

evolution from distinct sources in separate but synchronous magmatic pulses during extensional tectonism related to separation of Cimmeria from Gondwana.

Granites with distinct petrographic features have been tested to examine the influence of textural characteristics on the variation of their respective strength. Comparison of petrographic observations before and after the strength tests and the relationship of fracture propagation with mineral boundaries specifies vital impact of textural variation in evaluating the mechanical behaviour of granites. The important textural features include average grain size of rock, grain boundary recrystallization, maximum grain size of major rock forming minerals, mean grain size of cleaved minerals, mineral exsolution and variation of grain size within a rock. The petrographic observations, however, are more effective to describe the strength variation of granites having analogous weathering grade as change in degree of weathering has a dominant effect on rock mechanics.

Table of Contents

List of Figures

List of Tables

Acknowledgments

I am thankful to my supervisors, Jens Andersen and John Coggan, for their demonstrative guidance and valuable input throughout the research project. Their welcoming and encouraging attitude is always helpful for clarification of any problem faced during research work. I am also indebted to Mohammad Arif for his help and valuable suggestions during the various aspects of research.

I am grateful to Commonwealth Scholarship Commission, UK for funding my PhD research. The financial support for fieldwork and conference travels is extended by Department of Geology-University of Peshawar, Society of Geology Applied for mineral deposits (SGA) and Applied Mineralogy Group (AMG).

The laboratory staff of CSM is thanked for their help and guidance during the sample processing and data collection i.e. Steve Pendray (thin section preparation), Ian Faulks (Rock mechanics), Gavyn Rollinson (QEMSCAN), Joe Pickles (EPMA), Sharon Uren (ICP-MS) and Malcolm Spence (XRF). Encouragement from Gavyn Rollinson will always be appreciated in several aspects of my research despite not being formally involved with it. The academic staff of CSM especially Ben Williamson, Frances Wall and Robin Shail are also acknowledged for their support.

Stuart Kearns has been very cooperative during the EPMA analysis at University of Bristol. Adrian Wood and Nick Roberts (NIGL) assisted in zircon separation at BGS. Michael Wiedenbeck, Alex Rocholl, Frédéric and Uwe (GFZ-Potsdam, Germany) are highly acknowledged for their help in U-Pb isotopes analysis and data processing. Rasheed Maseeh and Sajid (Department of Geology-University of Peshawar) helped in cutting the rock chips for thin sections. Laboratory staff of HydroTech-Pakistan facilitates the preparation of cylindrical samples for mechanical testing.

I am grateful to Irfan Hashmi, Haroon, Abid Nawaz, Nowrad, Imran, Umair, Shuja and Hareem for their help during fieldwork. I am grateful to my friends Hammad, Sultan Ghani and Tahir Asif for their moral and consistent support. Amos Ambo, Abdulqadir (late), Luke, Shekwo, Sam, Safaa, Siti, Beth, Dora, Ricardo and other fellow PhD students have been very helpful and provided pleasant working environment in CSM research room.

Last but not least, special thanks to my lovely wife and kids (Shuja and Mustafa) for their continuous support and understanding. My family members, especially parents, deserve sincere regards and special thanks for their moral and financial support throughout my educational carrier.

To my Lovely Mother

Her Prayers lead me to what I am today and what I always hope to be ...

** Yes Ammi, it is a funny thing to get back home every time with rocks in hand*

CHAPTER 1

Introduction

1.1 Project Statement

The northern Indian plate has experienced different kinds of tectonic environments through its geological history. In the early Cenozoic, it records convergent tectonic conditions during the Himalayan orogenic episodes initiated due to the intra-oceanic subduction in the Tethys Ocean (Searle et al., 2009; Jagoutz et al., 2010; Burg, 2011). Preceding this, it had been subjected to extensional settings during the late Paleozoic indicated by the presence of rift-related alkaline lithologies (Kempe and Jan, 1970; Garzanti et al., 1999; Noble et al., 2001). The diverse tectonic signature of the northern Indian plate attracts researchers due to its assorted mixture of lithological units with a great scope of geological investigation.

The Indian plate rocks in northern Pakistan are separated from Kohistan Island arc (KIA) by a regional fault zone known as the Main Mantle Thrust (MMT) (Searle and Treloar, 2010; Burg, 2011) (Fig. 1.1). The KIA formed as the result of intra-oceanic subduction in the Tethys Ocean (Burg, 2011). The Indian plate consists of Early Proterozoic to Mesozoic metasedimentary rock sequence (DiPietro et al., 1993; Pogue et al., 1999) which were intruded by magmatic rocks in the Precambrian (DiPietro and Isachsen, 2001) and Phanerozoic (Smith et al., 1994; Ahmed et al., 2013) and strongly deformed and metamorphosed during the Late Cretaceous-Cenozoic Himalayan Orogeny (Treloar et al., 1989a; Searle and Treloar, 2010). The principal research focus in the region is dominated by the magmatism and tectonism related to Himalayan orogeny, however, the pre-Himalayan details are relatively scarce.

The peraluminous granites formed one of the major component of intrusive rocks found in the northern Indian plate, NW Pakistan (Fig. 1.1). The geochemical details and whole rock Rb-Sr geochronology (Le Fort et al., 1980, 1983; DiPietro and Isachsen, 2001) show the early Paleozoic age of these granites. However, their petrogenesis and significance in the tectono-magmatic evolution of the Indian plate continental margin during the Cambrian period needs substantial elaboration. Their detailed petrogenesis, precise radiometric dating and regional tectonic correlation is important to unravel the petrogenetic evolution, emplacement time, tectonic setup and relationship with other granitic rocks from Himalayan terrane and other regions of northern Gondwana margin. The peraluminous systems are also considered as potential source of economic minerals (e.g. W, Sn, Be etc.) (Baker et al., 2005; Ruiz et al., 2008; Clemens, 2013). The comprehensive assessment of these granitoids for mineralization prospects is essential to categorise the mineralization systems in the region. The Mansehra, Swat and Utla regions are the dominant locations in north-western Pakistan where these granites are excellently exposed (Fig. 1.1) and can be studied in ample detail. The current investigation is largely based on the samples from the Utla Granites which are compared and discussed with the fresh as well as pre-existing data set of Mansehra Granites (Le Fort et al., 1980; DiPietro and Isachsen, 2001).

Figure 1.1. Tectonic map of north-western Pakistan showing locations of different granitic plutons in northern Indian plate (Pogue et al., 1999; Khattak et al., 2005). Outlines of Pakistan are shown in inset (box show location of area covered in map).

The granites and other associated rocks in the region are intruded by dykes of basic composition, which are linked with rift related alkaline magmatism that occurred during the late Paleozoic (Rafiq and Jan, 1988; Papritz and Rey, 1989; Pogue et al., 1992a). On the basis of field relation, these dykes are considered as youngest phase of the alkaline magmatism, however detailed information about their source, characterization and tectonic relations is lacking and need to be properly addressed on regional scale. Similar basic intrusions are reported from several locations in NW India (e.g. Chauvet et al., 2008) and Tibet (e.g. Zhai et al., 2013). Their comprehensive geochemical investigation and correlation with other relevant basic magmatism in the Himalayas (e.g. Pogue et al., 1992a; Shellnutt et al., 2014) will give assured insights about the rifting episodes and timings in Himalayan terrane.

The granitic rocks from northern Indian plate are extensively mined for their use as building material and dimension stone. Variation in mechanical behaviour of granites that have different mineralogical and textural features is observed. The importance of textural characteristics in assessing the geotechnical properties have been emphasized in certain studies (e.g. Lindqvist et al., 2007; Yilmaz et al., 2011; Rigopoulos et al., 2013). A targeted study encompassing the identification of textural differences between the granites and its effect on their mechanical properties will aid understanding of the textural control on rock mechanics. Comparison of the current results with already published literature (e.g. Yilmaz et al., 2011; Arif et al., 2013; Sousa, 2013) will highlight novel perceptions about the textural and mineralogical controls and clarify the discrepancies between the different interpretations from earlier research (e.g. Tugrul and Zarif, 1999; Sousa, 2013; Sajid and Arif, 2015).

1.2. Major Objectives and Scope

The nature of current project is dual and can be divided into a) geochemical and b) geotechnical aspects of magmatic suites from the northern Indian plate in NW Pakistan.

1.2.1. Geochemical aspects

The research questions related to geochemical studies that are the major focus of investigation can be summarized as:

1. How the emplacement of the Utla and Mansehra granites is related to known tectonic setup of the Indian plate margin and what are their implications in evolution and mineralization in the region?

   The following series of analysis has been conducted to systematically address the research question:

a. Thorough sampling of the granites from different field exposures and their modal mineralogical analysis using polarizing microscopy to appropriately characterize the pluton
b. The comprehensive geochemical investigation of major and accessory minerals using electron probe micro-analyser (EPMA)
c. Whole rock major and trace elements analyses using X-ray Fluorescence Spectrometry (XRF) and Inductively Coupled Plasma Mass Spectrometry (ICP MS) respectively
d. Radiometric geochronology using zircon U-Pb isotope analysis via Secondary Ion Mass Spectrometry (SIMS)

The comprehensive mineralogical, geochemical and isotope analytical data has been explored for the first time for the investigation of magmatic characterization and petrogenetic evolution of the Utla and Mansehra Granitoids. The data is compared with other pertinent magmatic suites from the Himalayas and other northern Gondwana Terranes to address their regional relationship. The U-Pb radiometric ages of zircons from the Utla and Mansehra Granites have been analysed that has not been investigated before. It helps for the improved understanding of their timing and relationship with known magmatic events and tectonic division. Furthermore, trace element and REE data tied with field features has been employed to discuss their source rock characteristics and mineralization potential.

2. What are the tectonic significances of association of basic dykes with Permian rift-related basic magmatism in northern Indian plate?

The various analytical approaches described above for granitic rocks has also been extended for the samples of studied basic dykes. The comprehensive and novel mineralogical and geochemical dataset is compiled for these intrusions to investigate their petrogenesis. The major and trace elements data is used for the geochemical characterization of dykes. The trace element ratios and REE based models have been used to interpret the composition of mantle source. The existing literature about the related basic dykes from the other Himalayan regions (e.g. Pogue et al., 1992a; Shellnutt et al., 2014; Xu et al., 2015) has been used to discuss their relationship and regional tectonic circumstances.

1.2.2. Geotechnical aspects

The major aim of the geotechnical approach used in the current study answer the following question:

1. Can petrographic characteristics of a rock be an effective indicator of its mechanical nature?

Four texturally different granites from the northern Indian plate have been tested to answer the research question. The various textural parameters including grain size and grain shape has been addressed as important aspect effecting the rocks strength (e.g. Tugrul and Zarif, 1999; Lindqvist et al., 2007). However, the influence of textural features in controlling the strength of granites with analogous alteration grade has been investigated for the first time in this research. The polarizing microscopy and QEMSCAN analysis has been conducted for the textural description of rocks. Pre- and post-compression textural observations have been thoroughly studied to see the relationship between fracture propagation and rock textures. The results from previous literature about investigation of similar relationship (e.g. Tugrul and Zarif, 1999; Yilmaz et al., 2011; Coggan et al., 2013) have been compared for discussion.

1.3. Structure of thesis

Chapter 2:
This chapter describes the geological setup of the northern Indian plate in NW Pakistan. It presents various magmatic events and host rock characteristics along with the known geochronological data to describe the tectonic evolution of the region.

Chapter 3:
This chapter elaborates the significance of studies relating the rocks texture with their mechanical characteristics. The different methods of classifying the rock on the basis of weathering have also been discussed.

Chapter 4-7:
Chapter 4 is written in the form of a manuscript related to petrogenesis and tectonic relations of the Utla granites. The corresponding geochronological data is presented in chapter 6. Both of these chapters will be combined as a single

manuscript before submission for publication. The geochronology chapter is not placed immediate after Chapter 4 as it also contains some data related to Chapter 5.

Chapter 5 and 7 demonstrate two separate manuscripts which address the major research questions about the geochemical/ tectonic implications of basic dykes and textural controls on rock mechanics respectively. Manuscripts are in different stages of publication i.e. fully published or in the process of review. The manuscripts are reformatted according the general layout of thesis. The text, figures and tables presented here are the same as those submitted to the journal for the publication process. The cited references from manuscripts and rest of the thesis chapters have been collected together in the major reference list at the end of thesis.

The title page of chapter shows the status of article, co-authors names and their respective contributions and name of journal to which manuscript is submitted. Each chapter has its own abstract, introduction and methodology section to maintain the consistency of the script. Some of the procedures concerning rock mechanical tests have not been incorporated in relevant manuscript i.e. chapter seven; however, they have been described in Appendix-5. The details of these chapters are as following:

Chapter 5:
Petrogenesis and tectonic association of rift-related basic Panjal dykes from northern Indian Plate, NW Pakistan: evidence of High-Ti basalts analogous to dykes from Tibet. Mineralogy and Petrology, (in review)

Chapter 7:
Petrographic features as an effective indicator for the variation in strength of granites. Engineering Geology, (fully published)

Chapter 8:

This chapter discusses the interpretations that have been made in earlier chapters and anticipate the tectonic model for the evolution of Indian plate margin based on these considerations. It also describes the overall contributions of the current investigation.

Chapter 9:

The final chapter summarizes the overall conclusions of the project and recommendations for future research.

CHAPTER 2

Regional Geology

2.1. Tectonic division of Himalayas

The Himalayan terrane is divided in three principal litho-tectonic regions separated by major fault zones (Searle et al., 2009; Kohn, 2014). From south to north, these regions are termed as a) Lesser Himalayan Sequence (LHS), b) Greater Himalayan Sequence (GHS) and c) Tethyan Himalayan Sequence (THS) (Fig. 2.1). The Main Boundary Thrust (MBT) is a regional fault which separate LHS from the foreland sediments lying towards south (Hodges, 2000; Kohn et al., 2014). The Main Central Thrust (MCT) separates the LHS from the over thrusted GHS (Heim and Gansser, 1939; Gansser, 1964) which has been detached from the THS by a regional fault system known as South Tibetan Detachment system (STDS) towards north (Hodges, 2000). The STDS represent a series of extensional shear structures (Kohn et al., 2014).

The LHS contain complex fold and thrust system of Proterozoic metasedimentary units metamorphosed from greenschist to lower amphibolite facies (Schelling, 1992; Hodge, 2000). This sequence constitutes the foothills of Himalayas with numerous lithological units including quartzites, psammitic phyllites and schists, impure marble and orthogneisses (Gansser, 1964; Valdiya, 1980; Colchen et al., 1986). The basement of this zone is not exposed and is believed to be deposited on the northern passive margin of the Indian plate (Gansser, 1964; Brookfield, 1993). The Himalayan granitic belt has been intruded in the Proterozoic metasedimentary sequence during the Cambrian-Ordovician time (LeFort, 1986) confirmed by U-Pb dating from different regions (~460 Ma to ~510 Ma) (e.g. DeCelles et al., 1998; Wang et al., 2013). This granite belt extends for around 1900 km along strike from southeast of Kathmandu (Nepal) to at least NW Pakistan (LeFort et al., 1986). The Andean type orogeny has been proposed for this granitic belt in the northern Indian plate following Gondwana clustering (Cawood et al., 2007), however, some researchers relate it Pan-African orogenic episodes (Girard and Bussy, 1999; Kwatra et al., 1999).

The GHS, also known as Higher Himalayan zone or Central Crystallines, mainly contain high grade metasedimentary and meta-igneous rocks. Three different formations have been identified in this zone (Hodges, 2000). The basal formation contains metasedimentary rocks including mica schist, phyllites and paragneisses overlain by middle to upper amphibolite facies calcareous rocks of second formation. Both formations are separated by sharp and conformable contact (Colchen et al., 1986). The third formation consists homogenous augen orthogneisses majorly noticed in central to eastern Nepal (LeFort et al., 1986) and extend up to Bhutan towards east (Gansser, 1983) and as far west as Zanskar, NW India (Pognante et al., 1990). Numerous Rb-Sr and U-Pb studies (e.g. Pognante et al., 1990; Hodges et al., 1996) confirm the Cambro-Ordovician age of these gneisses. Several leuco-granitic bodies have also been identified in GHS (LeFort et al., 1987; Guillot et al., 1993; Hodges et al., 1996) with younger ages ranging from <4 Ma in Nanga Parbat region (Zeitler et al., 1993; Burg et al., 1998) to 23 Ma in the central Nepal (Harrison et al., 1995; Searle et al., 1999).

The region between STDS and Main Mantle Thrust (MMT) constitute the THS that represent the complete stratigraphic record of the northern Indian plate i.e. Paleocene to Eocene (Gaetani and Garzanti, 1991). The stratigraphic division of this zone has been extensively described (e.g. Searle et al., 1983; Gaetani et al., 1985; Pogue et al., 1992b). The litho-stratigraphic units of this zone are mostly unmetamorphosed, however, low grade metamorphism is also reported in certain regions (Coleman, 1996; Hodges et al., 1996). The rift related Permian basaltic magmatism (Panjal Traps) have been extensively reported from this zone in several regions of NW Pakistan (e.g. Papritz and Rey, 1989; Pogue et al., 1992a), NW India (e.g. Chauvet et al., 2008).

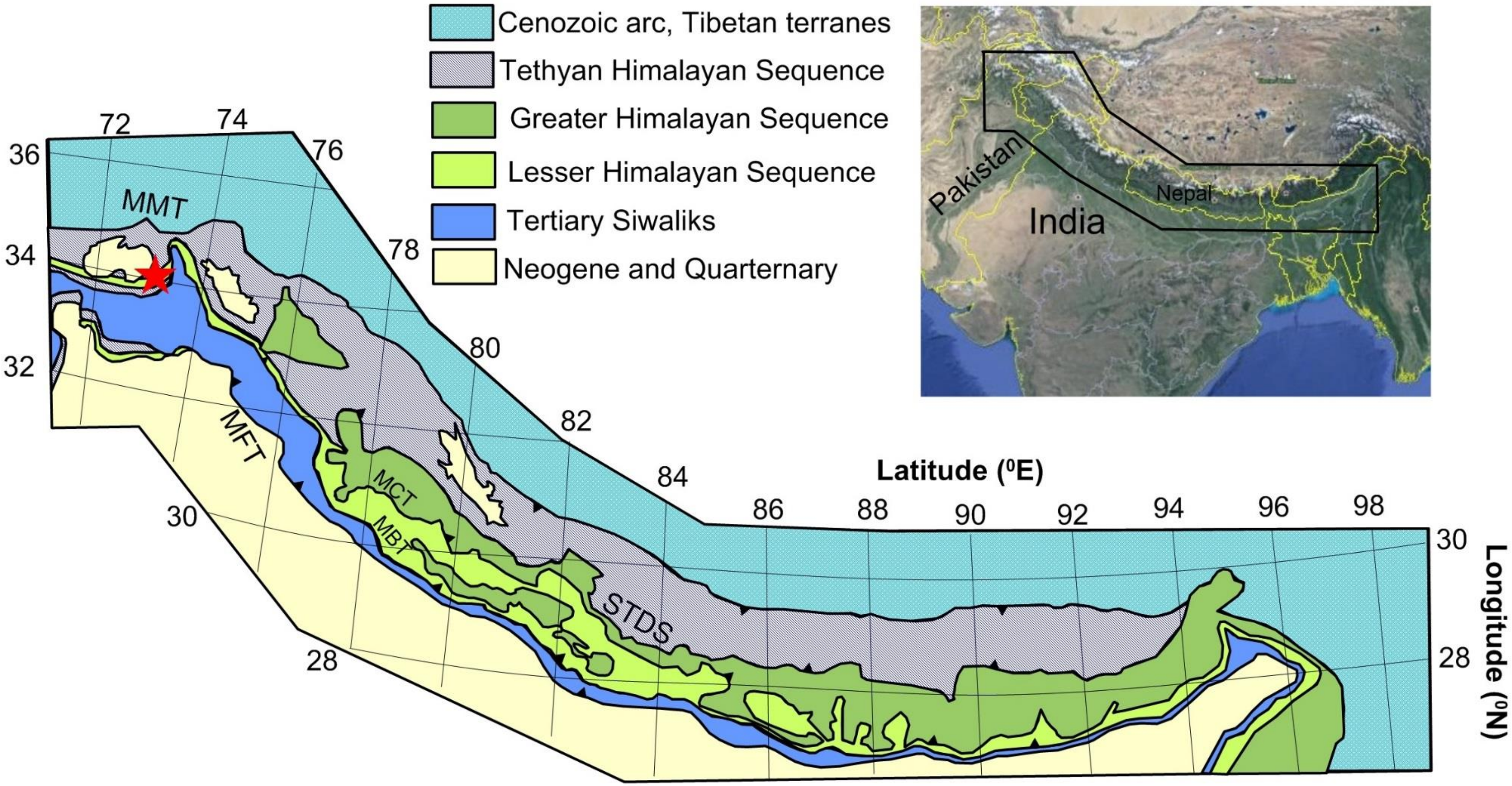

Figure 2.1. Simplified regional geologic map of the Himalayan terrane (redrawn after Kohn, 2014). The major litho-tectonic units and their general structural trends are illustrated. Star showing location of study area. Inset elaborate geographic location of geological map. MBT (Main Boundary Thrust), MFT (Main Frontal Thrust), MCT (Main Central Thrust), MMT (Main Mantle Thrust), STDS (South Tibetan Detachment System).

2.2. Geology and tectonic setup of NW Pakistan

Three distinct petro-tectonic domains have been identified in the northern Pakistan including, from north to south, Eurasian plate, Kohistan Island Arc (KIA) and Indian plate (Coward et al., 1986). The southern part of Eurasian plate is known as Karakoram Terrane that has been broadly divided into different units. The Karakoram Batholith separates the northern sedimentary belt from southern Karakoram Metamorphic Complex (Searle et al., 1999). The northern sedimentary belt is characterized by Ordovician to Early Cretaceous sedimentary rocks (Gaetani and Garzanti, 1991). Variety of metasedimentary and meta-igneous rocks with fold and thrust-related culminations, multiphase metamorphism and deformation have been recognized in southern metamorphic complex (Searle, 1986; Searle and Tirrul, 1991; Searle et al., 1992). Early Miocene Baltoro granite in central and eastern Karakoram form one of the major unit of the Karakoram batholith which includes monzogranites and garnet bearing two-mica leucogranites (Parrish and Tirrul, 1989; Searle et at., 1992). The batholith also includes a number of pre-collisional hornblende and biotite-bearing granodiorites and tonalites (Searle et al., 1989; Crawford and Searle, 1992).

The northern Pakistan is widely regarded for the exposure of complete sequence of KIA formed as a result of intra-oceanic subduction of Indian plate (Coward et al., 1987; Searle et al., 1999). The KIA is separated from Eurasian plate to the north by the Shyok Suture, and bordered to the south by the Main Mantle Thrust (MMT) along which it thrust southward onto the continental Indian plate (Treloar et al., 1996; Searle et al., 1999). The KIA consists of late Cretaceous and Eocene plutonic belts, gabbronorites/ pyroxene granulites, calc-alkaline volcanics, amphibolites and minor meta-sediments (Coward et al., 1986). The base of arc contains ultramafic-mafic Jijal Complex which represents the upper mantle to lower crust transition (Ringuette et al., 1999; Dhuime et al., 2007). The overlying amphibolite-facies metaplutonic and metavolcanic rocks (Khan et al., 1997) originated from distinct mantle sources (Schaltegger et al., 2002) dominate in amphibolite belt. A massive gabbronorite unit form the core of arc namely Chilas complex. A genetic model of combined flux and decompression melting on the basis of petrological data in the back-arc was proposed for the ultramafic-mafic rocks of Chilas complex by Jagoutz et al.

(2011). Towards the northern end of arc, basic to acid volcanics of the Chalt Group are overlain by Albian-Aptian sediments of the Yasin Group (Pudsey, 1986). The Chalt Group rocks have been intruded by the Kohistan Batholith predominantly gabbroic, gabbroic diorite and granite or trondhjemite in composition (Petterson and Windley, 1991; Petterson, 2010).

The Indian plate is separated from the KIA by a regional fault zone known as MMT or Indus Suture Zone (ISZ) (Fig. 2.2A). MMT zone consist mantle derived ultramafic and mafic rocks marking the series of faults with different ages and tectonic history (DiPietro et al., 2000). The rocks of Himalayan sequence from the northern Indian plate are exposed in the region of NW Pakistan. These rocks are divided into northern internal metamorphosed zone and southern external unmetamorphosed zone (Treloar et al., 1989a) by Khairabad Thrust (lateral equivalent of MCT according to some authors e.g. DiPietro and Pogue, 2004) (Fig. 2.2A). The MBT in further south separate these rocks from the Tertiary foreland basin deposits (Fig. 2.2A). The magmatic suites originated via different events are present in the region between MMT and Khairabad thrust (Fig. 2.2A). On the basis of different timing and origin, the magmatic events can be divided into a) early Paleozoic and b) Permian event.

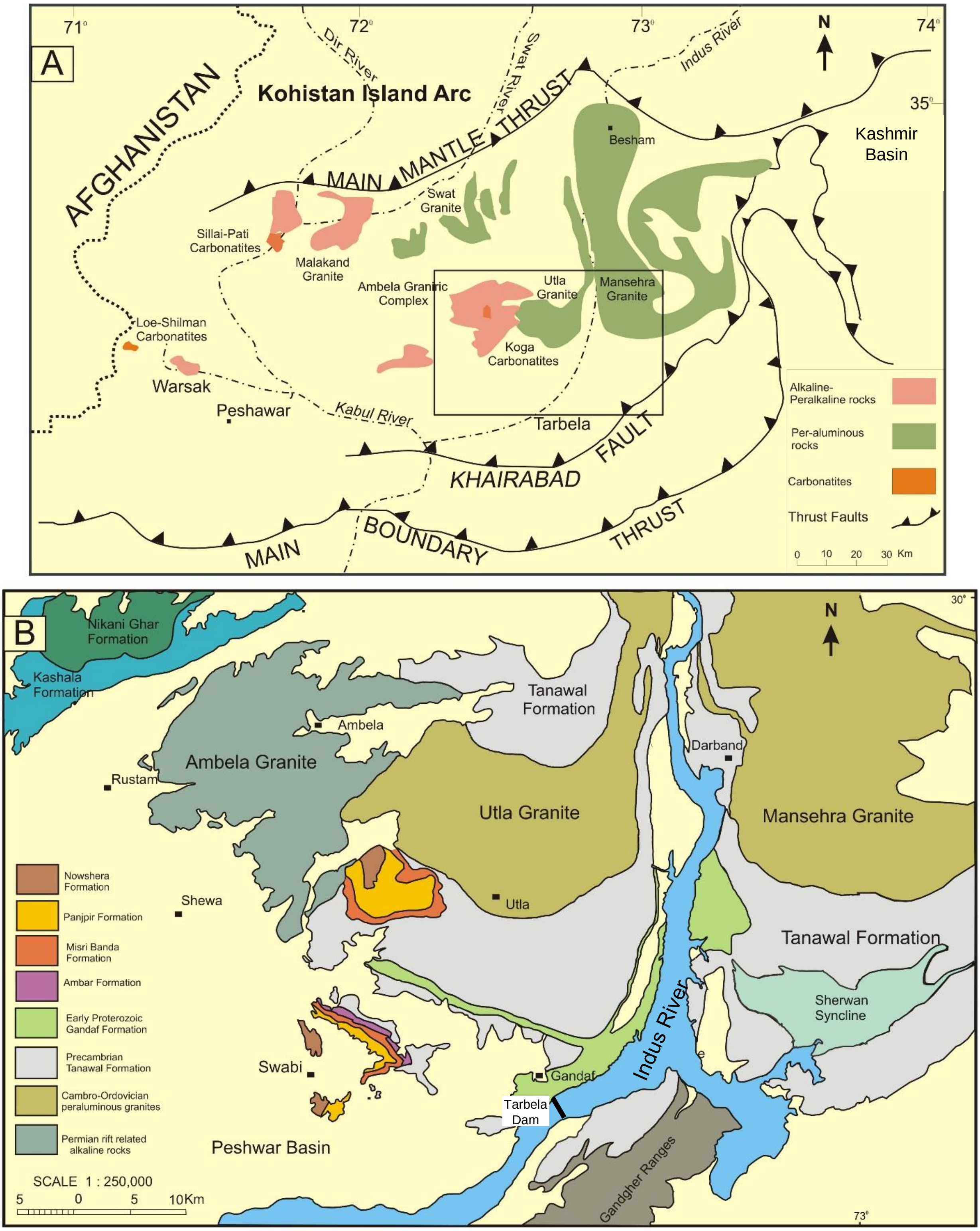

Figure 2.2. A) Tectonic map of northern Indian plate in north-western Pakistan (after Pogue et al., 1999; Khattak et al., 2005) showing locations of Utla and Mansehra granitic plutons. Box showing location of Figure 2.2B, B) Geological map of the study area (from Hussain et al., 2004).

2.2.1. Early Paleozoic magmatism in the northern Indian plate

The Himalayan granitic belt extending from Nepal in east towards Pakistan in west through India form one of the important lithological unit of northern Indian plate (LeFort et al., 1983, 1986; Pognante et al., 1990). The constituent granitic bodies are mostly peraluminous and ranging in age from Cambrian to Ordovician (LeFort et al., 1980; Debon et al., 1981; Miller et al., 2001).These granites are most likely to be associated with extension of regional scale, synchronous magmatic event in northern margin of Gondwana (LeFort et al., 1986; Miller et al., 2001; Cawood and Buchan, 2007). Cawood et al. (2007) designated this early Paleozoic event as Bhimphedian orogeny which refer to the initiation of subduction along the northern margin of Gondwana (including Indian plate) and its conversion from passive to Andean type margin around ~510 Ma (Fig. 2.3). This model described the southward subduction of proto-Tethys oceanic lithosphere beneath the northern margins of Gondwana continents e.g. the Indian plate (Fig. 2.3). They gathered the evidences of resultant Cambrian magmatic arc activity in the Tethyan Himalaya and large scale crustal anatexis triggered by this collision. This anatexis eventually have led to the formation of granitic belts in the northern margin of Indian plate around 470-500 Ma. It has also been suggested that the Bhimphedian Orogeny along the proto-Tethyan Ocean margin and the coeval Ross–Delamerian Orogeny along the proto-Pacific Ocean margin of Gondwana might represent a trans-Gondwana margin orogeny that began around 510Ma at the termination of the Gondwana assembly (Cawood and Buchan, 2007). Further support to this model is extended by Zhu et al. (2013) who propose the analogous subduction of proto-Tethys oceanic lithosphere beneath the Australian Gondwana responsible for the Cambrian magmatism in Lhasa terrane of Tibetan plateau. The Bhimphedian Orogeny ceased at ~470 Ma followed by the passive setting of the northern margin of Gondwana characterized by siliciclastic and carbonate sedimentation and evolution that likely persisted until Tertiary Himalayan collision (Cawood et al., 2007).

The similar age range of several plutons in NW India e.g. Tso-Morari granite (Trivedi et al., 1986; Girard and Bussy, 1999), Rupshu granite (Girard and Bussy, 1999), Miyar orthogneisses (Pognante et al., 1990) and Nepal e.g. Simchar granite (LeFort et al., 1983), Bhimphedi (Gehrels et al., 2006a), Kathmandu

(Cawood et al., 2007) support the existence of this magmatic event in Himalayan terrane.

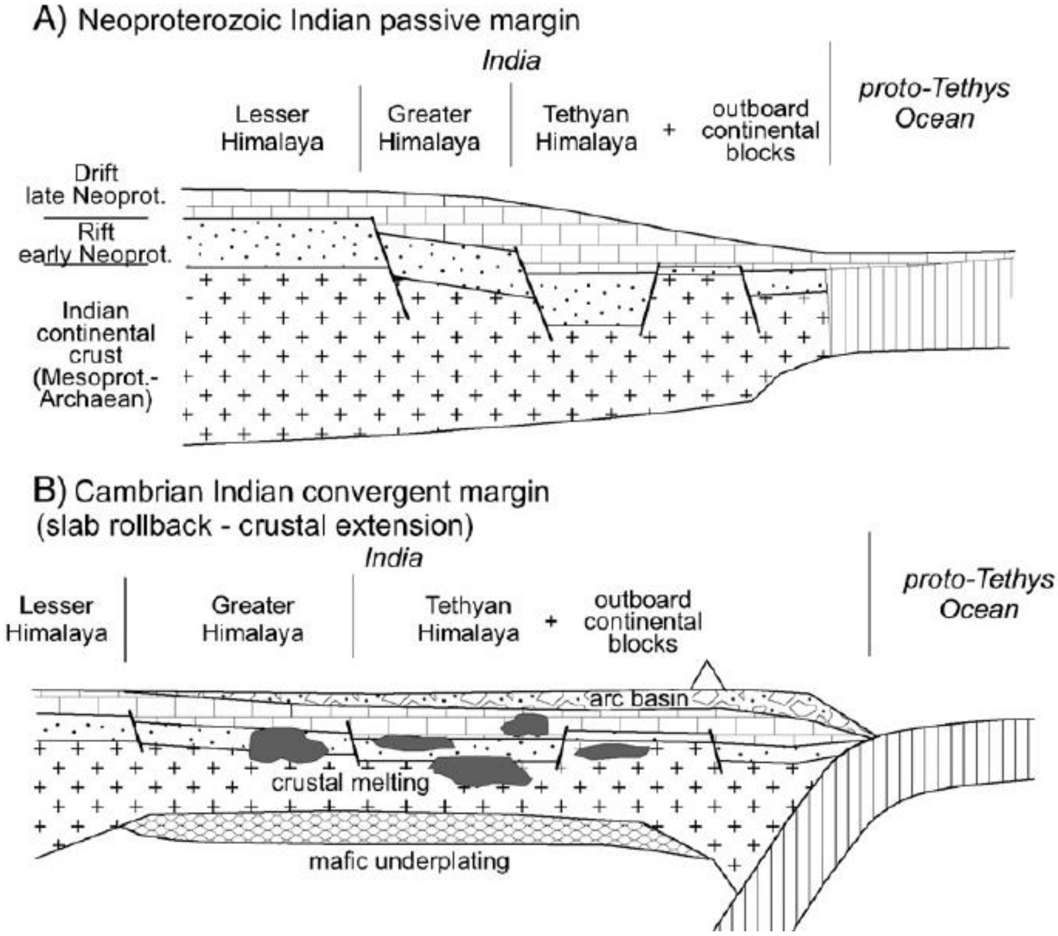

Figure 2.3. Sketches elaborating the tectonic setup and evolution of northern Indian plate in Neoproterozoic-Early Paleozoic time (from Cawood et al., 2007).

The major Himalayan granitic plutons in the northern western Pakistan are restricted to zone between Khairabad thrust and MMT (Fig. 2.2). Megacrystic Granites with augen-gneissose fabric at localized shear zones is known as Mansehra Granite in Hazara region (Fig. 2.2B). The Mansehra Granite for the first time has been regarded as the part of early Paleozoic belt due to its similar geochemical character and age (LeFort et al., 1980). The further investigation proves granitic suites from Swat area, lying towards the western bank of Indus River (Fig. 2.2A), contemporaneous to Mansehra Granite due to similar field and geochemical characteristics (DiPietro et al., 1993). The Mansehra Granite intrudes Tanawal Formation (Precambrian to Cambrian) which formed the basement sequence for the Hazara region rocks (Kazmi et al., 1984; DiPietro et al., 1993). In general, Mansehra Granites are biotite, muscovite, cordierite and tourmaline bearing granites with tabular phenocrysts of K-feldspar up to ten centimetres across (LeFort et al., 1980; DiPietro and Isachsen, 2001). Both Mansehra and Swat granites comprise several exposures in regions which are given different name on the basis of locality.

The Rb-Sr isotopes analyses of whole rock yield Cambrian age (516±16 Ma) for the Mansehra granite (LeFort et al., 1980) which was also considered as the age for Swat granites. However, Anczkiewicz et al. (1998a, b) observed U-Pb zircon ages of Swat granite to be 268 +7/-3 Ma and 468 ± 5 Ma in two different locations which suggest two different intrusive age of the pluton. In either case, both the plutons are much older and having no direct relation with Himalayan Orogeny (LeFort et al., 1980).

The Utla granites resemble Mansehra and Swat granites in terms of their field features, mineralogy and geochemical characteristics (DiPietro et al., 1998; Hussain et al., 2004; Sajid and Arif, 2010), however, some of the earlier workers (Rafiq and Jan, 1988; Pogue et al., 1992a) mapped them as eastward continuity of the alkaline Ambela granitic complex. A preliminary petrographic account of Utla granite is provided by Sajid et al., (2014), though their detailed characterization, geochemistry and geochronology need to be appropriately investigated which form one of the major objective of current investigation.

2.2.2. The Permian rifting event in the northern Indian plate

The intraplate magmatism during Permian rifting episode has been widely accepted in northern margin of Gondwana (including Indian plate) (Sengor, 1987; Noble et al., 2001; Metcalfe, 2006). Different alkaline suites in the form of granitic complexes and mafic dykes have been investigated in the northern Indian plate that have been considered to originate in response to Permian rifting (e.g. Pogue et al., 1992a; Noble et al., 2001; Chauvet et al., 2008; Ahmed et al., 2013). The roughly linear array of alkaline rocks in NW Pakistan is known as Peshawar Plain Alkaline Igneous Province (PPAIP) (Kempe and Jan, 1970, 1980) and believed to be associated with Permian rifting episode (LeBas et al., 1987; Rafiq and Jan, 1988; Ahmed et al., 2013).

The PPAIP is extended from the Afghanistan border in the west to the Tarbela region in the east between MMT and Khairabad Thrust (Fig. 2.2). A large data set of radiometric ages is available (Kempe, 1986; Le Bas et al., 1987; Smith et al., 1994; Anczkiewicz et al., 1998a; Ahmed et al., 2013) which show the alkaline granites and related rocks as the product of rift-related magmatism in the late Palaeozoic (350-268 Ma). The Ambela complex, Shewa complex and Warsak granites are the principal exposures of alkaline granitic lithologies (Fig. 2.2). The Ambela and Shewa are referred as complexes due to different phases of magmatism observed.

Rafiq and Jan (1988) identified silica saturated (granites and alkaline granites), silica undersaturated (alkali syenites and nepheline syenites) and basic dykes in the Ambela complex (Fig. 2.2). The basic dykes form less than 5% of the complex and is concluded to be the youngest as indicated by its intrusion in the older two phases and other pre-Permian rocks of the region (Pogue et al., 1992a). Carbonatites also form the important component of alkaline province and exposed in certain locations (e.g. Loe-Shilman and Sillai Patti) (Fig. 2.2). Khattak et al., (2005, 2008) described the Oligocene age for the emplacement of these carbonatites.

Two ideas about the emplacement of alkaline rocks associated with PPAIP has been suggested by earlier workers. Some researchers illustrate that all the alkaline rocks in northern Indian plate were emplaced during a single major phase of rifting in late Paleozoic time between 290-250 Ma. This interpretation is supported by geochronological data of constituent alkaline rocks e.g. Tarbela and Babaji syenites (Kempe, 1986; Smith et al., 1994), Ambela syenite (Le Bas et al., 1987), Malakand granite (Zeitler et al., 1988) and Chakdara granite (Dipietro and Isachsen, 2001) (Fig. 2.2). Pogue et al. (1992a) described the tectonic model of alkaline rocks during the late Paleozoic on the basis of the stratigraphic, structural and geochemical evidences. Jan and Karim (1990) questioned the existence of carbonatities and other alkaline rocks in the post-Paleozoic sequence and proposed the emplacement of PPAIP during Permo-Carboniferous extensional tectonic settings. Butt et al. (1989) studied the Sillai-Patti carbonatites and relate them to the Carboniferous Koga carbonatites in the region and concluded them to be pre-Himalayan.

The second idea proposed the emplacement of PPAIP in more than one episode i.e. late Paleozoic and Oligocene (Tertiary). This interpretation is mainly based on the geochronological studies on carbonatites which constitute the important part of PPAIP. Khattak et al. (2005, 2008) described the fission track apatite dating in host carbonatites from PPAIP and confirm its Oligocene emplacement time. Furthermore, Tertiary aged (26 Ma: zircon U-Pb) fresh ignimbrites are reported in PPAIP region by Ahmed et al. (2013). The Tertiary age of the Warsak Granite is confirmed by Kempe (1973) and Maluski and Matte (1984).

A large, fresh and undeformed granitic pluton exists in the Swat region known as the Malakand Granite after the name of local town (Fig. 2.2). The Malakand Granite intrude Mesozoic metasedimentary rocks and also consist tourmaline and fluorite bearing pegmatites and aplites. The hydrothermal fluids of this pluton are considered as the source of Beryllium for the genesis of Swat emerald deposits (Dilles et al., 1994; Arif et al., 1996, 2011). The age of Malakand granite is provocative, Zeitler (1988) and Smith et al. (1994) obtained late Paleozoic U-Pb zircon ages for the pluton and linked it with the rift related magmatism similar to other alkaline rocks of province. In contrast, Maluski and Matte (1984) and Le Bas et al. (1987) interpret Malakand Granite to be younger and the product of post-collision magmatism on the basis of a muscovite Ar-Ar age of 22.8 ± 2.2 Ma and biotite K-Ar age of 31 ± 2 Ma respectively. This assumption is also supported by U-Pb zircon age of 32.7 ± 0.5 Ma for the undeformed Malakand Granite by DiPietro (2008).

2.2.3. Precambrian and Paleozoic stratigraphy of study area

The Proterozoic metasedimentary sequence serves as the host rocks for the early Paleozoic magmatic event. This metasedimentary sequence is divided into different formations in NW Pakistan including Hazara formation, Salkhala Formation, Tanawal Formation, Gandaf Formation and Manglaur Formation. The Hazara Formation predominantly contain slates and phyllites with intercalated calcareous and graphite layers in certain places. Slate and phyllite are green to dark green and black, but are rusty brown and dark green on weathered surface (Shah, 2009). Some thick -bedded, fine- to medium-grained sandstone is also present. Certain clastic rocks from this formation has been dated using Rb-Sr whole rock isotopes method (Crawford and Davies, 1975). Two samples yield 765 ± 20 Ma age while one sample turn out to be 950 ± 20 Ma which show the mid Proterozoic age of the Hazara Formation.

The Salkhala Formation contain quartz and graphite schist, marbles and quartz-feldspathic gneisses in locations close to the current study area (Shah, 2009). This formation is divided into a basal Gandaf unit and upper Kundal unit (Khan and Khan, 1994). The lower Gandaf unit is regarded as a separate formation (Shah, 2009) and has been exposed in the southern localities of study area. Lithologically, the Gandaf unit/ formation consist dark coloured schistose rocks with interlayered graphitic slates, phyllites, graphitic and non-graphitic marble and calcareous schist (Shah, 2009). DiPietro et al. (1998) reported the intrusion of Swat and Mansehra granites in the upper portion of Gandaf Formation. The age of Salkhala Formation is considered pre-Cambrian on the basis of positional order and correlations (Shah, 2009). The Tanawal formation is lying on the top of it having transitional contact.

The Tanawal Formation mainly contains medium grained quartzite, andalusite-staurolite schist and quartz-mica schist (Calkins et al., 1969). This formation is also correlated with the Silurian-Devonian unit known as Muth Quartzite exposed in Shimla region northern India (Calkins et al., 1969). The Tanawal Formation is believed to be late-Proterozoic in age based on intrusion of Cambro-Ordovician aged granite (LeFort et al., 1980; Pogue et al., 1992b). This formation is unconformably overlain by Paleozoic succession of the Indian plate (e.g. Peshawar basin rocks) (Shah, 2009). The sharp intrusive contacts of the currently investigated Utla and Mansehra Granite with Tanawal Formation has been exposed in certain locations. The Manglaur Formation is lateral correlative of Tanawal Formation (Lawrence et al., 1989) which serve as the host rocks for analogous granites in the Swat regions.

The Paleozoic stratigraphic record of Peshawar Basin in the northern Indian plate host the Permian rift-related magmatic event. These rocks include Ambar Formation, Misri Banda Quartzite, Panjpir Formation, Nowshera Formation, Jafar Kandao Formation (Pogue and Hussain, 1986; Pogue et al., 1992b). The detailed stratigraphic column is presented in Figure 2.4. The complete and fossiliferous stratigraphic record inferred that these sedimentary units belong to the THS as the lesser Himalayan facies is characterized by the absence of Ordovician through Devonian strata (Pogue et al., 1992b). The analogous sedimentary record has been observed in the Zanskar Tethyan Himalayas of northern India (Gaetani et al., 1990). In contrast, relatively closer Kashmir basin (Fig. 2.2A) preserve both lesser and Tethyan Himalayan facies and show marked dissimilarities except the existence of extensively observed mafic magmatism in the form of Panjal Traps (Pogue et al., 1992a, b).

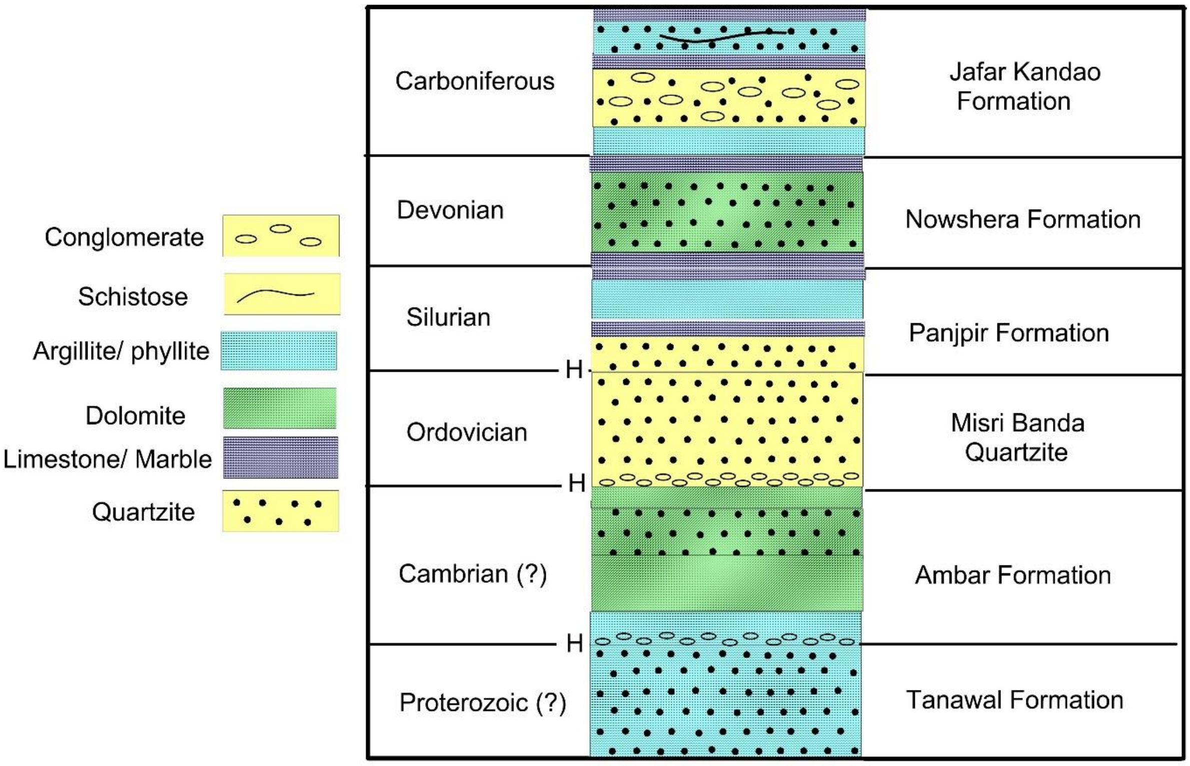

Figure 2.4. Paleozoic stratigraphy of Peshawar basin after Pogue et al. (1992b). H = Major Hiatus.

2.3. The Panjal Traps

The terms Panjal Traps has been introduced for the Permian basaltic flows in the northern margin of Indian plate associated with rifting event (Lydekker, 1883). Their geological and stratigraphic relationship with surrounding Paleozoic rocks were subsequently studied by Middlemiss (1910), Wadia (1961) and Nakazawa et al. (1975). The term arises from “Pir Panjal ranges” in Kashmir (Calkins, 1975), however, their occurrence has been reported from numerous zones in northern Indian plate including Pakistan (e.g. Papritz and Rey, 1989) and India (e.g. Honegger et al., 1982; Gaetani et al., 1990). The over- and underlying sedimentary strata indicate coastal to subaerial conditions during the eruption of these basalts (Nakazawa et al., 1975). The Artinskian to Kungurian time span has been suggested as the age of their eruption on the basis of geological relationship with surrounding strata (Nakazawa et al., 1975; Kapoor, 1977) which was later confirmed by first U-Pb dating (289 ± 3 Ma) of Panjal traps from NW India (Shellnutt et al., 2011).

The Panjal Traps are tholeiitic to alkaline basaltic flows with massive and aphyric appearance (Honegger et al., 1982). A certain degree of metamorphism ranging from zeolite to upper greenschist facies has been reported from their exposure in Kashmir, however, the metamorphic grade increases up to amphibolite facies towards the northeast exposure (Honegger et al., 1982). The petrographical and geochemical account of these basaltic flows has been described by Singh et al. (1976) and Honegger et al. (1982) from Zanskar and Suru region respectively from NW India. Papritz and Rey (1989) and Pogue et al. (1992a) present their distribution and geochemical affinity in the northern Hazara and lower Swat regions of Pakistan respectively. These studies relate Panjal traps to the late Paleozoic rifting phase in the northern Indian plate.

Geochemical and isotopic investigations of these basalts from Zanskar and Spiti areas in NW India reveal their emplacement in the northern Indian platform during the Neotethys opening (Chauvet et al., 2008). Trace elements and isotopic constraints suggest the derivation of these lava flows via higher degrees of partial melting from OIB-like mantle source (Chauvet et al., 2008). Hence, the origin of Panjal traps was related to deep mantle plume activity. However, recent comprehensive geochemical and isotopic investigation led Shellnutt et al. (2014) to suggest subcontinental lithospheric mantle (SLM) as their source. They oppose the mantle plume origin due to lack of connected high temperature lavas (ultramafic) and absence of crustal doming which was further supported by the trace elements ratios and REE modelling results.

2.3.1. Panjal Traps in NW Pakistan

The Panjal magmatism in the form of basic dykes connected with late Paleozoic rifting occur widespread in rocks lying between the Khairabad Thrust and MMT (Fig. 2.2). They are mostly restricted to pre-Permian units and have not been observed in Mesozoic or younger rocks (Pogue et al., 1992b). A stratigraphically consistent amphibolite horizon has been reported from Swat region in the Paleozoic strata of Peshawar Basin (King, 1964; Pogue et al., 1992b). This horizon was termed as metamorphosed sill (King, 1964) which was later named as Karapa greenschist after the name of its type locality (Pogue et al., 1992b). It overlies the Jafar Kandao Formation (Fig. 2.4) with sharp contact and restricts to the Carboniferous period as indicated by the overlying Kashala formation of Triassic age (Pogue et al., 1992b, 1999). The Panjal trap dykes were limited to the rocks underlying the Karapa green schist and the equivalent amphibolite horizons, hence these concordant lava flow horizons were regarded as the extrusive equivalent of Panjal traps dykes (Pogue et al., 1992a). The widespread occurrence of Panjal Dykes is reported in the rift related Ambela granitic complex and older peraluminous Utla and Mansehra granitoids.

The dykes intruding the Mansehra Granite in the Hazara region yielded 284 ± 4 Ma (hornblende) and 262 ± 1 Ma (biotite) ^{39}Ar/^{40}Ar ages (Baig, 1990) which further support the above mentioned stratigraphic relations. Majid et al. (1991) provide a petrographic account of such intrusions from the Malka area in lower Swat. These dykes are also reported from other regions including the Shewa-Shahbaz Garhi complex (Ahmed et al., 1990), Ambela granitic complex (Rafiq and Jan, 1988), Tarbela alkaline complex (Jan et al., 1981b), southern Hazara (Calkins et al., 1975), Attock-Cherat ranges (Yeats and Hussain, 1987), northern Hazara and Kashmir (Papritz and Rey, 1989) and Khyber agency (Shah et al., 1980).

The Panjal traps from Kashmir, Spiti and Zanskar area from NW India have been investigated in terms of their detailed geochemistry, source characteristics and geochronology (Chauvet et al., 2008; Shellnutt et al., 2014). However, apart from the timing and field relations, previous studies have not elaborated the formation of these basic intrusions in regions of NW Pakistan. The detailed geochemical characterization, investigation of source material and comparison with well-studied counterparts of these intrusions will aid understanding their regional tectonic implications.

CHAPTER 3

Implications of Rock Textures to Rock Mechanics

The size, shape and mutual arrangement of mineral grains in a rock, collectively known as its texture, is an effective indicator towards the various evolutionary and deformational/ tectonic stages during its creation history. Apart from the petrological significance, textural relation of minerals in a rock is also an important factor in formulating the mechanical nature of rock (Bell, 2007; Lindqvist et al., 2007). Intrusive rocks are characterized by granular textures, massive appearance and uniform composition with adequate strength for engineering requirements. However, different secondary processes (weathering, deformation, hydrothermal interaction etc.) during rock evolution can significantly affect these characteristics. The mechanical behaviour of rocks is generally controlled by several factors including degree of weathering, rock textures, mineralogical composition and porosity (Hecht et al., 2005; Undul and Tugrul, 2012; Zhang et al., 2012; Coggan et al., 2013; Sajid and Arif, 2015; Wazir et al., 2015).

Density and porosity are the fundamental properties of rocks influenced by mineral composition and arrangement (Sousa et al., 2005; Tullborg and Larson, 2006; Sajid and Arif, 2015). Increase in porosity results in density decrease of a rock. Porosity depends on voids in the rock and is also affected by various processes during the rock formation and post-crystallization conditions (dissolution and recrystallization) (Tugrul, 2004; Molina et al., 2011; Hu et al., 2014).

Granites are most common and abundant rock in the continental crust and widely used in construction industry due to their stability and persistent mechanical character. These rocks are also extensively used as dimension stone and building material. The important factors controlling mechanical behaviour of granite include its textural/ compositional characteristics and weathering degree (Sousa et al., 2005). Several environmental aspects (e.g. variability in temperature and moisture) are responsible for the weathering and alteration of rocks (Halsey et al., 1998). The mineralogical composition and textural relations (including the change in voids area) are the principal factors involved in controlling the physical and chemical changes caused by the weathering processes (Hudec, 1998).

3.1. Rocks Textures as a Controlling Factor

The mechanical properties of granites are generally controlled by their petrographic characteristics including grain fabric (i.e. size, shape, arrangement and degree of interlocking), type of grain contacts, mineralogical composition and the degree of weathering (Irfan, 1996). The importance of textural characteristics of rocks in describing the mechanical behaviour has been elaborated by several workers (e.g. Tugrul and Zarif, 1999; Fujii et al., 2007; Lindqvist et al., 2007; Yilmaz et al., 2011; Sousa, 2013).

Lindqvist et al. (2007) described the strong influence on functional properties of rocks by their respective intrinsic properties including chemical and mineralogical composition and textural features. The grain size, mineral orientation and distribution of grain size, are important features affecting the rock strength (Akesson et al., 2003; Tugrul, 2004; Zorlu et al., 2008; Yilmaz et al., 2011; Sousa, 2013). The mineralogical composition of major rock forming minerals is essential when assessing the mechanical behaviour of rocks together with assessment of the potential influence of texture (Tugrul and Zarif, 1999; Yilmaz et al., 2011; Arif et al., 2013). The petrographic observation of a rock is commonly used to investigate the modal concentration of minerals, their textural relationship and the intensity of intra- and inter-granular micro fractures. The significance of modal mineralogy and textural features of mineral grains for the evaluation of mechanical properties is elaborated below:

3.1.1. Concentration of minerals

The concentration and composition of individual mineral is an important factor in examining the overall strength of rock (Tugrul, 2004; Lindqvist et al., 2007; Yilmaz et al., 2011). The mineral composition is likely to be very sensitive to certain types of alteration e.g. comparing the behaviour of quartz and calcite to interact with acidic hydrothermal fluids. The silicates are generally more resistive to chemical weathering than carbonate minerals, however, there are some silicate minerals which deteriorate significantly when exposed to acidic fluids e.g. nepheline (Lindqvist et al., 2007).

Several petrographic indices were proposed based on the concentration of constituent minerals, their genetic relationship and fractures densities. These indices emphasise the reliance of mechanical properties on the petrographic features. Lumb (1962) proposed a quantitative index (X_d) for decomposed granite i.e.

$$X_d = N_q - N_{qo} / 1 - N_{qo}$$

where Nq and Nqo are the ratio between weight percentage of quartz and K-feldspar in decomposed and fresh granite respectively. Weinert (1964) described the index based on the concentration of secondary minerals for basic rocks. According to Weinert, rocks having more than 30% concentration of altered minerals are regarded as low quality material for engineering purposes. Mendes et al. (1966), Irfan and Dearman (1978) and Irfan (1996) proposed indices based on the percentage of sound and unsound minerals e.g.

$$I_p = \text{sound constituents } \% / \text{ unsound constituents } \%$$

The unsound constituents include alteration products of major rock forming minerals i.e. kaolinite after feldspar or serpentine after olivine. The content of voids and fissures mainly resulting from weathering are included in unsound constituents. The sound minerals include primary rock forming minerals. The higher value of the index indicates less weathering and mechanically sound nature of the rock. Onodera et al. (1974) described the index based on the density of micro fractures along the length of a measured traverse using a point counting method. Higher fracture density was associated with mechanically weaker/feebler nature of rock. Rigopoulos et al. (2010) divided the constituent minerals of mafic rocks on the basis of their physical properties and proposed a micro-petrographic strength index (I_{ps}) based on their modal concentration i.e.

$$I_{ps} = S_o/H + S_e/P$$

where S_o = secondary minerals formed during metamorphism, P = primary minerals (magmatic), S_e = soft minerals (≤ 5 hardness on Moho scale) and H = hard minerals (≥ 5 on Moho scale).

These indices are widely employed in assessment of rock’s mechanical nature. Furthermore, concentration of individual minerals have also been investigated to see its relation with mechanical properties. The rock composed of a higher concentration of physically strong minerals (e.g. quartz) is generally strong. However, the effect of minerals concentration including quartz and K-feldspar on the granite strength yield differences between the interpretations of different researchers. The concentration of quartz gives a positive relationship with strength of granitic rocks from different regions (Tugrul and Zarif, 1999; Khalil et al., 2015; Sajid and Arif, 2015) however, similar comparisons can portray either a negative relation (Sousa et al., 2013; present study) or no relation (Yilmaz et al., 2011) with granites from other areas. Such results show that concentration of individual mineral alone (apart from its harder nature) is not significant when describing the strength of rocks. This suggests that additional factors, such as textural characteristics, may also have a significant influence on the engineering behaviour of granites.

3.1.2. Textural description of rock

The coarse grained rocks are generally weaker than fine grained ones (Bell, 2007). This interpretation is favoured by a number of researchers (Onodera and Asoka, 1980; Tugrul and Zarif, 1999; Sajid et al., 2009; Yilmaz et al., 2011). However, the reason behind the fine texture of rock might be a limiting factor, for example, Sajid and Arif (2015) reported very fine-grained granites having high porosity formed due to intense deformation along the shear zones. Though looking very fine grained, when compared to their coarse grained counterparts, these rocks yield very low strength due to highly porous nature.

The variation of grain size and grain shape within a rock is also important in controlling its mechanical behaviour. The increase in complexity in grain geometry actually increases bond strength with adjacent grains (Howarth, 1988; Akesson et al., 2003; Lindqvist et al., 2007). This implies that suturing of minerals along grain boundaries has a positive impact on strength of rock. Idiomorphic rocks tend to more flexible for initiation of rock fracturing due to less resistance along grain boundaries. Sajid et al. (2009) compared strength of amphibolites having irregular mineral boundaries with idiomorphic gabbronorites and found similar outcomes. Distribution of different sized grains in a rock also show greater resistance to applied stresses and result in increased strength of rock relative to equigranular rocks (Raisanen, 2004; Lindqvist et al., 2007).

The investigations examining the dependence of rock mechanics on mineralogical and textural characteristics is not only restricted to granitic lithologies. The understandings have also been successfully used for other rock types including dolerite, serpentinite, limestone, sandstone, quartzite, amphibolite and argillite. Rigopoulos et al. (2013; 2014) described the micro-petrographic index for basic and ultrabasic rocks which demonstrate the effect of secondary processes on the mechanical nature of these rocks. The interaction of fractures formed during the compressional testing with mineral grains and mineral boundaries revealed predominant intra-granular fracturing due to alteration of minerals in troctolites (Rigopoulos et al., 2013). The relationship between different mechanical properties including strength (both uniaxial and tensile), specific gravity, degree of polishing and ultrasonic velocity of dolomites, sandstone and limestone and their respective petrographic features has been described by Mustafa et al. (2016). They describe the negative effect of deleterious components (e.g. chert) and micro-granular fractures on the strength of these rocks. The mineralogical controls of ultrabasic rocks (serpentinites) has been discussed by Diamantis et al. (2014). Following their thorough regression analysis, they presented different statistical relations between the mechanical and petrographic properties.

3.2. Weathering effects and Classification

The suitability of a rock for use as a construction material can be affected by deviation from their normal mechanical character caused by different processes including weathering, deformation etc. The variability in rock’s performance is usually dependant on the extent of weathering and type of weathering which needs to be properly quantified. Several authors have described the negative impact of weathering on the strength of different rock types (Fahimifar and Soroush, 2007; Ceryan et al., 2008; Basu et al., 2009; Rigopoulos et al., 2010).

Weathering and hydrothermal alteration are important factors negatively affecting the engineering characteristics of granites (Ceryan et al., 2008). Major minerals including plagioclase and orthoclase are altered to less resilient minerals e.g. kaolinite, sericite during the chemical weathering process eventually making the host rock mechanically weaker. Different mechanical properties of hydrothermally weathered granites were determined by Coggan et al. (2013). They described the marked reduction in strength of granites with increasing degree of weathering. The degree of kaolinization and associated mineralogical changes are responsible for the reduction of mechanical strength of granites (Coggan et al., 2013).

Apart from influencing the mineralogy and chemical composition of minerals, the weathering intensity also influences the frequency, length, and appearance of joints on the granite surface (Ehlen, 2002). The joint spacing in highly weathered rocks is more as compared to slightly weathered which make the rock mass weaker. The changes in the nature, appearance and mineralogical composition along the joint surfaces with increasing weathering grade have also been reported (Ehlen, 2002). The thorough investigations of weathering grade and changes associated with it are important in the precise rock mass classification which result in the accurate engineering design.

Different approaches have been used to designate the weathering grade of rocks. Brown (1981) and Hencher et al. (1990) describe the discoloration, visibility of any alteration features and its extent on rock surface as the major classifying criteria of weathering degree. Irfan (1996) introduced micro-petrographic index depending upon the concentration of secondary mineral and other chemical indices to classify the granitic rocks on the basis of weathering. Major element oxides were used to calculate the chemical indices including weathering potential index, weathering product index, mobiles index etc.

Aydin and Basu (2005) describe the use of the Schmidt hammer for classifying the weathering grade of granites. They indicate that the multi impact used to calculate the hardness of the given rock surface yielded more reliable results and a better indication of weathering grade than the single impact. The Schmidt value of 45 is regarded as the dividing value between weathering grade-II and grade-II rocks by Hencher et al. (1990). Ceryan et al. (2008) described the physical changes in rock during the weathering processes via ultrasonic velocity testing. These changes were combined with slake durability to introduce the weathering index which designates rock to soil ratio of rock material. This ratio was further used to quantify the engineering behaviour of rocks.

Various physical and mechanical properties of rocks including ultrasonic velocity, porosity, uniaxial and tensile strength and point load index are used for weathering classification by Heidari et al. (2013). Simple regression analysis of properties against each other were used to describe the classification diagrams (e.g. Fig. 3.1). Previously published data on granites has been used for this classification. Momeni et al. (2015), for example, presented a triangular classification diagram using mechanical properties at the top corner and two mineralogical indices [micro-fracture index (MI) and decomposition index (D_{pob})] at the bottom line of triangle (e.g. Fig. 3.2). The mineralogical indices determine the degree of physical and chemical weathering and combined four different mechanical properties including point load index, compressive strength, p-wave velocity and quick water absorption to describe the weathering grade of granites. These diagrams can be applied to a wide range of granitoids for quantitative weathering classification.

The above mentioned and several other researchers describe the importance of weathering classification of rocks in determining their respective mechanical behaviour. The general agreement is that rocks with higher weathering grade are mechanically weaker. However, weathering is not the only criteria that controls rock behaviour as significant variation of strength of rocks can exist in rocks with similar weathering grade (Arif et al., 2013; Sajid and Arif, 2015). Evaluation of textural characteristics are therefore important for investigation of further factors that affect the mechanics of rock.

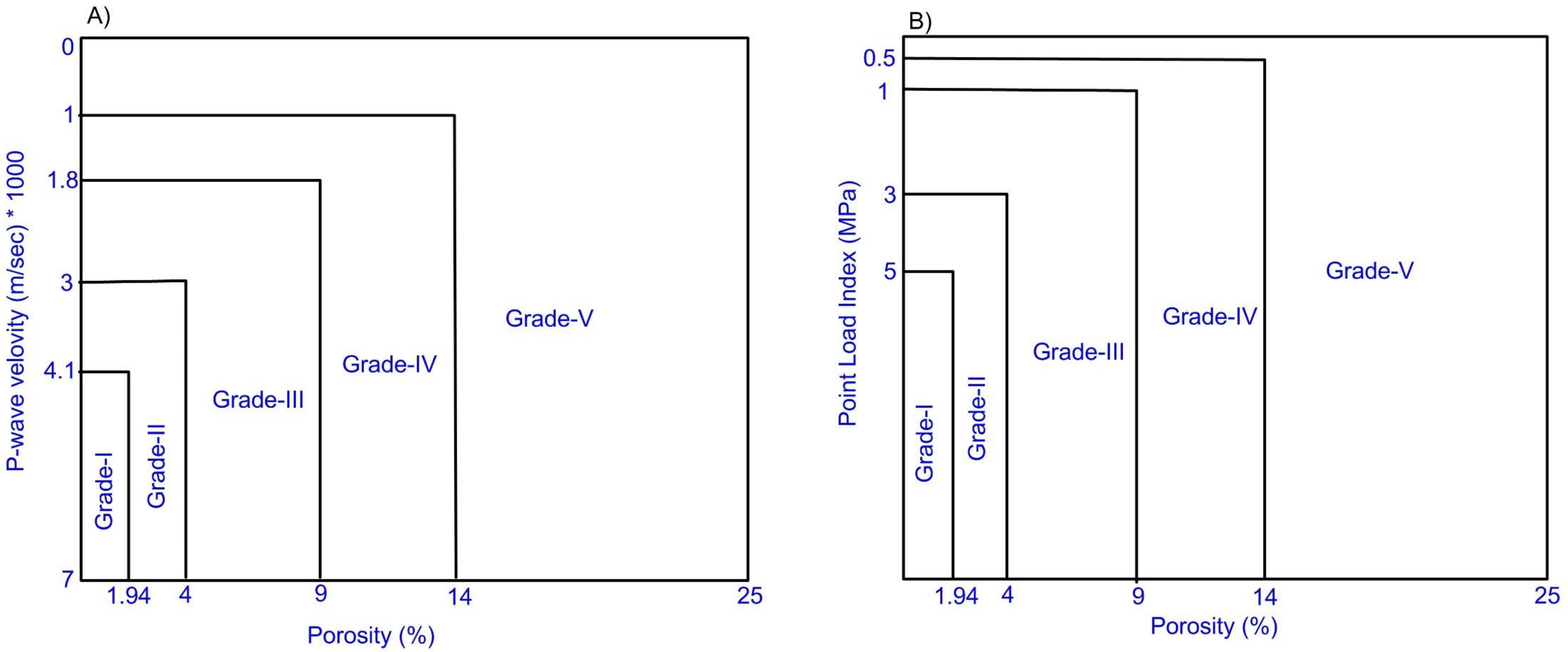

Figure 3.1. The classification of weathering grade using ultrasonic velocity and Point load index against porosity of granites (Heidari et al., 2013).

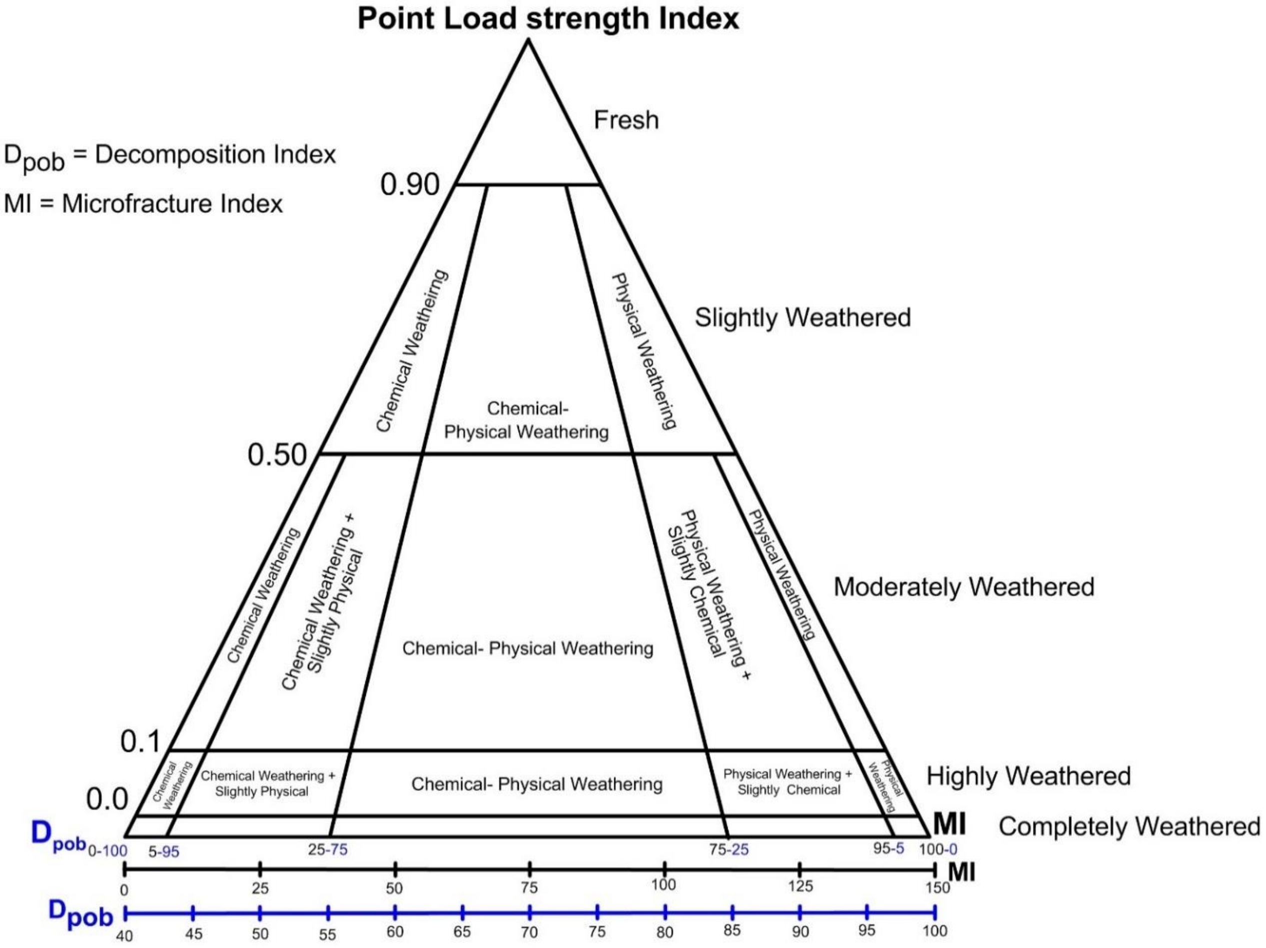

Figure 3.2. Triangular weathering classification of granites based on Point load strength index and mineralogical properties. MI = number of cracks/ 50mm traverse; $D_{pob} = D_{weathered} \times 100 / D_{total}$ where "$D_{weathered}$" is concentration of decomposed feldspars and biotite, "D_{total}" is total concentration of feldspar and biotite (see Momeni et al., 2015 for further details).

3.3. Scope of the current investigation

The study area is in the vicinity of the Tarbela Dam, one of the largest earthen dam of the world located on the Indus River (Fig. 2.2). Several tributaries are feeding the Indus River passing through the Utla and Mansehra Granites, some of which are proposed for the small dam sites to be built on, for hydro-power and irrigation projects. Apart from the geological and tectonic significance of the area, the location of these engineering project enhances the geotechnical research on rocks exposed in the region. The mechanical aspects of these granites, therefore have been an important consideration to be appropriately addressed for these projects. The investigation of their feasibility to host a large scale engineering structure and suitability for use as constriction material opens a wide area for geotechnical research on these granites.

Granites are also one of the common rock types used in various engineering operations throughout the world. The other important reason for selecting granite is its stability in diversity of conditions relative to other rock types. Four different granites each from the Utla, Mansehra, Ambela and Malakand area with distinctive textural and compositional characteristics from NW Pakistan have been examined (Fig. 3.3).

The important petrographic features controlling strength of rocks include overall grain size of rock (Bell, 2007), size and shape of individual mineral, modal concentration of harder minerals (Tugrul and Zarif, 1999; Yilmaz et al., 2011), nature of the grain boundaries (Sousa, 2013), arrangement of grains and their preferred alignments (Sajid and Arif, 2015). However, some uncertainties still exist which need to be properly explored particularly concerning the effect of modal concentration of individual minerals and the overall grain size of rocks (Yilmaz et al., 2011).

Increasing degree of weathering generally reduce the mechanical behaviour of rocks (Ehlen, 2002; Ceryan et al., 2008; Coggan et al., 2013). However, certain variations exist in the mechanical response/behaviour of rock with similar weathering grade. The role of textural parameters need to be investigated/assessed appropriately as a cause for these variations.

The weathering grade of studied samples has been identified using various schemes described in earlier section. The three granite types have similar weathering grade which will investigate the textural controls on the variation in their mechanical properties. Pre- and post-tests petrographic observations have been examined to identify the interaction of mineral grains and mineral boundaries with newly formed fractures. The outcomes of different tests have been thoroughly compared with previously available data for granites and other rock types from different localities to make interpretations. The details of each sample, procedures of testing and subsequent analyses has been described in relevant chapter.

Figure 3.3. Characteristic granite samples from NW Pakistan used in current investigation for mechanical testing.

CHAPTER 4

Geochemical characterization, petrogenesis and mineralization potential of the Utla and Mansehra Granites, North-West Pakistan

4.1. Introduction

The northern edge of Indian plate contains the pre-Himalayan granitic suites in the NW Pakistan which include both peraluminous and alkaline granitic systems (Fig. 4.1). A detailed mineralogical and geochemical investigation of these granitoids has always been important for a better understanding of the process of formation of continental crust, its evolution through geologic times and its economic significance. The peraluminous systems are regarded as one of the major source of economic minerals including Sn, W, Zn etc. (Ruiz et al., 2008; Clemens, 2012; Solomovich et al., 2012). The mineralization associated with magmatic or hydrothermal process is ensued by the higher concentration of these elements in pertinent granitic systems (Cerny et al., 2005).

The biotite-rich megacrystic granites are exposed in different regions of NW Pakistan i.e. Utla, Mansehra and Swat (Fig. 4.1). The Mansehra Granite yielded whole rock Rb-Sr age of 516 ±16 Ma (LeFort et al., 1980) which is also considered as the age of Swat granite due to their similar field and petrological character (Anczkiewicz et al., 1998; DiPietro and Isachsen, 2001). The Utla Granites were initially considered as representing the eastward extension of per-alkaline and relatively younger Ambela Granite due to their geographically close location (Fig. 4.1) and field similarities e.g. megacrystic nature (Rafiq and Jan, 1988; Pogue et al., 1992a). However, Sajid et al. (2014) highlighted their preliminary geochemical signature which is incompatible with their comagmatic origin and correlated Utla granites with the peraluminous Mansehra Granite lying towards the east (Fig. 4.1).

The main purpose of this study is to explore the lithological variations and geochemical characteristics of Utla granitoids and to assess their petrogenetic controls on evolution and mineralization in the area. The targeted approach using detailed mineral chemistry and comprehensive whole rock geochemical data (both major and trace elements) has been applied for the first time for any pertinent granitic suite for the investigation of their origin and petrogenetic history. The mineral chemistry of principal phases has been used to describe fractional crystallization, physical/ chemical variations and post-crystallization processes during the granites evolution. Rare earth elements geochemical modelling has been used to evaluate the source rock characteristics, partial melting conditions and role of fractionation. The assessment of mineralization potential of these granites is also essential to identify the prospects of economic elements particularly Sn-W in the area. Trace elements data set have been used to evaluate mineralization potential of granites using different elemental ratios (Olade, 1980; Lehman, 1987; Srivastav and Sinha, 1997; Baker et al. 2005).

The Cambro-Ordovician peraluminous granites in the northern edge of Indian plate and other northern Gondwana regions is reported (e.g. LeFort et al., 1986; Girard and Bussy, 1999; Zhang et al., 2004). The geochemical data of these granites (e.g. Miller et al., 2001; Dong et al., 2013) has also been compared with studied granitoids to explore their petrogenetic and tectonic relationship.

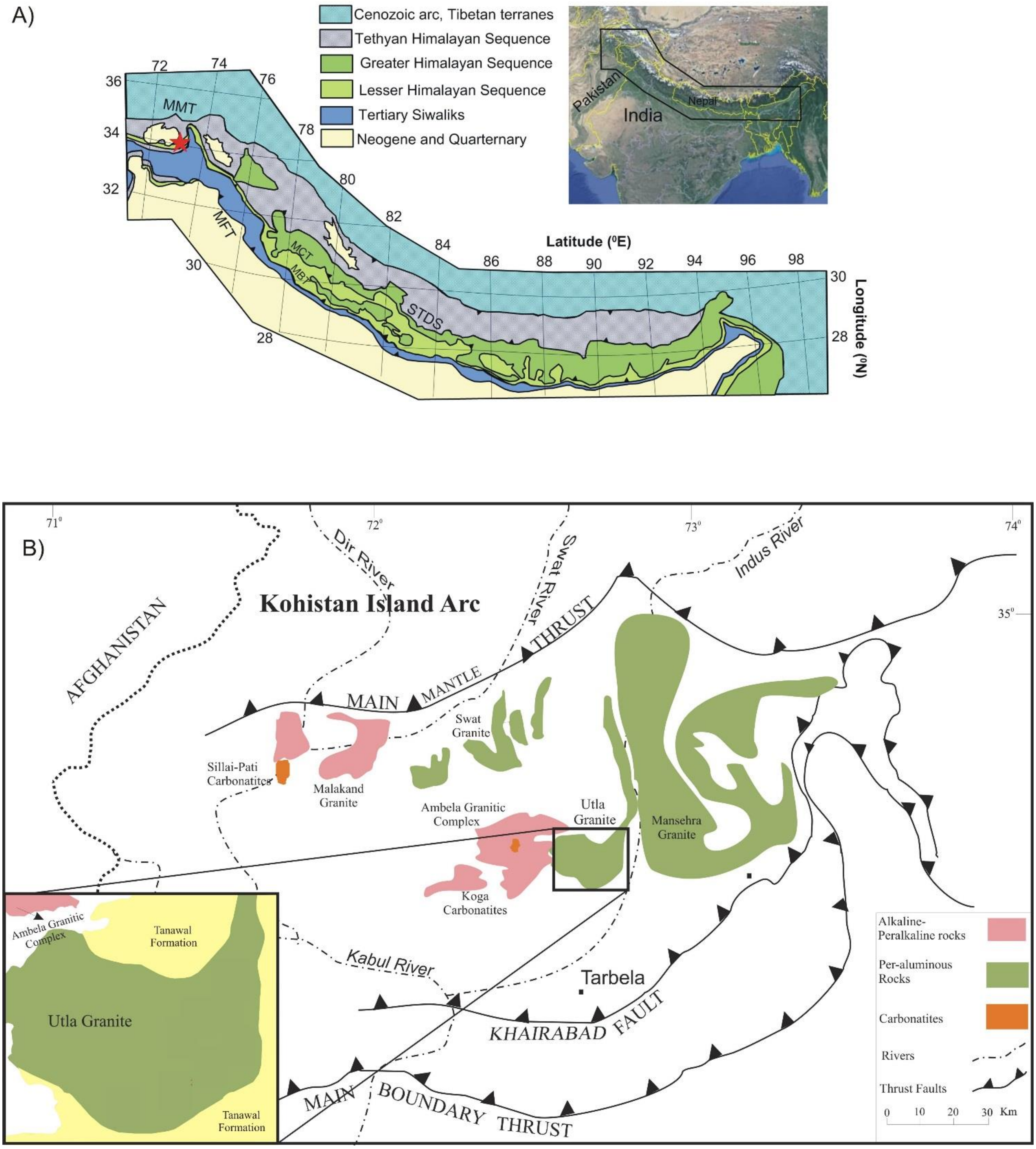

Fig. 4.1. A) Geologic map of the Himalayan terrane (redrawn after Kohn, 2014), star showing location of Fig. 1B, B) Regional tectonic map of NW Pakistan (after Pogue et al., 1999; Khattak et al., 2005) elaborating the major granitic suites, inset showing the geological map of the study area.

4.2. Regional Geology

The Indian plate, Kohistan Island Arc (KIA) and Eurasian plate are the three principal petro-tectonic domains present in north-western Pakistan. The KIA originated as a result of intra-oceanic subduction within the Tethys Ocean and collided with the Indian plate along a regional fault zone known as Main Mantle Thrust (MMT) (Fig. 4.1) (Searle and Treloar, 2010; Burg, 2011). The northern Indian plate is divided in three tectonic units known as Lesser Himalayan sequence (LHS), Greater Himalayan Sequence (GHS) and Tethyan Himalayan sequence (THS) separated two regional fault systems termed as Main Central Thrust (MCT) and South Tibetan Detachment system (STDS) (Fig. 4.1). Different granitic suites have been identified in Himalayan terrane i.e. early Cenozoic linked to Himalayan collision (e.g. Searle et al., 2009; King et al., 2011), rift related late Paleozoic (e.g. Noble et al., 2001; Ahmed et al., 2013) and early Paleozoic due to accretionary orogenesis (e.g. LeFort et al., 1986; Schelling, 1999; Cawood et al., 2007; Wang et al., 2013). The early Paleozoic granitic rocks intrude different GHS and LHS lithologies confirmed by their several geochronological investigations (e.g. Girard and Bussy, 1999; Miller et al., 2001; Gehrels et al., 2006a).

The study area lies towards the south of the MMT in the northern portion of the Indian plate (Fig. 4.1) and constitutes a portion of the Himalayan zone. The peraluminous granitic rocks in the region (Fig. 4.1) are believed to be the continuation of early Paleozoic belt in Himalayan terrane (LeFort et al., 1986; DiPietro and Isachsen, 2001; Wang et al., 2013). Pre-Cambrian Tanawal Formation containing meta-pelites and quartzites serves as country rock for the intrusive Utla and Mansehra granites (Fig. 4.1). Swat granite is hosted by Manglaur Formation which is considered as lateral correlative of Tanawal Formation (DiPietro et al., 1993). The region is mainly effected by regional Barrovian metamorphism due to Tertiary collision of Indian plate with KIA (Treloar, 1997). The systematic study of metasedimentary units indicates increase in metamorphic grade from chlorite to sillimanite grade towards the collision boundary (Treloar et al., 1989a). The pre-Himalayan deformation and tectonism in early Paleozoic have also been identified in the region shown by metamorphic imprint of Proterozoic strata i.e. Hazara Formation and Manglaur Formation (Baig et al., 1988; Williams et al., 1988) and unmetamorphosed Paleozoic sequence (Pogue et al., 1992b). Analogous pre-Himalayan tectonism has also been noticed in other Himalayan regions from NW India and Nepal (Gehrels et al., 2006a, b).

Alkaline rocks belonging to Peshawar Plain Alkaline Igneous Province (PPAIP) associated with Permian rifting event also exist in similar region (Fig. 4.1).

Associated with this event, dyke intrusions of basic composition are noticed in the Utla and Mansehra granites.

4.3. Methodology

The chemical composition of minerals from representative rock samples were determined using a JEOL JXA-8200 Superprobe at Camborne School of Mines (CSM), University of Exeter, UK. An accelerating voltage of 20 kV, beam current 10 nA and beam diameter of 5 µm were used for analysis of all minerals. The instrument was calibrated (elements and X-ray lines shown in parentheses) using orthoclase (SiKα, KKα), almandine (FeKα, AlKα), albite (NaKα), wollastonite (CaKα), periclase (MgKα), rhodonite (MnKα), rutile (TiKα), tugtupite (ClKα) and fluorite (FKα) standards. Mineral formulas were calculated on the basis of stoichiometry and charge balance. Tourmaline formulae were calculated with the spreadsheet of Tindle et al. (2002).

The whole rock major element compositions were determined using the Bruker S4 Pioneer wavelength dispersive X-ray fluorescence (XRF) spectrometer at CSM on glass disks. Standards (SARM-1 and DNC-1) were run at the start and at the end of each batch to monitor drift and the precision of the instrument during data acquisition. For sample preparation, fresh rock samples were crushed and ground using an agate mill. Analytical error on the total concentration of each element is <1% for SiO_2, Al_2O_3, Na_2O and K_2O, <2% for CaO, Fe_2O_3 and TiO_2 and <10% for MgO, MnO and P_2O_5.

The trace elements, including rare earth elements (REEs) were determined by Inductively Coupled Plasma Mass Spectrometry (ICP-MS) at CSM. Four acids including HF, HNO_3, $HClO_4$ and HCl were used to digest the rock powder in Teflon tubes for analysis following the procedure of Yu et al. (2001). Two blanks and two reference solutions (Sarm-1: granite and DNC-1; Dolerite) were prepared and analysed during each analytical run to assess the elemental contamination and precision. A reference solution, with a known concentration of elements, was also analysed after each six unknowns to observe instrumental drift. The precision is <5% for all the element except for La, Ce and Zr which is <10%.

4.4. Field features

The Precambrian Tanawal Formation has been intruded by the Utla and Mansehra granites with a sharp intrusive contact observed in different regions (Fig. 4.2A). The map relations suggest extremely folded and deformed geometry of the Utla and Mansehra Granites (Fig. 4.1) which is in response to the Tertiary Himalayan collision. Such relations can lead to misinterpret the emplacement mode of these granites however, continuous exposure of these granites for several kilometres in field exposure confirm their emplacement as large granitic pluton. On the basis of field features, the Utla granites can be divided in to megacrystic granites (MPG), aplite dykes having granitic composition with fine to medium grained texture (AMG) and quartz rich veins (QRV) (Fig. 4.2B-D). The mineralogical composition and field characteristics of these intrusive units are summarized in Table 4.1. QRV contain < 5% feldspars and range in thickness from few centimetres up to several centimetres. Apart from textural differences, the darker minerals content is less in AMG than MPG. Dykes of mafic composition also cross cut the host granites at certain places. Most of the granites are fresh and compact however, foliation is observed in some areas particularly along shear zones. In certain places, surface of granitoids show intense weathering and appears dark brown in colour. Samples from such area show marked distinctions in trace elements composition from the rest of granitoids (details are given in later sections). Tourmaline rich veins cross cut both the MPG and AMG (Fig. 4.2E). Moreover, tourmaline nodules are observed in certain areas (Fig. 4.2F).

4.5. Petrography and mineral chemistry

The modal mineralogical composition of the Utla and Mansehra granites is presented in Table 4.2. All the samples are plotted in the field of granites in the IUGS classification with subtle variation in the concentration of major minerals (Fig. 4.3A). Both the Utla (MPG) and Mansehra granites have plagioclase and alkali feldspar (including both orthoclase and microcline) as phenocrysts. Plagioclase is mostly cloudy displaying partial to complete alteration to sericite and clay minerals. Micas (including biotite and muscovite) and tourmaline are commonly occurring accessory minerals as well as lesser amounts of rutile, garnet, apatite and andalusite. Rounded to sub-rounded nodules formed by accretion of dark coloured tourmaline is observed in AMG. In addition to quartz and subtle amount of feldspar, QRV also contain well developed coarse grained (up to 1cm long) dark tourmaline grains. In subsequent text, the chemical composition of important minerals is described (the complete set of minerals composition is provided in Appendix-1):

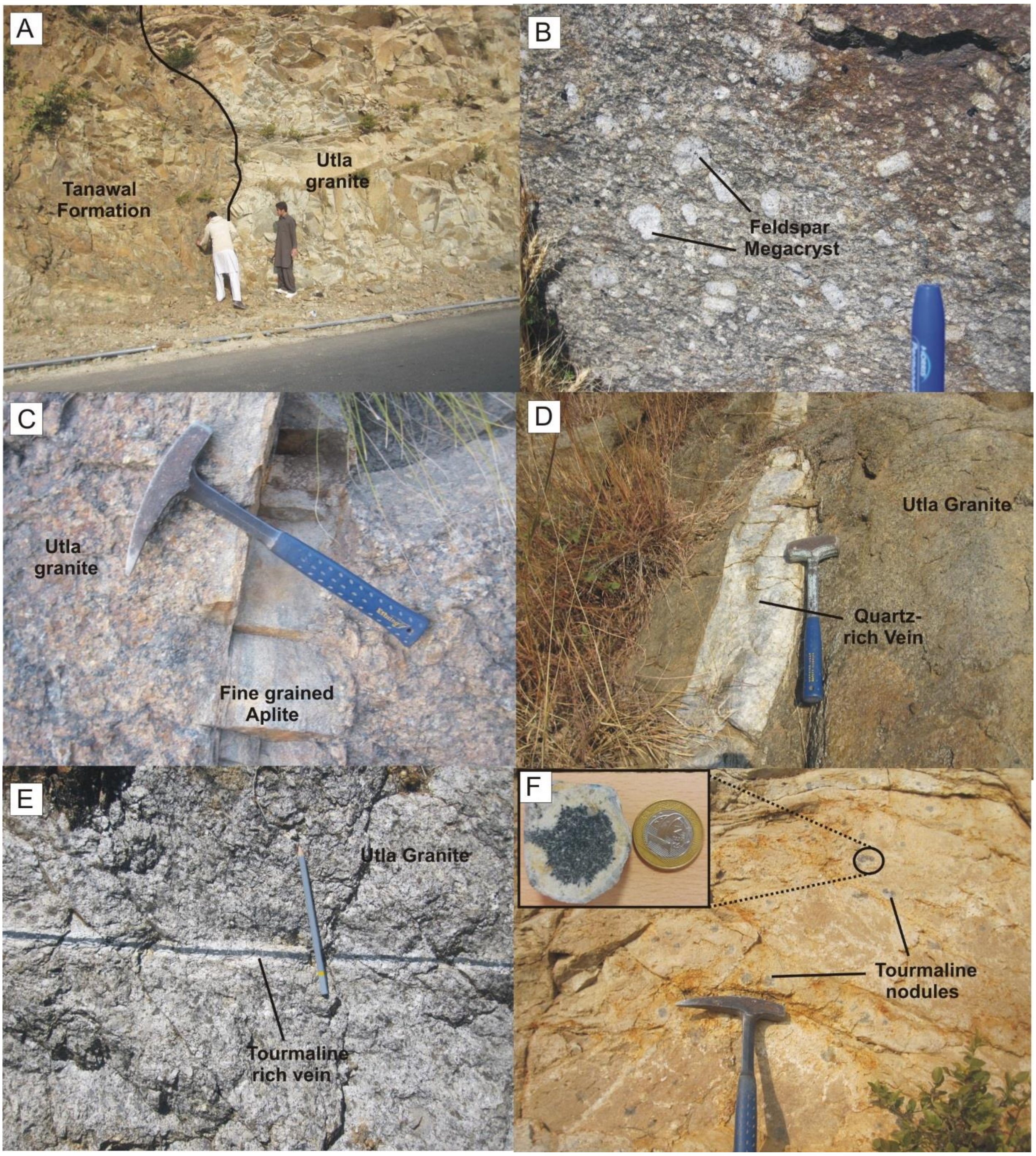

Fig 4.2. Field photographs: A) Sharp intrusive contact between the Utla granite and Tanawal Formation, B) Feldspar megacrysts in the Utla Granites, C) aplite dyke (AMG) crosscutting MPG rocks D), cross cutting QRV, E) tourmaline vein in Utla Granite, F) nodular tourmaline in Utla Granites, inset showing close-up of polished tourmaline nodule.

Table 4.1. Field and mineralogical features of Utla granites

Magmatic Unit	Field characteristics	Major Minerals	Minor assemblage (dominant minerals in bold letters)
Megacrystic granite (MPG)	K-feldspar and plagioclase phenocrysts, medium to coarse grained groundmass, tourmaline and biotite recognisable in field, foliated along shear zones	Plagioclase, K-feldspar (orthoclase and microcline), quartz	**Tourmaline, biotite, muscovite**, andalusite, apatite, rutile, zircon, beryl
Fine to medium grained aplite dykes (AMG)	Texturally homogenous, nodular tourmaline in places	Plagioclase, orthoclase, quartz	**Tourmaline, biotite, muscovite, epidote, garnet,** rutile, zircon
Quartz rich veins (QRV)	Coarse grained, extremely fresh and white in colour	Quartz, feldspars (<5%)	**Tourmaline**

4.5.1. Feldspars

Plagioclase occurs as phenocrysts as well as forming part of the MPG groundmass. Some of the phenocrysts display distinct zoning (Fig. 4.3B). The albite content of zoned plagioclase grains systematically increases from core to margin (core: An_{36}, margin: An_{16}) (Appendix-1) elaborating the fractional crystallization of melt. Margins with less calcic compositions are fresh while calcic cores show alteration to clay minerals and sericite (Fig. 4.3 B-C). Plagioclase in the ground mass is mostly uniform in composition ranging from An_{23} to An_{11} (Fig. 4.4A). In comparison, plagioclase from AMG is mostly unzoned and has a high albite content ($An_{0.22}$-An_{6}) (Fig. 4.4A).

Alkali feldspar, including both orthoclase and microcline, occurs as phenocryst as well as groundmass in the MPG. Perthite exsolution is observed in orthoclase grains; hence indicates their re-equilibration under sub-solidus conditions. Feldspars from the AMG samples do not show exsolution showing their faster cooling rate relative to MPG.

Table 4.2. Modal Mineralogical composition of Utla and Mansehra granites

Sample	Type	Qtz %	K-Feldspar%	Pl%	Bt %	Ms%	Tur %	*Others
UT-10	MPG	45.22	25.66	10.11	7.52	9.96	1.1	0.43
UT-11	MPG	43.22	26.3	11.2	8.21	8.85	0.9	1.32
UT-17	MPG	35.22	30.12	18.11	5.1	9.93	1.24	0.38
UT-19	MPG	34.23	24.2	22.23	8.99	7.23	2.1	1.02
UT-31	MPG	32.65	22.65	25.3	9.65	8.53	0.89	0.33
UT-34	MPG	28.22	26.32	28.23	8.12	7.52	1.2	0.39
UT-35	MPG	30.26	23.65	29.23	10.23	6.21	0.23	0.19
UT-40	MPG	26.29	25.21	30.62	10.23	5.21	0.85	1.62
UT-41	MPG	30.11	24.81	29.63	4.21	9.63	0.52	1.1
UT-48	MPG	27.32	24.71	32.22	5.52	8.23	1.12	0.89
UT-59	MPG	35.26	22.13	28.62	7.94	4.56	0.64	0.85
UT-65	MPG	28.63	24.21	33.09	6.8	4.2	2.11	0.96
UT-66	MPG	30.16	26.38	31.21	5.69	5.98	0.21	0.37
UT-69	MPG	26.32	26.21	33.24	6.58	4.62	2.01	1.02
UT-73	MPG	30.15	29.93	28.36	4.22	5.69	0.96	0.79
UT-18	AMG	34.21	29.52	21.03	5.32	7.69	0.97	1.26
UT-24	AMG	34.21	31.24	24.12	4.12	5.17	0.26	0.54
UT-29	AMG	36.21	29.61	20.12	3.68	8.93	0.82	0.63
UT-30	AMG	32.18	31.27	22.63	5.84	7.98	0.26	0.74
UT-36	AMG	29.54	29.82	24.21	5.23	8.21	1.83	1.01
UT-38	AMG	34.21	27.25	23.61	6.23	7.63	0.89	0.28
UT-42	AMG	36.23	26.23	24.62	5.23	6.21	0.23	0.65
UT-43	AMG	36.21	30.26	19.36	5.32	7.92	0.23	0.71
UT-44	AMG	32.12	29.63	22.15	6.21	6.39	1.69	1.81
UT-46	AMG	36.23	34.09	17.02	3.21	8.96	0.12	0.63
UT-77	AMG	39.02	34.21	16.23	3.2	6.81	0.36	0.21
M-3	MG	23.45	26.23	34.08	8.41	6.11	1.12	0.65
M-4	MG	28.63	24.65	30.19	7.52	6.91	0.98	1.12
M-5	MG	29.71	25.23	30.19	5.21	7.26	1.23	1.18
M-11	MG	30.14	25.02	28.32	7.62	7.32	1.06	0.65
M-17	MG	32.11	21.01	28.07	9.93	7.32	0.85	0.71
M-19	MG	35.15	27.62	22.42	8.65	5.12	0.21	0.84
M-22	MG	38.26	27.02	23.24	6.98	3.01	0.65	0.84
M-26	MG	29.26	27.12	27.69	7.23	6.32	1.21	0.63
M-27	MG	32.16	27.32	23.61	8.21	7.62	0.56	0.52
M-29	MG	39.02	28.91	21.02	5.21	4.32	0.65	0.87

* include apatite, zircon, andalusite, garnet, epidote, rutile and opaque ores

Abbreviations: MPG = Megacrystic Utla granites, AMG = Aplite dykes in Utla granites, MG = Mansehra granites, Qtz = quartz, Pl = plagioclase, Bt = biotite, Ms = muscovite, Tur = Tourmaline

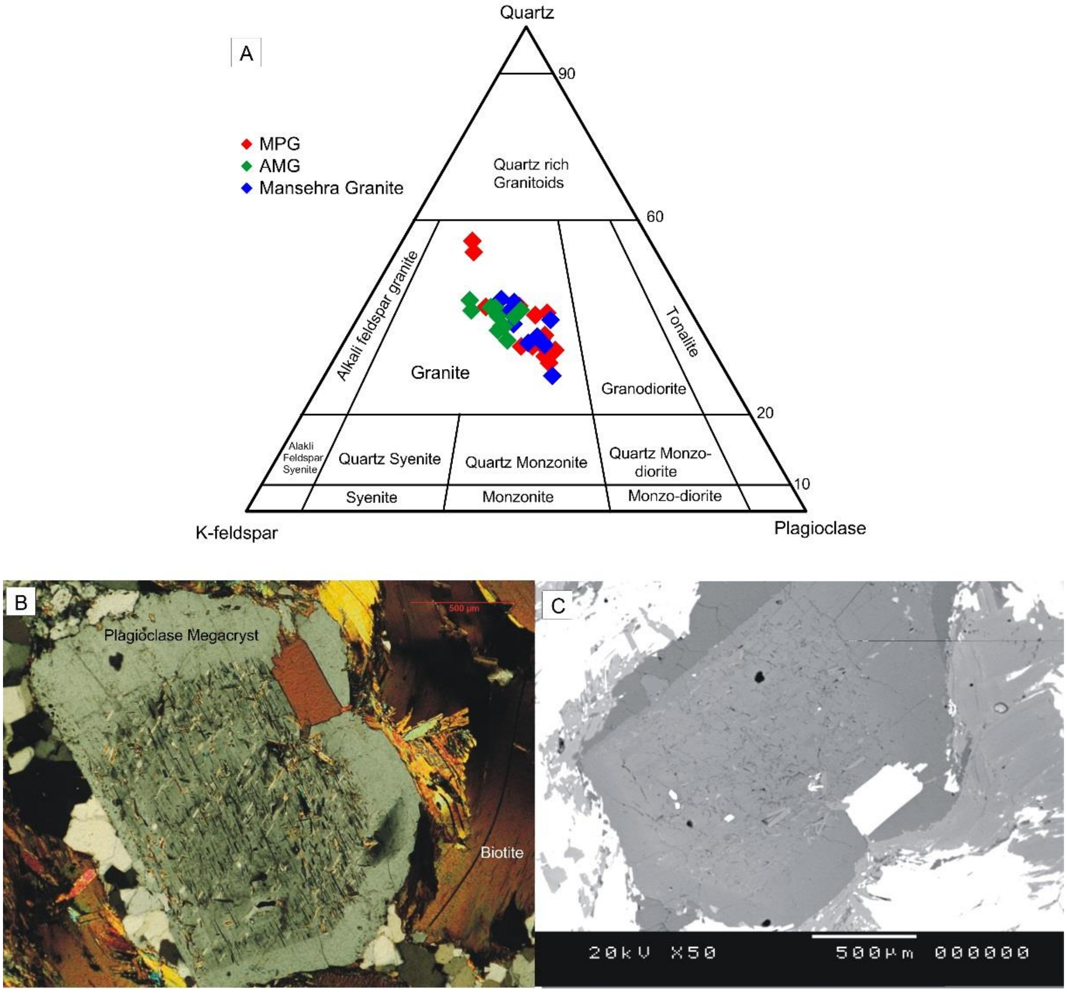

Fig. 4.3. A) Classification of the Utla and Mansehra Granites on the basis IUGS triangular plot after Le Maitre (2002), all the studied samples fall in the field of granite, B-C) Zoned plagioclase phenocryst micrograph and BSE image. Core if the grain is altered to sericite due to higher anorthite content.

4.5.2. Micas

The chemical variations in micas provides an excellent opportunity for distinguishing between the various phases of magmatism. The Fe+Mn+Ti–Al^{VI} vs Mg–Li plot (Tischendorf et al., 2001) groups the analyses into two clusters and thus effectively separates MPG and AMG biotites (Fig. 4.4B). Magnesian siderophyllite (Fe biotite) dominates in the MPG samples; however, the composition changes to siderophyllite in the AMG. The concentration of F is relatively higher in the MPG than AMG biotite (Appendix-1). The analyses of muscovite from both the rock types fall mostly in the region of muscovite, however some of the MPG data points approach the ferroan muscovite field.

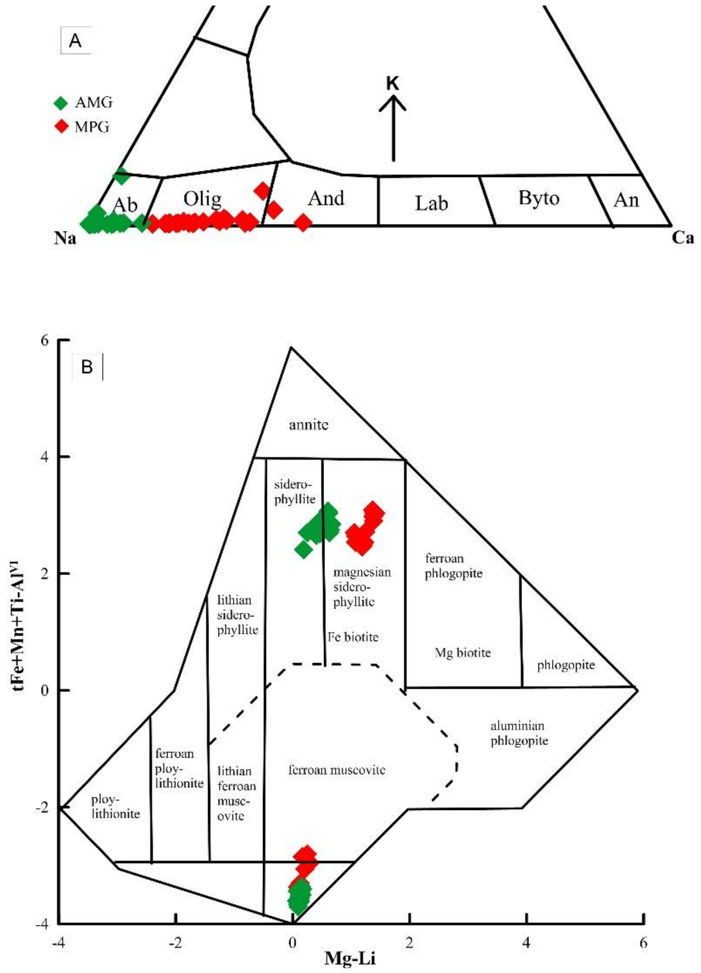

Fig. 4.4. Minerals classification of MPG and AMG, A) composition of plagioclase, symbols: Ab: albite, Olig: Oligoclase, And: Andesine, Lab: Labradorite, Byto = bytownite, An: Anorthite, B) classification of biotite and muscovite after Tischendorf et al. (2001), Mr enrichment in MPG biotites relative to AMG indicates fractionation during the evolution of magma.

4.5.3. Tourmaline

Tourmaline is of interest here because of its varying colours, composition and mode of occurrence in the Utla granites. It ranges from coarse discrete grains in the MPG to nodular/spotted appearance in AMG (Fig. 4.5A-B, 4.2F). Tourmaline rich veins, which crosscut both the MPG and AMG are also present in certain places (Fig. 4.2E). Beautifully zoned, larger tourmaline crystals (Fig. 4.5C) with distinct chemical compositions are present in the QRV. The classification scheme for tourmaline, based on the formula $XY_3Z_6(T_6O_{18})(BO_3)_3V_3W$, recommended by Henry et al. (2011) is followed in this study. Tourmalines with brown, green and bluish colour from the MPG, AMG and tourmaline rich veins all fall in the category of alkali tourmaline with mostly schorlitic composition (Fig. 4.6). However, the composition of some grains from tourmaline rich veins falls in the field of dravite. Tourmalines from QRV are mostly foitite (belong to the X-site vacant group) reflecting difference in their petrogenesis from the other tourmalines hosted by MPG and AMG due to the chemical differences observed.

Figure 4.7 show plots of different elements in tourmaline with various substitutions vectors shown for reference. $MgFe_{-1}$ seems to be the most important substitution in tourmaline from MPG, orbicules and tourmaline veins. No significant variation is shown by this substitution in QRV tourmalines. It roughly follows the trend exhibited by $rAl(Na, Fe^{2+})_{-1}$. Al^{Y}-Al^{T}vs Y^{2+}+ Al^{T} plot shows that significant amount of Al in Y site is compensated for by $[AlO, (Y^{2+}, OH)_{-1}]$, where is Y^{2+}= $(Fe+Mg+Mn)^{Y}$. Al^{T} is subtracted on abscissa and vice versa in order to minimize the effect of tschermak substitution (Ferla and Meli, 2007). The dominant substitution in QRV tourmaline seems to be $[rAl(Na, Y^{2+})]$. The significance of this substitution is also shown by Al^{Y} vs r plot. Less than 6 apfu of Si on T-site in most of the MPG and nodular tourmalines is explained with $Y^{2+}Si$ $(Al)_{-2}$ substitution. However, a significant amount of boron may also be present at this site (Ertl et al., 2006).

The Fe^{2+}/Mg ratio is plotted against Si which clearly discriminates tourmalines on the basis of colour (Fig. 4.7). Green and blue tourmalines, mostly from tourmaline nodules and QRV, show enrichment in Fe^{2+} relative to Mg (Fe^{2+}/ (Fe^{2+}+Mg) > 0.6). Vein tourmaline plot towards high Si as compared to tourmaline from MPG groundmass.

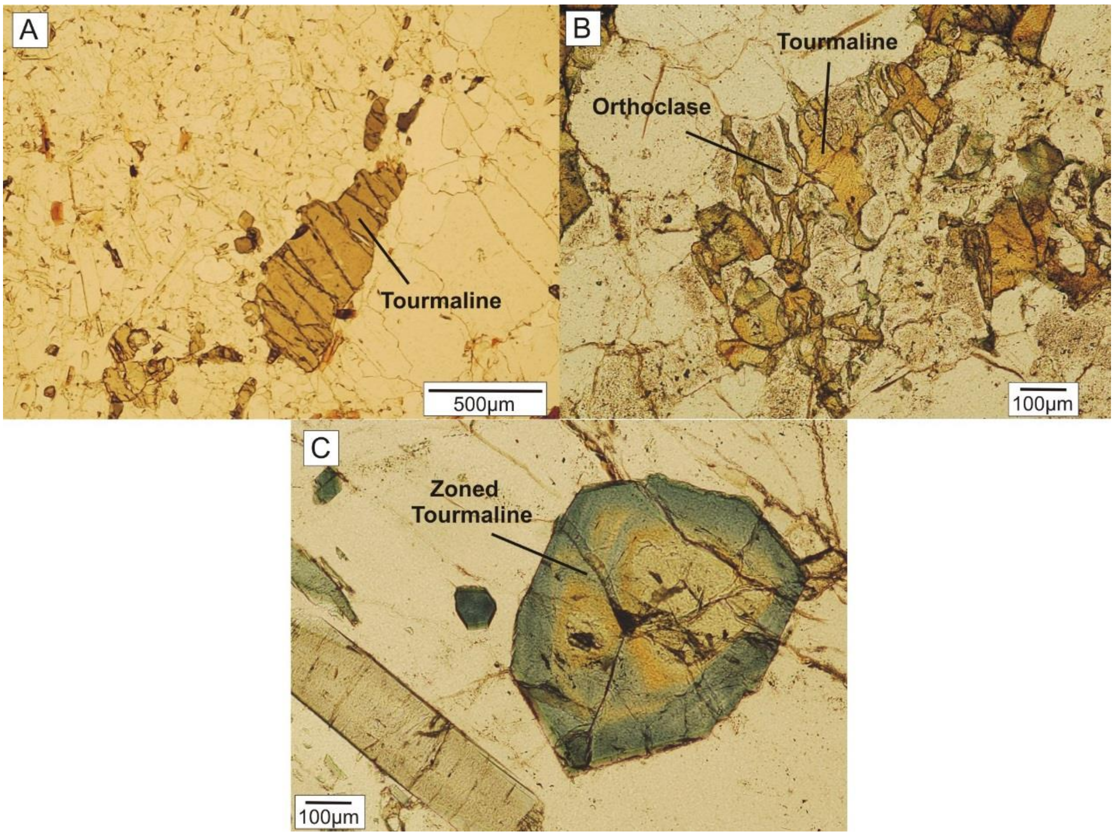

Fig. 4.5. A) Discrete brown coloured tourmaline in MPG, B) replacement of orthoclase by tourmaline in nodules C) coarse grained beautifully zoned tourmaline in QRV.

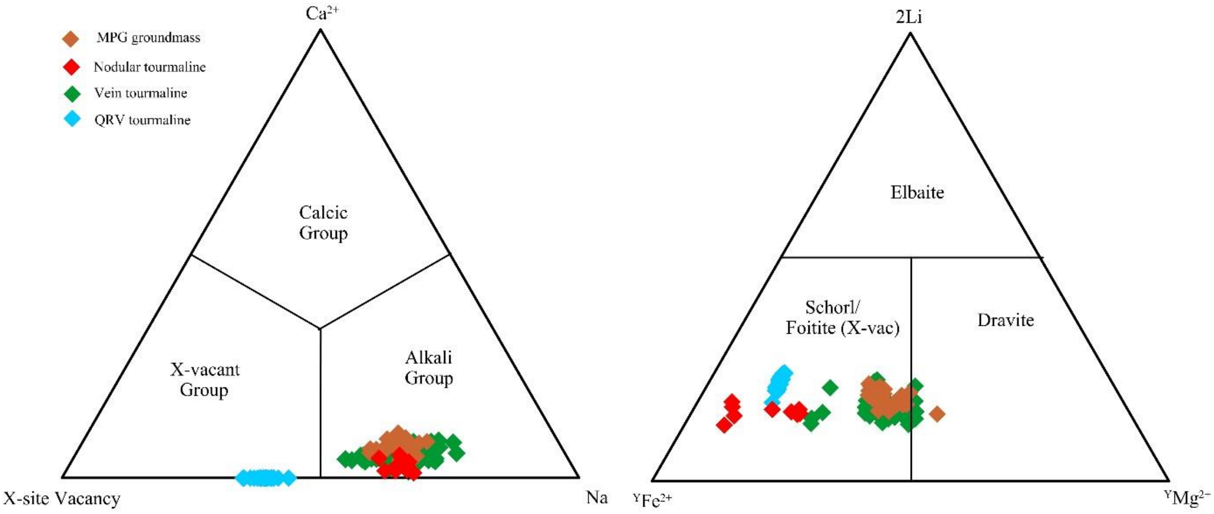

Fig. 4.6. Classification of tourmaline on the basis of A) X site occupancy, B) Y site occupancy (Henry et al., 2011). QRV tourmaline belong to X-vacant group with foitite composition. Other tourmaline fit to alkali group with mostly schorlitic composition.

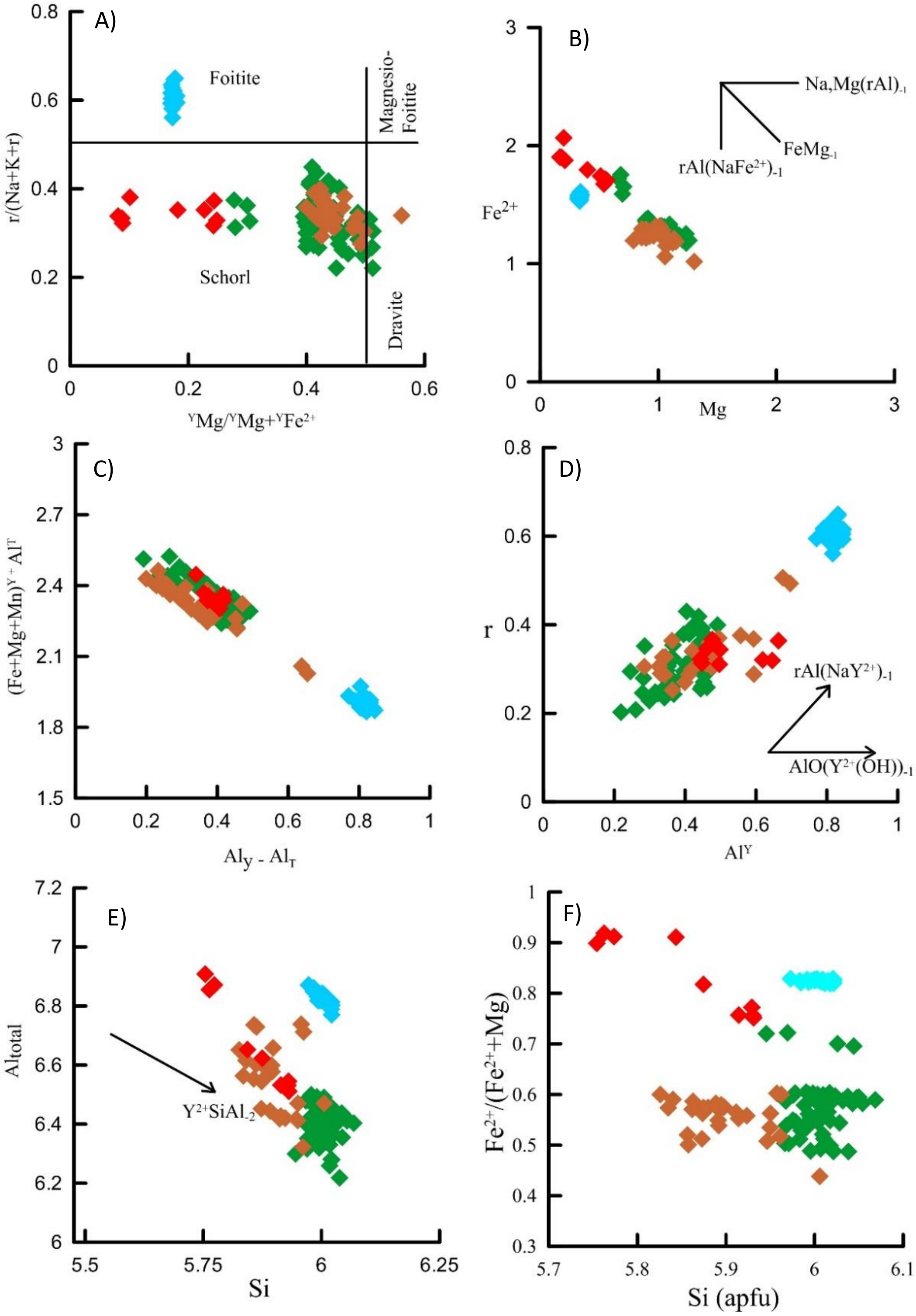

Fig. 4.7. Plots elaborating the cations substitution in different varieties of tourmalines with possible exchange vectors A) Tourmaline classification based on Mg content and vacancy on X-site (Henry et al., 2011), B) Fe vs Mg plot showing the significance of their substitution in most of the tourmaline except QRV, C) Al^Y-Al^T vs $(Fe+Mg+Mn)^Y$+ Al^T plot showing coupled substitution of Al with divalent cations on Y site, D) r (X-site vacancy) vs Al^Y plot showing rAl(Na, Y^{2+}) substitution in QRV tourmaline, E) Si vs Al-total plot showing the significance of Al substitution for Si and divalent cations in QRV, F) Fe^{2+}/(Fe^{2+} + Mg) vs Si plot showing discrimination between different tourmaline modes. Symbols are same as in Fig. 4.6.

4.5.4. Epidote

The petrographically two different types of epidotes have been recognized in AMG samples. Textural association with clay minerals and sericite, finer grain size and irregular crystal growth show one of these types to be the product of secondary processes e.g. hydrothermal alteration. The other type of epidote is low in abundance but texturally very distinct. It occurs in the form of fresh euhedral grains without any sign of alteration (Fig. 4.8A-C) and is commonly associated with biotite and muscovite. The occurrence of euhedral epidote is restricted to AMG. Some of the euhedral epidote grains are partially or totally enclosed in biotite grains and hence indicate their magmatic or restitic/ inherited origin. Their compositional difference from epidote in the host rock (Tanawal Formation) favours a magmatic origin (Appendix-1). This variety of epidote also occurs as inclusions in grains of garnet (Fig. 4.8D). The chemical composition of these igneous epidotes is more or less uniform i.e. SiO_2: 37.7-38.9, Fe_2O_3: 7.8-9.12, Al_2O_3: 25.7-27.6, CaO: 23-24.1 (Appendix-1). MnO and TiO_2 are mostly less than one percent. However, some of the grains display zoning with marked differences in Al_2O_3 and Fe_2O_3 between core and rims. The cores contain more Fe and less Al than the margins.

4.5.5. Garnet

Garnet mostly occurs in association with biotite, muscovite and orthoclase. The grains of garnet are subhedral to anhedral and their size ranges from 100 to 700μm. Fracturing is commonly observed. In terms of chemical composition (Appendix-1), the studied garnets contain varying levels of the end-member's spessartine, almandine and grossular (Sp-Alm-Gr), collectively forming more than 95% of the garnet composition. The pyrope and andradite contents are low making up the remaining 5%. The compositional range of the homogenous garnet grains is: $Gr_{29.2-34.7}$-$Sp_{32.1-27.9}$-$Alm_{34.6-37}$.

The distinctive core-rim chemical zoning in some grains can be used to interpret the variation in composition of crystallization fluids. The central zone is enriched in Sp (47-50%) and Alm component with lower Gr (4-10%) (Fig. 4.9). The exactly opposing trend of Alm and Sp show the implications of $Fe^{2+} \leftrightarrow$ Mn in this zone. The outer zone is considerably richer in Gr (28-35%) component relative to the central zone. Here, the cationic substitution is dominated by Ca ↔

Mn as shown by the opposite trends of grossular content relative to spessartine. The almandine trend is almost parallel to that of spessartine in outer zone.

Such a drastic difference in core-margin composition shows the growth of later garnet over the already present one with distinct composition. This is supported by the sudden drop in the spessartine compositional trend in central zone (Fig. 4.9). The drop in the curve is due to the fracture present in the central zone which is the likely area for the growth of new garnet. The analogous spessartine component in the fracture and marginal zone further supports the interpretation. The analysed unzoned garnets have composition comparable to the outer section of zoned garnets, hence their growth seems to be synchronous.

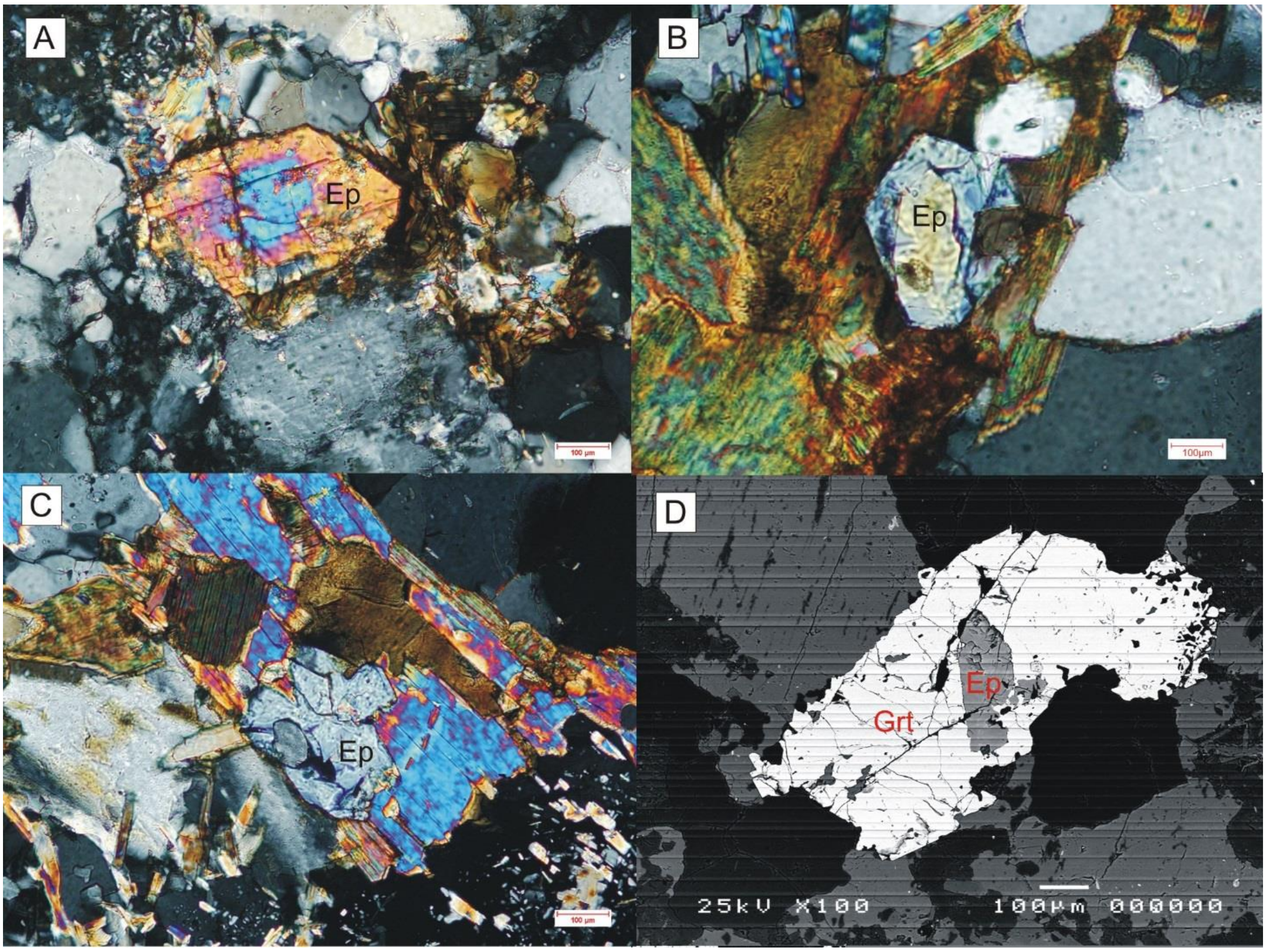

Fig. 4.8. A-C) Photomicrographs of euhedral magmatic epidotes from AMG host associated with biotite and muscovite, D) BSE image showing inclusion of epidote in garnet.

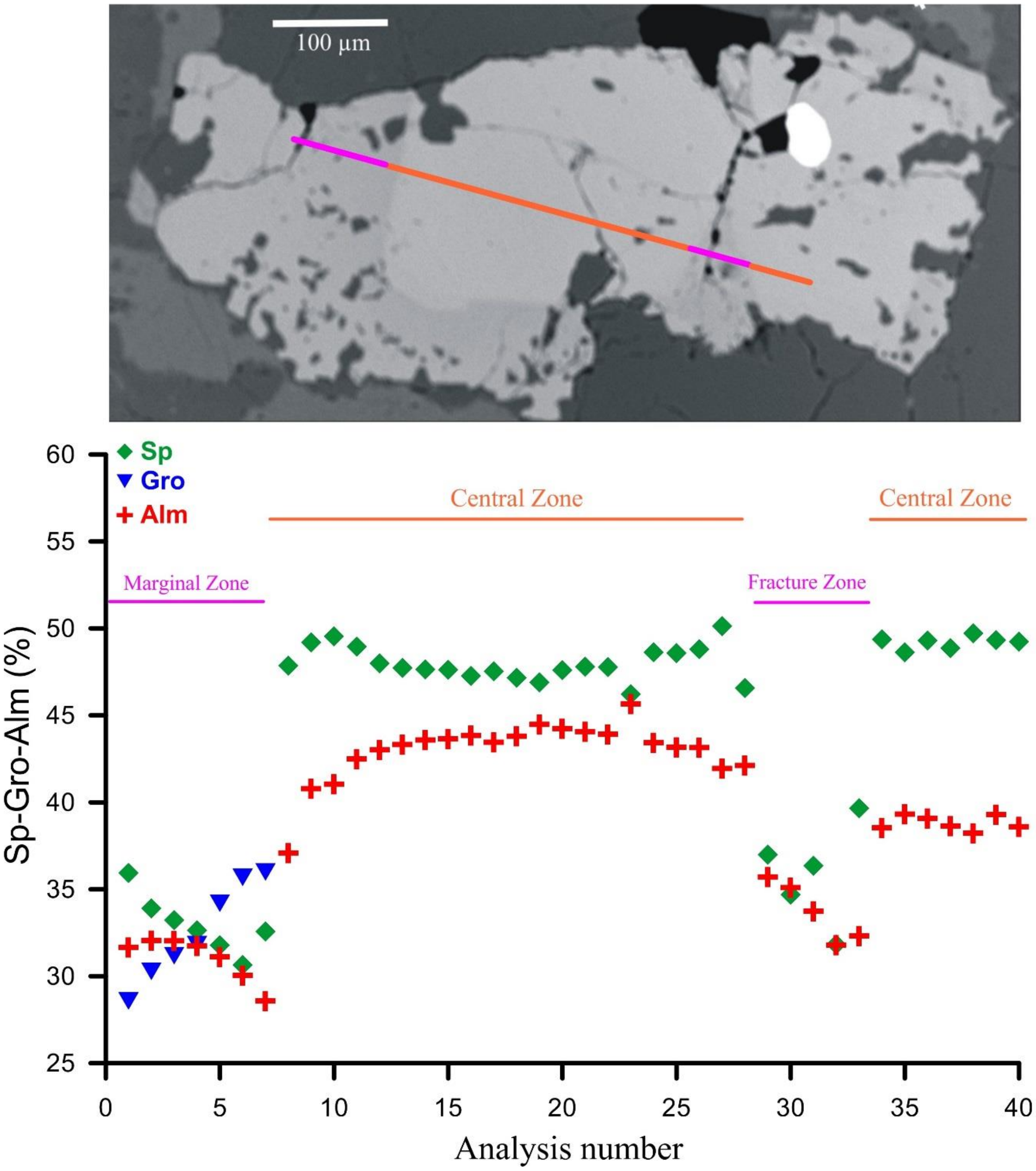

Fig. 4.9. Compositional traverse along Zoned garnet grain, spessartine content showing inverse bell shaped profile in central zone (Sp rich). Outer and fracture zone show similar garnet composition (Gr rich).

4.6. Whole rock major and trace element geochemistry

The comprehensive whole rock geochemical data of the Utla Granitoids is investigated for the first time in current study. The concentration of major and trace elements in studied samples is presented in (Table 4.3). Generally, samples from both the MPG and AMG are strongly per-aluminous as suggested by high A/CNK values (> 1.11; Fig. 4.10) which is also supported by the mineralogical characteristics described earlier. Likely, all the samples are sub-alkaline as described in total alkalis vs silica plot (Fig. 4.10). The variation plots of major elements are presented (Fig. 4.11). Decreasing trend of Al_2O_3, MgO, Fe_2O_3 and CaO against SiO_2 points to fractionation of plagioclase and biotite. Negative relation of P_2O_5 and CaO with SiO_2 indicates the fractionation of apatite. Inclusion of apatite in biotite further support this observation. TiO_2 show negative relation with increasing SiO_2 content. Analogous negative trend of CaO, Fe_2O_3 and Al_2O_3 against silica show the possibility of epidote crystallization in studied granitoids which support the interpretation of their magmatic origin (detail in later section). The decreasing trend of MnO against silica also favour the crystallization of garnet (Sp rich) in these granites.

The samples from Mansehra Granite (Fig. 4.1) were also analysed during the current investigation (Table 4.3) and their corresponding data is presented (Fig. 4.10; 4.11). They show parallel petrographic and geochemical behaviour to Utla granites (MPG) i.e. megacrystic, strongly peraluminous, sub-alkaline. Their major elements trends against silica (Fig. 4.11) are also analogous to the Utla Granites (MPG).

A curve trend has been observed in plot of Rb/Sr (differentiation index) against Fe_2O_3 mainly due to enrichment of Rb in AMG (Fig. 4.11). Both the rock types show LREE enriched pattern with negative Eu anomaly (Fig. 4.12). However, total REE content of MPG (ΣREE = 89.2) is greater than AMG (ΣREE = 36.2) (Table 4.3). The Eu anomaly is much stronger in case of AMG (Eu/Eu*=0.23) than MPG (Eu/Eu*=0.42) (Fig. 4.12). Multi element spidergram normalized to primitive mantle portrays similar pattern for both MPG and AMG (Fig. 4.12). It shows enrichment of Rb, Th, U and Pb and depletion of Ba, Sr, Ti, Zr and Nb. Mansehra granites show mostly similar trace elements and REE pattern to MPG rocks, however, certain degree of HREE depletion is observed

(Fig. 4.12). The geochemical composition of granites can be used to interpret the tectonic environment of granite emplacement. Different trace elements including Rb, Nb and Y has been used to interpret the tectonic setting of granites (Pearce et. al., 1984). These plots show syn-collisional to volcanic arc settings for both Utla and Mansehra granitoids (Fig. 4.13).

Anomalously high concentration of Sn (165 ppm) is yielded from one sample from Utla granites (UT-23) that also displays distinct field character from the rest of rocks. It is relatively soft, shows brown colour and higher degree of alteration. Such alteration may be caused by fluids with higher concentration of Sn and other components of economic significance. This feature can be used as a guide for tracing possible mineralization in Utla granitoids.

Table 4.3. Whole rock major (%age) and trace (ppm) element concentration of representative samples from studied granites

Sample	**UT-10**	**UT-11**	**UT-17**	**UT-19**	**UT-31**	**UT-34**	**UT-35**	**UT-40**	**UT-41**	**UT-48**	**UT-59**
Type	**MPG**	**MPG**	**MPG**	**MPG**	**MPG**	**MPG**	**MPG**	**MPG**	**MPG**	**MPG**	**MPG**
SiO_2	76.84	77.52	76.26	76.73	76.36	75.66	69.56	75.12	76.46	71.26	68.03
TiO_2	0.12	0.15	0.12	0.23	0.19	0.17	0.24	0.24	0.11	0.69	0.71
Al_2O_3	12.71	13.04	12.87	12.38	12.57	13.06	17.13	13.03	13.01	14.29	15.33
Fe_2O_3	1.43	1.56	0.76	2.02	1.59	1.73	0.94	2.10	1.05	2.50	4.85
MnO	0.02	0.01	0.02	0.02	0.03	0.04	0.02	0.02	0.02	0.05	0.09
MgO	0.29	0.69	0.22	0.67	0.30	0.33	0.48	0.58	0.19	0.92	1.39
CaO	0.29	0.27	0.22	0.22	0.87	0.57	0.34	0.76	0.26	1.61	
Na_2O	3.02	0.61	2.54	2.11	2.48	2.70	2.55	3.99	2.74	3.53	3.08
K_2O	4.21	4.29	6.08	4.28	4.67	4.95	7.09	3.22	5.15	2.87	3.38
P_2O_5	0.15	0.14	0.11	0.11	0.13	0.14	0.20	0.13	0.11	0.13	0.17
LOI	0.83	1.78	0.68	1.21	0.77	0.74	1.37	0.79	0.85	2.15	0.75
Total	99.93	100.08	99.91	100.01	99.99	100.12	99.94	100.04	99.96	100.02	97.82
Trace and REEs											
V	3.37	8.05	0.95	14.39	8.29	7.28	11.39	13.10	2.89	47.38	55.01
Cr	4.18	3.68	1.52	7.17	4.64	4.41	5.18	8.09	2.47	23.14	28.74
Rb	111.38	171.64	139.88	131.01	198.29	249.14	278.81	105.83	275.30	150.06	170.43
Sr	11.08	16.00	11.78	6.44	14.92	16.86	18.21	78.12	11.61	46.40	54.49
Y	8.94	20.64	10.08	6.47	19.32	19.35	14.02	18.60	14.92	47.53	12.99
Zr	19.74	37.52	12.14	6.50	8.38	13.18	7.51	6.21	9.79	2.44	1.15
Nb	8.47	9.35	6.95	8.38	8.62	8.34	10.73	8.70	12.22	12.49	15.37
Sn	7.72	10.06	5.78	6.73	6.84	9.42	31.52	4.41	13.20	5.47	6.94
Ba	82.98	229.01	154.01	112.93	108.86	137.31	306.79	389.49	34.02	178.11	333.72
La	4.19	10.38	2.99	11.40	13.72	10.68	2.25	16.86	5.62	72.65	29.54
Ce	6.93	23.34	4.43	20.06	24.98	19.68	3.60	26.15	10.96	126.70	61.73
Pr	1.19	2.76	0.74	3.08	3.73	2.87	0.67	4.47	1.60	17.68	7.80
Nd	4.43	9.85	2.78	10.52	13.71	10.44	2.87	16.57	5.75	65.44	29.65
Sm	1.28	2.64	0.77	2.34	3.53	2.70	1.22	3.98	1.74	13.65	6.19
Eu	0.09	0.32	0.08	0.51	0.45	0.33	0.20	0.49	0.10	1.59	0.90
Gd	1.27	2.66	0.96	1.97	3.33	2.71	1.97	3.65	1.82	11.93	5.27
Dy	1.63	3.54	1.70	1.57	3.78	3.60	2.92	3.84	2.62	10.09	3.59
Ho	0.34	0.76	0.37	0.54	0.79	0.74	0.56	0.74	0.53	1.80	0.54
Er	1.04	2.38	1.19	0.98	2.26	2.18	1.66	2.16	1.65	4.87	1.27
Tm	0.16	0.41	0.18	0.41	0.37	0.34	0.23	0.31	0.26	0.66	0.15
Yb	1.09	2.65	1.21	0.92	2.08	2.16	1.57	1.86	1.76	4.18	0.95
Lu	0.18	0.41	0.16	0.40	0.32	0.36	0.21	0.28	0.28	0.65	0.15
Hf	0.76	1.43	0.45	0.60	0.48	0.56	0.31	0.30	0.46	0.19	0.05
Ta	1.97	1.26	1.26	1.23	1.15	1.36	1.48	0.99	2.68	1.18	1.43
W	5.23	9.16	3.03	5.53	2.85	4.45	6.28	2.10	32.45	5.42	2.75
Pb	1.81	2.78	6.56	1.03	7.86	12.32	3.07	3.59	16.22	11.40	13.84
Th	3.43	10.75	2.57	6.25	7.69	6.79	9.84	8.81	5.52	16.92	15.74
U	0.82	2.11	0.43	0.92	1.04	3.00	1.40	1.09	4.06	1.88	2.03
ΣREE	23.80	62.10	17.58	54.69	73.05	58.77	19.94	81.35	34.70	331.89	147.73
A/CNK	1.26	2.12	1.15	1.45	1.17	1.20	1.37	1.14	1.23	1.21	1.76
Eu/Eu*	0.21	0.37	0.28	0.73	0.40	0.38	0.39	0.39	0.18	0.38	0.48
GCI	15.20	16.45	16.09	15.35	16.88	17.22	17.83	16.35	16.73	16.63	17.10

MPG and AMG = Utla granites, MG = Mansehra granites, LOI = loss on ignition, A/CNK = molar ratio Al_2O_3/ ($CaO+Na_2O+K_2O$), Eu/Eu* = Eu_N/ $(Sm_N*Gd_N)^{0.5}$, GCI = geochemical characterization index (section 4.7.6 for details)

Table 4.2 continued

Sample	**UT-65**	**UT-66**	**UT-69**	**UT-73**	**UT-18**	**UT-22**	**UT-24**	**UT-26**	**UT-27**	**UT-28**	**UT-29**
Type	**MPG**	**MPG**	**MPG**	**MPG**	**AMG**	**AMG**	**AMG**	**AMG**	**AMG**	**AMG**	**AMG**
SiO_2	71.38	68.87	71.89	78.24	76.64	76.86	76.48	76.24	76.77	75.55	77.01
TiO_2	0.61	0.49	0.35	0.20	0.07	0.19	0.13	0.12	0.14	0.11	0.14
Al_2O_3	13.97	14.04	14.73	11.46	13.04	12.35	12.79	13.05	12.49	13.20	12.82
Fe_2O_3	4.07	3.15	2.55	1.54	0.88	1.88	1.25	1.13	1.40	1.88	0.56
MnO	0.06	0.05	0.05	0.03	0.01	0.01	0.02	0.02	0.02	0.02	0.01
MgO	1.11	0.75	0.63	0.42	0.27	0.50	0.23	0.32	0.27	0.20	0.14
CaO	1.78	0.62	0.86	0.54	0.19	0.20	0.16	0.16	0.19	0.21	0.14
Na_2O	2.39	2.36	2.31	2.23	3.21	2.82	2.28	2.02	2.15	2.26	2.53
K_2O	3.55	5.30	5.15	4.33	4.90	4.03	5.77	6.04	5.33	4.92	5.97
P_2O_5	0.14	0.16	0.20	0.11	0.10	0.09	0.07	0.08	0.10	0.13	0.08
LOI	0.81	1.48	1.21	0.81	0.81	1.27	1.02	1.13	1.03	0.80	0.78
Total	99.90	97.36	99.96	99.94	100.12	100.20	100.21	100.30	99.88	99.28	100.18
Trace and REEs											
V	56.53	36.81	25.54	10.88	0.54	3.82	1.42	1.04	5.11	1.70	1.79
Cr	26.46	15.95	13.48	7.22	1.47	1.34	1.48	0.74	3.18	1.11	2.03
Rb	145.36	187.92	220.53	146.20	82.89	99.05	283.08	226.00	201.75	173.67	213.72
Sr	63.99	46.82	27.64	18.32	6.98	15.02	10.48	13.78	14.42	8.35	20.63
Y	19.85	12.89	14.53	14.61	4.08	7.96	15.26	6.39	10.25	6.55	6.99
Zr	2.98	2.56	13.91	4.26	8.53	12.97	57.06	18.03	11.18	8.53	11.07
Nb	16.02	13.53	15.39	6.27	3.39	9.00	10.28	8.49	8.46	6.18	10.33
Sn	6.74	10.71	13.59	4.70	4.88	6.89	11.53	13.28	19.84	10.27	17.63
Ba	372.39	701.82	209.83	184.30	104.06	105.53	21.95	99.29	134.46	39.23	74.78
La	35.21	17.07	17.92	13.60	2.18	7.14	6.11	2.56	6.28	4.67	3.85
Ce	65.24	30.88	25.27	21.39	3.24	11.28	15.92	4.47	12.27	9.76	6.35
Pr	8.94	4.55	4.69	3.51	0.57	2.04	1.82	0.81	1.83	1.37	1.06
Nd	33.84	17.26	17.86	13.07	1.92	7.54	6.60	2.94	6.90	4.83	3.86
Sm	7.07	3.84	4.13	3.05	0.53	1.98	1.86	0.80	1.85	1.44	1.06
Eu	1.04	0.83	0.66	0.41	0.09	0.19	0.04	0.05	0.13	0.06	0.09
Gd	5.97	3.52	3.64	2.89	0.59	1.73	1.82	0.73	1.73	1.20	1.02
Dy	4.29	2.95	3.14	2.89	0.80	1.77	2.60	1.16	2.03	1.42	1.36
Ho	0.75	0.56	0.56	0.57	0.18	0.35	0.56	0.25	0.40	0.27	0.26
Er	1.99	1.48	1.56	1.60	0.51	0.99	1.76	0.86	1.20	0.82	0.78
Tm	0.28	0.24	0.22	0.23	0.10	0.15	0.29	0.14	0.18	0.13	0.12
Yb	1.74	1.37	1.38	1.37	0.52	0.97	2.05	0.97	1.22	0.90	0.81
Lu	0.26	0.26	0.18	0.24	0.11	0.13	0.29	0.11	0.16	0.12	0.13
Hf	0.10	0.15	0.49	0.23	0.39	0.39	1.78	0.66	0.42	0.35	0.46
Ta	1.58	1.62	2.15	0.75	0.63	1.12	1.13	1.32	1.37	1.26	1.74
W	3.72	4.24	4.90	3.06	2.72	1.39	2.21	1.69	2.64	0.70	2.05
Pb	17.03	11.73	10.66	11.20	0.76	2.89	16.12	9.05	4.01	8.11	8.56
Th	15.51	8.77	8.88	6.98	1.42	5.98	8.80	2.40	6.22	4.51	4.62
U	4.52	0.86	1.71	1.06	0.41	0.88	3.00	1.35	2.07	2.08	2.64
ΣREE	166.62	84.81	81.19	64.81	11.36	36.24	41.72	15.84	36.19	26.99	20.77
A/CNK	1.27	1.31	1.34	1.23	1.19	1.32	1.24	1.28	1.29	1.40	1.18
Eu/Eu*	0.49	0.69	0.52	0.42	0.51	0.31	0.07	0.20	0.22	0.14	0.27
GCI	17.10	17.89	17.55	16.38	14.75	15.28	16.31	16.66	16.63	15.77	16.85

MPG and AMG = Utla granites, MG = Mansehra granites, LOI = loss on ignition, A/CNK = molar ratio Al_2O_3/ ($CaO+Na_2O+K_2O$), Eu/Eu* = Eu_N/ $(Sm_N*Gd_N)^{0.5}$, GCI = geochemical characterization index (section 4.7.6 for details)

Table 4.2 continued

Sample	**UT-30**	**UT-36**	**UT-38**	**UT-42**	**UT-43**	**UT-44**	**UT-46**	**UT-70**	**UT-77**	**UT-23**	**UT-47**
Type	**AMG**	**AMG**	**AMG**	**AMG**	**AMG**	**AMG**	**AMG**	**AMG**	**AMG**	**Altered**	**Tour Vein**
SiO_2	74.32	76.02	76.85	74.90	76.83	76.30	76.58	72.39	75.52	67.14	76.98
TiO_2	0.12	0.10	0.08	0.09	0.10	0.11	0.10	0.30	0.12	0.34	0.31
Al_2O_3	13.87	12.96	13.20	13.22	12.96	13.34	12.62	14.70	13.16	17.45	12.31
Fe_2O_3	1.40	1.52	0.65	1.46	0.71	0.92	1.03	2.41	1.10	1.95	2.43
MnO	0.04	0.03	0.01	0.03	0.02	0.01	0.01	0.05	0.02	0.01	0.02
MgO	0.22	0.15	0.12	0.13	0.14	0.41	0.19	0.61	0.18	0.98	1.21
CaO	0.58	0.34	0.18	0.38	0.38	0.24	0.44	0.63	0.30	0.06	0.28
Na_2O	2.66	2.65	2.87	2.49	2.62	3.75	2.59	2.41	2.37	3.04	2.30
K_2O	5.58	5.42	5.46	6.08	5.58	4.11	5.80	5.28	6.55	5.81	1.92
P_2O_5	0.10	0.15	0.10	0.15	0.11	0.11	0.10	0.22	0.13	0.06	0.12
LOI	0.98	0.79	0.70	1.08	0.74	0.82	0.57	1.02	0.79	2.87	1.39
Total	99.88	100.14	100.23	100.00	100.17	100.11	100.03	100.02	100.25	99.71	99.28
Trace and REEs											
V	4.57	1.63	0.50	0.47	1.14	2.33	2.42	21.15	1.33	10.17	25.47
Cr	2.68	1.67	0.98	0.79	1.33	1.43	1.28	10.59	1.38	6.46	15.00
Rb	346.67	312.64	225.30	296.80	292.13	100.59	197.44	297.43	268.72	217.18	101.49
Sr	15.38	7.55	6.02	10.87	12.39	13.92	20.06	33.38	12.60	56.20	15.75
Y	20.74	21.71	4.84	20.28	20.26	9.40	25.64	15.55	11.48	4.11	13.98
Zr	21.57	16.33	13.02	15.26	25.86	22.93	13.50	22.44	9.34	11.22	5.06
Nb	8.55	8.54	6.65	7.56	7.00	5.81	4.81	16.07	8.48	10.08	7.61
Sn	10.20	10.16	7.95	8.81	12.24	10.54	6.96	13.65	7.17	165.37	33.88
Ba	100.85	14.91	9.14	8.51	13.59	100.49	29.43	221.60	43.34	85.65	62.06
La	11.25	6.37	1.55	4.86	5.13	5.13	7.94	19.44	3.81	10.86	25.43
Ce	22.46	11.79	3.17	9.79	9.07	7.51	15.28	39.94	7.39	21.19	49.78
Pr	3.12	1.95	0.42	1.60	1.51	1.33	2.20	5.00	1.10	3.53	6.21
Nd	11.45	7.15	1.52	6.03	5.47	4.85	8.02	19.00	4.02	12.67	22.50
Sm	3.00	2.29	0.53	1.96	1.67	1.35	2.43	4.47	1.26	2.68	4.58
Eu	0.29	0.06	0.02	0.06	0.05	0.13	0.16	0.61	0.08	0.43	0.48
Gd	2.88	2.45	0.56	2.11	1.87	1.30	2.69	4.25	1.37	1.63	3.58
Dy	3.92	3.84	0.92	3.58	3.29	1.61	4.38	3.61	2.12	1.25	2.98
Ho	0.80	0.78	0.19	0.74	0.72	0.32	0.91	0.61	0.43	0.21	0.51
Er	2.38	2.49	0.62	2.34	2.32	0.98	2.78	1.57	1.35	0.55	1.37
Tm	0.38	0.40	0.10	0.38	0.38	0.15	0.42	0.20	0.21	0.08	0.18
Yb	2.57	2.74	0.74	2.49	2.62	0.98	2.64	1.34	1.42	0.49	1.18
Lu	0.38	0.39	0.10	0.35	0.35	0.13	0.35	0.22	0.24	0.09	0.19
Hf	0.79	0.58	0.57	0.54	0.88	0.81	0.55	0.75	0.36	0.42	0.24
Ta	1.41	1.23	1.08	1.08	1.00	0.62	0.79	2.11	1.30	1.13	0.91
W	1.86	1.90	1.98	1.06	1.35	1.50		5.30	2.31	6.00	5.74
Pb	17.79	10.93	5.10	14.18	18.57	3.93	19.41	19.65	20.16	0.38	3.15
Th	10.90	8.01	3.56	6.20	6.44	3.08	7.58	11.92	4.22	9.44	11.05
U	1.78	2.97	3.47	3.64	3.23	0.56	2.44	2.19	1.08	1.45	2.15
ΣREE	64.88	42.69	10.46	36.28	34.47	25.78	50.22	100.26	24.79	55.65	118.95
A/CNK	1.21	1.19	1.20	1.16	1.17	1.21	1.11	1.36	1.14	1.93	1.93
Eu/Eu*	0.31	0.08	0.10	0.08	0.09	0.30	0.19	0.43	0.19	0.62	0.36
GCI	17.88	16.59	15.61	16.33	16.62	15.25	16.33	17.97	16.62	17.76	14.55

MPG and AMG = Utla granites, MG = Mansehra granites, LOI = loss on ignition, A/CNK = molar ratio Al_2O_3/ ($CaO+Na_2O+K_2O$), Eu/Eu* = Eu_N/ (Sm_N*Gd_N)$^{0.5}$, GCI = geochemical characterization index (section 4.7.6 for details)

Table 4.2 continued

Sample	**M-3**	**M-4**	**M-5**	**M-11**	**M-17**	**M-19**	**M-22**	**M-26**	**M-27**
Type	**Mansehra**	**Mansehra**	**Mansehra**	**Mansehra**	**Mansehra**	**Mansehra**	**Mansehra**	**Mansehra**	**Mansehra**
SiO_2	73.98	75.34	70.05	72.57	69.37	75.06	69.81	75.66	71.66
TiO_2	0.31	0.08	0.56	0.21	0.66	0.06	0.53	0.09	0.46
Al_2O_3	14.13	14.78	14.86	14.47	15.00	14.19	15.15	14.26	14.17
Fe_2O_3	2.68	0.92	3.85	1.70	4.77	0.38	3.54	1.05	3.24
MnO	0.64	0.19	1.06	0.39	1.31	0.13	0.95	0.13	0.85
MgO	0.04	0.04	0.06	0.03	0.07	0.01	0.06	0.05	0.05
CaO	0.85	0.60	1.51	0.72	1.57	0.14	1.35	0.50	1.19
Na_2O	2.12	3.10	2.58	3.04	2.43	1.32	2.47	4.73	2.36
K_2O	4.26	3.87	4.15	5.28	4.12	8.01	5.02	2.32	4.31
P_2O_5	0.21	0.27	0.21	0.27	0.24	0.17	0.18	0.26	0.18
LOI	0.70	0.98	0.82	0.60	0.47	0.74	0.78	0.88	1.37
Total	99.96	100.17	99.74	99.31	100.04	100.23	99.91	99.94	99.88
Trace and REEs									
V	24.65	2.80	35.57	8.73	67.27	2.26	28.85	1.21	23.75
Cr	11.10	1.64	17.94	4.04	29.70	1.20	16.34	0.89	14.13
Rb	126.88	194.21	142.12	213.08	204.95	258.73	150.56	143.69	167.11
Sr	24.69	7.42	36.35	16.26	61.73	21.75	41.01	11.18	30.70
Y	9.40	6.87	16.10	8.61	19.89	1.29	11.79	5.38	17.70
Zr	14.92	5.40	8.14	11.74	7.95	1.25	5.47	17.06	13.68
Nb	11.47	10.62	14.52	12.97	22.89	2.52	12.52	13.78	12.47
Sn	5.56	18.39	5.41	8.96	7.06	6.91	5.35	45.25	9.71
Ba	210.24	26.96	271.88	157.35	433.17	286.39	443.72	20.85	235.13
La	20.26	4.61	23.95	15.59	58.34	1.02	23.22	1.89	20.41
Ce	44.57	8.47	46.85	34.76	127.61	1.72	46.91	2.53	46.50
Pr	5.41	1.24	6.99	4.35	15.34	0.25	6.56	0.61	5.69
Nd	20.81	4.73	27.52	16.52	58.99	0.99	25.81	2.36	22.23
Sm	4.36	1.18	5.89	4.03	12.04	0.28	5.29	0.69	4.95
Eu	0.61	0.14	0.73	0.35	1.03	0.41	0.75	0.04	0.55
Gd	3.36	1.14	4.84	3.25	9.09	0.24	4.19	0.72	4.16
Dy	2.34	1.31	3.68	2.22	5.32	0.26	2.94	0.99	3.55
Ho	0.37	0.25	0.64	0.34	0.79	0.05	0.49	0.19	0.67
Er	0.95	0.77	1.72	0.84	1.74	0.12	1.20	0.60	1.88
Tm	0.14	0.13	0.23	0.12	0.20	0.02	0.15	0.11	0.27
Yb	0.92	0.92	1.33	0.69	1.04	0.16	0.89	0.81	1.75
Lu	0.11	0.11	0.16	0.08	0.13	0.02	0.11	0.11	0.25
Hf	0.60	0.26	0.24	0.36	0.25	0.06	0.16	0.91	0.51
Ta	1.95	6.38	1.74	2.20	1.78	0.35	1.51	4.28	1.89
W	0.25	6.95	2.28	3.12	3.10	3.12	0.90	20.36	2.23
Pb	21.69	13.27	11.89	8.08	24.81	21.77	17.55	2.32	17.15
Th	11.55	2.39	16.25	12.37	30.70	0.52	14.55	1.38	14.15
U	1.86	0.81	1.46	1.32	2.94	0.40	0.93	1.56	1.94
ΣREE	104.21	25.02	124.52	83.14	291.67	5.52	118.53	11.64	112.85
A/CNK	1.46	1.42	1.29	1.20	1.32	1.28	1.27	1.27	1.32
Eu/Eu*	0.49	0.38	0.42	0.30	0.30	4.85	0.49	0.17	0.37
GCI	16.47	15.76	16.78	17.11	17.86	18.12	17.15	15.87	17.01

MPG and AMG = Utla granites, MG = Mansehra granites, LOI = loss on ignition, A/CNK = molar ratio Al_2O_3/ ($CaO+Na_2O+K_2O$), Eu/Eu* = $Eu_N/ (Sm_N*Gd_N)^{0.5}$, GCI = geochemical characterization index (section 4.7.6 for details)

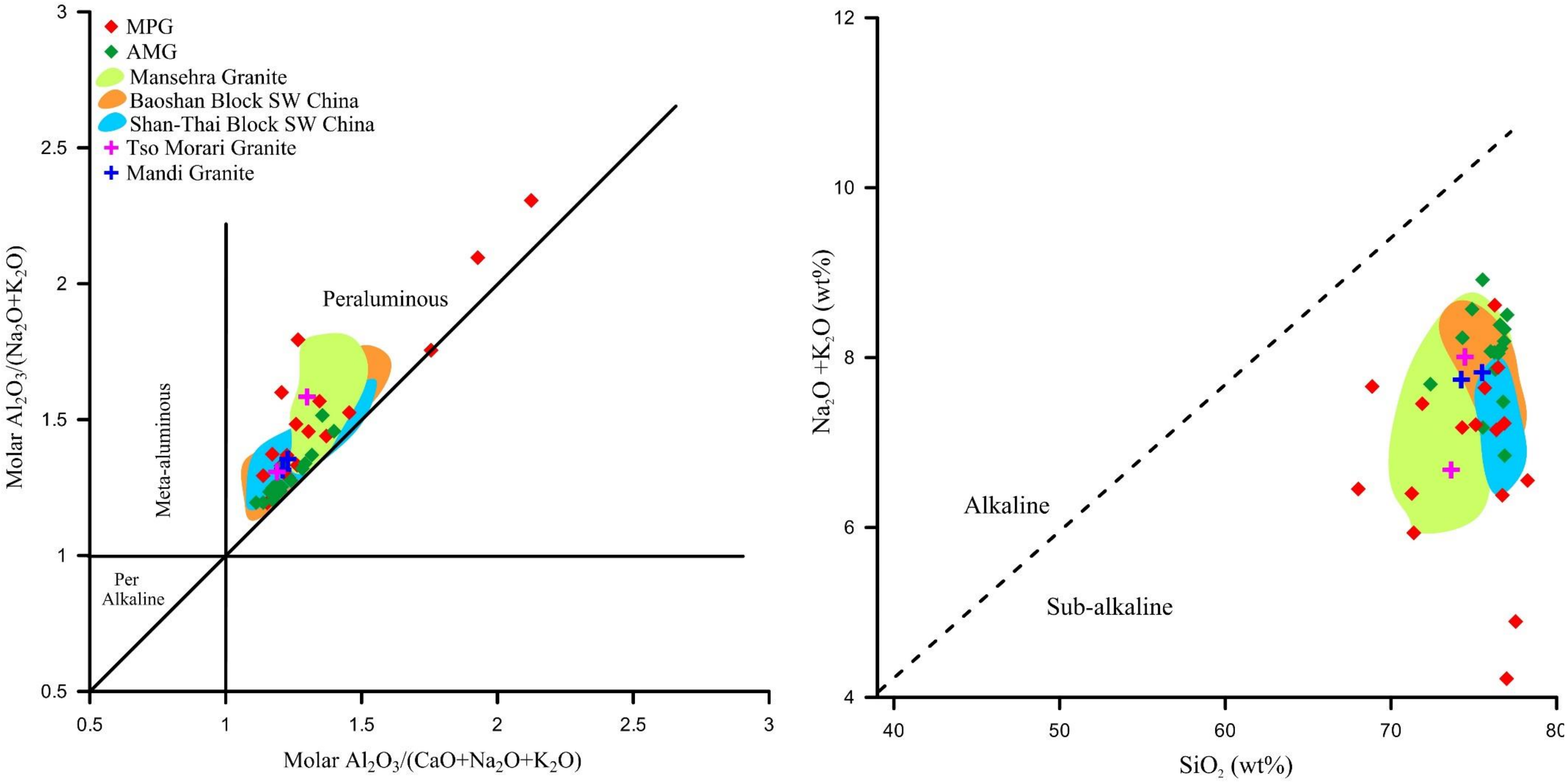

Fig. 4.10. Classification of Utla (MPG and AMG) and Mansehra granites show peraluminous and sub-alkaline signature (A) Al_2O_3/ $(CaO+Na_2O+K_2O)$ versus $Al_2O_3/(Na_2O+K_2O)$ (Maniar and Piccoli, 1989) B) Alkalis vs SiO_2 plot after Miyashiro (1973). The corresponding data of Mansehra granites (this study), Baoshan Block, SW China (Dong et al., 2013), Shan-Thai block, SW China (Wang et al., 2013), Tso Morari granites (Girard and Bussy, 1999) and Mandi Granite (Miller et al., 2001) is also shown for comparison.

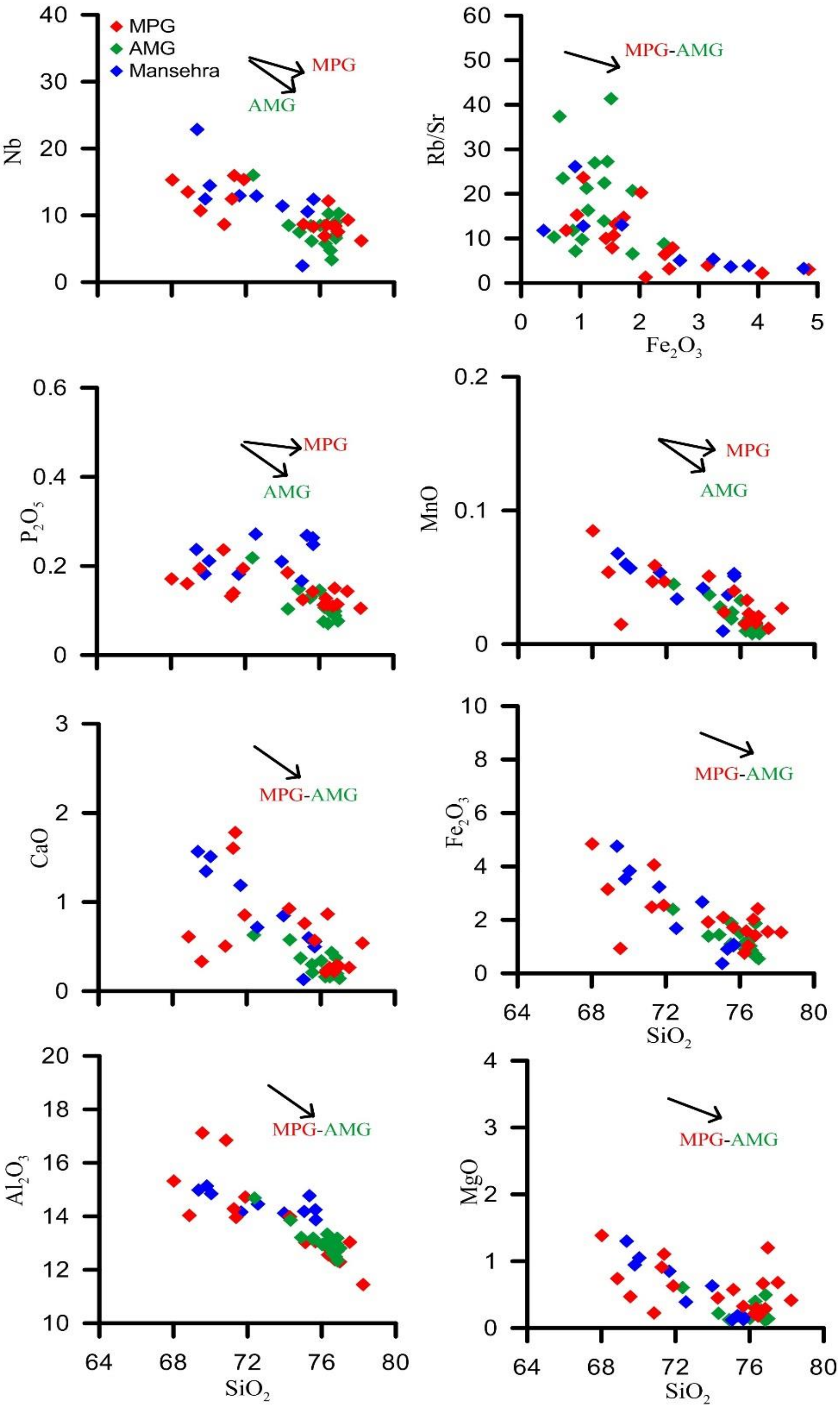

Fig. 4.11. Major elements Harker diagrams of Utla (MPG and AMG) and Mansehra granites. MPG and Mansehra granites show analogous trends against silica. AMG samples plot along the higher silica content which elaborate their evolved signature. Rb/Sr against Fe$_2$O$_3$ show relatively curve trend due to enrichment of Rb in AMG which signify the process of differentiation during the evolution of melt.

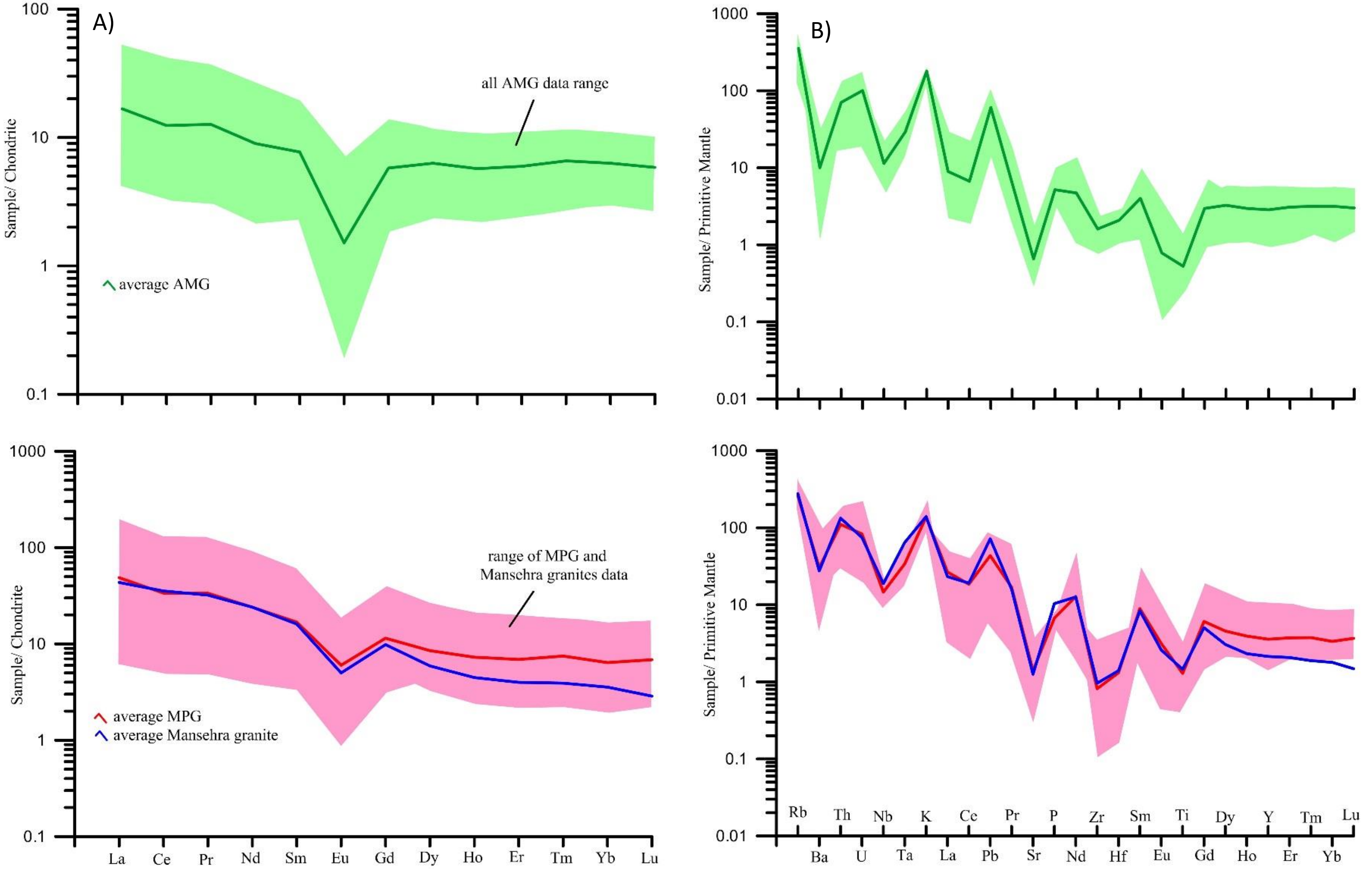

Fig.4.12. A) Chondrite normalized REE pattern show stronger Eu anomaly in AMG, normalized data from McDonough and Sun (1995), B) Primitive mantle normalized multi-element spidergram, normalized data from McDonough et al. (1992). The trend of Mansehra granite samples (blue line) analysed in this study showing the average values (n = 9) is also presented along the MPG samples.

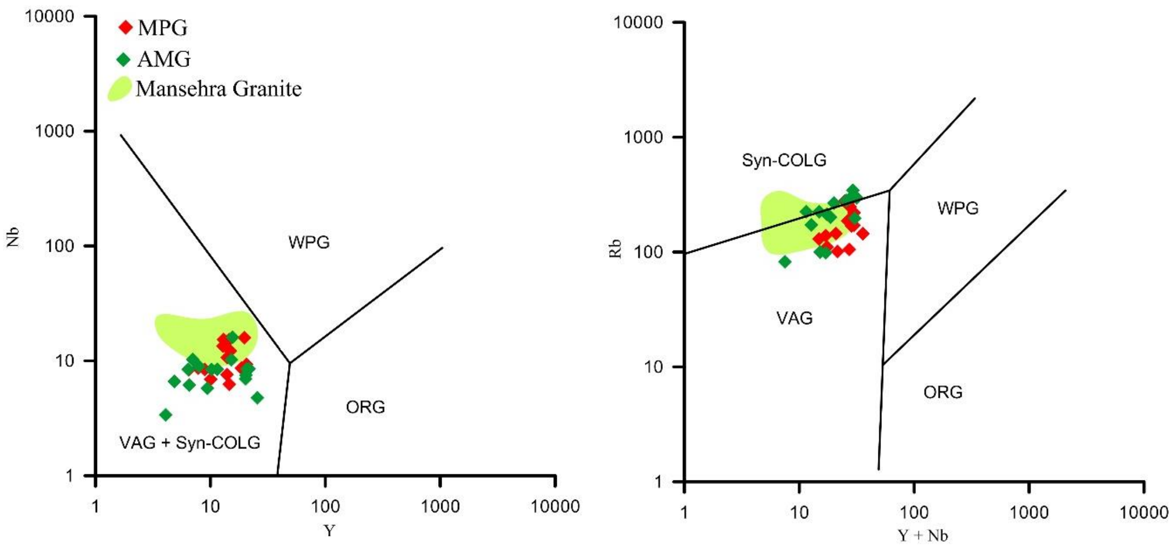

Figure 4.13. The Utla (MPG and AMG) and Mansehra granites show volcanic arc to syn-collisional tectonic settings on trace elements discrimination plots (after Pearce et al., 1984). VAG=volcanic arc granites, WPG= within plate granites, ORG=ocean ridge granites, Syn-COLG= syn-collisional granites.

4.7. Discussion

4.7.1. Evidence of fractional crystallization

The evolution of Utla granitoids via fractional crystallization is depicted by Harker plots (Fig. 4.11) and mineralogical compositions. The fractionated minerals mainly include feldspars (plagioclase and orthoclase), biotite, apatite and zircon. Normal zoning (increase in Ab content from core to rim) observed in plagioclase from MPG and enrichment in albite content of plagioclase in AMG relative to MPG is strong indication of plagioclase fractionation. Furthermore, AMG samples plot towards the higher silica content relative to MPG showing their more evolved character (Fig. 4.11). Despite such a strong evidence for fractionation process, the total REE content of AMG is less than MPG. This can be explained by the fractionation of REE bearing phases in MPG including zircon and apatite which are most likely hosts for REEs. The presence of these minerals as inclusions in biotite supports this interpretation.

The negative Eu anomaly in chondrite normalized REE pattern also supports the fractionation of plagioclase as Eu^{2+} normally substitutes for Ca in feldspar lattice (Rollinson, 1993). The negative Eu anomaly can also happen to a lesser extent due to fractionation of other minerals including hornblende, titanite, garnet but in opposite sense to that of feldspar. The higher LREE/HREE ratio is very typical of granitic systems and caused mostly fractionation of zircon in the system (Rollinson, 1993).

The negative Ba, Sr, Nb and Ti anomalies (Fig. 4.12) also show the highly fractionated nature of the studied granites (Chappell, 1999). Fractionation of Ti bearing minerals (e.g. rutile, ilmenite and sphene) normally results in negative Ti anomaly. Negative Sr and Ba anomalies are indicative of plagioclase and orthoclase fractionation respectively (e.g., Miller, 1985; Patiňo Douce et al., 1990; Wu et al., 2003; Healy et al., 2004; Li et al., 2015). The identical geochemical behaviour of Utla and Mansehra granitoids (Fig. 4.10-4.14) are consistent with an origin related to a single coeval magmatism.

4.7.2. Source rock characteristics and partial melting

The concentration and variation of CaO and Na_2O in per-aluminous granites can give a strong indication about the composition of source rocks in terms of their feldspar and clay content (Chappell and White, 1992; Sylvester, 1998). The results of experimental work by Sylvester (1998), Skjerlie and Johnston (1996) and Patino Douce and Johnston (1991) also highlight the significance of plagioclase to clay ratio in the magma source and its effect on the CaO and Na_2O content of the resultant granite. These experiments reveal that granites derived from plagioclase poor/clay rich source display lower (<0.3) CaO/Na_2O ratios whereas those derived from plagioclase rich/clay poor show higher (>0.3) (Sylvester, 1998). The Utla (MPG and AMG) and Mansehra granites yield pelitic source (clay-rich, plagioclase-poor) for their parental melt (Fig. 4.14). The molar $Al_2O_3/(MgO + FeO_T)$ vs. $CaO/(MgO + FeO_T)$ of Altherr et al. (2000) diagram also depicts similar source rock composition for these granitoids (Fig. 4.14).

The REEs modelling were used to interpret the conditions of partial melting for MPG and AMG samples using batch melting and fractional melting equation (Appendix-2). Some REEs were not used in modelling either due to lack of analysis i.e. Tb, or due to limited partitioning data i.e. Pr, Ho and Tm. As clay rich source has been inferred for these rocks (Fig. 4.14), the modal mineralogical abundance of metapelites (3% plagioclase, 20 %orthoclase, 20% quartz, 35% biotite, 15% muscovite, 2% garnet and 5% alumina-silicates) was used (Nabelek and Barlett, 1999). The higher abundances of mica and lower plagioclase content distinguish metapelites from metagreywackes (Nabelek and Barlett, 1999). The analogous mineralogical composition has also been reported in already published literature (e.g.

Le Breton and Thompson, 1988) and has been applied for REE modelling of granitic rocks (e.g. Simons et al., 2016). Due to the dearth of relevant available data of metapelites from the region, average lower crustal abundances of concerned elements (Rudnick and Gao, 2003) were used as starting material. Iterative modelling suggests up to 30% melting of source to produce the melt of approximate similar composition to the primitive granite (MPG) (Fig. 4.15A).

Generally, the vapour-absent breakdown of muscovite in metapelites leads to generate the granitic melt, however, relatively more mafic, granodioritic melt, follows the biotite dominated dehydration melting (Clemens and Vielzeuf, 1987; Nabelek et al., 1992). The minimum amount of melt required for segregation, the critical melt fraction (CMF), is estimated to be >15% (Clemens and Vielzeuf, 1987) which can be achieved via melting of dehydration melting of muscovite due to its higher concentration in metapelites. However, the least evolved studied granites (i.e. MPG) contain considerably higher concentration of mafic minerals i.e. biotite and tourmaline (Table 4.2), which implies the enrichment of ferromagnesian components in source. Taking this into account, it is inferred that the studied granites are derived from muscovite dominated dehydration melting up to the temperature which also initiate the biotite dehydration melting to a certain degree. A totally biotite dominated dehydration melting does not imply as all the studied samples are granitic (Fig. 4.3) and due to the reason that certain concentration of biotite can also be produced from the ferromagnesian component of muscovite during its dehydration melting (Patino Douce and Harris, 1998).

The implications of fractional crystallization are elaborated by the fractionation modelling using REE. The result suggests up to 20% fractionation (Fig. 4.15B) of assemblage containing 30% K-feldspar, 45% plagioclase, 18% biotite, 5% garnet, 0.3% allanite, 0.6% apatite, 0.9% monazite, 0.1% zircon and 0.1% ilmenite during the evolution of AMG from MPG. The fractionation model is consistent with the evidences of mineral-melt separation from mineralogical compositions mentioned in earlier sections e.g. change in plagioclase composition from MPG to AMG (Fig. 4.15B). The REE modelling inferred the partial melting of single pelitic source for the formation of melt parental to Utla granitoids that has undergone fractional crystallization to evolve from MPG to AMG.

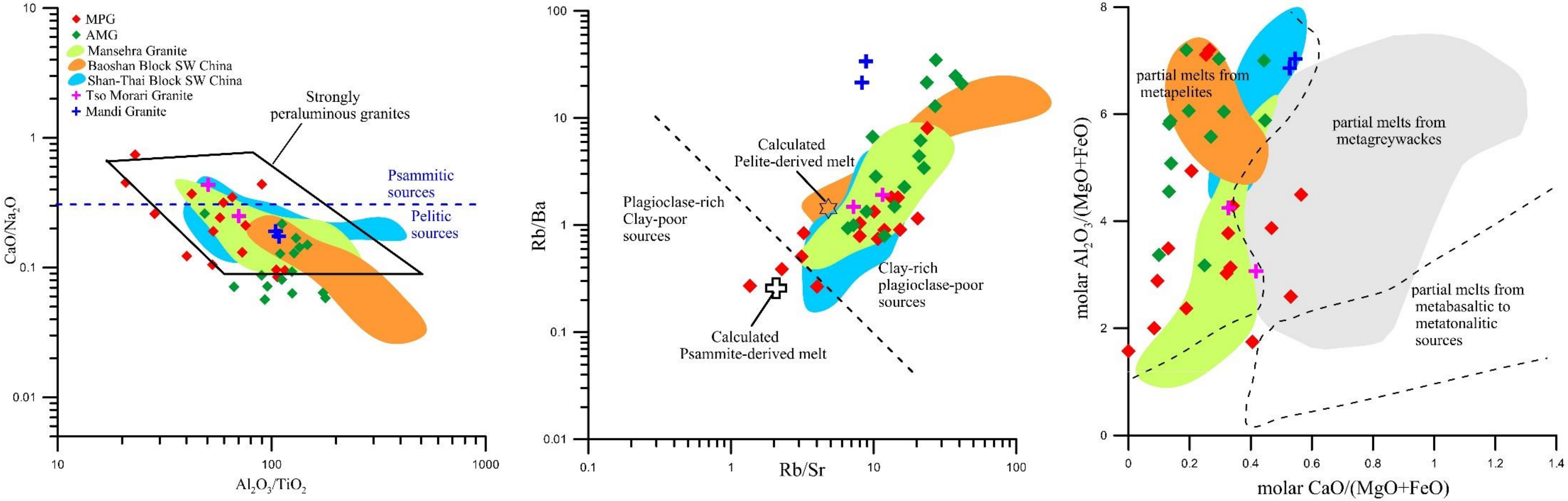

Fig. 4.14. Interpretation of source rock composition A) Al_2O_3/TiO_2 versus CaO/Na_2O, field of strongly peraluminous rocks from Sylvester (1998) (B) Rb/Ba versus Rb/Sr diagram, calculated source composition after Sylvester, 1998, C) molar $Al_2O_3/(MgO + FeO_T)$ vs. $CaO/(MgO + FeO_T)$, source fields after Altherr et al. (2000). Data source of other mentioned plutons are same as in Figure 4.10.

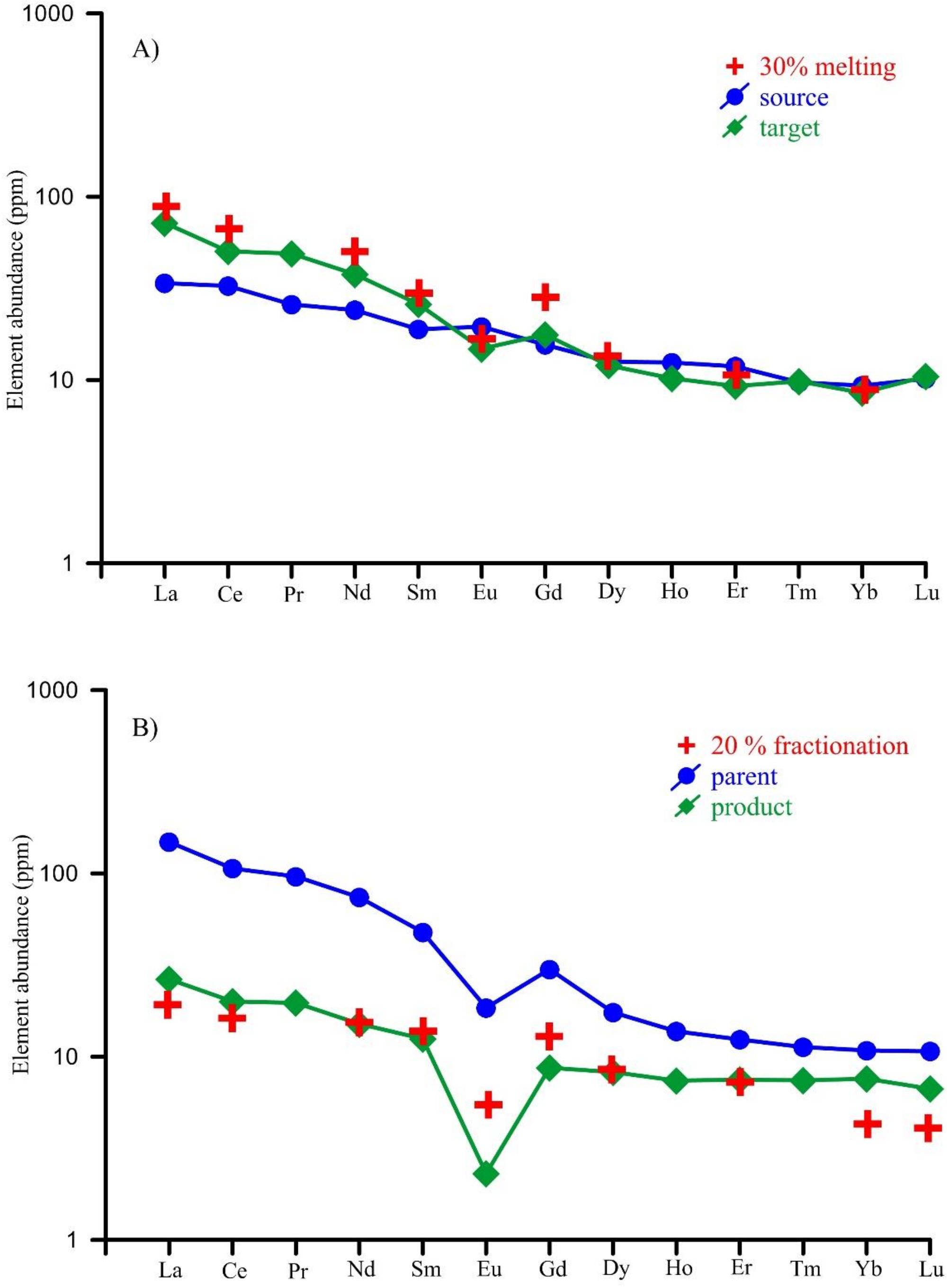

Fig. 4.15. A) Batch melting REE modelling of pelitic source to produce MPG rocks. MPG represent the least evolved granites from Utla area. The plot shows 30% partial melting of source to produce melt with approximate similar composition to target, B) Fractional crystallization REE modelling of least evolved MPG to produce most evolved AMG (see text for fractionating assemblage and other details). REE concentrations are normalized to chondrite values after McDonough and Sun (1995).

4.7.3. Significance of tourmaline chemistry

Four different modes of tourmaline occurrence in Utla granitoids have been recognized, a) as an accessory phase in ground mass of MPG (Fig. 4.5A), b) nodular tourmaline spread over the host AMG (Fig. 4.2F), c) tourmaline rich veins cross cutting both the MPG and AMG (Fig. 4.2E) and d) coarser and chemically distinct tourmaline in QRV (Fig. 4.5C). The tourmaline from MPG ground mass ranges from brown to yellowish brown in colour with schorlitic composition. Vein tourmaline is similar in composition but ranges in colour from green to brownish green. QRV tourmalines are mostly colour zoned ranging from yellowish brown to blue. Colour of tourmaline correlates well with Fe^{2+}/Mg ratio. Brown to yellowish brown tourmaline are richer in Mg [$Fe^{2+}/(Fe^{2+}+Mg < 0.6$] while green and blue tourmaline are richer in Fe^{2+} [$Fe^{2+}/(Fe^{2+}+Mg) > 0.6$] (Fig. 4.7). No significant correlation with Ti is shown. Similar relationship of major element composition to tourmaline colour is noticed in earlier studies (e.g. Sinclair and Richardson, 1992; Mylnarcz and Williams, 2006). They also pointed the relationship of Ti with yellow and brown colour which is not observed in the tourmalines studied here. This might suggest that factors other than major elements concentration are also important in describing the colour of tourmaline (Slack and Coad, 1989).

Apart from colour discrimination, the Fe^{2+}/Mg ratio also shows characteristic differences in different tourmaline modes. Tourmaline from the MPG groundmass and vein tourmalines have similar range of Fe^{2+}/Mg ratio, however the evolved nature of crystallizing fluid for vein tourmaline is shown by their higher silica content (Fig. 4.7). Nodular and QRV tourmaline is significantly richer in Fe relative to MPG and vein tourmaline. The iron-rich tourmaline in granitic systems is mostly noticed in late stage fractionated fluids which has the greater potential for Sn enrichment (e.g. Manning, 1982; Sinclair and Richardson, 1992; Broska et al., 1998). The elevated Fe in late stage tourmaline (nodular and QRV) from Utla granitoids might also indicate the Sn enrichment in late stage residual fluids and their subsequent mineralization potential. The higher Sn whole rock concentration (39 ppm) of a sample from a tourmaline rich vein (UT-47) relative to other granites support this interpretation (Table 4.2).

The textural relations (Fig. 4.2F) reveal replacement of orthoclase by tourmalines in nodules. Such textural relations and cross cutting tourmaline veins point towards the post magmatic hydrothermal alteration of crystallized granites. Furthermore, more than one boron rich hydrothermal alteration stages have been recognized as indicated by difference in composition of the QRV tourmaline. Residual magmatic hydrothermal fluids enriched in B seem to have caused alteration/ auto-metasomatism of feldspar (Fig. 4.2F) in AMG and also led to the formation of thin tourmaline veins crosscutting the crystallized granite. Later on, fluids might have mobilized boron either from the same granite or some other source for crystallization of compositionally distinct coarse grained tourmaline in quartz veins.

As the composition of nodular tourmaline is comparable (e.g. TiO_2, Na_2O) to tourmaline from MPG ground mass, the former seems to have crystallized from residual fluids derived from the same magmatic system (Trumbull et al., 2008; Drivenes et al., 2015). Lack of any fractures and veins connecting nodules to any possible external fluid source further supports this interpretation. However, other models have also been proposed for the formation of tourmaline nodules. According to Rozendaal and Bruwer (1995), post-magmatic metasomatism by externally derived fluids leads to tourmaline nodule formation. Perugini and Poli (2007) have attributed the nodule formation to aggregation of tourmaline grains through limited diffusion of elements.

4.7.4. Epidote as a magmatic phase in Utla granitoids

Epidote as a magmatic product has always been debatable. However, several researchers described it on the basis of pertinent observations (Evans and Vance, 1987; Sial et al., 1999, 2008; Schmidt and Poli, 2004; Ferreira et al., 2011; Pandit et al., 2014; Silva et al., 2015). Several chemical and textural features are described to distinguish between magmatic and metamorphic/ hydrothermal epidotes. However, textural relations are much significant in this regards (Schmidt and Poli, 2004). Tulloch (1979, 1986) used pistacite [$Ps= Fe^{3+}/(Fe^{3+}+Al)*100$] as a distinguishing criterion where Ps = 25-29 represents magmatic epidote, Ps = 0-24 shows epidotes formed as alteration product of feldspar and Ps = 36-48 are representative of those formed by alteration of biotite. This chemical criterion is not very useful because of a larger array of Ps shown by metamorphic epidotes i.e. Ps = 0-100 (Schmidt and Poli, 2004). Evans and Vance (1987) described that magmatic epidotes have < 0.2 wt. % TiO_2, whereas secondary epidotes have >

0.6 wt. %.

Several textural features suggesting a magmatic origin for epidote are described by Tulloch (1986), Zen and Hammarstrom (1984), Zen (1985), Schmidt and Poli (2004) and Sial (2008). These include: a) subhedral to euhedral shape with sharp and clear grain boundaries, b) oscillatory zoning with allanite rich core; however, lack of such zonation does not exclude the possibility of magmatic origin, c) embedded as euhedral grains in quartz and feldspar matrix and d) mineralogical association with hornblende and biotite and other accessory minerals including titanite and zircon (possibly as inclusions).

The chemical schemes described above are not applicable to the epidotes from Utla granitoids as their Ps is mostly low (15-18), though cores of zoned grains have higher Ps (21-23). Epidote from the host rocks (Tanawal Formation) of Utla granites has been analysed in order to check the possibility of xenocrystic origin. Their anhedral form, different coloration, unzoned nature and low pistacite ratio (Ps = 7-10) disprove any similarities, hence inherited source has been denied for the euhedral magmatic epidotes. Three zoned grains from studied granites with analogous pattern i.e. elevated Fe^{3+} content in core with increase of Al content towards the margin, were analysed during the present investigation. Similar zoning pattern and textural features have also been noted in magmatic epidote from Malanjkhand granitoids in central India by Pandit et al. (2014).

The zoning in epidote indicate changes in composition of crystallizing melt, oxygen fugacity and physicochemical conditions (Sial et al., 2008). The zoning pattern show depletion of melt in Fe^{3+} during the epidote crystallization. The occurrence of epidote in AMG and its absence in MPG support the faster cooling condition caused by the rapid ascent of melt. Epidote can crystallize from the peraluminous melt and escape the dissolution due to faster cooling of melt (Brandon et al., 1996). Photomicrographs show the partially corroded and resorbed nature of epidote grains (Fig. 4.8) which signify the instability of epidote in the system. The survival of such unstable grains from dissolution indicate the faster crystallization of surrounding grains.

4.7.5. Garnet zonation

The distinct chemical composition of central garnet (Sp_{47-50}) described above can be explained by assuming it as xenocrystic surrounded by secondary hydrothermally grown garnet. However, several garnet grains from the metasedimentary host rock i.e. Tanawal Formation yield utterly different composition with markedly lower Sp content ($Gr_{25\text{-}41}$-$Sp_{16\text{-}26}$-$Alm_{39\text{-}46}$) which exclude the inherited possibility of central garnet zone (Appendix-1).

Garnet is an uncommon mineral in granites, however, its existence in per-aluminous granitic systems as magmatic mineral is documented by several researchers (Kebede et al., 2001; Rene and Stelling, 2007; Villaros et al., 2009; Yang et al., 2013). Although it is a difficult task to distinguish between magmatic and metamorphic/ hydrothermal garnets within the same host, some recent studies have successfully addressed this issue with the help of major element zoning patterns (Dahlquist et al., 2007; Yang et al., 2013), oxygen isotope and trace element data and Sm-Nd geochronology of garnets (Jung and Hellebrand, 2006; Taylor and Stevens, 2010; Lackey et al., 2011). The higher concentration of Mn in melt is one of the chief controlling factors for the formation of magmatic garnet (Miller and Stoddard, 1981). The magmatic garnets, as described in the literature, contain spessartine as the principal constituent forming solid solution with almandine as a major component and only minor amounts of grossular, pyrope and andradite.

The characteristic Mn zoning pattern can distinguish magmatic garnet from others i.e. grain with uniform spessartine content in core with increasing trend towards the margins (inverse bell shaped profile) (Dahlquist et al., 2007). Such a pattern indicates its crystallization above 700°C from per-aluminous melt. This observation is also supported by garnet geochemistry from Xihuashan granite in southern China (Yang et al., 2013). The central zone of garnet from the present study described above, show similar inverse bell shaped profile of the spessartine content (Fig. 4.9) that can be achieved via crystallization directly from a per-aluminous melt. Furthermore, in agreement to studied magmatic garnets, the central zone is chiefly composed of spessartine and almandine components (>90%) with low to very low grossular content.

In contrast, the outer regions of zoned grains and the unzoned garnet grains from the matrix are enriched in Gr component showing solid solution with Alm and Sp. These seem to be the product of hydrothermal or metasomatic processes following crystallization of the main granitic body. Gr rich garnet composition along fracture within central zones strongly indicate its crystallization via secondary hydrothermal processes (Fig. 4.9). Considering epidote as a magmatic mineral, its inclusion in garnet (Gr rich) also support the secondary growth of latter. The intensity of post-crystallization processes is also shown by diverse tourmaline compositions and occurrence.

4.7.6. Mineralization potential of Utla granitoids

Certain chemical elements, especially Rb, Sr, Ba, Li, and Zr, are widely used in exploration geochemistry and considered as reliable indicators of mineralization in granitic suites (Haapala, 1977; DallAgnol et al., 1994; Srivastava and Sinha, 1997; Baker et al., 2005; Fogliata et al., 2012). The relationship between these elements has been used to distinguish between fertile and barren granites. Figure 4.16 shows the Rb-Ba and Rb-Sr relationship in MPG and AMG. Samples from both the suites fall in the fertile region. Most of the samples from MPG and AMG fall in the fields of Sn-W mineralized granites in the plot of total alkalis versus silica (Fig. 4.16) (Baker et al., 2005).

The geochemical comparisons between mineralized and barren granites have been discussed by Srivastava and Sinha (1997). Elemental ratios including Rb/Sr, Ba/Rb, Mg/Li and K/Rb are deemed particularly important for assessing the mineralization potential of granitic suites. Higher Rb/Sr and lower Mg/Li and Ba/Rb ratios are good indicators for Sn-W mineralization. An index known as geochemical characterization Index (GCI=Log_{10} ($Rb^3*Li*10^4/Mg*K*Ba*Sr$) has been introduced. The positive GCI values indicate mineralized granites, while negative values suggest the system to be barren. Calculations yield positive GCI values for the Utla granitoids (MPG = 9-17; AMG= 14-17) (Table 4.3). Furthermore, the indicator trace elements (Rb, Sr, Ba and Zr), mentioned above, as well as Th, U, Sn, W, Ga and Y in the Utla granitoids are normalized to their respective average concentrations in crustal granites (Fig. 4.17). The enrichment in Sn, W, Ga and Rb and corresponding depletion in Sr and Ba strongly indicate mineralization in both MPG and AMG. Sample (UT-23) from Sn-enriched alteration zone is particularized in the figure for the purpose of comparison with other Utla granitoid samples. The Rb/Sr vs Sn plot (Fig. 4.17) also shows the tin granite signature of Utla granitoids. The potential of these granitoids to host the late stage metal (Sn, W and Ga) vein deposits is further supported by the occurrence of nodular tourmalines. Fluids responsible for such a late stage alteration seem to be those rich in B as well as other economically important metals like Zn, Sn, Ga and W as suggested by Rozendaal and Bruwer (1995) for similar nodular tourmalines in Cape granite suite, South Africa. Similar quartz-tourmaline nodules with elevated Sn concentrations and quartz-tourmaline-cassiterite veins, are reported from leucocratic granite of the Seagull Batholith, Canada (Sinclair and Richardson, 1992).

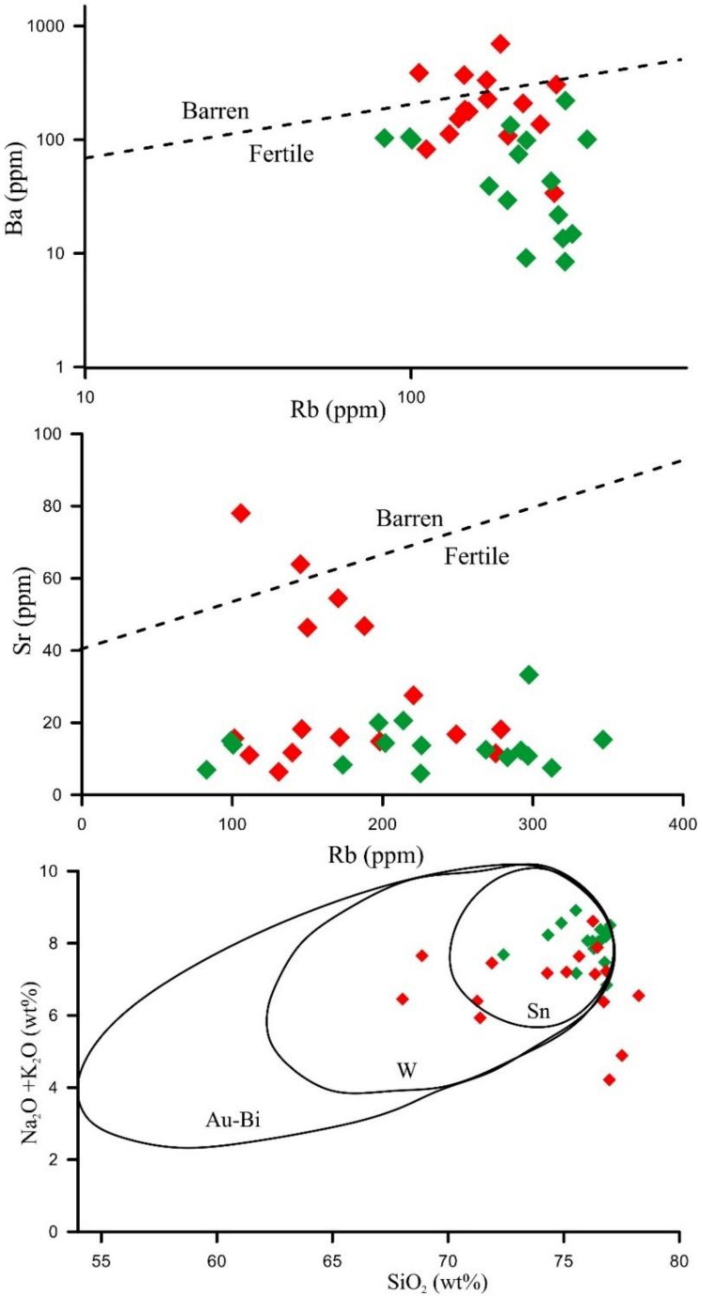

Fig. 4.16. A) Rb vs Ba and B) Rb vs Sr plots showing the mineralization potential of Utla granitoids, the fields of barren and fertile granites from Olade (1980), C) SiO_2 vs Na_2O+K_2O plot, fields for typical Sn, W and Au–Bi bearing granitoids (Baker et al., 2005). Symbols are same as in Figure 4.10.

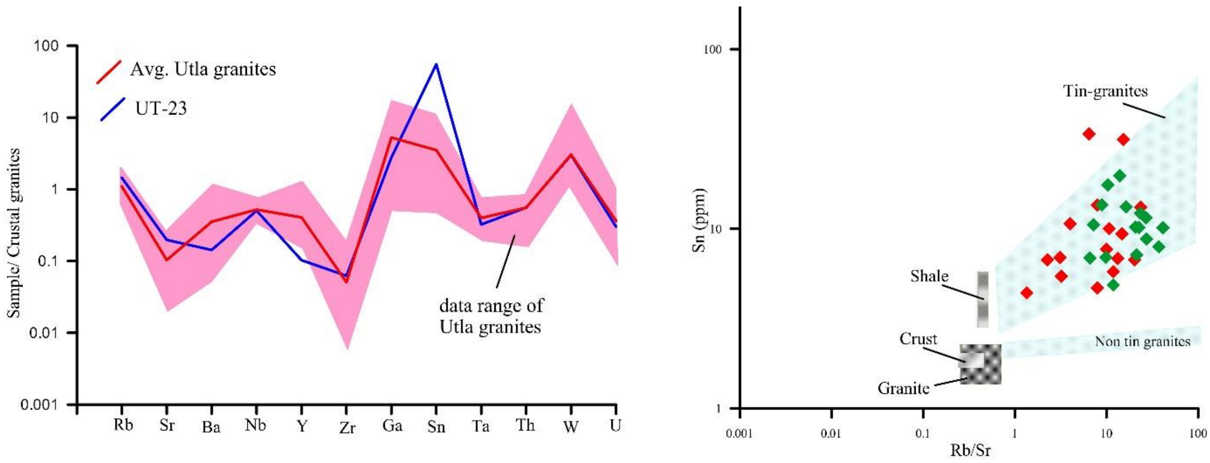

Fig. 4.17. A) Crustal granites normalized spidergram for interpretation of enrichment in economic minerals, normalized data from Rudnick and Gao, (2003), B) Position of Utla granites in Rb/Sr vs Sn plot of Lehman (1987) pointing towards stanniferous nature. Symbols are same as in Figure 4.10.

4.7.7. Comparison with other granitic suites

The granites with analogous geochemical signatures in similar tectonic regime are noticed in other Himalayan regions (e.g. LeFort et al., 1986). In NW India, several peraluminous granitic plutons with similar mineralogical and geochemical characteristics were reported e.g. Jispa granites (Islam and Gururajan, 1997), Tso Morari Granite (Girard and Bussy, 1999), Rakcham Granite (Kwatra et al., 1999) and Mandi Granites (Miller et al., 2001). Similar granitic suites from Nepal include Simchar Granite (LeFort et al., 1983), Palung Granite (Gehrels et al., 2006a) and Kathmandu (Gehrels et al., 2006b). Paleogeographic reconstructions indicate the juxtaposition of southern China blocks (e.g. Baoshan block) to northern Indian plate in early Paleozoic span (Metcalfe, 1996). The granitic plutons in SW China also show similar geochemical characteristics (Wang et al., 2010, 2013; Dong et al., 2013) to the Utla and Mansehra granites and other mentioned Himalayan granites (Fig. 4.10). The origin of these granites has been related to melting of metasedimentary source rock (Fig. 4.14) followed by fractional crystallization of feldspar and biotite (Dong et al., 2013; Wang et al., 2013). The whole rock geochemical data of Tso-Morari and Mandi pluton from NW India (Girard and Bussy, 1999; Miller et al., 2001 respectively) and Baoshan and Shan-Thai block from SW China (Dong et al., 2013; Wang et al., 2013) is presented for comparison (Fig. 4.10, 4.13, 4.14). Apart from geochemical similarities, these granites show early Paleozoic ages ranging from ~460 to ~530 Ma as evidenced from their extensive geochronological studies using Rb-Sr (e.g. LeFort et al., 1980; Debon et al., 1981; Trivedi, 1990; Einfalt et al., 1993) and U-Pb (e.g. Gehrels et al., 2006a; Dong et al., 2013; Wang et al., 2013) dating techniques. On the basis of geochemical and geochronological connections, Utla and Mansehra granites and other granites from the Himalayan terrane along the northern margin of Gondwana are most likely related to orogenic activity during early Paleozoic (Girard and Bussy, 1999; Miller et al., 2001; Cawood et al., 2007).

The studied granitoids also show similarities to other well studied peraluminous granites. For example, granites from SW England are similar mineralogically and originated from metasedimentary source (Muller et al., 2006; Simons et al., 2016). The different granite varieties are linked to each other via fractional crystallization as evidenced by their REE based models (Simons et al., 2016) and changes in the mineralogical composition e.g. feldspar and mica (Muller et al., 2006; Simons et al., 2016). Late stage tourmaline veins and nodular tourmaline have also been observed in these granites showing similar textural characteristics (e.g. replacement of orthoclase) to tourmaline associated with the Utla granitoids (Drivenes et al., 2015). Different tourmaline generations showing analogous compositional variations to studied tourmalines have also noticed in peraluminous San Rafael granitoids where late stage tourmaline are primarily associated with Sn deposits (Mlynarczyk and Williams, 2006).

4.8. Conclusions

The following conclusions have been drawn from the results and discussion stated above:

1. Field features, textural and mineralogical description divide Utla granitic pluton in to three units i.e. MPG, AMG and QRV. Chemical distribution in zoned plagioclase phenocrysts (Fig. 3), change in albite content of plagioclase from MPG to AMG and depletion of trace elements i.e. Ba, Sr, Nb and Ti indicate fractional crystallization in Utla granitoids.
2. Both MPG and AMG are strongly peraluminous generated from partial melting (up to 30% indicated by REE modelling) from a single pelitic source followed by their evolution through 20-25% fractional crystallization

of feldspars, biotite and REE bearing minerals. Analogous petrographic, geochemical features and source rock characteristics show the comagmatic origin of Utla and Mansehra granites.

3. Diversity in hydrothermal fluids triggering alteration of Utla granitoids is observed as evidenced from different modes of occurrence and chemical differences in tourmaline. Nodular tourmaline seems to have crystallized from residual fluids belonging to the same magmatic system, however, tourmaline from QRV shows its crystallization from fluids derived from some external source.
4. Anomalously high Sn concentration in some alteration zones and enrichment of Sn, W, Ga and Rb relative to average crustal granites is indicative of strong mineralization potential of Utla granitoids. Trace element systematics also depict similar interpretation.

CHAPTER 5

Petrogenesis and tectonic association of rift-related basic Panjal dykes from northern Indian Plate, NW Pakistan: evidence of High-Ti basalts analogous to dykes from Tibet

Submitted:

Sajid, M., Andersen, J., Arif, M. (in review). Petrogenesis and tectonic association of rift-related basic Panjal dykes from northern Indian Plate, NW Pakistan: evidence of High-Ti basalts analogous to dykes from Tibet. Mineralogy and Petrology

Co-authors contribution:

J. Andersen was involved in interpretation of analytical outcomes and geochemical modelling. M. Arif aided during fieldwork and petrographical studies. Both were also involved in elaboration of discussion section.

Abstract

Rift related magmatism during Permian time in the northern margin of Indian plate is represented by basic dykes in several Himalayan terranes including north western Pakistan. The field relations, mineralogy and whole rock geochemistry of these basic dykes reveal significant textural, mineralogical and chemical distinctions between two major types a) dolerite and b) amphibolites. Intra-plate tectonic settings for both rock types have been interpreted on the basis of low Zr/Nb ratios (<10), K/Ba ratios (20-40) and Hf-Ta-Th and FeO-MgO-Al_2O_3 discrimination diagrams. The compositional zoning in plagioclase and clinopyroxene, variation in olivine compositions and major elements oxide trends indicate a vital role of fractional crystallization in the evolution of dolerites. Dolerites show depletion in REEs and other incompatible elements as compared to amphibolites. The equilibrium partial melting models from primitive mantle using Dy/Yb, La/Yb, Sm/Yb and La/Sm ratios show that amphibolite form via smaller degree (<5%) of partial melting than the dolerites (<10%). Trace elements ratios suggest the dolerites originated from the subcontinental lithospheric mantle with some crustal contamination. This is consistent with a petrogenetic relationship with Panjal trap magmatism, reported from Kashmir and other parts of north western India. The amphibolites, in contrast, show affinity towards OIB with a relatively deep asthenospheric mantle source and minimal crustal contribution and are geochemically similar to the High-Ti mafic dykes of southern Qiangtang, Tibet. These similarities combined with Permian tectonic restoration of Gondwana indicate the coeval origin for both dykes from distinct mantle source during continental rifting related to formation of the Neotethys Ocean.

5.1. Introduction

Intraplate magmatism in response to Permian rifting event is widely reported in the northern edge of Gondwana (Sengor, 1979; Pogue et al., 1992a; Metcalfe, 2006; Zhu et al., 2010). Associated with this event, basaltic rocks were emplaced widespread across the Himalayas, Oman and Qiantang areas of Tibet (e.g. Spencer et al., 1995; Chauvet et al., 2009; Shellnutt et al., 2011; Xu et al., 2015). The term Panjal Traps has been introduced for the Permian basaltic flows in the northern margin of Indian plate. The term arises from “Pir Panjal ranges” in Kashmir (Calkins, 1975), however, the existence of Panjal traps has now been reported from several localities in Pakistan (e.g. Papritz and Rey, 1989; Pogue et al., 1992a; Spencer et al., 1995) and India (e.g. Gaetani et al., 1990; Chauvet et al., 2008; Shellnutt et al., 2014). The origin of Panjal Traps has been inferred to relate with deep mantle plume activity (Chauvet et al., 2008; Zhu et al., 2013; Zhai et al., 2013), however, Shellnutt et al. (2014) suggested that subcontinental lithospheric mantle (SLM) might be a more likely source on the basis of detailed geochemistry for these basalts from NW India. Basaltic dykes have also been reported from southern Qiangtang in Tibet (Pan et al., 2004; Wang et al., 2009, 2014a) which are divided into Low-Ti and High-Ti dykes with tholeiitic and alkaline character respectively (Zhai et al., 2013). The origin of these dykes has similarly been inferred to relate with a deep mantle plume (Zhai et al., 2013; Wang et al., 2014a).

In comparison to other Himalayan regions, the Panjal Traps exposure in Pakistan has been scarcely investigated. Papritz and Rey (1989) described the detailed geochemical account of basic intrusions from western Hazara-Kashmir syntaxis, Pakistan and relate them to the Panjal magmatic event. Pogue et al. (1992a) gathered magmatic and stratigraphic evidence of Permian rifting in northern Pakistan. The associated magmatism led to the formation of alkaline granites, granodiorites, syenites and dolerites. The dolerites were emplaced as late dykes that occur widespread in the pre-Permian lithologies along the northern margin of Indian plate (Pogue et al., 1992a). Apart from the timing and field relations, previous studies have not elaborated the formation of these basic intrusions. Current investigations reveal significant petrographic and mineralogical variations between these dykes. With this paper, these dykes are characterized on the basis of their mineralogical and geochemical details and the implications of their tectonic settings and emplacement in the context of the regional tectonic evolution have also been assessed. Furthermore, the likely source compositions for these mafic magmas during the rifting episodes is also explored. Previously reported geochemical data of similar basic intrusions from different localities in Pakistan (Pogue et al., 1992a) and NW India (Shellnutt et al., 2014) and high-Ti Qiangtang dykes (Xu et al., 2015) have also been used for comparison and to investigate their plausible relationship and mantle source.

5.2. Geological Setting

The northern Indian plate in NW Pakistan is divided into southern un-metamorphosed and northern metamorphosed zones that are separated by the Khairabad Thrust Fault

(Fig. 5.1A). The northern zone is truncated to the north by regional Indus suture zone (ISZ) or Main Mantle thrust (MMT) (Treloar et al., 1989a; Searle et al., 1999). The ISZ is a succession of mantle derived rocks that include peridotites, gabbros and blue-schists and mark the southern boundary of Kohistan Island arc (Jagoutz et al., 2006; Searle and Treloar, 2010; Burg, 2011).

The northern zone consists a succession of Paleozoic and Mesozoic rocks that are predominantly of metasedimentary origins (Pogue and Hussain, 1986; Pogue et al., 1992b). Intra-plate alkaline magmatism led to the formation of the Peshawar Plain Alkaline Igneous Province (PPAIP) during the Permian, which is considered to be associated with a continental rift environment (Kempe and Jan, 1980; Pogue et al., 1992a). The PPAIP includes the Loe-Shilman carbonatite intrusions (near the border to Afghanistan), alkali granites (the Warsak, Ambela, and Shewa complexes), Nepheline syenites (the Koga intrusion) and albitites in the Tarbela region further east (Fig. 5.1A) (Ahmed et al., 1969; Kempe, 1986; Rafiq and Jan, 1989; Khan et al., 1990; Ahmed et al., 2003; Khattak et al., 2005). Kempe and Jan (1970 and 1980) suggested that the PPAIP formed during an extensional tectonic regime. Sengor (1979) and Jan and Karim (1990) related these alkaline rocks to Permian rifting along the Gondwana continental margin. This interpretation is supported by Permian radiometric ages (250-290 Ma) of the constituent rock types (Le Bas et al., 1987; Zeitler, 1988; Ahmed et al; 2013).

The Ambela granite complex (AGC), one of the largest alkaline bodies in PPAIP (Rafiq and Jan, 1988; 1989), is divided into three units including alkali granites, nepheline syenites and basic dykes. Papritz and Rey (1989) and Pogue et al. (1992a) reported the widespread existence of similar basic intrusions in pre-Permian rock units in the northern metamorphosed zone and correlate them with Panjal trap magmatism (Fig. 5.1A). Mafic dykes intruding Mansehra granite yielded ^{39}Ar/^{40}Ar dates of 284 ± 4 Ma (hornblende) and 262 ± 1 Ma (biotite) confirming a Permian age for the basaltic magmatism (Baig, 1990). The age seems comparable to the U-Pb zircon age of 289 ± 3 Ma from volcanic sequence of Panjal traps in NW India (Shellnutt et al., 2011). Similar dykes also crosscut Palaeozoic and older rocks from e.g. Hazara (Calkins et al., 1975), Tarbela (Jan et al., 1981), the Attock-Cherat ranges (Yeats and Hussain, 1987) and Khyber agency (Shah et al., 1980).

The metamorphic history of the northern Indian plate tectonic units in NW Pakistan is described in Treloar et al. (1989b and c) and Greco and Spencer (1993). The region is mainly affected by prograde Barrovian regional metamorphic event occurred during the Himalayan shearing associated with collision of KIA with Indian plate (Searle and Treloar, 2010). The detailed investigation of metamorphic mineral assemblages from different lithological units show the increasing grade of metamorphism and deformation from southern Hazara regions towards Besham region in north (Treloar et al., 1989b). The recrystallization of basic dykes to amphibolites was noticed in the northern Hazara region by Papritz and Rey (1989) and associated with a similar metamorphic event.

For this study, samples were collected from basic dykes that crosscut the Tanawal Formation and Ambela-Utla-Mansehra granitoids in the region (Fig. 5.1B). Utla Granite was initially correlated with the PPAIP (Rafiq and Jan, 1988; 1989) but recent studies by Sajid et al. (2014) relate it to the Mansehra Granitoids on the basis of mineralogical and geochemical behaviour (Fig. 5.1B). The Utla granites intrude Precambrian Tanawal Formation which is mainly composed of quartzites and meta-pelites (Fig. 5.1B).

5.3. Analytical methods

5.3.1 Mineral chemistry (Electron probe and QEMSCAN)

Thin sections from the representative rock samples were made for the detailed petrographic observations. Selected thin sections were further used for chemical analysis of minerals using Cameca SX100 electron microprobe at the School of Earth Sciences, University of Bristol, UK. The analyses were carried out with an accelerating voltage of 20kV, beam current of 10nA and beam of diameter 5µm. The following standards were used for calibration (peaks shown in brackets): sanidine (KKα, AlKα), ilmenite (FeKα, TiKα), albite (SiKα, NaKα), wollastonite (CaKα), olivine (MgKα), manganese metal (MnKα), Cr_2O_3 (CrKα), Halite (ClKα) and MgF_2 (FKα) standards. Recalculations of mineral formula were determined using spreadsheets based on stoichiometry except for amphibole for which program of Locock (2014) is employed. The representative analyses of each mineral is presented in Table 5.2 and 5.3. The complete list of analysis of each mineral is given in Appendix 4.

A texturally and mineralogically representative thin section of dolerite was also processed with a QEMSCAN-4300 at Camborne School of Mines (CSM), University of Exeter, UK. Thin sections were measured using field scan mode at a resolution of 10 microns, and the data was processed as described by Rollinson et al. (2011). The mineral maps showing plagioclase composition and zoning has been presented here to supplement the mineral chemical data generated by electron microprobe.

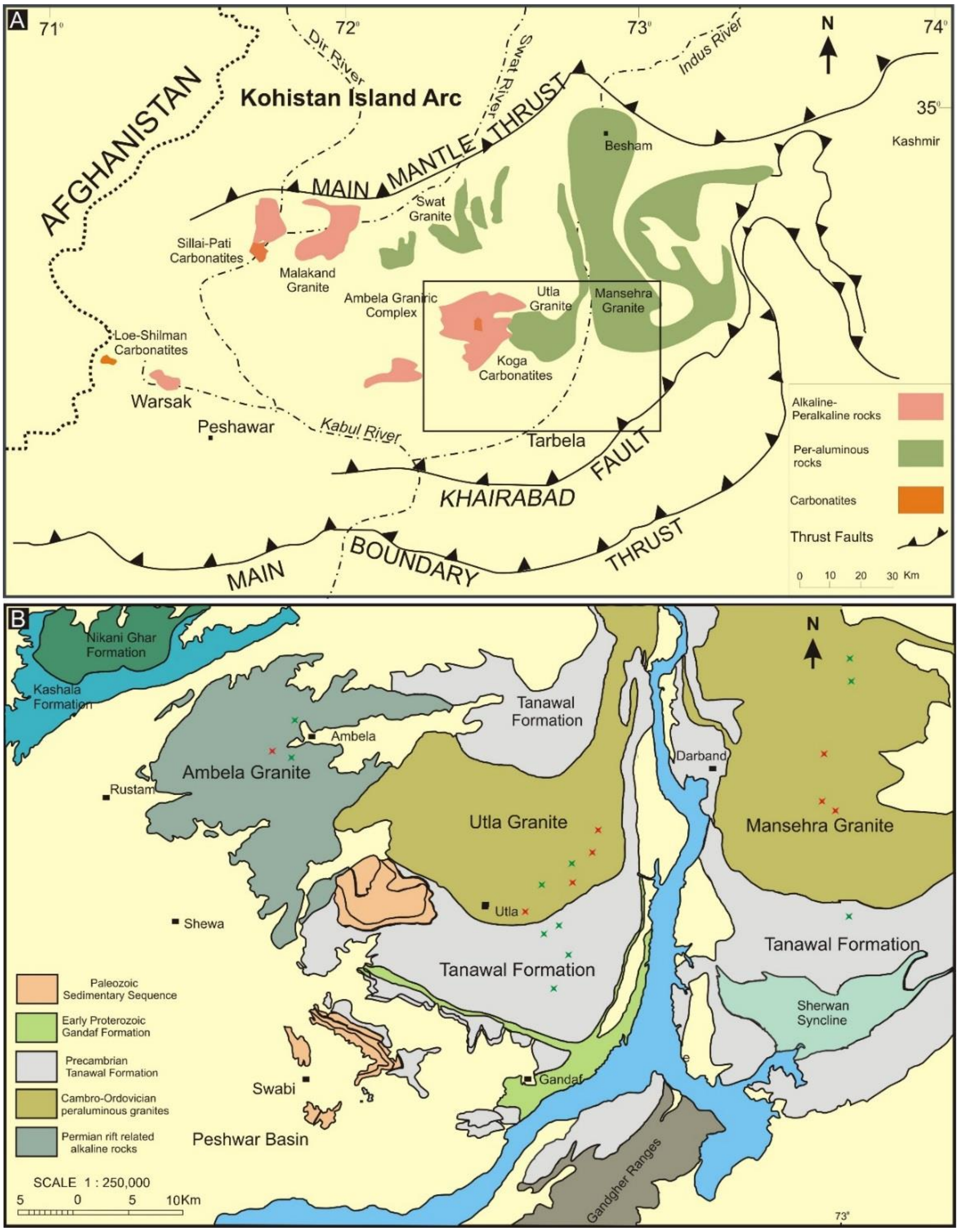

Figure 5.1. A) Regional tectonic map of NW Pakistan (Pogue et al., 1999; Khattak et al., 2005) showing major magmatic units, box showing location of 1B, B) the geological map of study area (Hussain et al., 2004) elaborating the different host rocks for studied dykes. Bold stars showing location of dyke samples (red = dolerites; green = amphibolites).

5.3.2. Whole rock geochemistry (XRF and ICP Mass Spectrometry)

Fresh representative rock samples were crushed and subsequently powdered using tungsten carbide mill. Major element oxides were analysed by X-ray fluorescence (XRF) spectrometry on fused discs at CSM. Standards (DNC-1; Dolerite and Sarm-1: granite) were analysed with each batch to monitor precision and drift. Analytical error on the total concentration of each element is <1% for SiO_2, Al_2O_3, Na_2O and K_2O, <2% for CaO, Fe_2O_3 and TiO_2 and <10% for MgO, MnO and P_2O_5.

Trace elements, including the rare earth elements (REEs) were determined by Inductively Coupled Plasma Mass Spectrometry (ICP-MS) at CSM. Sample powders were dissolved by multi acid digestion (Yu et al., 2001) prior to measurement. The precision and accuracy were monitored using two standard solutions (DNC-1 and Sarm-1) and two blanks with each analytical run. Instrumental drift was monitored using calibration solutions with known concentration of elements. The precision <10% for all the elements.

5.4. Petrography and Mineral Chemistry

The basic dykes intrude the Precambrian Tanawal Formation and granitoids of both Cambrian (Mansehra) and Permian age (Ambela) with sharp contacts and well developed chilled margins (Fig. 5.2a). In certain areas, they occur in clusters of parallel to sub-parallel dykes (Fig. 5.2b). Thickness of dykes varies from less than a meter to several meters across. Their geographic locations and petrographical characteristics are presented in Table 5.1. On the basis of modal mineralogy and textural characteristics, the studied dykes are divided into a) dolerites and b) amphibolites. The distribution of both dyke types is random and each dyke type is not limited to certain areas. However, amphibolites are found relatively common than dolerites.

5.4.1. Dolerites

The dolerite dykes have a fresh (Fig. 5.2c) and massive appearance (Fig. 5.2d) in the field without any sign of deformation and mineral alignment. Plagioclase and clinopyroxene dominate with subordinate olivine, amphibole, biotite and Fe-Ti oxides. Plagioclase is mostly tabular (Fig. 5.3a) and its composition ranges from An_{58} to An_{62} (Fig. 5.4a) in the homogeneous grains while zoned grains are also common (Fig.

5.3b). The zoned plagioclase has anorthite-rich cores and albite-rich margins (Table 5.2, Fig. 5.4b).

Clinopyroxene is mostly fresh but locally displays minor alteration along grain margins (Fig. 5.3c). Grains are mostly brown in colour indicating their titaniferous character. Compositionally, clinopyroxenes vary with wollastonite component ranging from 34 to 43%, enstatite from 34 to 48% and ferrosilite from 11 to 22% (Table 5.2; Fig. 5.5a). Tholeiitic character of host dolerites is shown by the clinopyroxene composition (Fig. 5.5b-c). Exsolution of orthopyroxene is commonly observed in the form of thin lamellae running across the larger augite grains. Olivine grains are mostly colourless with Fo_{32-34} and exhibit corroded margins. However, some dykes have deep brown olivine (Fig. 5.3d) with Fo_{55-67} (Table 5.2). Relatively rare, large grains of brown amphibole (Fig. 5.3e) are also present in some of the dykes. Compositionally (Table 5.3), the amphibole ranges from pargasite to ferro-pargasite (Fig. 5.6) according to the classification of Hawthorne et al. (2012). The oxide phases include titaniferous magnetite with exsolution lamellae of ilmenite (Fig. 5.7a). Chemical analysis (Table 5.2) confirms that these lamellae are nearly pure end-member ilmenite with minor Mg. Most of these oxide grains are bordered by plagioclase forming a reaction rim of light green colour (Fig. 5.7b).

5.4.2. Amphibolites

The amphibolites are altered and deformed (Fig. 5.2 e-f) and are easily differentiated from very fresh and rigid dolerites in the field. Though no cross cutting or any other age relations of the two different dykes has been observed in the field, yet their distinctive field characters and different mineralogical composition (Table 5.1) might be indicative of the difference in their emplacement. The sporadic distribution of amphibolites and lack of any localized shear zone exclude the possibility of deformation in amphibolites due to some localized process. The occurrence of these dykes in Precambrian Tanawal Formation, the Cambrian Utla-Mansehra Granites and early Permian Ambela Granites indicates their younger intrusion age which correlates with Panjal Traps as these are not reported from post-Permian hosts.

In contrast to the fresh dolerite dykes, amphibolite dykes are weathered with schistose fabric and show signs of intense deformation. They are foliated in outcrop (Fig. 5.2e), display a certain degree of preferred orientation (Fig. 5.3f) and have amphibole as the dominant mineral with minor feldspar and quartz. Amphibole is mostly green to light green in colour (Fig. 5.3f) with a composition (Table 5.3) of magnesio-hornblende (Fig. 5.6) according to classification scheme of Hawthorne et al. (2012). It shows elevated CaO and Al_2O_3 (Table 5.3) and less TiO_2, FeO and alkalis relative to the brown amphibole from the dolerite sample. Relict clinopyroxene is locally present enclosed within green amphibole and chlorite. Titanite is a common accessory phase in these rocks. Epidote and clinozoisite extensively replace amphibole and feldspar. The dominance of amphibole and chlorite at the expense of clinopyroxene suggest low grade retrograde metamorphism of these dykes.

Table 5.1. Location and description of studied dolerites and amphibolites samples

Sample	**Location***	**Type**	**Description**
UT-14	N 34^{0}14.849 E 72^{0}39.305	Amphibolite	Very fine grained mainly composed of amphibole in major. opaque minerals surrounded by thin rim of titanite
UT-16	N 34^{0}14.928 E 72^{0}39.377	Amphibolite	Very fragile and altered amphibolite mainly composed of amphibole and clays
UT-39	N 34^{0}15.482 E 72^{0}40.403	Amphibolite	Fine grained groundmass of plagioclase and amphibole. Amphibole phenocrysts are also present showing pseudomorphed relict pyroxenes.
UT-56	N 34^{0}21.205 E 72^{0}46.560	Amphibolite	> 90 subhedral to anhedral amphibole, relatively fresh. Plagioclase and ore minerals are rare and very fine grained
UT-64	N 34^{0}20.474 E 72^{0}45.695	Amphibolite	Foliated amphibolite showing signs deformation. plagioclase is very rare
UT-67	N 34^{0}19.010 E 72^{0}46.595	Amphibolite	Coarse grained. Plagioclase is relatively fresher than other samples. Pseudomorphed amphibole from relict pyroxenes
UT-79	N 34^{0}15.170 E 72^{0}39.139	Amphibolite	Acicular amphibole and ore minerals are present. The colour of amphibole is greenish brown
M-16	N 34^{0}27.258 E 72^{0}55.708	Amphibolite	Foliated coarser grained amphibolite showing signs of intense deformation
UT-1	N 34^{0}13.905 E 72^{0}49.540	Dolerite	Fresh plagioclase and clinopyroxenes in major with 5-10% of brown coloured olivine.
UT-4	N 34^{0}14.023 E 72^{0}39.397	Dolerite	Plagioclase and clinopyroxene but the concentration of olivine is less. Subtle sign of alteration of minerals
UT-63	N 34^{0}20.846 E 72^{0}46.359	Dolerite	Olivine is rare. Clinopyroxene show slight alteration along the grain margin
M-10	N 34^{0}29.629 E 72^{0}59.633	Dolerite	Fresh clinopyroxenes and plagioclase with euhedral amphibole grains
M-12	N 34^{0}27.374 E 72^{0}58.972	Dolerite	Mostly similar to M-10 with addition of brown olivine
M-14	N 34^{0}27.296 E 72^{0}55.757	Dolerite	Fresh clinopyroxenes, plagioclase, colourless olivine and amphibole
M-15	N 24^{0}27.193 E 72^{0}55.683	Dolerite	Medium grained. Resorbed colourless olivine is present

*coordinates data presented (degree-decimal-minute) notation

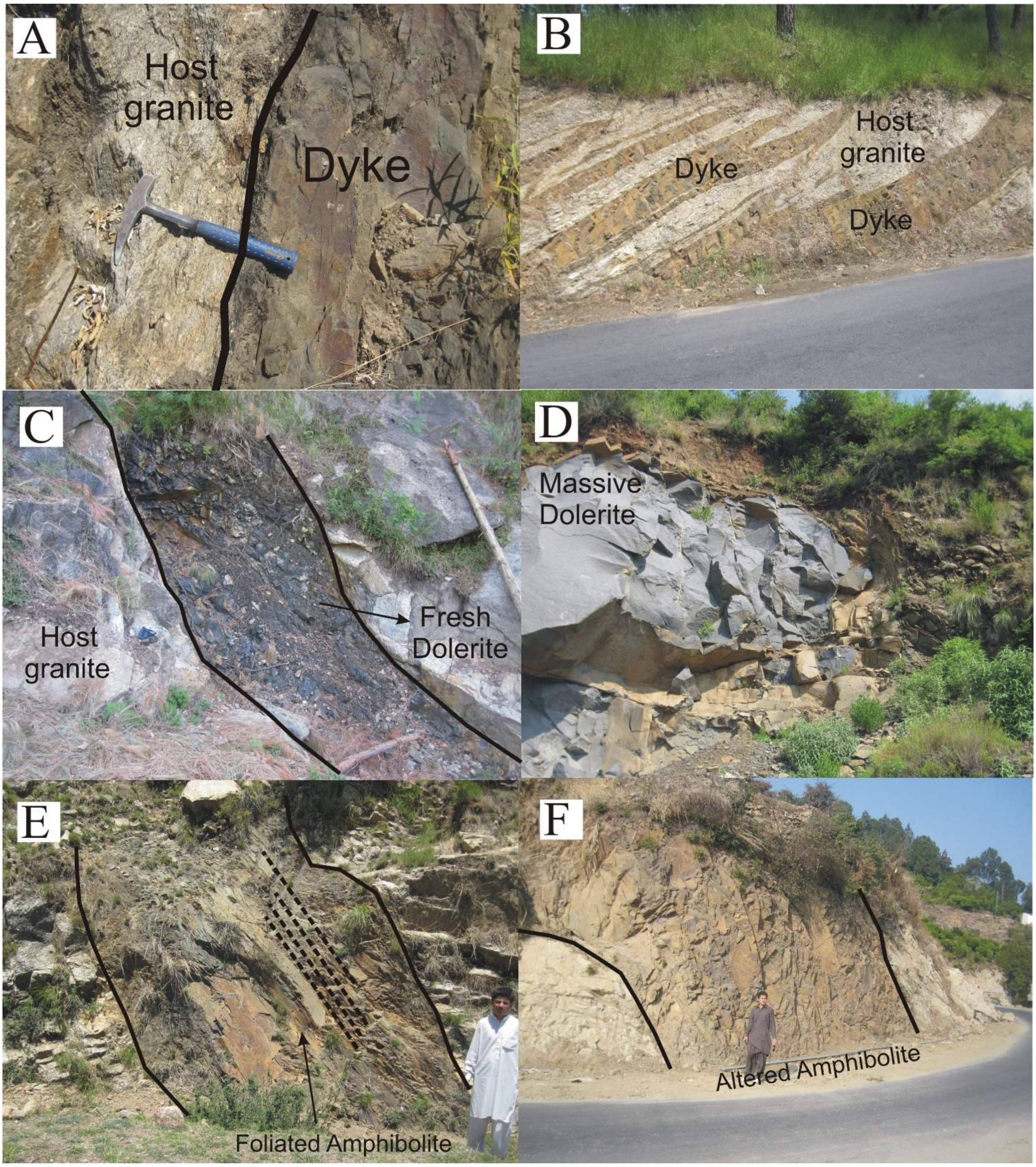

Figure 5.2. Field photographs: A) sharp intrusive contact between amphibolite dyke and Utla granites, B) Set of amphibolite dykes cross cutting the Mansehra Granite, C-D) Dolerite dykes: fresh and massive appearance without any sign of deformation intruding Utla Granites, E-F) Amphibolite dykes, hosted in Utla Granites, showing intense foliation and alteration.

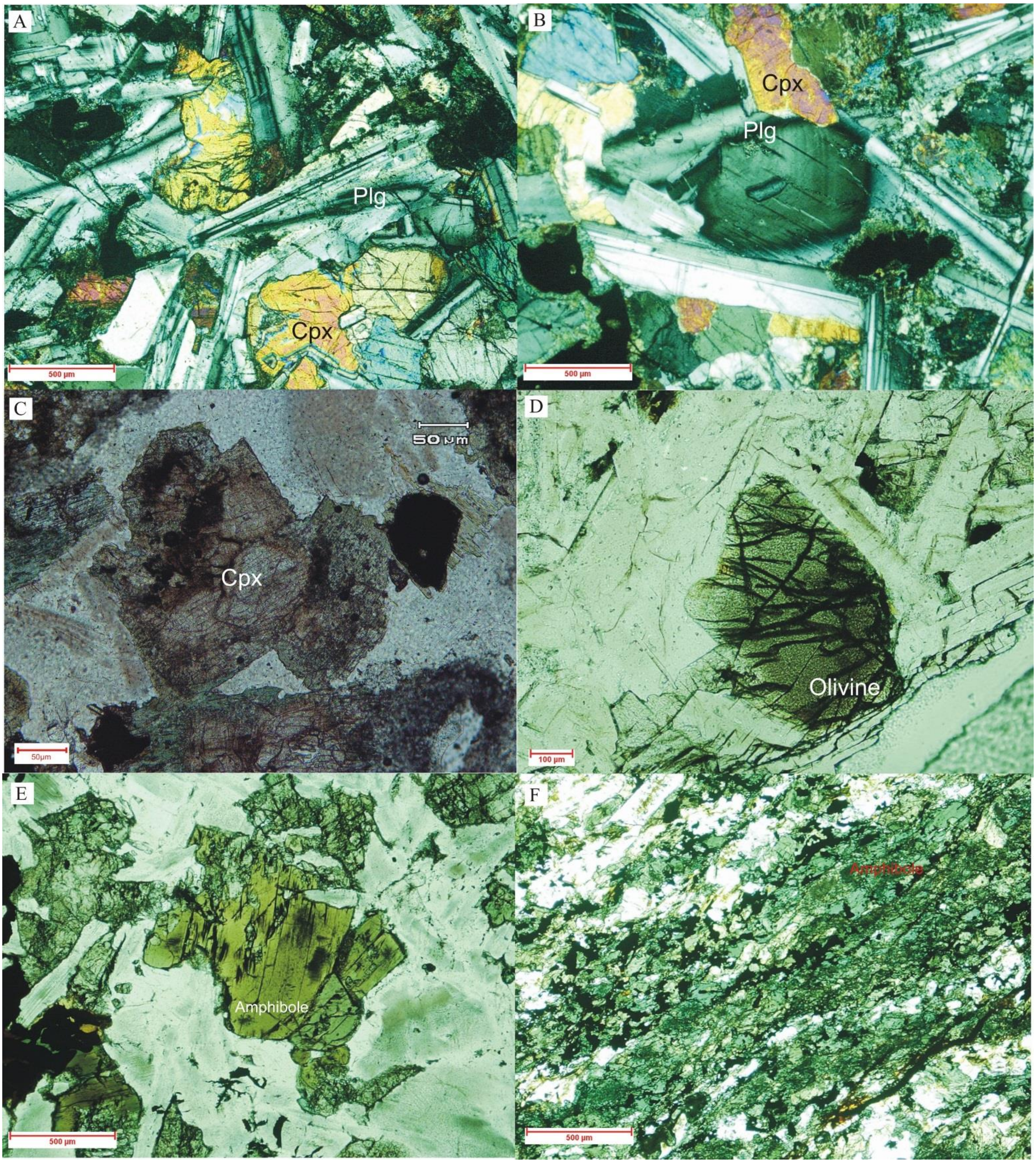

Figure 5.3. Micrographs: A) Tabular plagioclase and euhedral clinopyroxenes, B) Zoned plagioclase, C) Clinopyroxene alteration to amphibole along margins, D) Brown coloured olivine, E) Euhedral brown amphibole from dolerite, F) Preferred alignment of minerals in amphibolites.

Table 5.2. Representative analysis of major minerals from dolerites

	Plagioclase		**Clinopyroxene**	**Olivine**		**Oxides**	
	Core	Margin	--	Brown	Colourless	Magnetite	Ilmenite
SiO_2	52.02	58.48	50.27	36.63	32.96	--	0.20
Al_2O_3	29.46	24.64	3.46	--	--	1.05	2.02
MgO	--	--	16.17	31.11	14.94	--	0.22
CaO	12.78	6.54	18.04	0.25	0.05	--	--
Na_2O	3.96	7.17	0.32	--	--	--	--
K_2O	0.26	0.17	--	--	--	--	--
TiO_2	0.06	0.13	0.80	--	--	4.89	28.10
MnO	--	--	0.20	0.47	0.70		0.49
FeO	0.57	1.39	9.65	31.60	51.09	35.57	24.62
Fe_2O_3	--	--	--	--	--	57.86	44.15
Total	99.11	99.00	98.90	100.05	100.06	99.37	99.79
Formula	**8 O atoms**		**6 O atoms**	**4 O atoms**		**4 O atoms**	**3 O atoms**
Si	2.39	2.66	1.89	1.00	1.00	0.00	0.01
Al	1.59	1.32	0.15	--	--	0.05	0.06
Mg	--	--	0.91	1.26	0.68	0.00	0.01
Ca	0.63	0.32	0.73	0.01	0.00	0.00	0.00
Na	0.35	0.63	0.02		--	--	--
K	0.02	0.01	--	--	--	--	--
Ti	0.00	0.00	0.02	--	--	0.14	0.54
Mn	--	--	0.01	0.01	0.02	0.00	0.01
Fe^{3+}	--	--	--	--	--	1.67	0.85
Fe^{2+}	0.02	0.05	0.30	0.72	1.30	1.14	0.53
***An**	64.07	33.51	--	--	--	--	--
***Ab**	35.93	66.49	--	--	--	--	--
***En**	--	--	46.81	--	--	--	--
***Fs**	--	--	15.66	--	--	--	--
***Wo**	--	--	37.52	--	--	--	--
***Fo**	--	--	--	63.70	34.27	--	--
***Fa**	--	--	--	36.30	65.73	--	--

* An= Anorthite, Ab= Albite, En= Enstatite, Fs= Ferrosilite, Wo=Wollastonite, Fo= Forsterite, Fa= Fayalite

Table 5.3. Comparison between representative amphibole composition from dolerites and amphibolites

Point #	**M-14-1**	**M-14-2**	**M-14-41**	**M-14-4**	**M-8-3**	**M-8-11**	**M-8-12**	**M-8-13**
	Dolerite				**Amphibolite**			
SiO_2	43.27	43.08	43.31	43.35	42.32	43.89	42.34	44.22
TiO_2	2.27	2.36	2.19	2.39	0.52	0.54	0.47	0.61
Al_2O_3	10.22	10.09	10.46	10.04	15.82	14.15	15.93	13.50
MnO	0.21	0.14	0.15	0.21	0.22	0.23	0.16	0.15
FeO	17.14	16.88	17.79	17.11	13.01	12.97	13.38	13.14
Fe_2O_3	1.75	1.86	0.95	2.11	1.02	1.15	1.28	0.95
MgO	9.24	9.49	8.65	9.38	9.22	10.08	9.02	10.29
CaO	10.61	10.63	11.06	10.51	11.61	11.77	11.65	11.76
Na_2O	1.76	1.72	1.44	1.70	1.28	1.22	1.28	1.22
K_2O	0.91	0.93	1.00	0.90	0.62	0.52	0.50	0.58
F	0.03	0.10	0.05	0.12	0.07	0.00	0.04	0.03
Cl	0.02	0.02	0.01	0.02	0.04	0.03	0.05	0.04
O=F, Cl	0.02	0.05	0.02	0.05	0.04	0.01	0.03	0.02
Total	97.44	97.24	97.04	97.79	95.71	96.55	96.07	96.45
Formula on basis on 22 O atoms								
Si	6.55	6.53	6.59	6.54	6.34	6.51	6.33	6.57
Al	1.82	1.80	1.88	1.79	2.80	2.47	2.81	2.36
Fe^{3+}	0.20	0.21	0.11	0.24	0.12	0.13	0.14	0.11
Fe^{2+}	2.17	2.14	2.26	2.16	1.63	1.61	1.67	1.63
Mg	2.09	2.15	1.96	2.11	2.06	2.23	2.01	2.28
Ti	0.26	0.27	0.25	0.27	0.06	0.06	0.05	0.07
Mn	0.03	0.02	0.02	0.03	0.03	0.03	0.02	0.02
Ca	1.72	1.73	1.80	1.70	1.87	1.87	1.87	1.87
Na	0.52	0.51	0.52	0.51	0.34	0.29	0.28	0.32
K	0.18	0.18	0.19	0.17	0.12	0.10	0.10	0.11
F	0.01	0.05	0.02	0.06	0.03		0.02	0.01
Cl	0.01	0.01	0.00	0.01	0.01	0.01	0.01	0.01

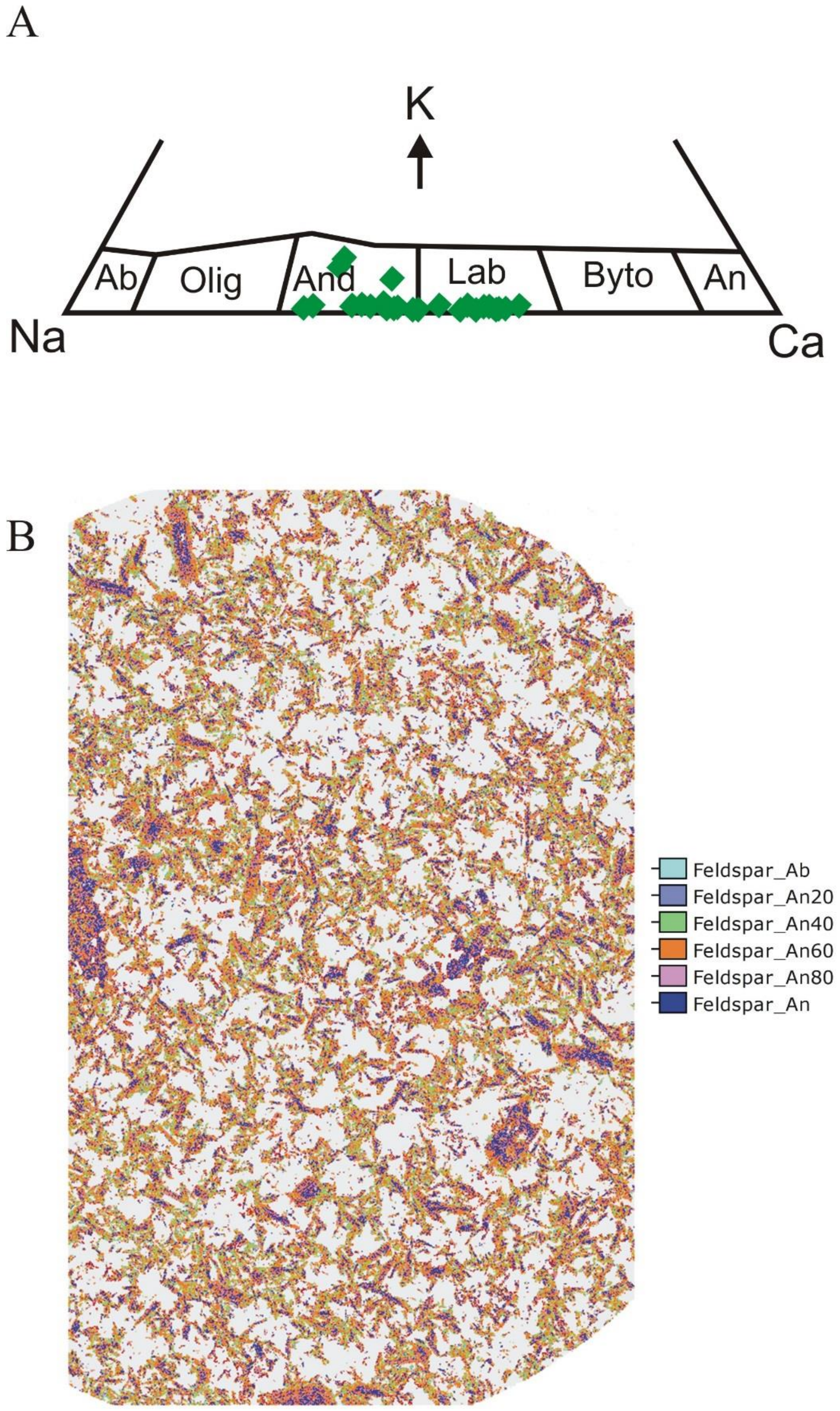

Figure 5.4. Minerals classification, A) Composition of plagioclase from dolerite samples. Symbols: Ab: albite, Olig: Oligoclase, And: Andesine, Lab: Labradorite, Byto = bytownite, An: Anorthite, B) Mineral map of representative dolerite sample generated via QEMSCAN analysis. Zoned plagioclase phenocrysts are clearly illustrated.

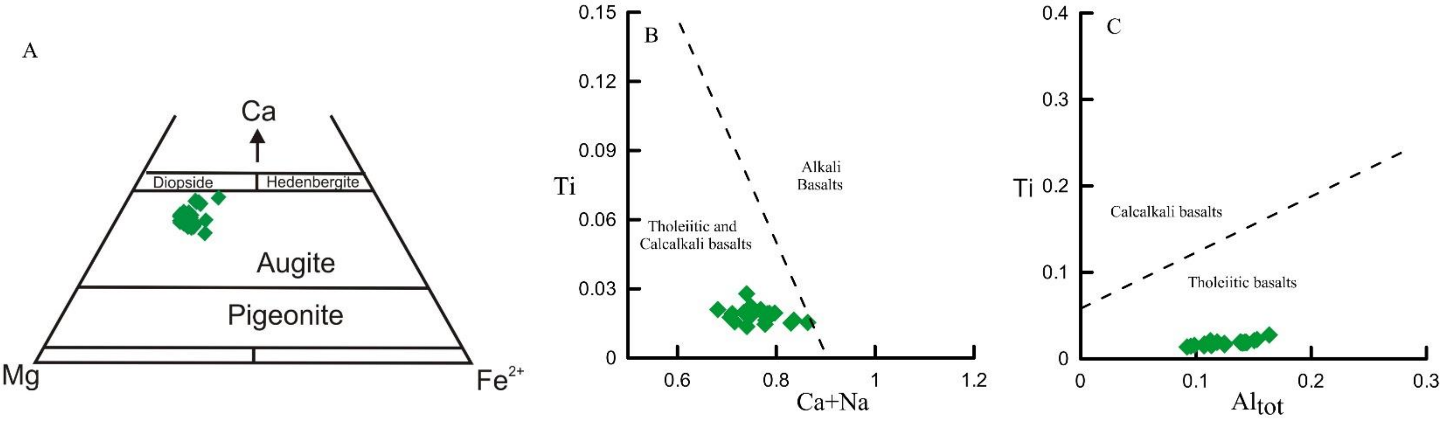

Figure 5.5. A) Composition of clinopyroxenes from dolerites, B-C) Characterization of host rocks based on clinopyroxene composition, division of different fields from Leterrier et al. (1982).

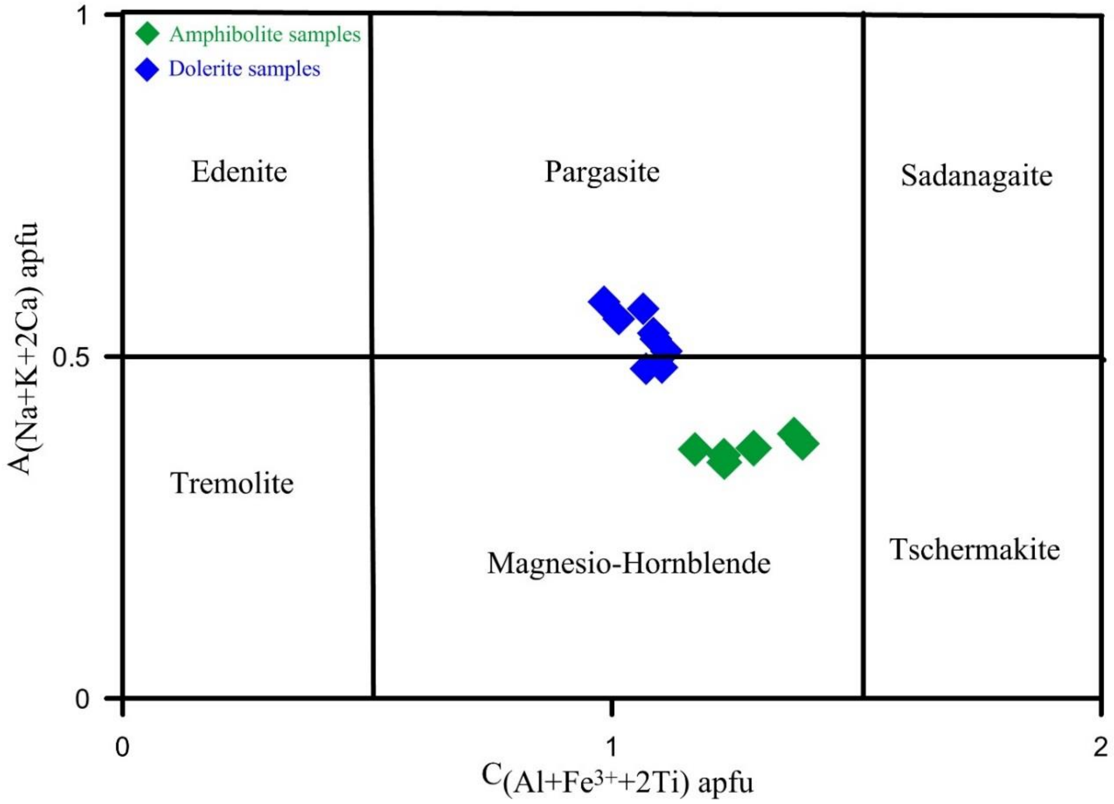

Figure 5.6. Classification and comparison of amphiboles from studied dolerites and amphiboles (Hawthorne et al., 2012). Amphibole from dolerites are pargasitic in composition while they are magnesio-hornblende in amphibolites.

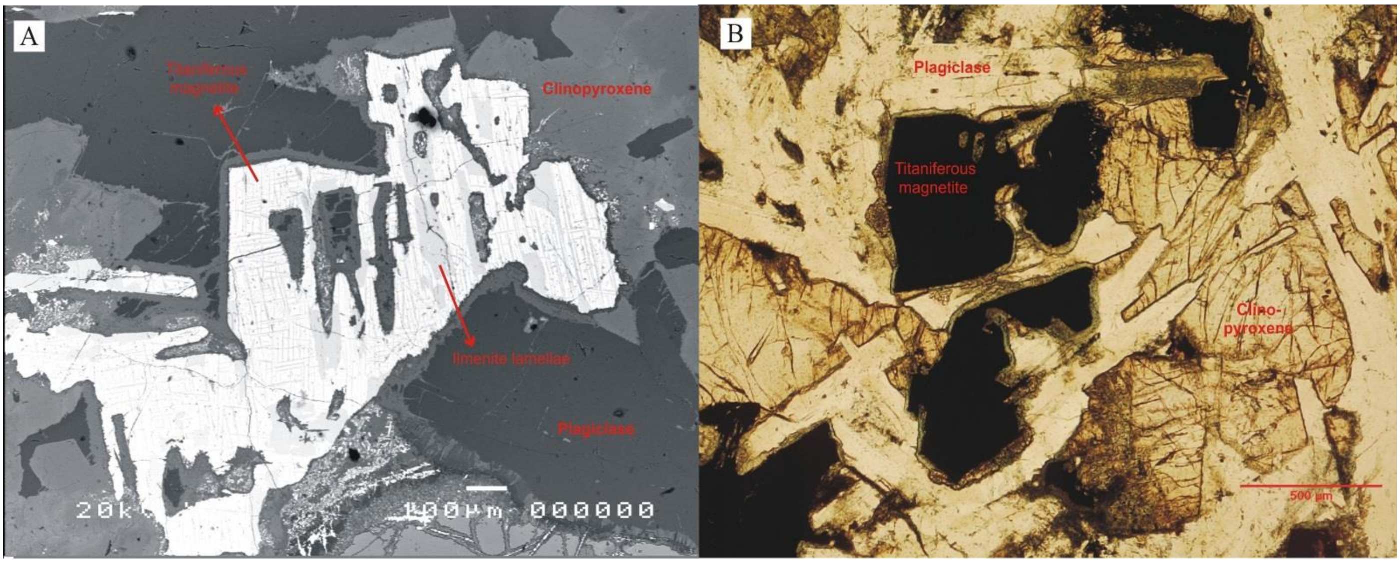

Figure 5.7. A) Back scattered electron image showing exsolution of ilmenite in host magnetite, B) Thin reaction rim of green colour along ore margins.

5.5. Major and trace element geochemistry

The major and trace element concentrations of studied rocks are presented in Table 5.4. The samples of amphibolite show alkaline to sub-alkaline affinity, while most of the dolerite samples are sub-alkaline (Fig. 5.8a). The dolerites show tholeiitic character on Nb/Y vs Zr/TiO_2 plot while most the amphibolites are alkaline (Fig. 5.8b). The TiO_2 content is high (>1.8%) in both types, however, amphibolites are markedly enriched in Ti (>3%) relative to the dolerites (TiO_2 = 1.8-2.7%). The negative relation of CaO, Al_2O_3 against SiO_2 represent fractionation of plagioclase (Fig. 5.9). The fractionation of olivine and clinopyroxene is indicated by the negative trend of Fe_2O_3 and MgO. The SiO_2, CaO and MgO are notably higher in dolerites. The higher abundance of titanite is supported by higher concentration of TiO_2 in the host amphibolites and most likely represent metamorphic replacement of ilmenite.

The chondrite normalized REE pattern and multi-element spider diagrams normalized to primitive mantle are presented (Fig. 5.10). Dolerites are low in LREE relative to the amphibolites, which follow the general REE trend for ocean island basalts (OIB) with negligible Eu anomaly (Table 5.4). The dolerites in contrast, show relatively flat trends. The total REE content of dolerite (ΣREE= 100-147 ppm) is less than amphibolite (ΣREE= 160-345 ppm). The enrichment of HFSE and LILE in amphibolites is evident from the multi-element diagram.

Intra-plate tectonic setting for both the rock types is indicated also by the Hf-Ta-Th and FeO-MgO-Al_2O_3 discrimination plots (Fig. 5.11). Lower Zr/Nb (<10) and K/Ba ratios (amid 20-40) for both the rock types further support their formation through within-plate magmatism.

5.6. Petrogenetic Discussion

The field relations, mineralogy and whole rock geochemistry of basic dykes intruding the pre-Permian rocks in the northern margin of Indian plate are presented. Marked mineralogical and geochemical differences advocate subdivision of the studied dykes into two i.e. dolerites and amphibolites. Both the rock types exhibit alkaline to sub-alkaline nature (Fig. 5.8); however, mineralogical variation, Ti content, the REEs and other trace elements discriminate well between the two.

5.6.1. Evidence of magmatic fractionation in dolerites

The mineral compositions reveal that fractional crystallization has played a major role in the evolution of the dolerite dykes. Zoned plagioclase phenocrysts have higher An content in core and higher Ab content in margin, and clinopyroxene displays zoning with Mg/Ca rich cores and Fe rich margins. The compositional variation in olivine grains in different dolerite dykes further supports the role of fractionation i.e. samples with Fo richer olivine grains solidified earlier from the parent melt than Fo-poorer olivine. Clinopyroxene associated with the Fo-rich olivine displays higher Mg/Mg+Fe^{2+} ratio than the one accompanying Fo-poorer olivine. All of these features are consistent with progressive crystallisation and crystal growth in a cooling and evolving magma.

The Pearce Elements Ratio (PER) is also used to assess the fractional crystallization of mineral or group of minerals in a magmatic system (Pearce, 1968; Nicholls and Russell, 1990). The stoichiometric amount of major elements in common basaltic minerals against an element that is not affected by fractionation (conserved element) is used as the basis for these ratios (Pearce, 1968; Russell and Nicholls, 1988; Nicholls and Russell, 1990). Titanium is used as conserved element in the current approach to assess the fractionation of olivine, clinopyroxene and plagioclase in the dolerite dykes. The fractionation of olivine and plagioclase is revealed from the PER ratios (Fig. 5.12) having slope of unity and r-squared value of 0.98. The results, however, oppose fractionation of clinopyroxene because of deviation from unity slope, however, the r-squared value is 0.93. The PER ratios in support to the mineral zoning and chemical data also indicate the strong influence of fractional crystallization on the evolution of dolerite dykes.

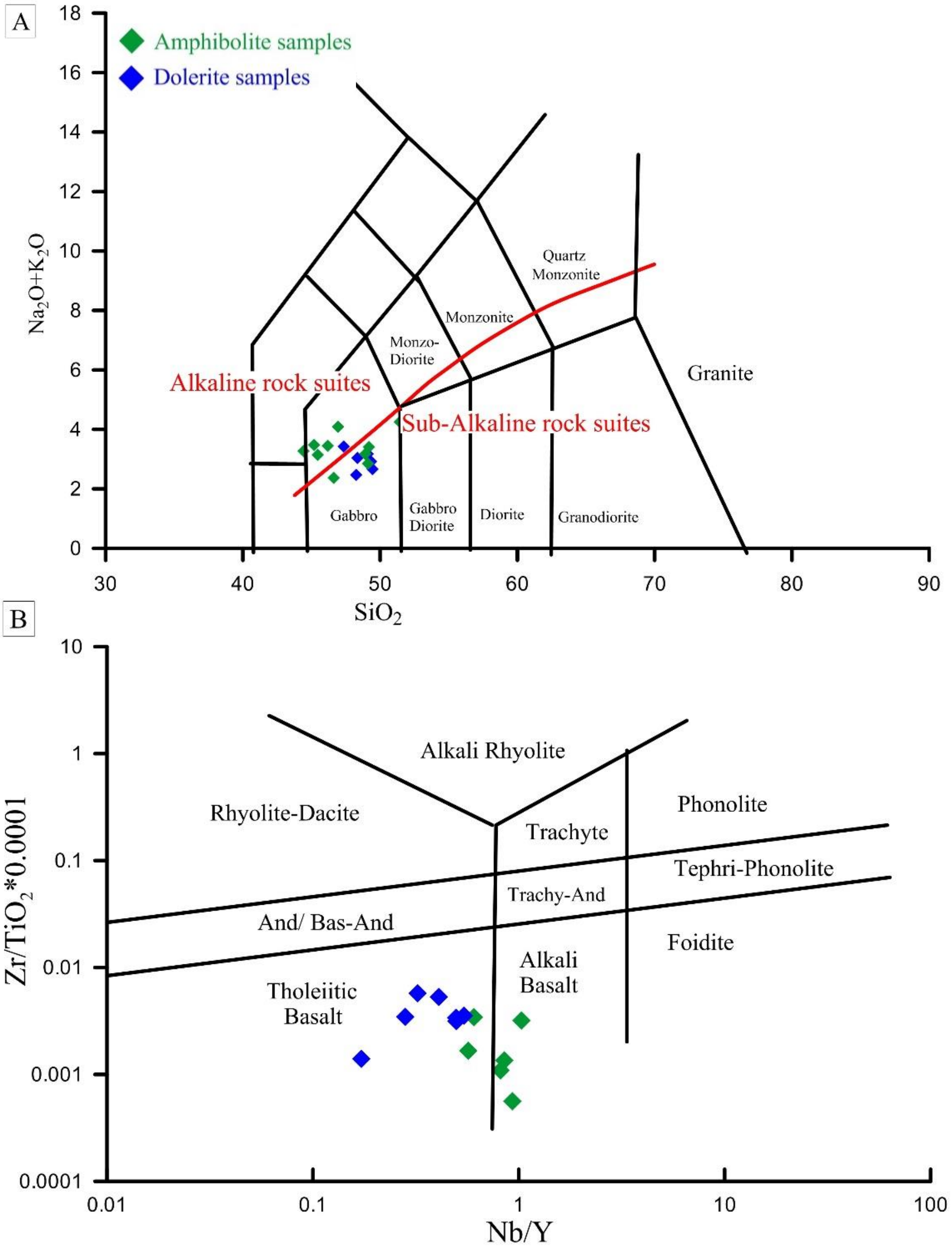

Figure 5.8. Geochemical classification of studied dolerites and amphibolites, A) SiO_2 vs total alkalis plot, dolerites are mostly sub-alkaline while amphibolites are alkaline; B) Nb/Y vs Zr/TiO_2 * 0.0001 plot after Winchester and Floyd (1977), dolerites fall in the field of tholeiitic basalts and amphibolites mostly in alkaline.

Table 5.4. Major (%) and trace elements (ppm) concentration of studied dykes

Sample	**UT-1**	**UT-4**	**UT-63**	**M-10**	**M-12**	**M-14**	**M-15**	**UT-14**	**UT-16**	**UT-39**	**UT-56**	**UT-64**	**UT-67**	**UT-79**	**M-16**
	Dolerites							**Amphibolites**							
SiO_2	49.10	49.34	48.34	49.44	49.18	48.26	47.36	51.43	46.94	44.41	45.45	46.19	48.92	49.19	51.43
TiO_2	2.06	2.01	2.72	2.39	2.64	1.87	2.69	3.17	4.31	5.46	5.26	4.76	3.24	3.73	3.17
Al_2O_3	13.78	13.46	12.34	13.76	13.76	13.60	14.54	13.14	14.57	12.96	13.14	12.88	13.22	12.94	13.14
Fe_2O_3	14.26	14.53	17.60	13.04	14.20	15.04	15.28	14.04	14.53	15.31	16.24	14.85	15.75	14.47	14.04
MnO	0.21	0.21	0.26	0.18	0.19	0.22	0.21	0.16	0.20	0.20	0.20	0.20	0.21	0.17	0.16
MgO	6.29	6.41	5.29	6.87	6.16	6.59	6.40	3.26	3.22	5.46	5.17	5.61	5.16	4.22	3.26
CaO	10.61	10.88	9.57	11.19	10.20	11.65	9.48	7.28	6.28	10.28	9.85	10.08	9.13	8.40	7.28
Na_2O	2.49	2.40	2.35	2.21	2.33	2.23	2.55	2.10	1.76	2.69	2.38	2.74	2.55	2.03	2.10
K_2O	0.69	0.53	0.70	0.47	0.54	0.25	0.88	2.16	2.34	0.59	0.77	0.72	0.63	1.38	2.16
P_2O_5	0.29	0.22	0.33	0.22	0.26	0.17	0.49	1.04	1.11	0.79	0.51	0.74	0.38	0.44	1.04
LOI	0.03	0.26	0.33	0.25	0.40	0.03	0.03	1.78	4.31	1.60	0.69	0.81	0.68	2.86	1.78
Total	99.81	100.23	99.82	100.03	99.87	99.91	99.91	99.55	99.56	99.76	99.67	99.58	99.87	99.83	99.55
Mg#	46.62	46.64	37.31	51.08	46.23	46.48	45.37	31.50	30.52	41.39	38.70	42.81	39.35	36.63	31.50
Trace elements concentrations															
Cr	41.90	37.51	40.26	228.66	133.42	48.76	96.28	15.96	14.19	31.74	23.17	70.54	44.55	56.12	60.26
Ni	57.35	56.08	43.31	94.35	77.74	61.96	62.11	9.13	25.81	52.94	48.78	62.41	41.67	40.28	57.88
Cu	145.17	175.34	169.39	134.08	138.74	219.76	86.83	7.54	35.48	50.72	45.20	63.52	72.10	25.46	37.14
Zn	113.15	112.59	140.16	112.92	119.17	120.37	126.78	145.12	123.66	137.21	148.52	132.37	131.55	129.53	145.32
Rb	26.08	23.94	27.52	31.00	19.72	19.96	40.80	82.97	126.63	19.10	35.95	26.52	20.72	74.14	32.98
Sr	254.61	229.93	169.26	275.09	264.38	188.30	352.36	576.26	509.38	804.77	664.96	673.85	292.45	319.96	778.71
Y	32.12	31.80	48.22	30.12	30.92	31.19	34.83	43.55	48.54	33.03	36.41	39.97	39.05	40.39	40.77
Zr	110.01	116.00	94.55	81.48	94.09	26.30	85.55	84.39	49.24	175.76	57.99	64.63	111.63	62.68	26.41
Nb	13.13	10.27	13.54	14.97	16.73	5.37	17.33	48.47	50.95	34.05	29.71	33.96	23.63	22.92	37.98
Ba	209.71	150.66	192.07	120.80	130.84	72.23	392.13	371.48	169.12	238.77	231.85	192.98	165.65	135.64	201.86
La	17.23	14.83	19.20	18.06	18.19	9.83	24.92	62.64	53.91	36.46	38.24	41.71	24.11	28.16	44.19
Ce	37.67	31.85	42.75	39.74	40.58	21.49	52.74	135.50	124.40	84.27	84.79	90.73	55.55	60.25	102.36
Pr	5.11	4.64	5.97	5.56	5.82	3.45	6.83	17.70	17.14	12.04	12.01	13.27	7.60	8.71	14.70
Nd	22.91	20.77	27.50	24.61	25.90	16.63	29.50	74.57	76.51	55.49	53.34	58.98	34.15	38.83	66.38
Sm	5.81	5.56	7.50	6.08	6.51	4.95	6.95	15.53	16.80	12.29	12.32	13.59	8.59	9.53	14.68
Eu	1.97	1.78	2.40	2.03	2.17	1.74	2.40	4.73	5.31	4.47	3.96	4.51	2.79	3.06	4.81
Gd	6.61	6.26	8.85	6.62	6.92	6.06	7.37	13.99	15.49	11.44	11.52	12.55	9.08	9.90	13.57
Dy	6.67	6.59	9.77	6.37	6.68	6.47	7.25	10.31	11.33	8.21	9.02	9.93	8.54	8.90	10.04
Ho	1.32	1.30	1.97	1.19	1.29	1.29	1.40	1.79	1.97	1.41	1.57	1.73	1.64	1.64	1.73
Er	3.74	3.67	5.75	3.28	3.45	3.59	3.95	4.52	4.83	3.44	3.95	4.42	4.43	4.30	4.31
Tm	0.50	0.50	0.81	0.43	0.48	0.48	0.54	0.56	0.58	0.41	0.49	0.55	0.57	0.54	0.52
Yb	3.20	3.18	5.09	2.67	2.83	3.11	3.35	3.18	3.17	2.38	2.86	3.17	3.46	3.19	3.08
Lu	0.56	0.55	0.87	0.44	0.50	0.51	0.57	0.46	0.45	0.36	0.44	0.50	0.55	0.49	0.46
Hf	3.33	3.45	3.13	2.46	2.93	1.15	2.57	2.71	1.65	5.51	3.03	2.95	3.95	2.72	1.81
Ta	3.41	1.76	1.57	1.63	1.95	1.65	1.72	4.00	3.62	1.79	1.69	2.36	2.09	1.90	2.20
Pb	8.20	5.73	5.10	5.08	2.19	3.08	9.06	13.60	7.10	3.79	6.24	8.09	3.06	8.70	3.08
Th	3.47	3.36	3.86	3.41	2.76	1.96	4.96	12.21	4.91	3.28	4.42	4.60	3.19	3.91	4.52
U	0.73	0.78	0.67	1.04	1.40	0.51	0.91	2.34	2.74	2.15	4.41	1.65	1.00	1.99	1.44
Nb/Y	0.41	0.32	0.28	0.50	0.54	0.17	0.50	1.11	1.05	1.03	0.82	0.85	0.61	0.57	0.93
Eu/Eu*	3.31	3.06	3.53	3.37	3.51	3.12	3.75	5.12	5.50	5.40	4.77	5.19	3.92	4.10	5.33
$(Th/Nb)_{PM}$	2.24	2.78	2.42	1.93	1.40	3.09	2.43	2.14	0.82	0.82	1.26	1.15	1.15	1.45	1.01
Nb/Ta	3.85	5.83	8.60	9.19	8.60	3.25	10.09	12.13	14.09	18.97	17.53	14.38	11.28	12.09	17.27

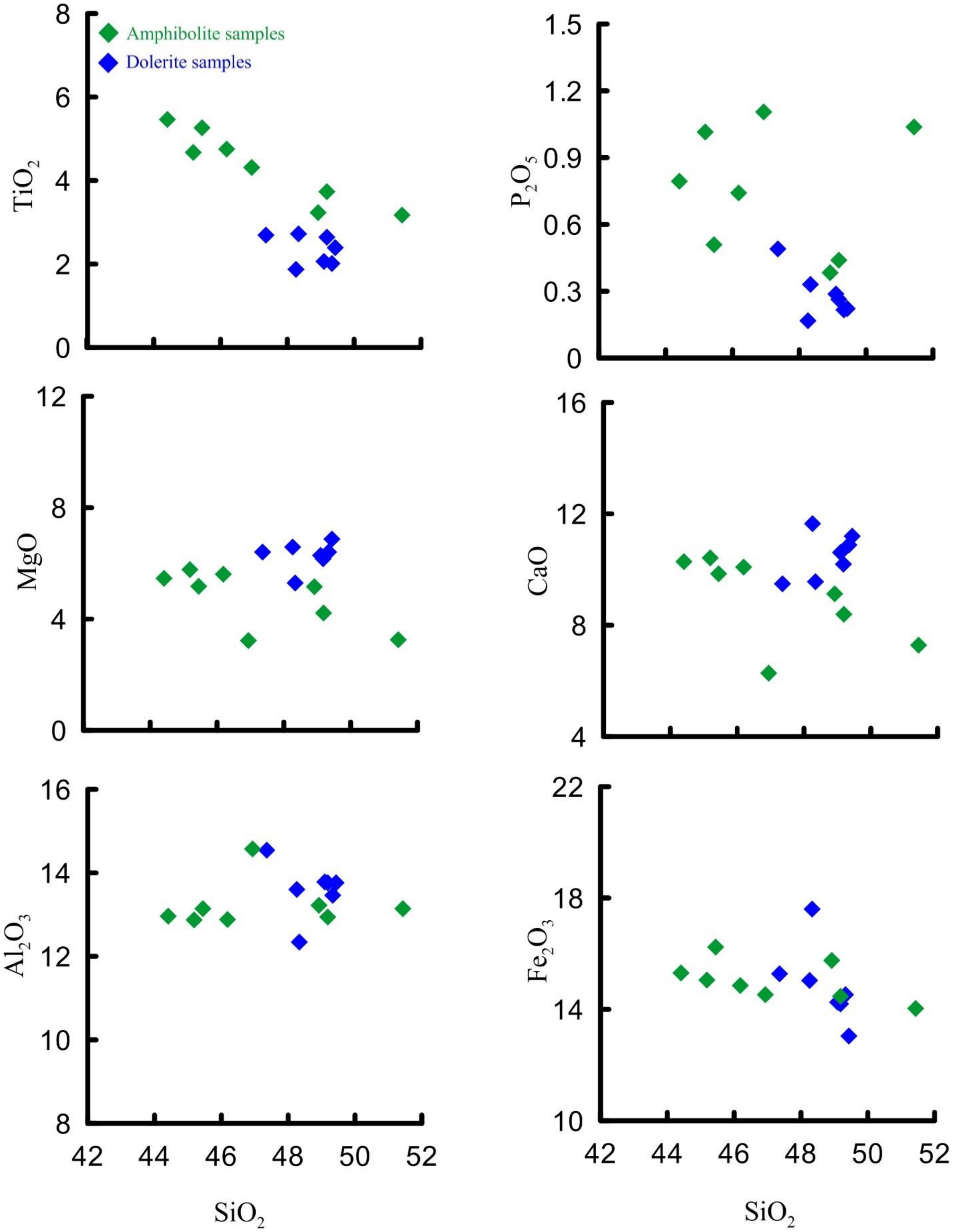

Figure 5.9. Major element Harker diagrams of studied dolerites and amphibolites. SiO_2, CaO and MgO are higher in dolerites. Amphibolites are richer in TiO_2 (>3%) relative to dolerite (<3%). The higher concentration of Ti in amphibolites is supported by the presence of significant amount of Titanite in amphibolites.

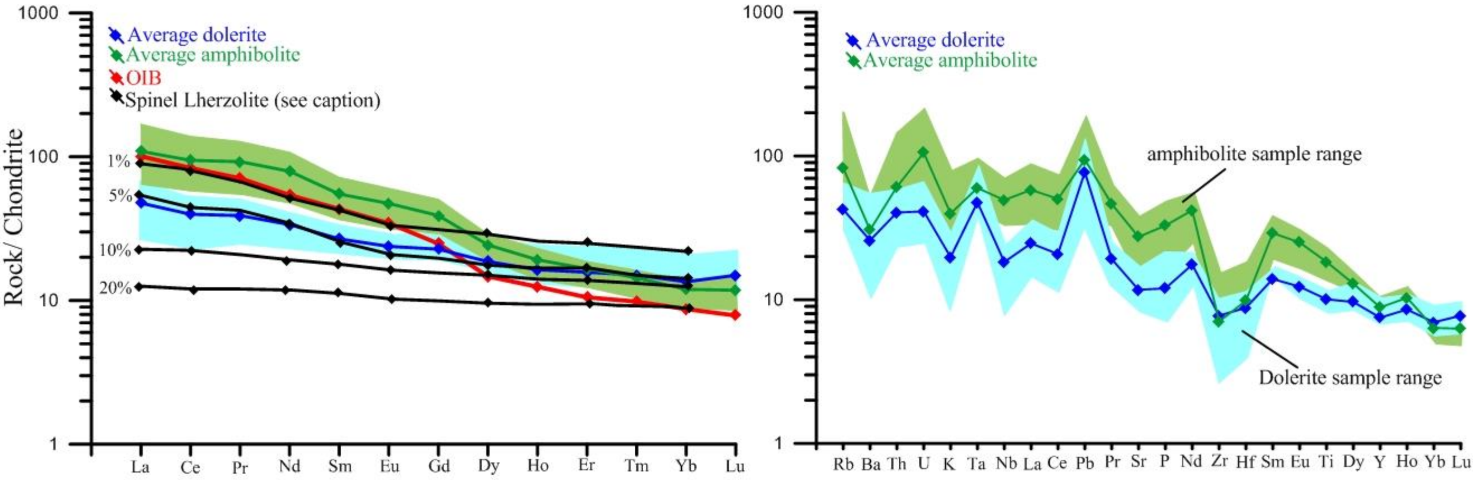

Figure 5.10. A) Chondrite normalized REE pattern of studied dolerites and amphibolites, normalized data from Taylor and McLennan (1985), Ocean Island basalts (OIB) data after Sun and McDonough (1989), the modelling curves represent partial melting of spinel lherzolite (olv60 + opx20 + cpx10 + sp10), (B) Primitive mantle normalized multi-element spidergram, normalized data from McDonough et al. (1992). Shaded area show range of values obtained (dolerites = blue; amphibolites = green).

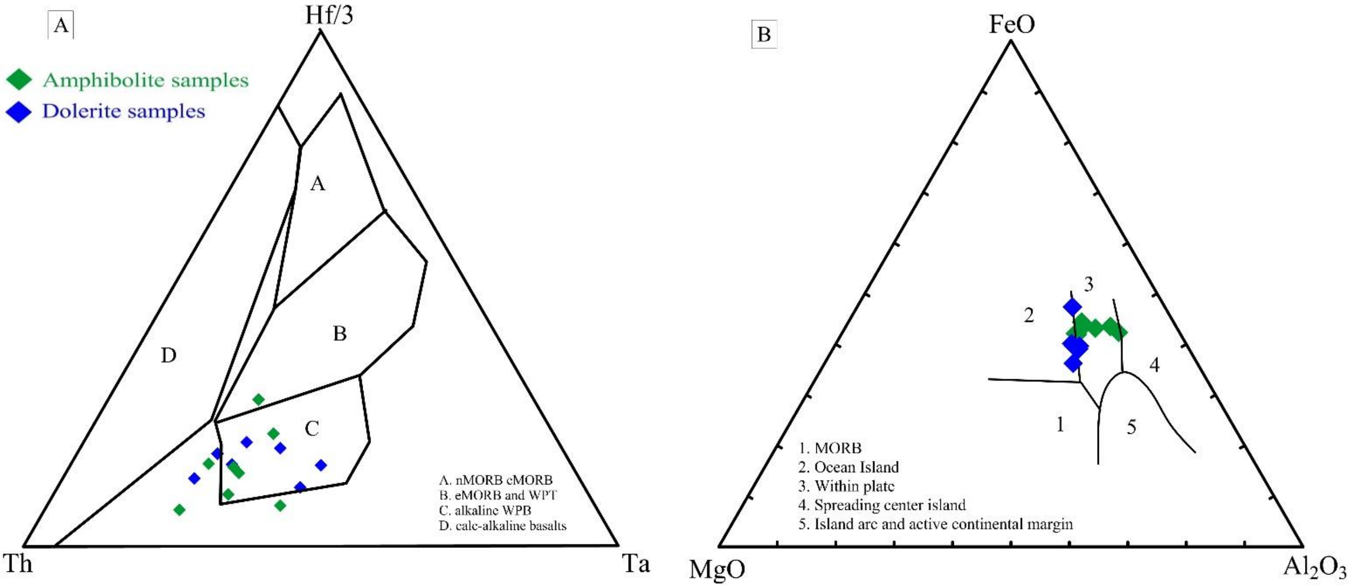

Figure 5.11. Tectonic discrimination diagrams, A) Ta-Th-Hf plot (Wood, 1980); B) MgO-FeO-Al_2O_3 diagram (Pearce et al., 1977). Both the dyke types fall in the field of within-plate basalts.

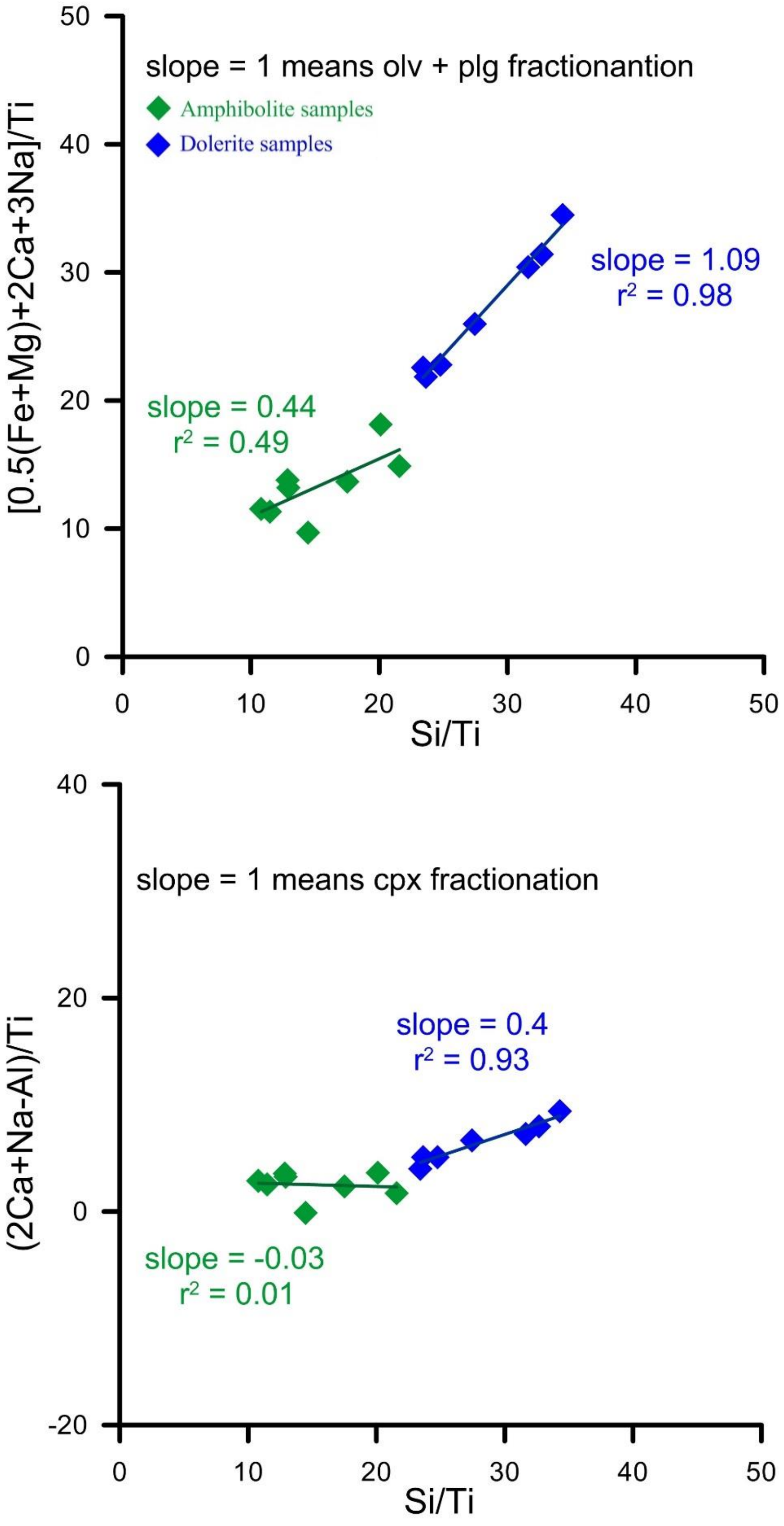

Figure 5.12. Assessment of fractional crystallization using Pearce element ratios (PER) in studied samples (Nicholls and Russell, 1990): A) slope of line is closer to unity in case of dolerites which show the fractionation of olivine and plagioclase in the magma chamber, B) slope of the line deviated from unity which means no clinopyroxene fractionation.

5.6.2. Partial melting of mantle source

The trace elements ratios are potential gauges to provide indications of magmatic processes and mantle source characteristics including depth, composition and amount of partial melting (Fitton et al., 1997; Baksi, 2001; Hughes et al., 2014). Incompatible elements e.g. REE are enriched in a system formed due to lower degree of partial melting as compared to higher degree (Winter, 2010; Zhao and Asimow, 2014). The La/Yb, Nb/Y, Sm/Yb and Zr/Y ratios can be used to estimate the degree of partial melting of the mantle source for mafic magma (Class et al., 1998; Kerr et al., 2010; Xia et al., 2013).

The contrasting mineralogical and geochemical characteristics shown by the two types of dykes suggest derivation of their parent melt at different time episodes and through different degrees of partial melting from distinct sources in the mantle. The amphibolite dykes with higher concentration of incompatible elements most likely represent melt formed by lower degree of partial melting than the dolerite dykes. This interpretation is supported by equilibrium partial melting models from primitive mantle for the studied rocks. The Dy/Yb, La/Yb, Sm/Yb, La/Sm and Nb/Y ratios of studied dykes are plotted along with the melting curves of garnet lherzolite and spinel lherzolite (Fig. 5.13). Whereas the amphibolite samples follow the spinel lherzolite melting curve and represent low degree of partial melting (<5%), the trend of dolerite samples tracks the same curve but reflects a relatively higher degree of partial melting (<10%). The amphibolites show enrichment in LREE and lie above the 5% REE modelling curve for the partial melting of spinel lherzolite on the chondrite normalized plot, while dolerites are mostly below the 10% curve (Fig. 5.10).

Different origins have been inferred for the High-Ti and Low-Ti basalts (Peate et al., 1992; Chauvet et al., 2008; Shellnutt et al., 2014). Low-Ti basalts are most likely derived from sub-continental lithospheric mantle (SLM) or may be representative of crustal assimilation of basaltic magma (Peate et al., 1992; Xiao et al., 2004). High-Ti basalts are interpreted to be originated via mantle plumes from deep mantle (Xiao et al., 2004; Shellnutt and Jahn, 2011). Shellnutt et al. (2014) described the extent of partial melting of similar source to be responsible for Ti division of Panjal trap basalts.

The trace element modelling supports the interpretation of Shellnutt et al. (2014), however, the difference of MgO content and compatible trace elements like Ni, Cr etc.

between dolerites and amphibolites (Table 5.4) points towards the diversity of the source regions in upper mantle as different degrees of partial melting will not affect the concentration of these elements in melt. Continental basaltic melts can be generated by the interaction of asthenosphere and lithosphere (Turner and Hawkesworth, 1995; Wang et al., 2014b). The effective distinction between sub-continental lithospheric mantle (SLM) and asthenospheric mantle can be made using Nb/La ratio. The asthenospheric mantle-derived melts are generally characterized by high Nb/La ratios, however, SLM-derived melts display low Nb/La ratios approaching those of continental crust (Wang et al., 2014b). The Nb/La ratio is more or less the same (average= 0.9 ± 0.08) in all the amphibolite samples, but is lower and shows significant sample-to-sample variation in case of dolerites (average= 0.7 ± 0.12). The higher and more or less uniform Nb/La ratios in amphibolites and analogous Nb/Ta ratio to OIB suggest derivation of its parental melt from asthenospheric mantle (Wang et al., 2014; Cui et al., 2015). However, the lower values and greater variation in Nb/La ratio and lower Nb/Ta ratios of dolerites indicate the source of these rocks to be SLM. Higher $(Th/Nb)_{PM}$ ratio of dolerites than amphibolites also show greater involvement of SLM in former than latter (Fig. 5.14). The lower Nb/Y ratio designates the shallower source basaltic flow (SLM) relative to higher ratios which points towards deeper asthenospheric origin (Shellnutt et al., 2014). The shallower source for dolerites is also supported by their lower Nb/Y ratio (average = 0.3) than high-Ti amphibolites (average = 0.8) (Fig. 5.8b).

5.6.3. Prospects of crustal contribution

The involvement of crustal rocks during the magma ascent can be identified by using Nb/La ratio of rocks (Kieffer et al., 2004; Xia et al., 2013). The depletion of Nb (relative to Th and La) and Ti (relative to Eu) are representative of continental crust in comparison to primitive mantle (Frey et al., 2002; Rudnick and Gao, 2003; Xu et al., 2015). Hence magma contamination associated with continental crust can significantly dilute the concentration of certain elements (e.g. Nb, Ti) which may lead to misinterpreting the rock tectonic setting i.e. contaminated intra-plate basalts can be mistaken for subduction related basalts (having low Nb and low Ti) (Ernst et al., 2005; Xia et al., 2007). Various trace element ratios are used to assess the input of continental crust within basaltic magma including Nb/La, Nb/U, $(Th/Nb)_{PM}$ due to their definite content in crust relative to mantle (Rudnick and Gao, 2003). For example, the primitive mantle have higher Nb/La, Nb/U ratios with lower $(Th/Nb)_{PM}$ ratio in comparison to average continental crust (Saunders et al., 1992; Campbell, 2002; Kieffer et al., 2004). So the contaminated basaltic rocks should have lower Nb/La, Nb/U and higher $(Th/Nb)_{PM}$ ratios than uncontaminated basalts.

The dolerite samples display relatively lower Nb/La and Nb/U ratios and hence their parental melt might have undergone a certain degree of contamination with crustal rocks (Fig. 5.14a and b). The amphibolites also have lower Nb/U ratio similar to dolerites, however $(Th/Nb)_{PM}$ vs $(La/Nb)_{PM}$ plot (Frey et al., 2002) discriminate amphibolites towards lower $(Th/Nb)_{PM}$ ratios which indicates lack of crustal input. The deviation of dolerites is illustrated towards the crustal composition (Fig. 5.14c). The corresponding fields of Hawaiian OIB and Emeishan high-Ti basalts are also shown which are regarded as typical examples of uncontaminated basalts. It illustrates that dolerites from the study area clearly have input form the crustal rocks likewise the other Panjal trap basalts (Fig. 5.14c). The strong negative Nb anomaly observed in the dolerite samples (Fig 5.10) can also be explained by invoking the involvement of crustal component during its ascent. Conversely, lower $(Th/Nb)_{PM}$ analogous to uncontaminated examples, lack of Nb anomaly and higher Nb/La ratios (>0.8) of most of the amphibolite samples show dearth of crustal contamination in their parental melt.

The Nb/Ta ratio is also sensitive to crustal input because of its contrasting values in crustal rocks and asthenosphere mantle-derived melts (Weaver, 1991; Barth et al., 2000). The Nb/Ta ratio of dolerite (7.1 ± 2.7) is significantly lower (Table 5.4) than studied amphibolite (14.5 ± 3.5) and standard OIB (15.9 ± 0.6). As similar i.e. within-plate tectonic setting has been interpreted for both the studied dykes (Fig. 5.11), lower Nb/Ta of dolerites is also indicative to crustal contamination of their parental melt.

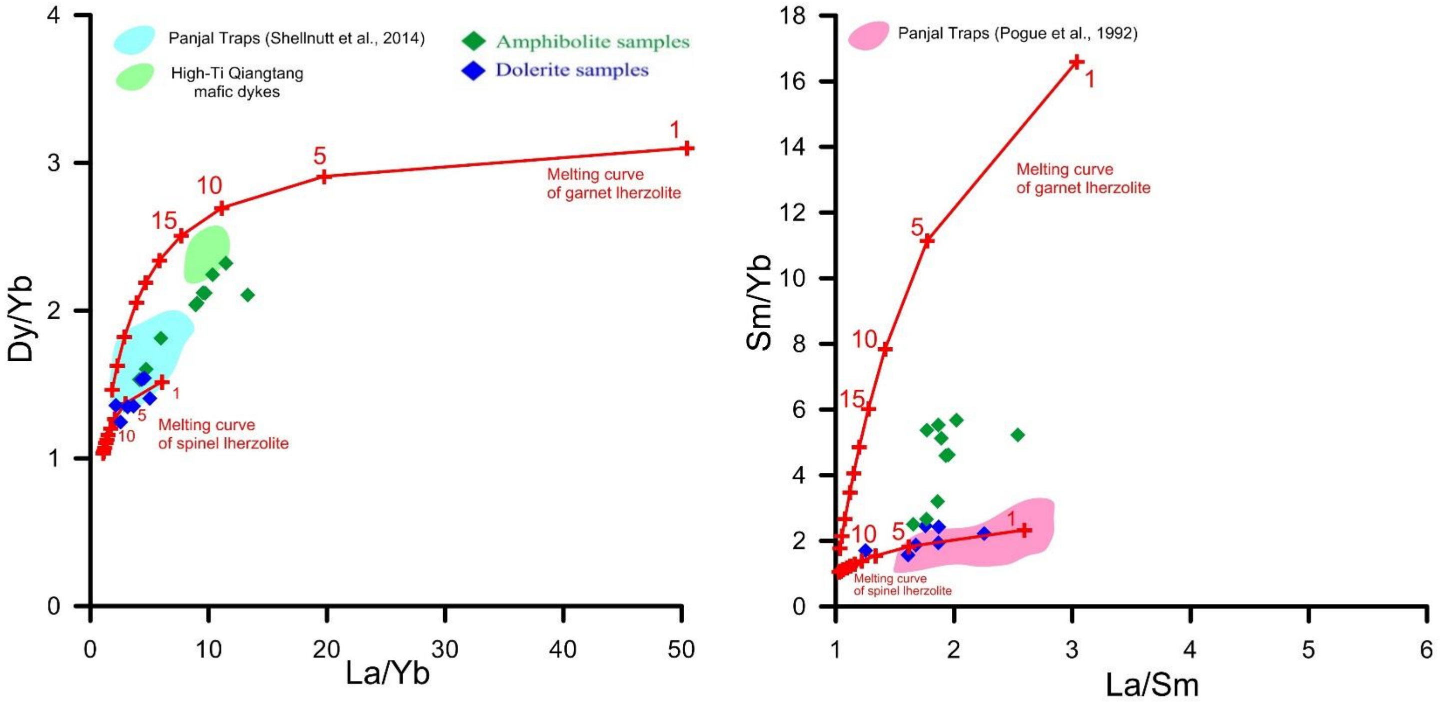

Figure 5.13. La/Sm vs Sm/Yb, La/Yb vs Dy/Yb and La/Yb vs Nb/Y plots of studied dolerites and amphibolites. Melting curves of garnet lherzolite (olv60 + opx20 + cpx10 + Gt10) and spinel lherzolite (olv60 + opx20 + cpx10 + sp10) are calculated from equilibrium partial melting modelling from the primitive mantle. The partitioning coefficients are acquired from the GERM database and Rollinson (1993). Numbers along the curves signify the degrees of partial melting. Panjal trap basalts after Pogue et al. (1992a) and Shellnutt et al. (2014), Qiantang mafic dykes after Xu et al. (2015).

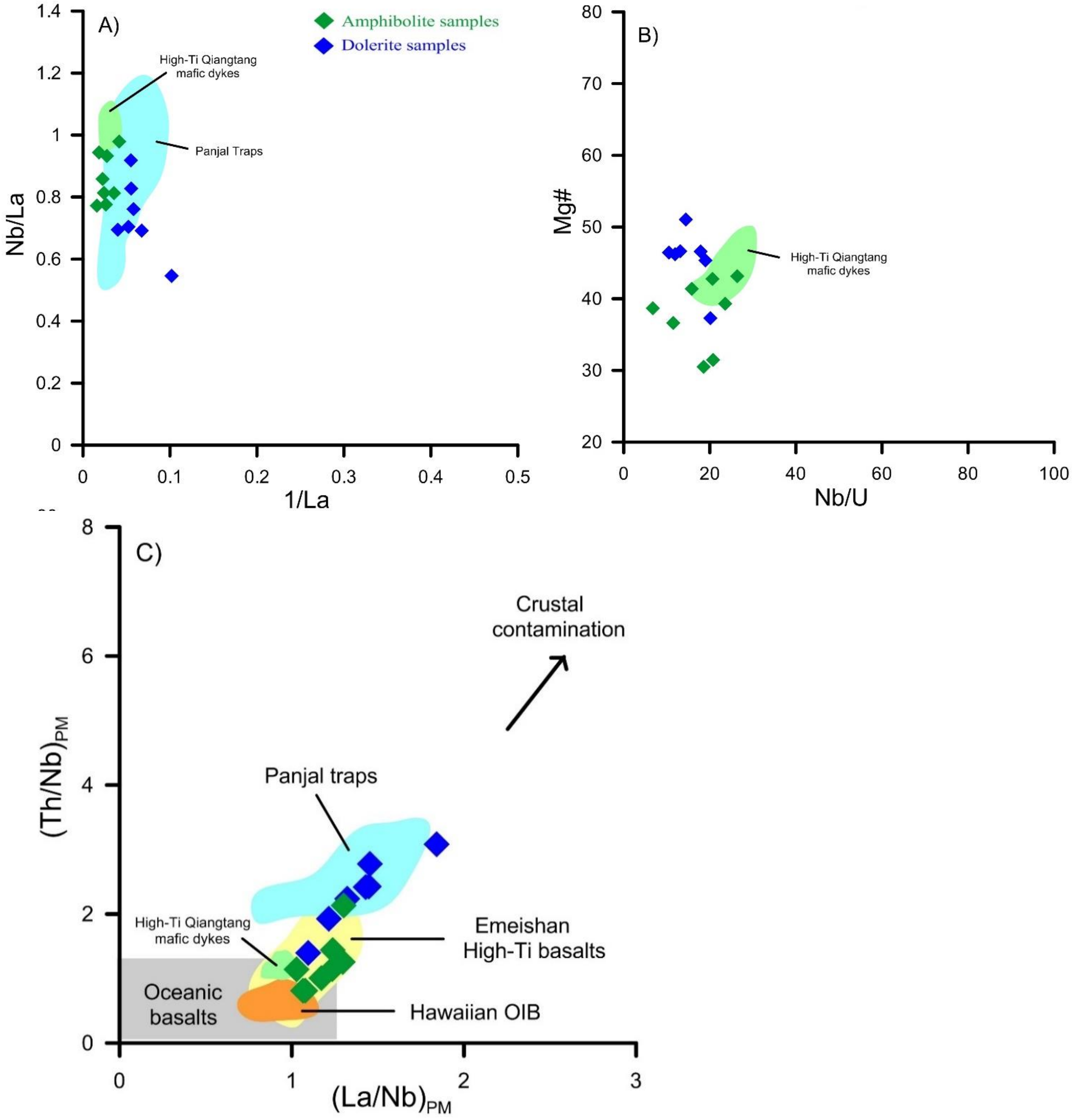

Figure 5.14. Nb/La vs 1/La, Mg# vs Nb/U and (La/Nb)PM vs (Th/Nb)PM plots used to interpret the crustal contamination in studied samples. The dolerites, just like Panjal Traps, show significant crustal contamination during magma ascent, however, amphibolite compositions lack crustal input similar to high-Ti Qiangtang dykes. Data source of Panjal traps (Shellnutt et al., 2014), high-Ti Qiantang mafic dykes (Xu et al., 2015), Oceanic basalts (Frey et al., 2002), Hawaiian OIB (GEOROCK database); Emeishan High-Ti basalts (Xu et al., 2001; Xiao et al., 2004).

5.6.4. Comparison with Panjal traps from other locations

The petrogenesis of mafic dykes related with Panjal traps has been documented from different areas in northern Pakistan and India (Papritz and Rey, 1989; Pogue et al., 1992a; Chauvet et al., 2008; Shellnutt et al., 2014). The corresponding data from Panjal traps after Pogue et al. (1992a) and Shellnutt et al. (2014) has been shown in certain plots (Fig. 5.13 and 5.14) for comparison and subsequent interpretation. The analogous compositional range of TiO_2, low Zr/Y and Nb/U and significant crustal contamination of host magma illustrates similarities of dolerites from the study area to Panjal Traps. These relations confirm the genetic link of studied dolerites to Panjal Trap magmatic event. Likewise, the REE modelling reflect the spinel lherzolite mantle as the magma source for dolerites. The higher $(Th/Nb)_{PM}$ and lower Nb/Ta ratios in dolerites also indicates generation of host melt from shallower SLM. With all the similarities we support the model of Shellnutt et al. (2014) for dolerites which elaborate the generation of melt from SLM and denied its derivation from a deep mantle plume.

In contrast to dolerite, the studied amphibolite shows a different behaviour. Though the REE modelling represent similar source composition, their uncontaminated signature, higher Nb/La ratio and analogous Nb/Ta ratio to OIB depict relatively deeper source i.e. asthenosphere. Their altered imprint also indicates their tectonic disparate relative to dolerites. The petrogenetic similarities between amphibolites and High-Ti dykes from southern Qiangtang has been observed due to their very high TiO_2 content (>3%), lack of crustal contamination, lower $(Th/Mb)_{PM}$ ratios and comparable REE modelling results (Fig. 5.13 and 5.14). The Qiangtang Terrane in Tibetan Plateau is a tectonic unit associated with the northern margin of Gondwana during early Permian (Fig. 5.15). The high-Ti mafic dykes are reported from southern Qiangtang terrane which was located adjacent to the present day northern Indian plate as presented in paleogeographic models of Gondwana in early-mid Permian (Zhu et al., 2010; Zhang et al., 2012). The origin of these dykes is related to a deep mantle plume arising from asthenosphere that played a key role in the early Permian rifting in the northern Gondwana (Zhai et al., 2013; Xu et al., 2015). The comparable Nb/Ta ratio of amphibolites (14.5 ± 3.5) to these High-Ti dykes (15.02 ± 0.2), their affinity towards OIB and indication of deeper source mantle support the interpretation of their genetic relationship. The analogous Nb/Y ratio of studied amphibolite and Qiantang dykes (average = 0.8 for either of these) and its marked enrichment than studied dolerites (average = 0.3) further support their asthenospheric source and petrogenetic connection.

The high-TiO_2 (>3%) amphibolites are also reported from the northern Hazara in NE Pakistan by Papritz and Rey (1989). The similar field and mineralogical characteristics to the studied amphibolites have been documented. Furthermore, higher and comparable Nb/Y ratio (ranging from 0.7-1.1) designate their coeval origin to the studied amphibolite and high-Ti Qiangtang dykes.

5.6.5. Tectonic implications

Two models for the emplacement of alkaline rocks associated with PPAIP in NW Pakistan have been suggested by earlier workers. The first idea illustrates that all the alkaline rocks in northern Indian plate were emplaced during a single major phase of rifting in Paleozoic time between 290 Ma and 250 Ma. This interpretation is supported by geochronological data of the constituent alkaline rocks e.g. Tarbela and Babaji syenites: 280±15 Ma (Kempe, 1986; Smith et al., 1994), Ambela Syenites: 297±4 Ma (Le Bas et al., 1987), Malakand Granite: 271±11 Ma (Zeitler, 1988) and Chakdara Granite: 278±4 Ma (DiPietro and Isachsen, 2001) (Fig. 5.1). Another idea is that emplacement of PPAIP has taken place in more than one episode i.e. late Paleozoic and Oligocene (Tertiary). This interpretation is mainly based on the geochronological studies on carbonatites which constitute an important part of PPAIP. Khattak et al. (2005) carried out fission track apatite dating which, according to them, confirms an Oligocene (25.2±1 Ma) emplacement time for carbonatites in PPAIP. Furthermore, Palaeogene (26 Ma) fresh ignimbrites are reported to occur in PPAIP (Ahmed et al. 2013). The Palaeogene age of the Warsak Granite is confirmed to 41 Ma and 42 ± 4 Ma respectively by Kempe (1973) and Maluski and Matte (1984).

The Permian ages ($^{39}Ar/^{40}Ar$: 284 ± 4 and 262 ± 1 Ma) of similar dykes intruding Mansehra granitoids (Baig, 1990) and the geochemical similarities with other synchronous coeval Panjal traps from other regions (Fig. 5.13, 5.14) confirm the Permian emplacement timing of dolerite dykes. Deformation and metamorphism of the amphibolites might indicate their exposure to an intense deformation event that predates the intrusion of the relatively fresh dolerites. Two major tectonic events have been recognized that caused deformation and metamorphism in the region. A regional prograde alpine metamorphic episode in Tertiary time which is triggered by the collision of Indian plate with KIA (Treloar et al., 1989b; Searle and Treloar, 2010). A former pre-Himalayan tectonism in early Cambrian-late Proterozoic time that has metamorphosed the pre-Cambrian strata in the northern Indian plate (Baig et al., 1988; Williams et al., 1988; Gehrels et al., 2006a). Pognante and Lombardo (1989) also noticed the coeval pre-Himalayan metamorphic events during the investigation of metabasic rocks from Zanskar region in NW India. The metamorphic imprint of amphibolite dykes due to early Paleozoic tectonism is improbable due to sporadic occurrence of both dyke types in similar aged younger rocks i.e. Permian Ambela granite. Hence the metamorphism of amphibolite is most likely due the regional Tertiary metamorphic event associated with Himalayan orogeny. The limited distribution of dolerites relative to amphibolites favours the relict likelihood of former that might escape from the deformational event. Both dyke types are hosted by granitic as well as metasedimentary rocks in the study area, however, the intrusion of dolerites with pure magmatic textures and limited alteration is only observed in granitic units. This might indicate the absence of fluids which prevent their conversion to amphibolites during tectonism. Based on the currently available geochemical data of these dykes, it is inferred that formation and emplacement of the studied dykes represent two different but synchronous magmatic pulses from relatively distinct mantle sources.

Similar to Panjal traps, the occurrence of synchronous high-Ti mafic dykes has been documented from the southern Qiangtang in Tibet (Pan et al., 2004; Wang et al., 2009; Zhu et al., 2010, 2013; Zhai et al., 2013; Xu et al., 2015). A recently presented model (Fig. 5.15) suggests that the Panjal Traps and high-Ti Qiangtang dykes are originated as a single Large Igneous Province (LIP) in around 290 Ma (Xu et al., 2015 and references there in). This model is based on the analogous isotopic constraints and paleogeographic and geochronological similarities between the two units (Xu et al., 2015). The source of Qiangtang dykes is interpreted to be the plume head derived from the deep mantle on the basis of REE modelling and isotopic compositions. Parallel to the present observations of dolerite dykes, the origin of Panjal traps has been related to relatively shallower SLM in this model. After origination as a single LIP, Indian Himalayan terrane that host Panjal Trap basalts, is separated from the southern Qiangtang in Artinskian times (i.e. before 280 Ma) during the extensional tectonism related to separation of the Cimmeria from Gondwana (Zhang et al., 2012).

The genetic relationship relation between the studied amphibolites and High Ti Qiangtang dykes has been observed due their geochemical similarities (section 5.6.4). The tectonic model (Xu et al., 2015) presented the complete segregation of plume originated High-Ti dykes from Panjal traps during the separation of Himalayan terrane from Tibet resulted in the formation of Neotethys Ocean. However, current studies show the extension of high-Ti magmatism (in the form of amphibolite dykes) in Himalayan terrane (Fig. 5.15) which aided the interpretation of their origin as a single LIP. The high-Ti (>3%) amphibolites with similar trace element character (e.g. Nb/Y ratio) are also reported from other parts in northern Pakistan i.e. (Pogue et al., 1992a; Papritz and Rey, 1989) which further support their existence in Himalayan terrane.

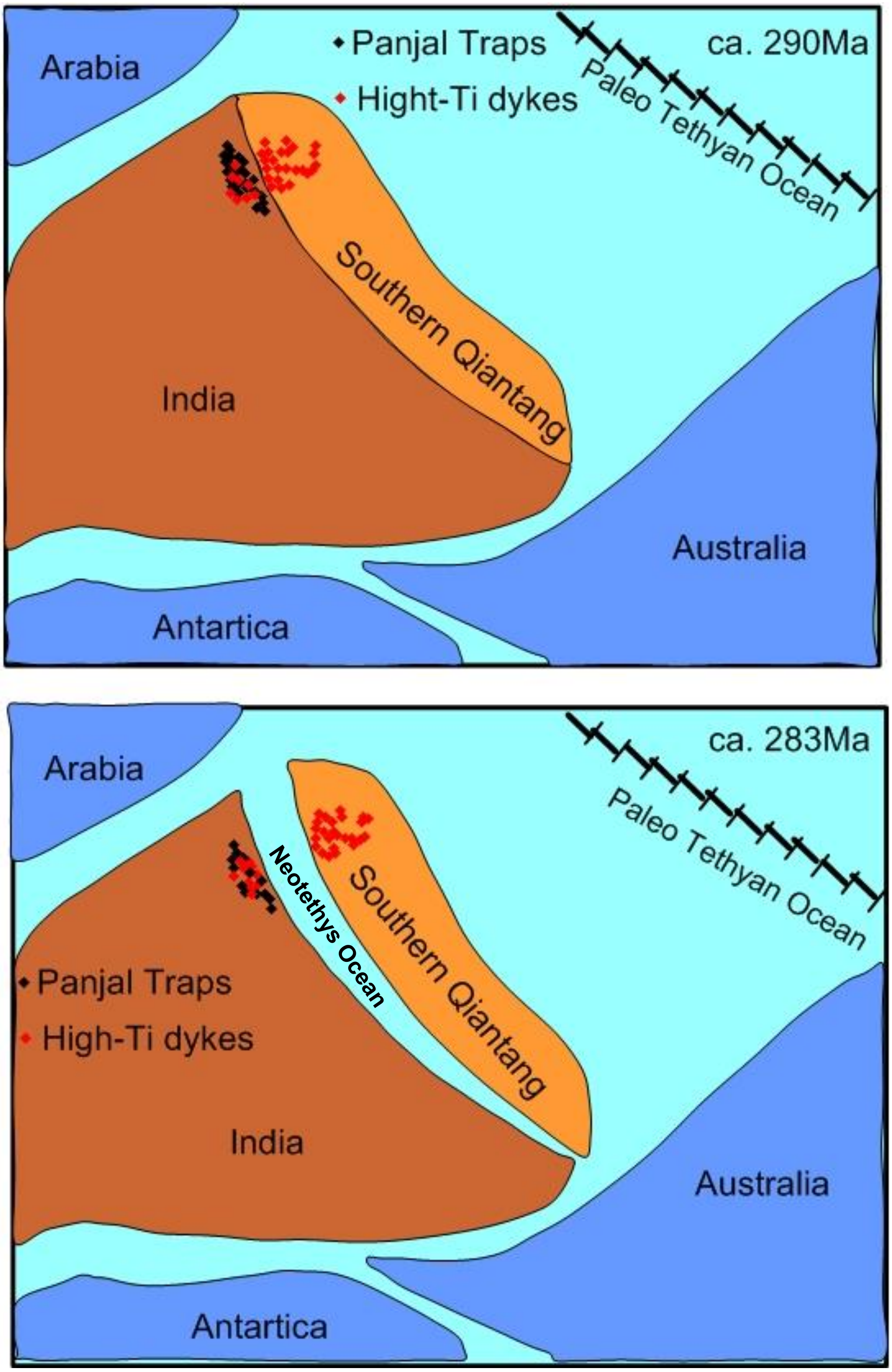

Figure 5.15. Tectonic model showing the origination of Panjal traps and High-Ti basalts from southern Qiangtang in the Permian during the initiation of Neotethys Ocean (modified from Xu et al., 2015). The scatter of both magmatic units as a single LIP is shown around ca. 290 Ma. The existence of High-Ti basalts in Himalayan terrane is shown after the separation of Qiantang terrane in Artinskian.

5.7. Conclusions

1. Significant textural and mineralogical differences make the basic dykes divisible into: a) dolerite and b) amphibolite, which cross-cut the rocks of PPAIP and other pre-Permian lithologies in the northern margin of Indian plate. Genetic relationship of these dykes has been inferred with other Permian magmatic events including Panjal trap magmatism and High-Ti Qiantang dykes.
2. The contrasting mineralogy and geochemistry (difference in amphibole composition and trace element concentrations) suggests that the two sets of dykes originated from compositionally distinct upper mantle in two separate pulses with different degrees of partial melting consequent upon intra-plate rifting followed by fractional crystallization. PER, compositional zoning in plagioclase and clinopyroxene and variation in olivine composition indicate the role of fractional crystallization in dolerite formation.
3. Trace elements ratios show derivation of melt for dolerites from subcontinental lithospheric mantle which also indicate a certain degree of crustal contamination during its ascent and evolution. In contrast, the amphibolite protolith originate from relatively deeper mantle (i.e. asthenospheric) and show connections to High-Ti mafic dykes of Qiangtang due their compositional resemblance, similar signs of mantle source and lack of any contamination cyphers.

CHAPTER 6

Geochronology

6.1. Introduction and Sample Description

The evaluation of geochronological data set of granitic rocks along the northern Gondwana margin suggests an extended granitic belt from NW Turkey to southern Tibet through Central Iran, NW Pakistan, NW India and Nepal (LeFort et al., 1986; Pognante et al., 1990; Miller et al., 2001; Cawood et al., 2007; Wang et al., 2013). The geochronological studies of most of these granites from different Himalayan regions confirmed Cambro-Ordovician ages for the magmatism (LeFort et al., 1986; Pognante et al., 1990; Miller et al., 2001; Guynn et al., 2012). The detailed geochemical account presented in Chapter four revealed similarities between the Utla granitoids with other granitic plutons from the mentioned Himalayan belt e.g. peraluminous, mega-crystic feldspar, Al-rich minerals and similar source rock characteristics etc. (LeFort et al., 1980; Girard and Bussy, 1999; Miller et al., 2001; Wang et al., 2013). Following the detailed geochemical and mineralogical account, radiometric dating of the Utla granitoids will aid insights about its emplacement timing and comparison with other well studied plutons of Himalayan region.

The detailed geochronology of other magmatic events (both pre-Himalayan and Himalayan magmatism) along the northern Indian plate in NW Pakistan has been described (Treloar et al., 1989d; Treloar and Rex, 1990; Anczkiewicz et al., 1998; DiPietro and Isachsen, 2004). A Precambrian thermal event (1850 Ma: hornblende Ar-Ar) has been reported in the Besham nappe from the basement orthogneisses (Treloar and Rex, 1990). This magmatism is supported by U-Pb zircon dating of the Besham group basement orthogneisses by DiPietro and Isachsen (2004). Anczkiewicz et al. (1998, 2001) presented U-Pb zircon geochronology and muscovite Ar-Ar ages of different Himalayan and pre-Himalayan rock suites from the lower Swat area. A large geochronological data set of alkaline rocks in the region is reported which support the Permian rifting event ranging in age from 350 Ma to 268 Ma (Kempe, 1986; Le Bas et al., 1987; Smith et al., 1994; Anczkiewicz et al., 1998; Ahmed et al., 2013). Besides all these studies, the radiometric age data of peraluminous systems is relatively scarce from this region to properly compare and address them on regional scale.

The Utla granites are dominantly megacrystic granites (MPG) with cross cutting aplite (AMG) and quartz rich veins. The mineralogical and geochemical investigation reveal the evolution of AMG from MPG through fractional crystallization of melt originated from single source. However, AMG is emplaced later as aplite dykes within the already crystallized MPG as shown by their field relationship. The Utla granitoids intrude metapelites and quartzites of the Tanawal Formation (Fig. 4.1). The regional Barrovian type metamorphism from greenschist to amphibolite facies have been documented for these metasedimentary rocks (Baig et al., 1988, 1989; Kohn, 2014). The Tanawal Formation is middle to late Proterozoic in age based on the intrusion of Cambro-Ordovician aged Mansehra granite (LeFort et al., 1980; Pogue et al., 1992b). The U-Pb dating system, which is one of the most common and reliable dating technique, on zircons recovered from Utla granites has been employed in the current investigation. The zircons were recovered from MPG, AMG and dolerite dykes cross cutting the Utla Granites.

The Mansehra Granite lies towards the eastern extremity of Utla (Fig. 4.1) with analogous mineralogical and geochemical character (Chapter 4). It is 516 ± 16 Ma old on the basis of whole rock Rb-Sr dating (Le Fort et al., 1980), however, no previous U-Pb ages have been reported. To obtain a better tectonic picture of the Utla granites and their relationship with other granitic suites of Pakistan, zircons from Mansehra Granite have also been recovered and analysed. Though it has been dated earlier using Rb-Sr system, the comparison of Utla granite with Mansehra using the same radiometric system will elaborate more reliable and confident assessments.

6.2. Methods Description

6.2.1 Zircon Separation

The standard procedure for zircon separation is adopted using crushing, grinding, sieving, magnetic and heavy liquid separation in this particular order at NERC Isotope Geosciences Laboratory (NIGL). The granites from Utla and Mansehra area and a representative dolerite sample had been processed for zircon recovery. The samples were crushed and ground using a Jaw crusher and grinder. The grinded material was passed through 350 μm sieve to remove the coarser fragments.

The water shaking table was used to detach the heavy minerals from <350μm separates. The heavy mineral fractions were processed through Frantz magnetic separator which efficiently clean it from magnetic materials. The remaining fractions were passed through the heavy liquid (Di-iodomethane) to get the clean zircon separates. The separate was primarily composed of zircons in samples from Utla and Mansehra granite. The dolerite yielded nine zircon grains in total most of which are not very suitable for analysis due to fractures and blurred interiors. The back scattered electron (BSE) and Cathode Luminescence (CL) imaging of zircons was undertaken at GeoForschungs Zentrum (GFZ), Potsdam to choose the suitable spots for U-Pb isotope determination.

6.2.2. SIMS analysis

The U-Pb isotopes analysis was conducted by Secondary Ion Mass Spectrometry (SIMS) using the CAMECA 1280-HR instrument at GFZ Potsdam in Germany. The analyses employed a 10 nA, $16O^{2-}$ primary ion beam resulting in a beam diameter of 25 μm on the sample surface. The positive secondary ions were extracted using a +10 kV potential as applied to the sample holder. Each analysis was preceded by a 10 nA, pre-sputtering lasting 120 seconds and employed a 25 μm raster. The oxygen flooding was used to enhance lead sensitivity. The data were acquired using an ETP electron multiplier operating in mono-collection mode. A single analysis consisted of 16 cycles of the peak stepping sequence: $^{90}Zr_2\ ^{16}O$ (1 second integration time per cycle), $^{92}Zr_2\ ^{16}O$ (1s), 200.5 (4s), $^{94}Zr_2\ ^{16}O$ (1s), ^{204}Pb (6s), ^{206}Pb (4s), ^{207}Pb (6s), ^{208}Pb (2s), $^{177}Hf\ ^{16}O_2$ (1s), ^{232}Th (2s), ^{238}U (2s), $^{232}Th\ ^{16}O$ (2s), $^{238}U\ ^{16}O$ (2s) and $^{238}U\ ^{16}O_2$ (2s). Thus, including pre-sputtering, a single such analysis lasted approximately 16 minutes.

The software package Isoplot (Ludwig, 2012), was used to plot the data using the decay constants recommended by the IUGS sub-commission on geochronology in Steiger and Jäger (1977). A correction for common lead was based on the observed ^{204}Pb counts in conjunction with the modern common lead compositions from the model of Stacey and Kramers (1975).

The zircon 91500 ($^{206}Pb/^{238}U$ age: 1062.4 ± 0.4 Ma; $^{207}Pb/^{206}Pb$ age: 1065.4 ± 0.3, Wiedenbeck et al., 1995) was used as primary U-Pb calibration material, while Temora 2 ($^{206}Pb/^{238}U$ age: 416.78 ± 0.33 Ma, Black et al., 2004) was used as a quality control to evaluate the accuracy and stability of the measurements. The analysis of standard is regularly interspersed after every four unknown points during data collection. The analysis has been done in two sessions. In session-1, eleven determinations of 91500 yielded a Concordia age of 1064.1 ± 5.4 Ma (2σ, n = 11), while age of 1063.6 ± 2.7 Ma is obtained in second session (2σ, n = 16). Figure 6.1 present the collective data of 91500 zircon for both sessions. Temora 2 yielded an age of 415.4 ± 3.2 Ma (2σ) (N = 8) (Fig. 6.2). The repeatability of the U-Pb calibration on 91500 zircon as well as results of Temora 2 suggest that the data is reliable to better than ± 2%.

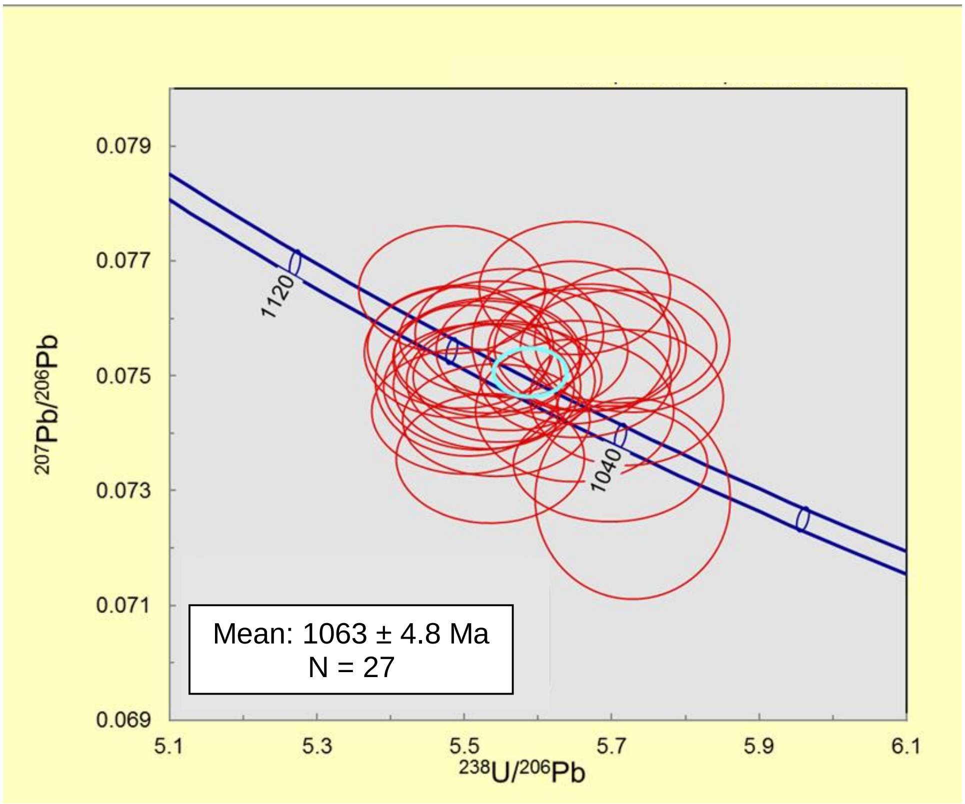

Fig. 6.1. U–Pb Concordia diagram for 91500 Zircon standard analysed in two separate sessions. Session one (n = 11, 1064.1 ± 5.4 Ma), Session two (n = 16, 1063.6 ± 2.7 Ma). Plot shows the mean age of both sessions.

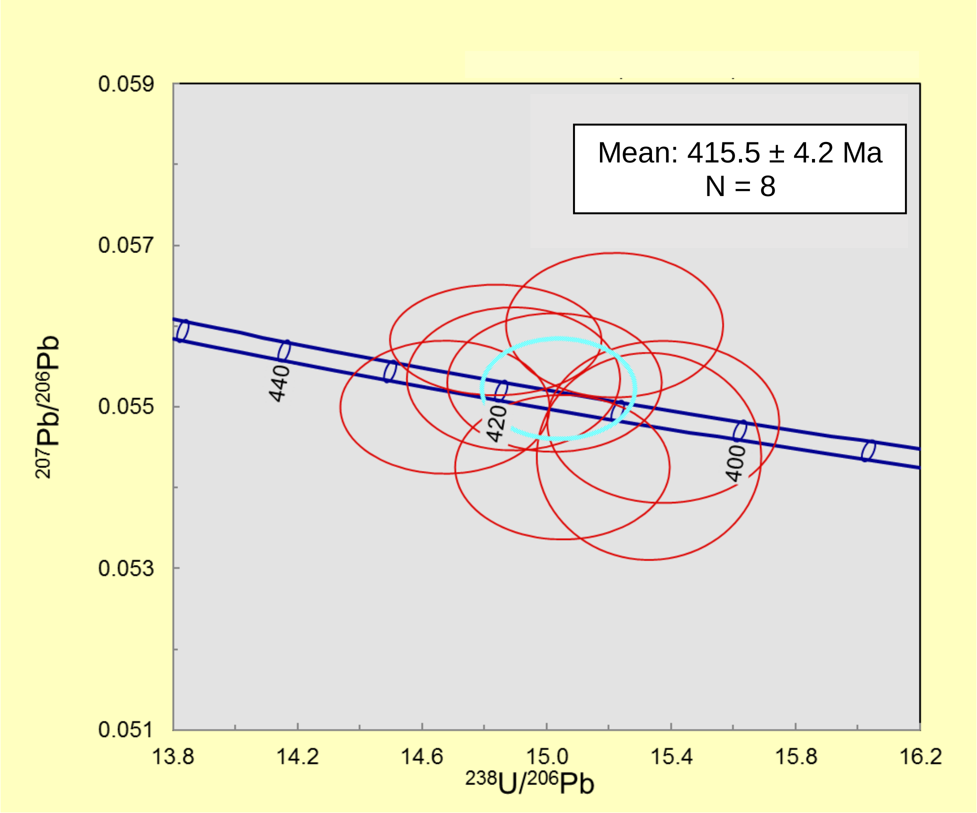

Fig. 6.2. U–Pb Concordia diagram for Temora-2 standard analysis.

6.2.3. Zircon Morphology

The zircons from all the samples show greater range in morphology (elongated to roughly oval shaped grains) and size (less than 20µm up to 120µm). Some grains had cracks, holes and inclusions of other minerals which limits the number of analytical spots.

Most of zircons had old cores surrounded by young rims (Fig. 6.3 A-B), the latter is believed to be the representative of the crystallization age of host. The rims show zoning by fine growth bands. Some of the data resulted from mixed core-rim analyses in cases where the rims were too narrow to be measured separately (Fig. 6.3C). In certain samples BSE and CL images cannot distinguish between old and younger growth bands in rims, hence the possibility of mixed analyses has been taken in account (Fig. 6.3D). The position of the analytic spots is shown in CL images (e.g. Fig. 6.3), where the inner diameter of the spot refers to the analysed area.

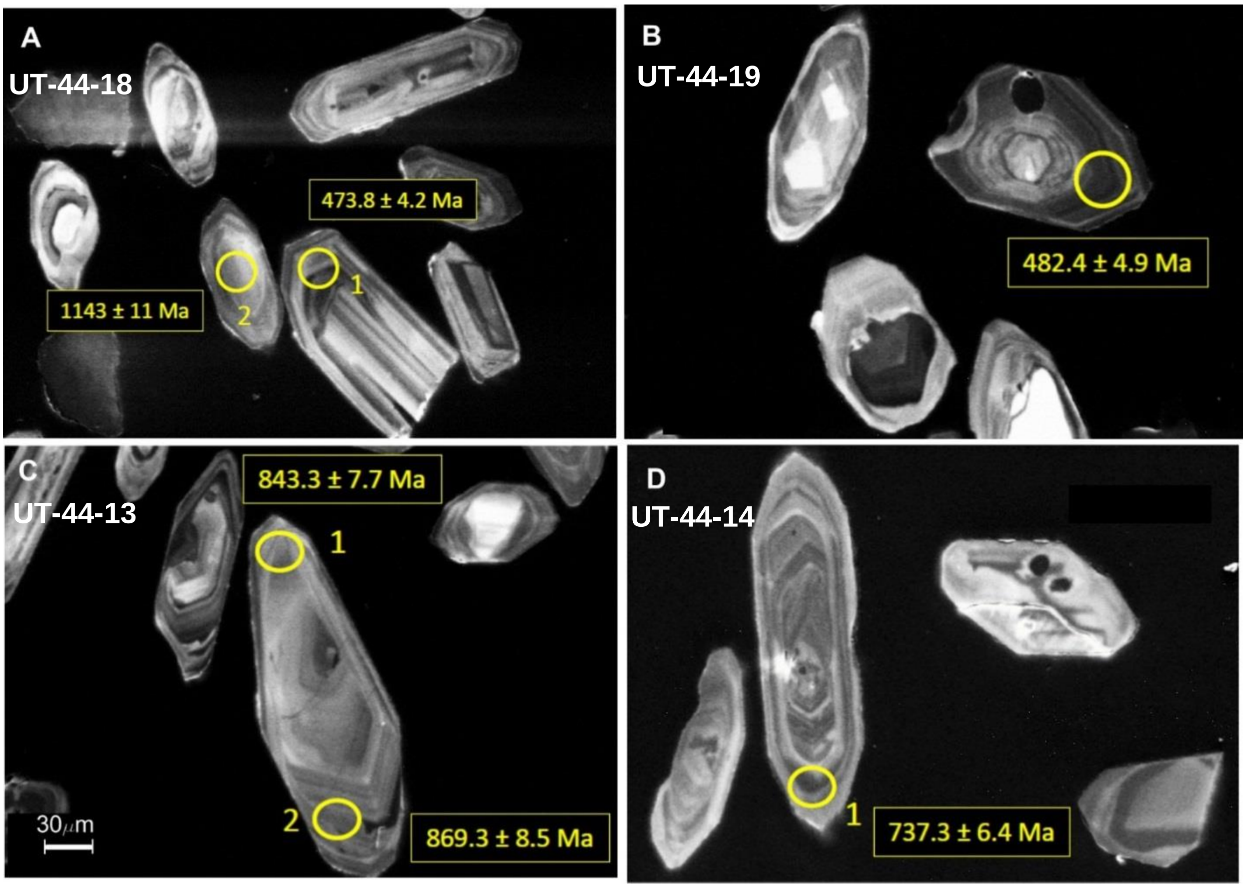

Fig. 6.3. CL images of zircons from studied samples showing examples of A-B) older cores and younger rims, C) narrow younger rims, D) mix core-rim analyses. Scale is same for all figures represented in C.

6.3. Results

6.3.1. Utla Granite (MPG)

^{206}Pb/^{238}U ages of MPG zircons are mostly concordant within error (Fig 6.4), ranging from 894 to 458 Ma (Table 6.1). Two major zircon growing events are recognizable. The first one occurred at around 900-800 Ma (Fig 6.4) and is noticed mainly in cores (Fig. 6.5 A-C) and in some rims (e.g. Fig. 6.5A, C). The second event occurred around < 500 Ma (Fig. 6.6). It is shown by rim analyses (Fig. 6.7 A-B) and documents the latest crystallization age of granite. The young rims can, in some cases, be extremely thin, e.g. in Figure (6.5B) the analyzed 825 Ma old core is surrounded by only a few micrometer thick rim of supposedly younger age.

The average age of the young rims is 481.53 ± 5.6 Ma (N = 11) and is interpreted as the best realistic estimate of the crystallization age. The single discordant data point 69-6-1bis is an artifact of a twice measured spot and has been excluded.

Table 6.1. Results of U-Pb Zircon dating of Utla Granites (MPG)

	$^{207}Pb/^{206}Pb$	±σ	$^{207}Pb/^{235}U$	±σ	$^{206}Pb/^{238}U$	±σ
UT-69-19-2	478.4	16.4	487.2	5	489.1	5
UT-69-19-1	480.3	10.8	482	4	482.4	4.2
UT-69-18-2	491.2	17.5	479.6	4.6	477.1	4.2
UT-69-18-1	451.8	13.3	482.1	4.2	488.5	4.3
UT-69-17-1	768.3	14.3	758.2	6.5	754.7	7.1
UT-69-16-1	820.5	9	815.2	7.1	813.2	9.1
UT-69-15-1	459.8	12.3	475	4.1	478.2	4.2
UT-69-14-3	874.2	6.9	888.2	5.8	893.8	7.6
UT-69-14-2	863.5	10.4	857.9	6.1	855.7	7.4
UT-69-14-1	471	25.7	481.3	5.7	483.5	4.2
UT-69-11-1	825.7	26.5	820.8	8.9	819	7
UT-69-10-2	827.8	10.2	828.9	5.9	829.4	7.1
UT-69-10-1	482.7	17.8	482.4	5.3	482.3	5.1
UT-69-8-1	467.5	18.9	481.6	5.9	484.6	6
UT-69-7-3	821.2	9.8	795.9	5.7	786.9	6.8
UT-69-7-1	461.6	20.7	467.7	5.2	469	4.5
UT-69-6-2bis	455.8	13.3	474.6	4.5	478.4	4.7
UT-69-6-1bis	520.5	14	468.6	4.4	458	4.3
UT-69-5-2	736.4	15.2	726.7	6.5	723.5	6.9
UT-69-5-1	870.4	7	873.9	6.8	875.3	9
UT-69-4-2	818.9	16.7	823.2	7	824.8	7.3
UT-69-4-1	460.7	10.2	479.7	5.6	483.7	6.4
UT-69-3-2	853.9	10.4	858.9	6.6	860.9	8.2
UT-69-3-1	803.3	19.9	819.4	7.5	825.3	7.2
UT-69-1-1	826.5	7	806.4	5.5	799.1	7

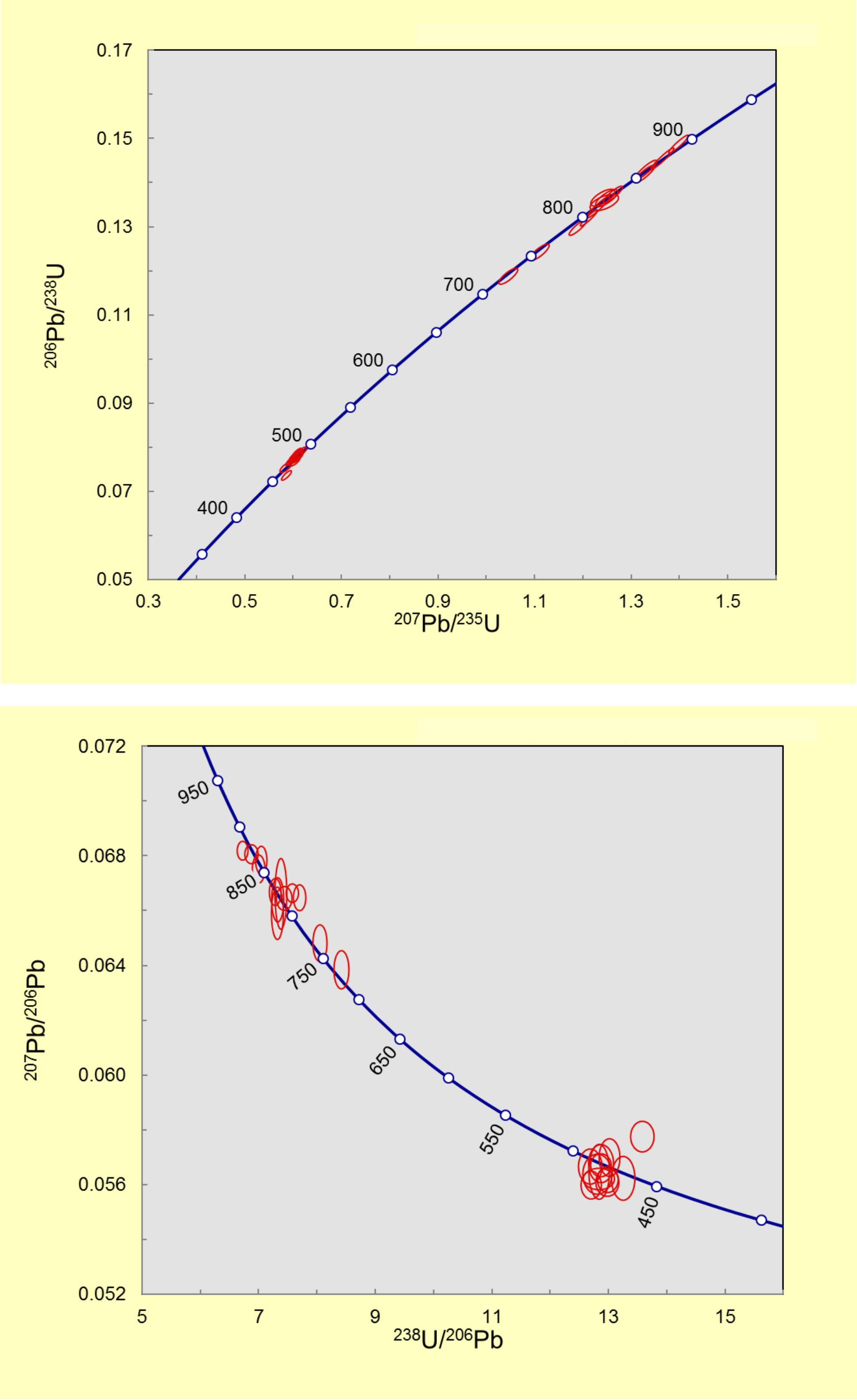

Fig. 6.4. U–Pb Concordia diagrams showing data of the Utla Granite (MPG) A) conventional and B) Tera-Wasserburg. Both plots show two zircon generations i.e. <500 Ma (shown by rims) and 800-900 Ma (mostly by cores but also in certain rims).

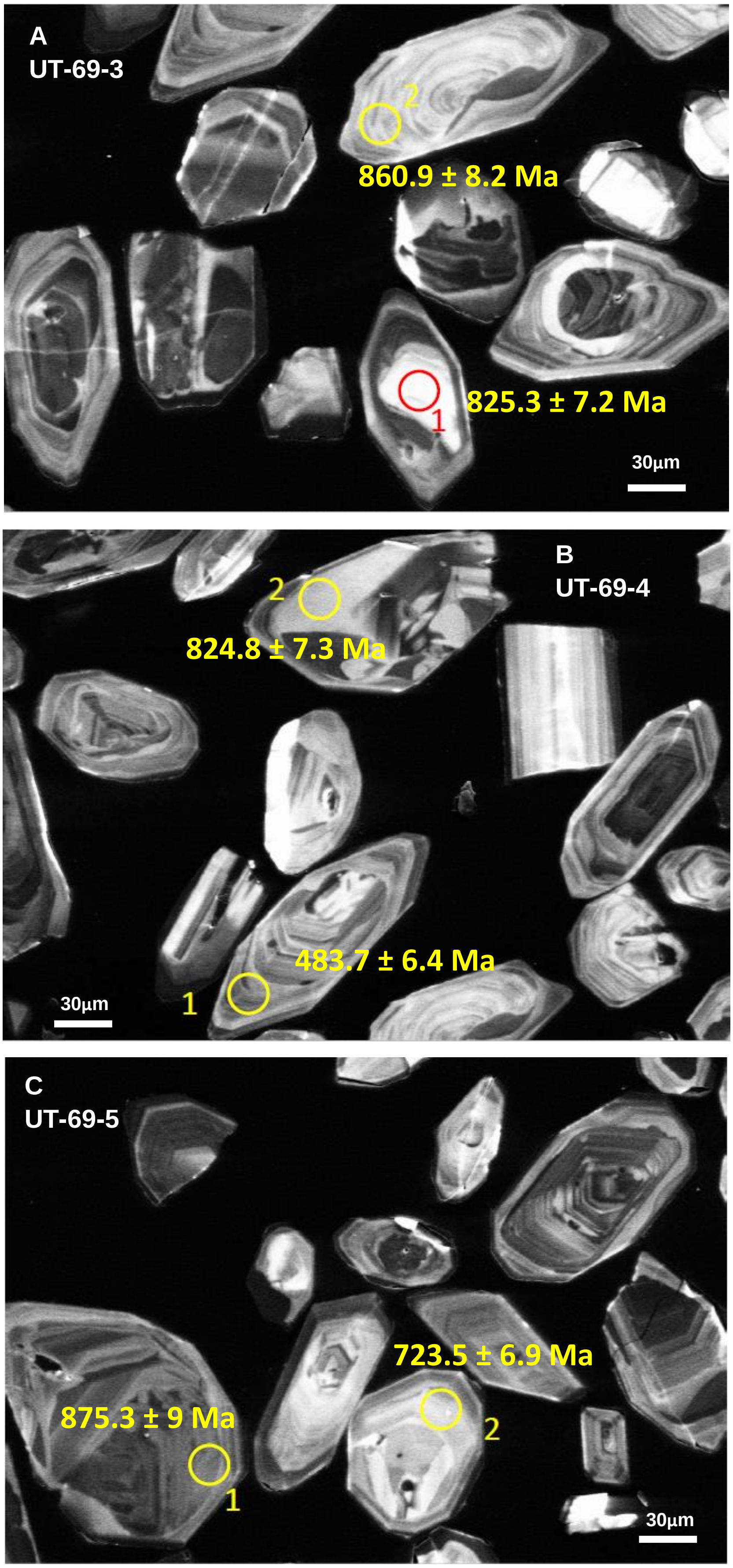

Fig. 6.5. CL images of analysed MPG zircons showing areas from both core and rims yielding older ages (800-900 Ma). A rim showing younger age (484 Ma) is shown in B. Mixed core-rim analysis is also shown by 723 Ma age in C.

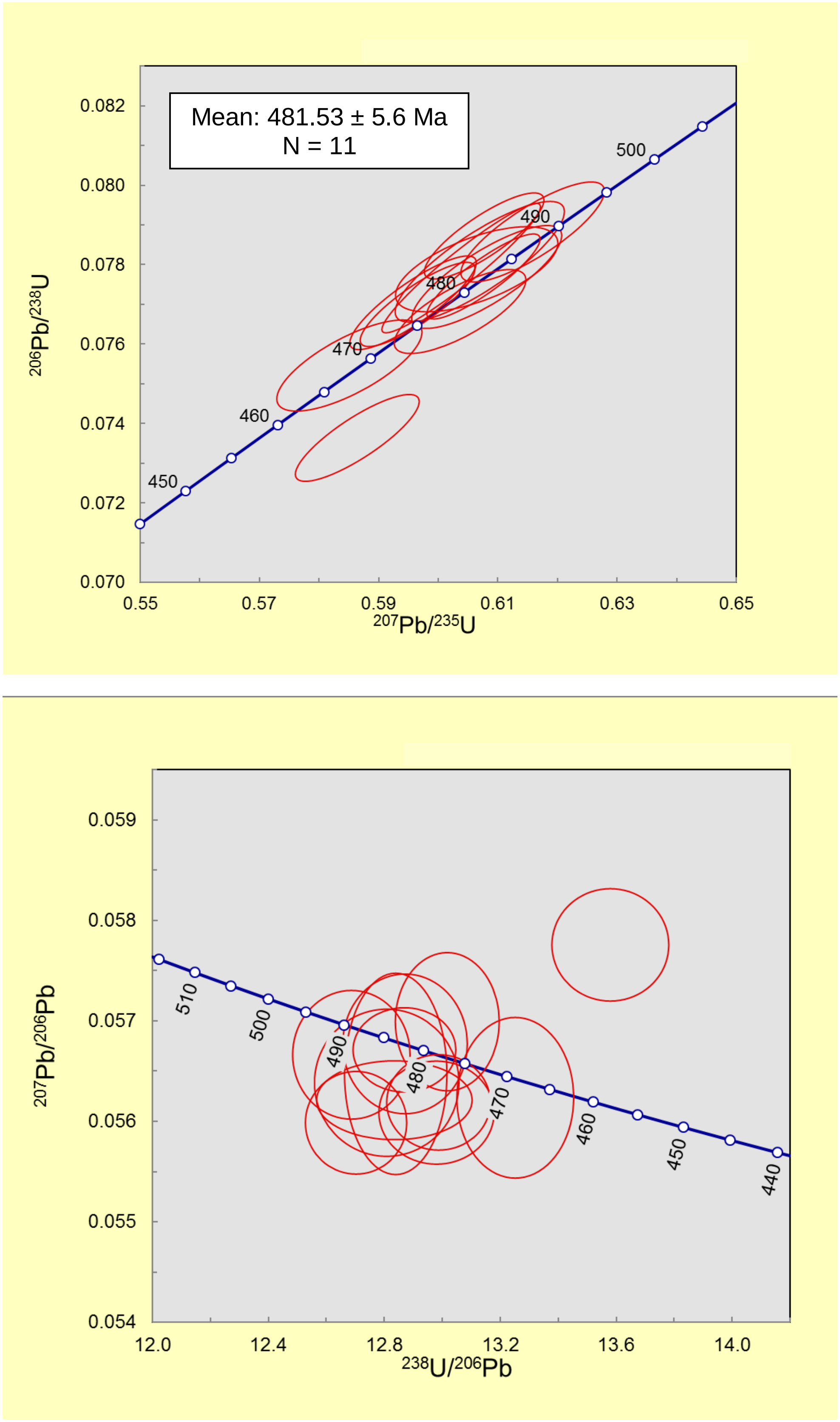

Fig. 6.6. U–Pb Concordia diagrams, A) conventional and B) Tera-Wasserburg, showing data of MPG zircon rims representing latest crystallization event. Apart from single point, all the rim analyses are concordant.

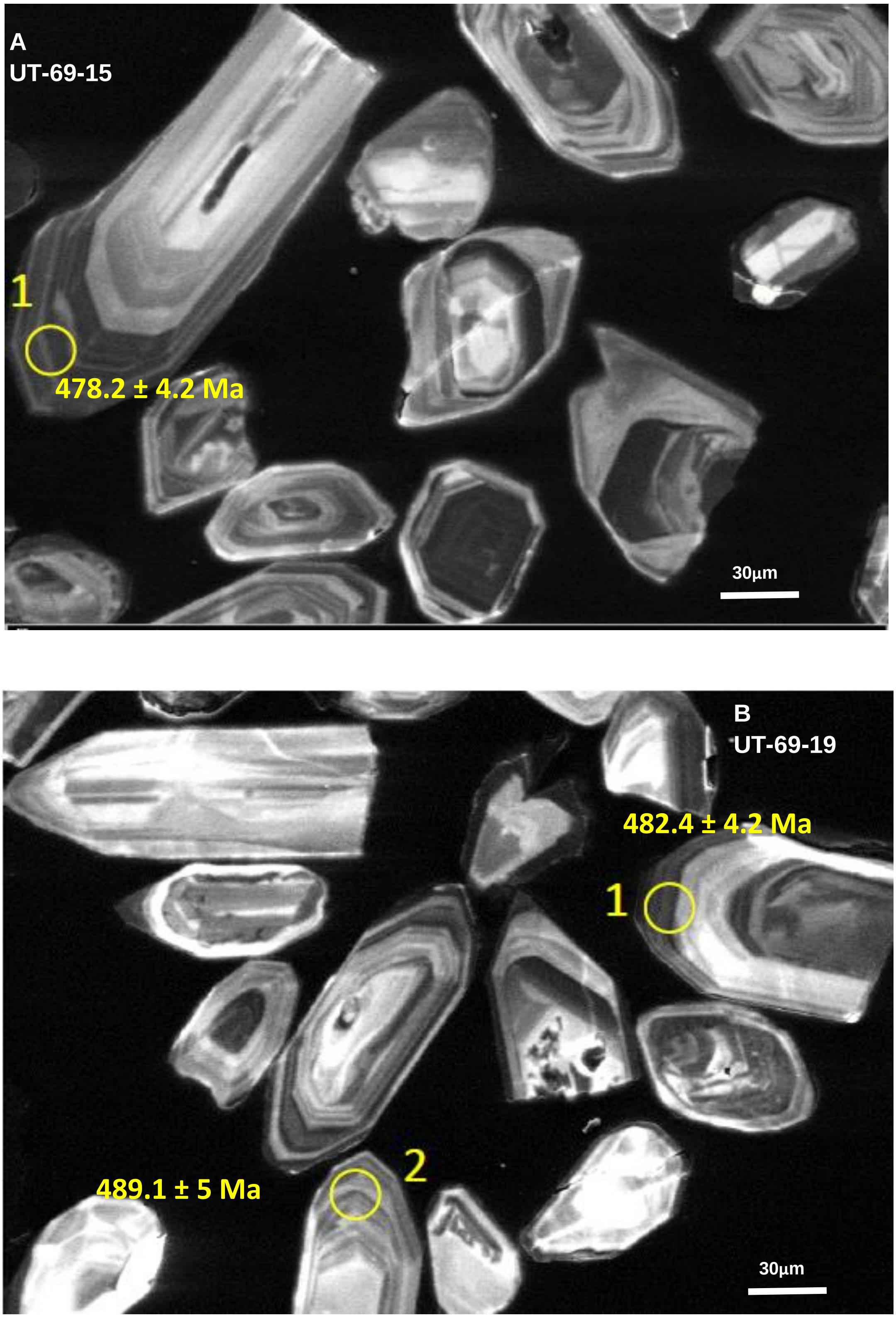

Fig. 6.7. CL images of MPG zircons showing spots for younger rims analysis (<500 Ma ages).

6.3.2. Utla Granite (AMG)

The ^{206}Pb/^{238}U age spectrum of AMG is mostly similar to MPG confirming an early major crystallization period at around 900-800 Ma followed by latest event in 470-490 Ma (Fig. 6.8; Table 6.2). The former event is dominated in core domains (Fig. 6.9A). In addition, inherited Proterozoic zircons has also been noticed i.e. 1683 Ma and 1143 Ma (Fig. 6.9B). The younger rim domains (Fig. 6.9C) show the average crystallization age of granites to be 478.5 ± 7.3 Ma (N = 11) (Fig. 6.10) which within error, is indistinguishable from MPG.

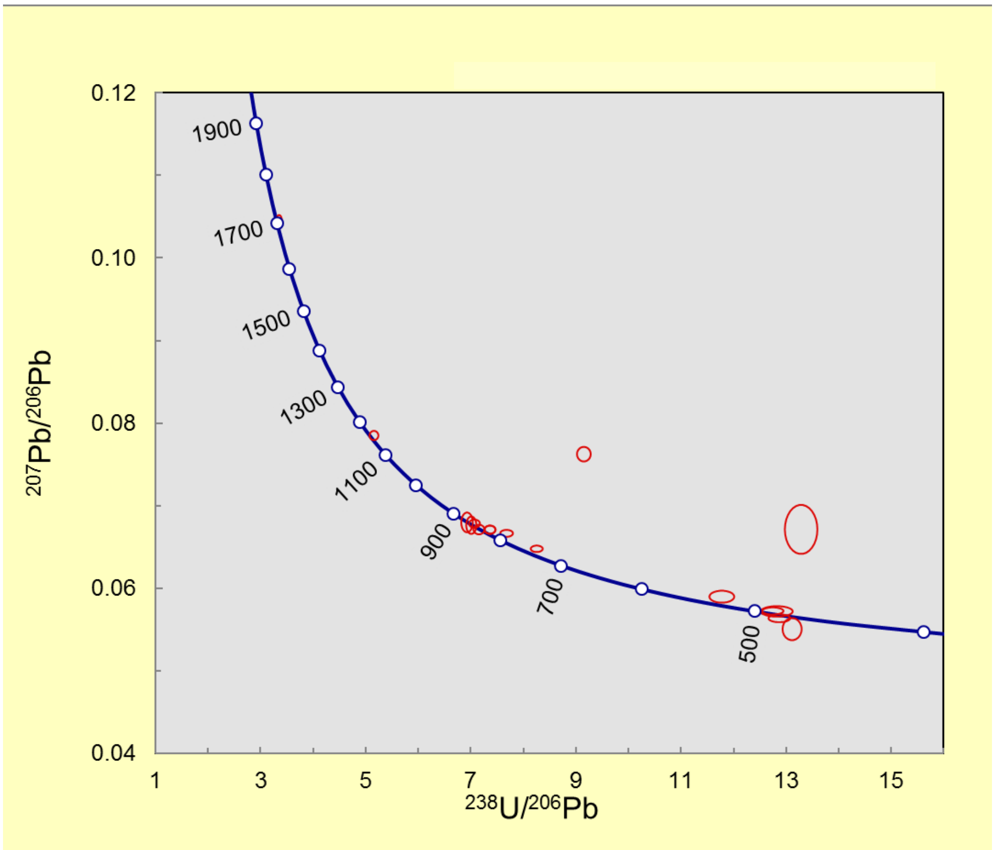

Fig. 6.8. U–Pb Concordia diagram showing data of the AMG zircons. Two spots show inherited Proterozoic nature of zircons. The <500 Ma ages is shown by zircon rims while older age (800-900 Ma) is shown mostly by cores domains.

Table 6.2. Results of U-Pb Zircon dating of Utla Granites (AMG)

Analysis #	**$^{207}Pb/^{206}Pb$**	**±σ**	**$^{207}Pb/^{235}U$**	**±σ**	**$^{206}Pb/^{238}U$**	**±σ**
UT-44-21-3	863.6	10	855.9	6.3	853	7.8
UT-44-21-2	499.9	16.2	486.9	6.7	484.1	7.3
UT-44-21-1	857.9	21.2	859.3	8	859.9	7.3
UT-44-19-1	467.6	12.4	479.8	4.6	482.4	4.9
UT-44-18-2	1159.8	9.3	1148.6	8.2	1142.7	11.4
UT-44-18-1	415.2	35.6	463.9	6.9	473.8	4.2
UT-44-17-1	1706.1	7.7	1693.5	9.1	1683.3	15.1
UT-44-16-1	827.4	8.7	799.2	6.2	789.1	7.8
UT-44-14-1	767.7	8.4	744.8	5.3	737.3	6.4
UT-44-13-2	868.3	23.9	869	9.2	869.3	8.5
UT-44-13-1	841.7	11.8	842.9	6.5	843.3	7.7
UT-44-12-3	1101.7	15.3	776.8	6.6	668.6	6
UT-44-24-2	841.2	10.1	826.3	6	820.9	7.3
UT-44-24-1	567	17.7	533.3	6.5	525.5	6.7
UT-44-25-2	842.2	59.7	536.9	13.9	467.9	6.9
UT-44-25-1	501.9	10.9	489.5	4.5	486.9	4.9
UT-44-24-2	841.2	10.1	826.3	6	820.9	7.3
UT-44-1-1	509.7	10.1	491.8	2.8	488	2.5
UT-44-7-1	478.6	11.3	481.9	2.8	482.6	2.4
UT-44-12-4	479.2	13.3	471.4	3	469.8	2.4
UT-44-16-2	621	13.9	578.9	3.6	568.2	2.8
UT-44-26-1	593.6	245.9	502.9	49.9	483.2	2.4
UT-44-27-1	490.5	14.2	474.5	3.1	471.1	2.3
UT-44-27-2	482.5	11.5	475.4	2.8	473.9	2.4

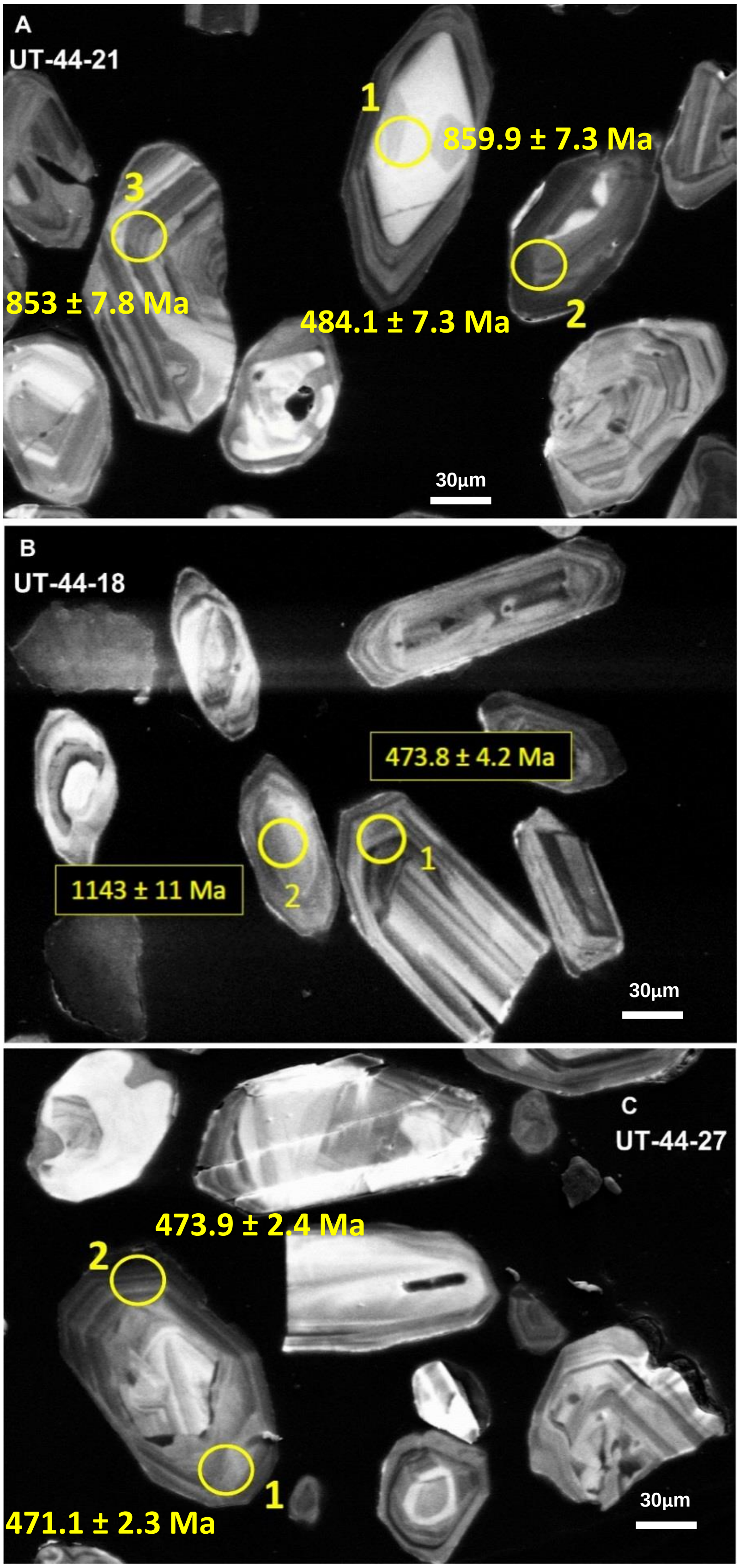

Fig. 6.9. AMG zircons CL images A) core/ rims showing ages between 800-900 Ma, B) inherited grain showing Proterozoic age, C) rims showing younger ages (<500 Ma).

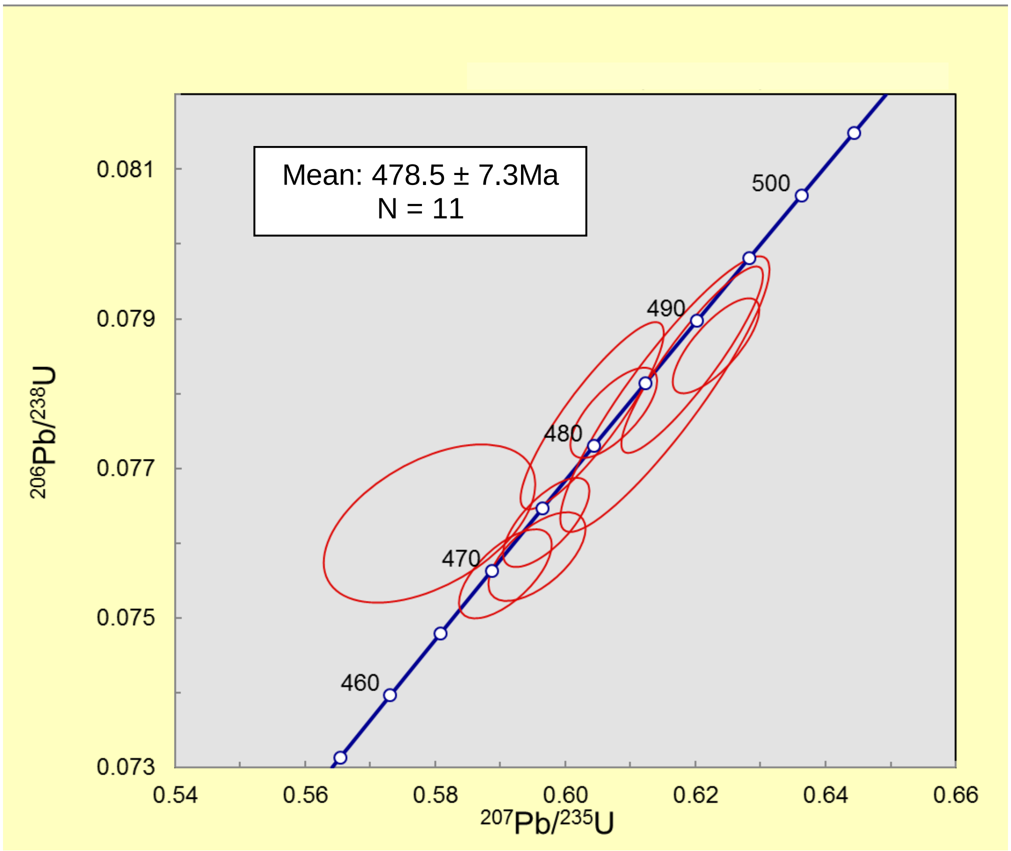

Fig. 6.10. Conventional U–Pb Concordia diagram showing data of AMG zircon rims confirming their younger age of crystallization (<500 Ma).

6.3.3. Mansehra Granite

Like samples from Utla granites (MPG and AMG), zircons from the Mansehra Granite also contain old cores surrounded by younger rims, the latter of which is believed to represent the crystallization age of the host. However, the very fine growth bands (Fig. 6.11A) has been observed in rims which increase the possibility of mixed analyses between younger rims and older cores.

22 analyses have been obtained from zircon rims ranging in age from 522 to 481 Ma ($^{206}Pb/^{238}U$) and 461 to 480 Ma ($^{207}Pb/^{206}Pb$) (Table 6.3). The average of < 500 Ma data is 492.96 ± 5.2 Ma ($^{206}Pb/^{238}U$, N=19) and 471.00 ± 7.9 Ma ($^{207}Pb/^{206}Pb$, N=22). The 20 Ma divergence between the two data sets is accompanied by a significant discordance in both the conventional and Tera-Wasserburg Concordia diagrams (Fig. 6.12). The core domains mostly range between around 600 to 1315 Ma (Fig. 6.13; Table 6.3) however, a 2 Ga old concordant core has also been noticed (Fig. 6.11B). The CL image shows a 2 Ga core (enriched in REE) is surrounded by a REE-poor (dark) rim (Fig. 6.11B). The old zircon cores (Fig. 6.11C) may have either been derived from the source rock itself (e.g. meta-sediments) or were picked up during magmatic ascent by crustal contamination.

Table 6.3. Results of U-Pb zircon dating of Mansehra Granites and dolerite dykes

	$^{207}Pb/^{206}Pb$	**±σ**	**$^{207}Pb/^{235}U$**	**±σ**	**$^{206}Pb/^{238}U$**	**±σ**
M-5-3-2	1399.8	33.3	949	18.8	766.7	17.8
M-5-7-2	696.7	10.7	610	7.3	586.9	8.5
M-5-10-2	466.4	6.4	490.1	2.4	495.2	2.5
M-5-10-3	461.5	7.9	495.6	2.5	503	2.6
M-5-11-1	485.5	6.1	499.8	2.3	502.9	2.5
M-5-11-2	858.9	6.6	886.5	3.7	897.6	4.5
M-5-12-1	597.8	6.7	575.3	2.7	569.6	2.8
M-5-12-2	466.7	7.6	512.1	2.5	522.4	2.6
M-5-13-1	468.7	7.1	486.7	2.4	490.6	2.4
M-5-13-2	1319.6	9.7	1317	5.4	1315.5	6.4
M-5-13-3	649.5	7	607.5	2.8	596.3	3
M-5-14-2	467.3	6.3	492.5	2.3	497.9	2.5
M-5-14-3	473.1	6.6	491.7	2.4	495.7	2.5
M-5-14-4	475.6	8.4	492.5	2.5	496.2	2.4
M-5-15-2	2036.1	12	2014.4	7.6	1993.3	9.2
M-5-16-3	466.3	9.3	482.3	2.6	485.7	2.4
M-5-16-4	468.5	6.1	493.4	2.3	498.8	2.5
M-5-17-3	465.3	8.3	489.2	2.5	494.4	2.5
M-5-17-4	463.4	7.3	489.8	2.4	495.5	2.5
M-5-19-3	479	6.7	486.4	2.3	487.9	2.4
M-5-19-4	469.5	7	483.8	2.3	486.8	2.4
M-5-20-4	798.1	4.6	796.9	3.1	796.5	3.8
M-5-20-5	488.5	8.3	482.5	2.5	481.2	2.4
M-5-21-2	465	5.2	490.6	2.2	496.1	2.4
M-5-22-2	823.2	2.8	842.8	4.3	850.2	5.8
M-5-24-1	802.4	8.5	751	3.6	733.8	3.7
M-5-24-2	518.2	8.7	518.3	2.6	518.4	2.6
M-5-24-3	455.8	7.7	487.6	2.4	494.3	2.4
M-5-25-1	471.1	8.8	494.6	2.5	499.7	2.5
M-5-25-2	477.3	5.9	490.5	2.3	493.4	2.5
M-5-25-3	863.5	3.6	885	3.2	893.6	4.3
M-5-26-2	478	7	485.6	2.3	487.3	2.4
M-5-26-3	469.7	11.1	494	2.8	499.3	2.5
M-5-28-1	1637.3	926.7	812.1	498.2	545	61.9
M-5-29-1	895.8	16.8	888.7	5.7	885.8	4.3
M-5-29-2	479.8	8	488.3	2.4	490.2	2.4
UT-4-07-1*	510.8	11.7	495.1	2.9	491.7	2.4
UT-4-08-1*	451.4	13.3	480.1	3	486.2	2.4
UT-4-04-1*	1612.9	4.1	1642.7	4.5	1666	7.5

* Analysis of dolerite dykes intruding Utla granites

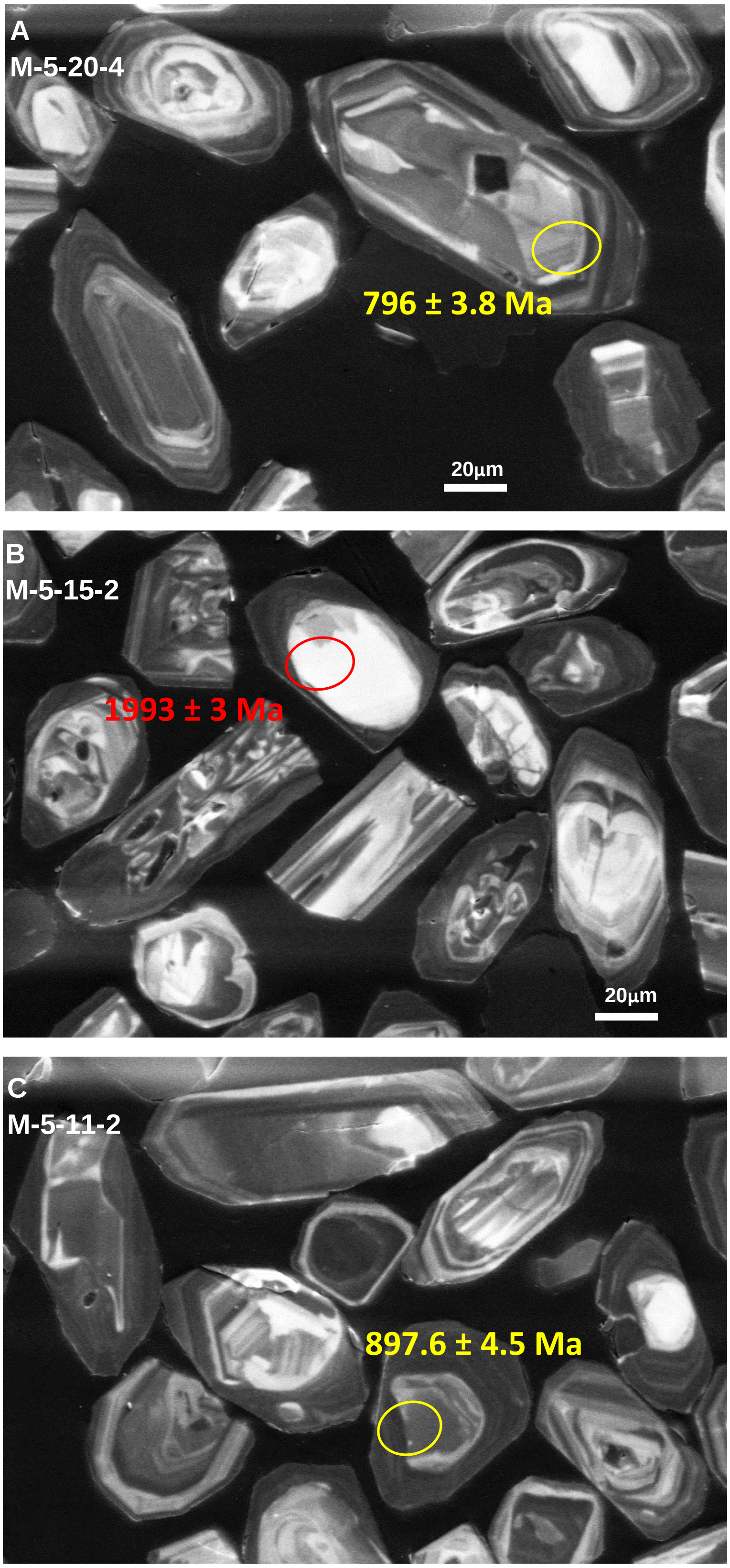

Fig. 6.11. Mansehra Granite zircons CL images A) fine growth bands in rims might causing age mixing, B) around 2 Ga old zircon core, C) example of analysed core giving age between 800-900 Ma.

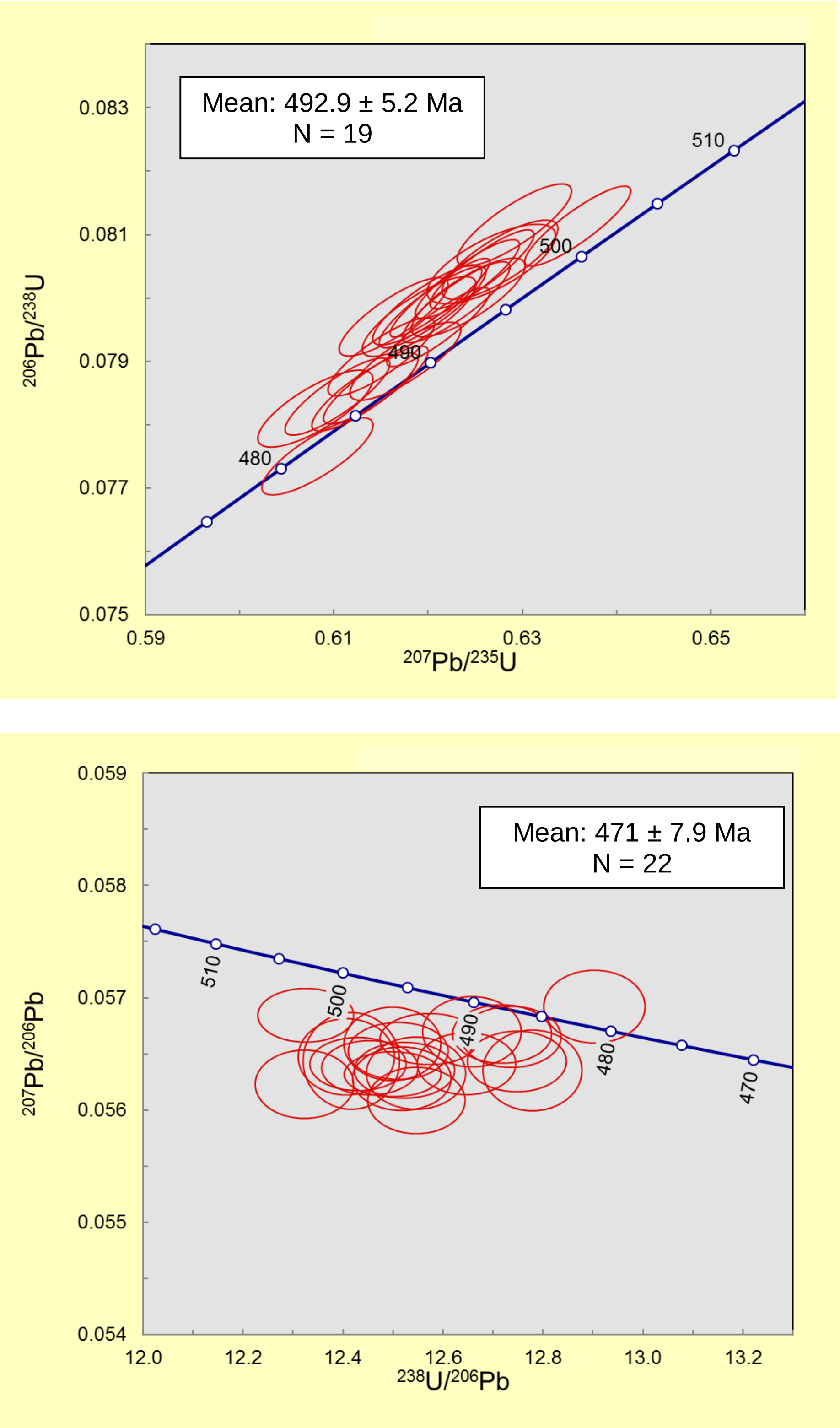

Fig. 6.12. the U-Pb Concordia diagrams A) conventional and B) Tera-Wasserburg showing discordant U-Pb data of zircon rims from the Mansehra Granite.

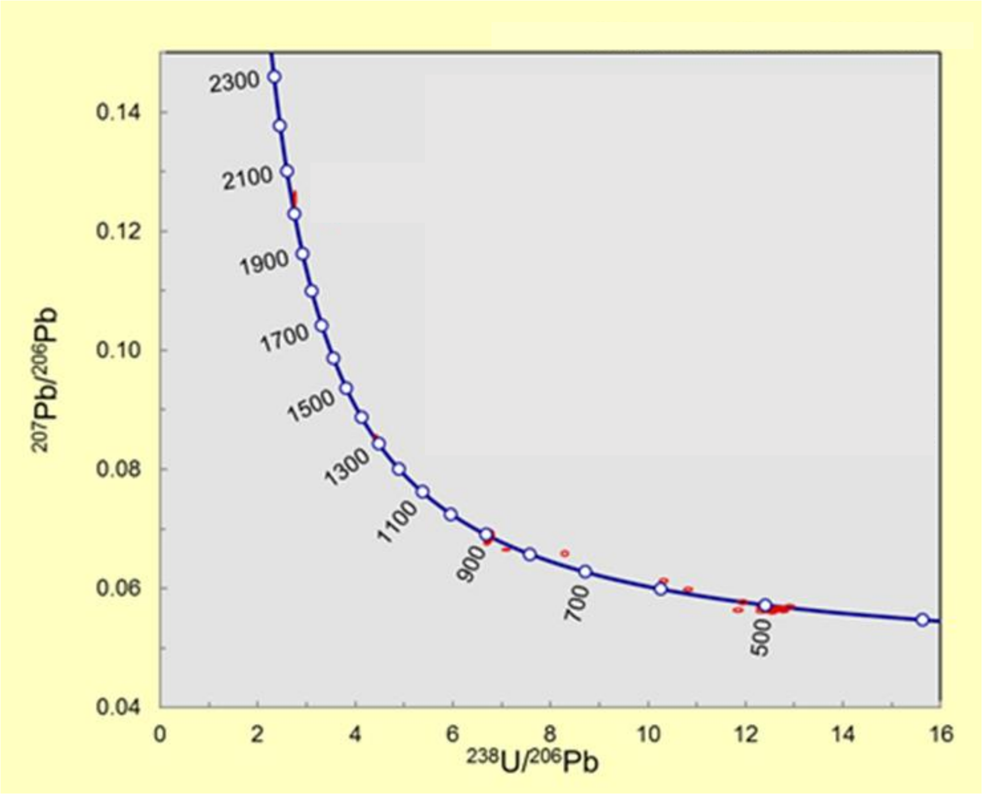

Fig. 6.13. U–Pb Concordia diagram showing data of all the analysed spots (including both cores and rims) on zircon from the Mansehra Granite. Likewise, the Utla Granites, two zircon generations are observed i.e. <500 Ma (shown by rims) and 800-900 Ma (mostly by core). In addition, around 2 Ga old concordant zircon core is also observed.

6.3.4. Dolerite dykes

Only nine grains have been recovered from from the dolerite with most of them having fractures. Three points have been targeted for analysis (Table 6.3). Rims of the two grains give similar ages to the host Utla granites (MPG) (Fig. 6.14). Figure (6.15A) show the rim zone giving the 486 Ma age. The rim has also been targeted in Figure (6.15B) but it may got some contribution from core. The age of around 492 Ma overlaps within errors with rim age (486 Ma) which does not seem to contain an inherited core. This show either the core contribution is very subtle or has more or less similar age to the rim. The latter explanation appears very plausible as the dyke cut through the Utla granite (MPG) which also cluster around 480 to 490 Ma (Fig. 6.6). The third spot show the mixed core-rim analyses giving age of 1666 Ma (Fig. 6.15C). It was not possible to avoid core due to size limitation of spot and grain.

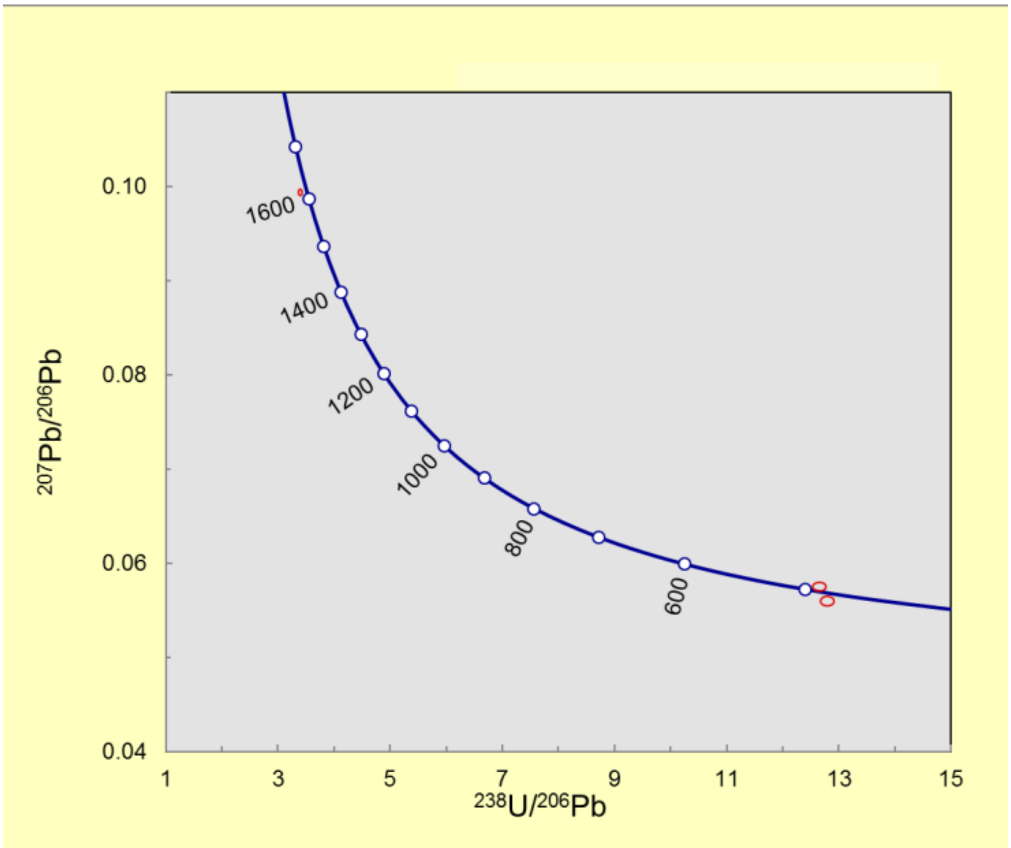

Fig. 6.14. U–Pb Concordia diagram of zircon from Dolerite intruding MPG.

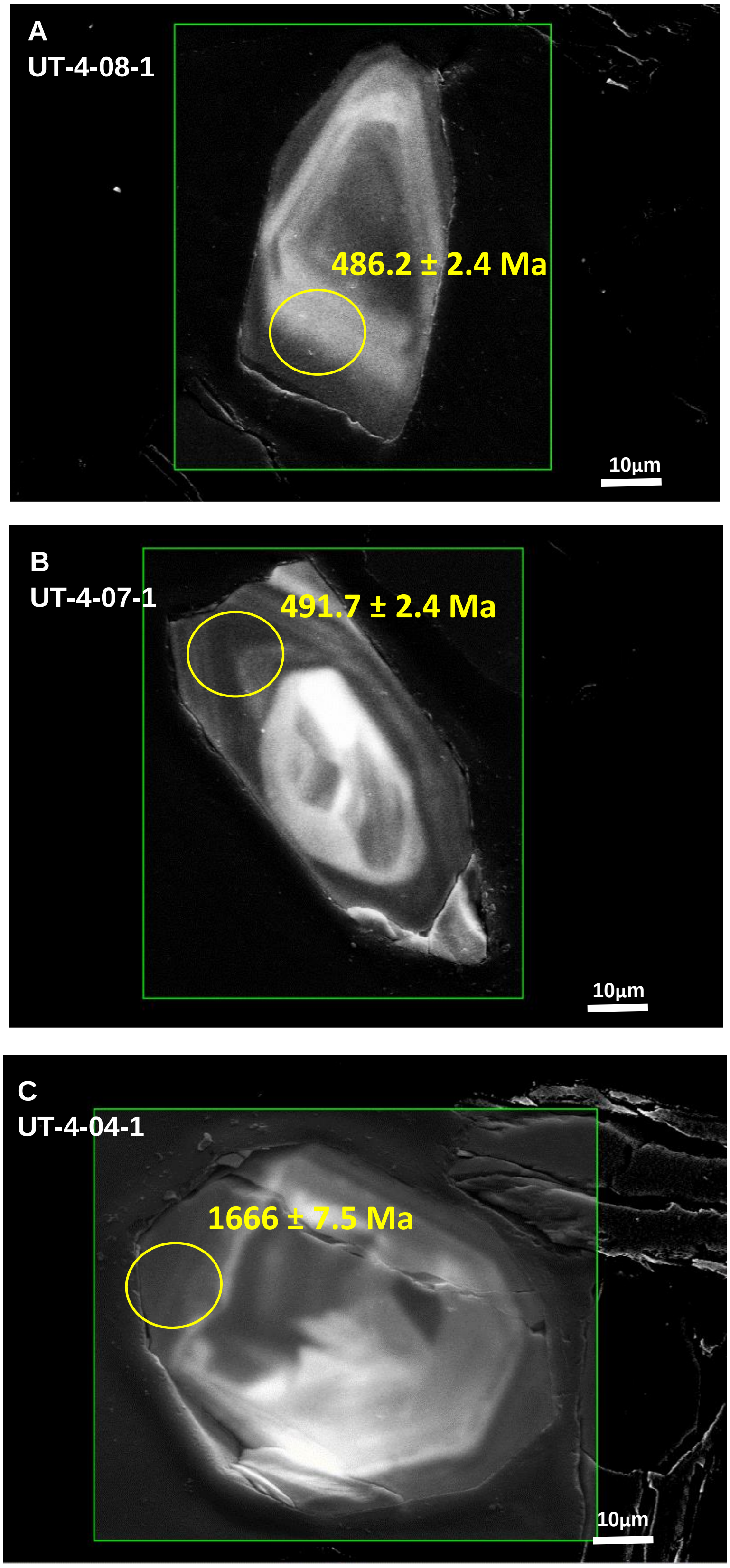

Fig. 6.15. CL images of zircons from dolerite dykes intruding Utla granite (see text for details).

6.4. Interpretations

In summary, zircons from Utla granites (both MPG and AMG) show its bimodal crystallization history roughly between 900-700 Ma and 490-470 Ma respectively. The MPG rocks suggest an average U-Pb crystallization age of 481.5 ± 5.6 Ma which is based on all the data acquired from rims. However, some authors have described the youngest age to be the best description of the last crystallization event. Hence, taking in account only the average of <480 Ma old rims would suggest a last crystallization of MPG rocks at around 475.7 ± 4.5 Ma.

The AMG rocks show more or less similar spectrum of U-Pb ages as the MPG with minor differences. These similarities may also signify the possibility of xenocrystic origin of some zircons from MPG. The average U-Pb age on the basis of all rim data is 478.5 ± 7.3 Ma which is within error identical to MPG. However, using only <480 Ma old AMG zircons rims, a last crystallization event around 471.3 ± 2.6 Ma is indicated. The mean ages indicate AMG to be younger by a few million years as compared to MPG, and this is in accordance with field evidence of AMG magma intruding MPG rocks. However, both ages are indistinguishable within 1σ error thus not allowing detailed dating of the time span between both events.

The reverse discordant crystallization ages of zircons from Mansehra Granite can be explained with their correlation with respective U concentration (Fig. 6.16). Similar excess ages have previously been documented for a 2700 Ma old zircon by Wiedenbeck (1995) and for 180 Ma old high-U zircons from Tasmanian dolerites by Williams and Hergt (2000) and White and Ireland (2012). In all these cases, the deviation is due to enrichment in uranium content relative to normal zircons. White and Ireland (2012) describe the discordance mainly due to an increase of the ion emission of Pb relative to U due to the degradation of the zircon matrix by radiation damage (metamictization). The increase in uranium apparently changes the relative sensitivity factors of Pb and U (matrix effect), hence the apparent U-Pb ages correlates with the U-content. The U-Pb age vs. U concentration plot shows the rims of Mansehra Granite zircons are highly enriched in U relative to rims of MPG and AMG zircons (Fig. 6.16) which explain the discordance of Mansehra Granite data due the mentioned reason. The Discordia line of the rim ages intercept the Concordia at 479.5 ± 6.4 Ma (Fig. 6.17) which is interpreted as the crystallization age of the Mansehra granite on the basis of U-Pb schematics.

The U-Pb ages of Utla (475.7 ± 4.5 Ma) and Mansehra granites (479.5 ± 6.4 Ma) seem comparable within errors which is also supported by their analogous chemical signature (Chapter 4). On this basis it is concluded that both complexes formed during the same crystallization event. Due to the limited zircon population recovered from dolerites intruding Utla granites and similar U-Pb ages noticed from rims of these grains, their exclusively inherited origin is inferred. It further confirm the crustal contribution in the melt parental to dolerites as interpreted by their trace elements composition (Fig. 5.14)

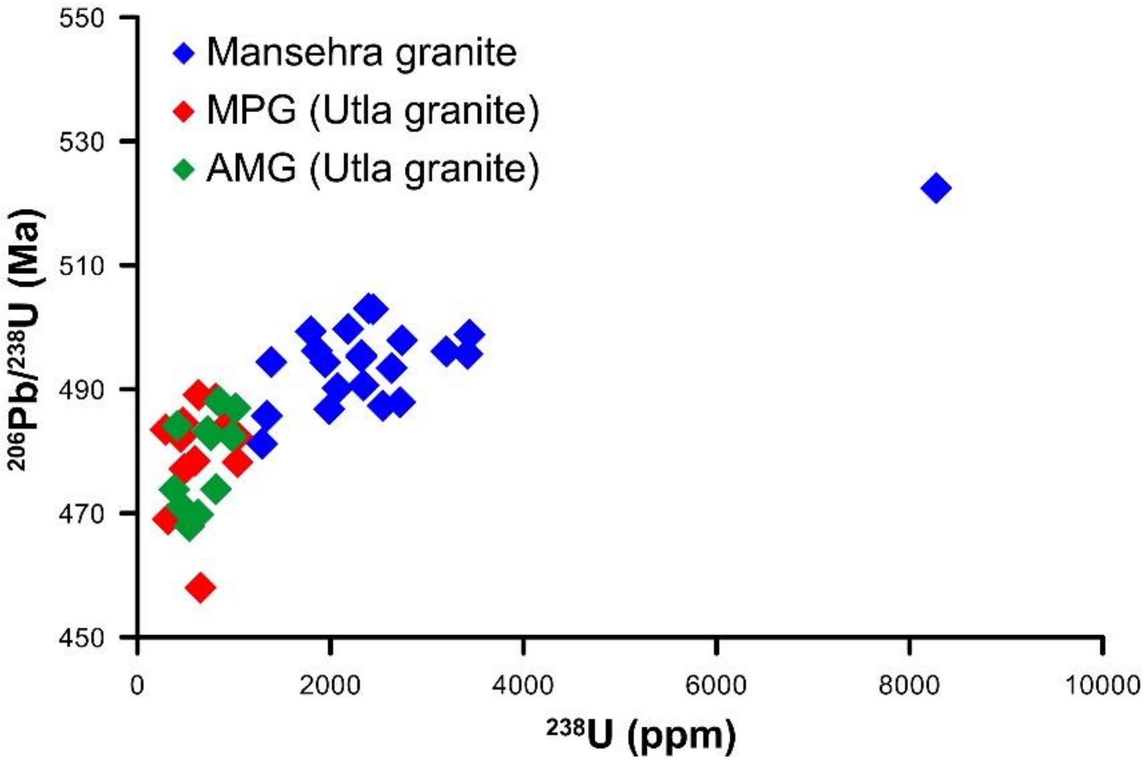

Fig. 6.16. U-Pb age vs U concentration show U enrichment in zircons Mansehra Granite.

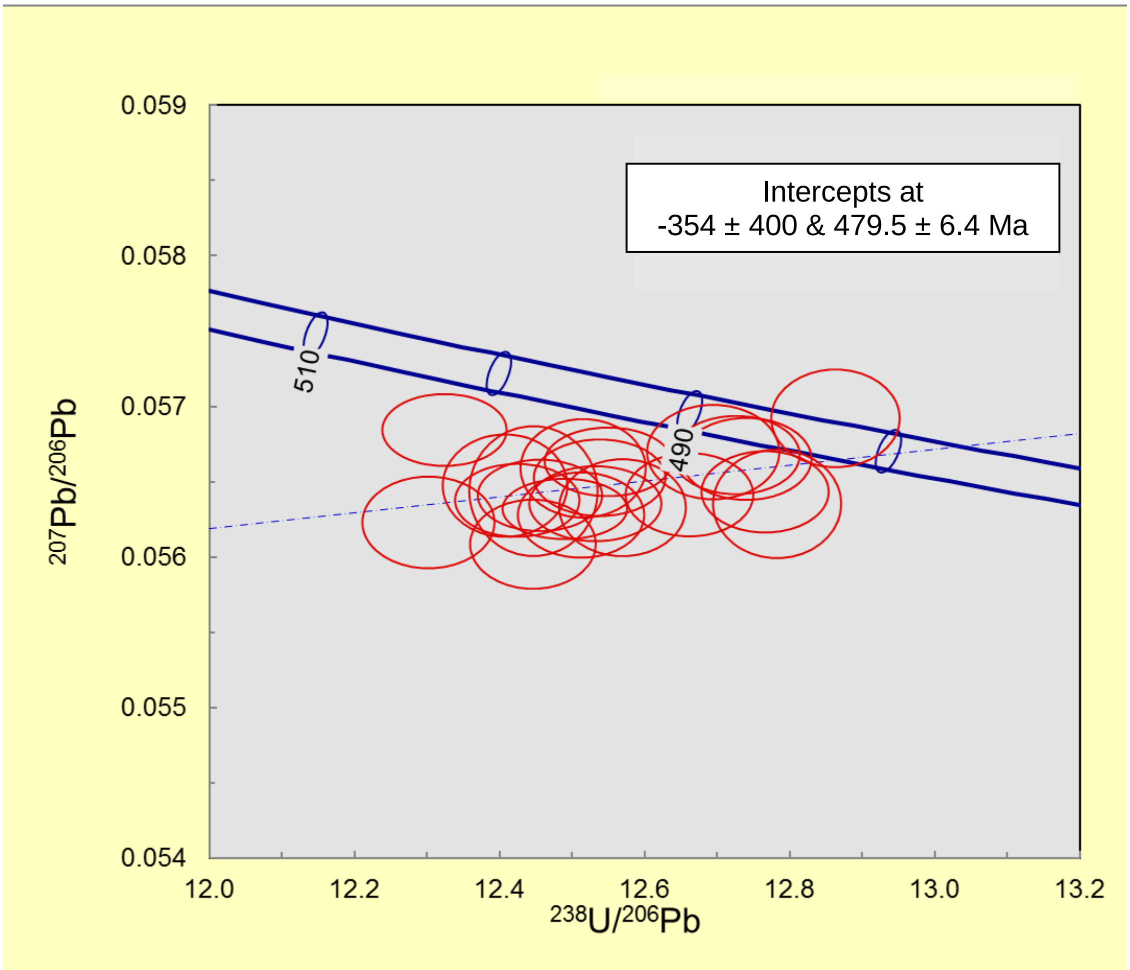

Fig. 6.17. U-Pb Concordia diagram showing the intercept of discordant data with Concordia line of zircons from Mansehra Granite.

6.5. Discussion

The U-Pb radiometric ages of both MPG and AMG rocks turn out to be 475.7 ± 4.5 Ma and 471.3 ± 2.6 Ma. For comparison, the Mansehra Granite with similar field and mineralogical characteristics have also been dated using similar procedure which also seems synchronous i.e. 479.5 ± 6.4 Ma.

The Himalayan-Tibetan orogeny was the result of collision between Indian and Eurasian plates over the past 50-70 Ma (Searle et al., 2009; Burg, 2011). During this collision, the Greater Himalayas (GHS), primarily consisting of pre-Cambrian to early Paleozoic meta-sediments and granitoids (Le Fort et al., 1986; Searle et al., 2008) have over thrusted the Lesser Himalayas (LHS) (Fig. 2.1) along Main Central Thrust (MCT) (Gansser, 1964; Kohn et al., 2010; Kohn, 2014). The LHS consist the Indian plate rocks including Proterozoic basement and cover sequence of Paleozoic meta-sedimentary series (Miller et al., 2001; Searle et al., 2009; Kohn et al., 2010). Both

GHS and LHS form the passive continental margin of Indian plate (Brookfield, 1993), however, Kohn et al. (2010) described the Paleo-Proterozoic assemblage of LHS as a continental arc rather than a passive margin.

A geochronological data set of granitic rocks from GHS and LHS is presented in Table 6.4 which show Cambrian-Ordovician age range. The similar age of Utla granitoids and analogous chemical signature (Chapter 4) confirm their association with these granites. LeFort et al. (1980) for the first time described the Mansehra granitic pluton from NW Pakistan as a part of this granitic sequence on the basis of geochemical studies and Rb-Sr whole rock age i.e. 516 ± 16 Ma. However, U-Pb zircon schematic show the age of Mansehra granite to be 479.5 ± 6.4 Ma in current investigation which also seems comparable within error limits to other granites from the same sequence.

The concordant core ages from all the studied zircons (both Utla and Mansehra Granites) mostly ranges between 813 Ma to 893 Ma. Similar U-Pb zircon ages have been reported from Black Mountain Complex (DiPietro and Isachsen, 2004) and Chingalai Gneisses (Ahmed et al., 2013). The Black Mountain Complex is present along the eastern bank of Indus River mainly composed of equigranular fine-grained biotite-quartz-feldspar orthogneisses and intruded by Mansehra Granite (DiPietro and Isachsen, 2004). Other subordinate lithologies include biotite and garnet bearing gneisses, migmatites and mafic rocks. Zircon from the main lithology yielded an age of 823 ± 2 Ma (DiPietro and Isachsen, 2004). The Chingalai Gneisses are present on the western side of Indus River and mapped as southeastern extension of Swat Granite by DiPietro et al. (1998). The U-Pb zircon age of 816 ± 70 Ma has been reported from these gneisses (Ahmed et al., 2013). Similar range of these ages and ages obtained from zircon cores in current investigation points towards the occurrence of small scale magmatism in late Proterozoic time in the northern Indian plate. DiPietro and Isachsen (2004) and Ahmed et al. (2013) relate these rocks with Malani magmatism, which show the age range between 750 and 850 Ma on the Aravalli craton exposed on the Rajasthan platform of northern India. However, comprehensive lithological and stratigraphical comparison is required to support this argument.

Table 6.4. Published ages of some lesser and higher Himalayan granite suites from different regions

Location	**Name of pluton**	**Method**		**Age (Ma)**	**Reference**
Pakistan	Utla Granite	U-Pb	Zirc	475 ± 4.5	Current investigation
	Mansehra Granite	U-Pb	Zirc	479 ± 6.4	Current investigation
	Mansehra Granite	Rb-Sr	WR	516 ± 16	LeFort et al., 1980
Nepal	Plaung Granite	U-Pb	Zirc, Mnz	470± 4	Scharer and Allegre, 1983
	Dadeldhura Granite	Rb-Sr	WR	470 ± 6	Einfalt et al., 1993
	Dadeldhura Granite	U-Pb	Zirc	478 ± 6	DeCelles et al., 2000
	Simchar Granite	Rb-Sr	WR	466 ± 40	LeFort et al., 1983
	Ruwa	U-Pb	Zirc	474 ± 3	Gehrels et al., 2006a
	Bhimphedi	U-Pb	Zirc	476 ± 3	Gehrels et al., 2006b
	Kathmandu	U-Pb	Zirc	476.9 ± 4.2	Cawood et al., 2007
NW India	Tso Morari Granite	U-Pb	Zirc	476 ± 2	Girard and Bussy, 1999
	Rupshu Granite	U-Pb	Zirc	482 ± 1	Girard and Bussy, 1999
	Miyar Orthogneiss	U-Pb	Mnz	479 ± 4	Pognante et al., 1990
	Kangan, Zanskar	U–Pb	Zirc	480 ± 16	Trivedi et al., 1990
	Manikaran Granite	Rb-Sr	WR	467 ± 45	Bhanot et al., 1979
	Kullu Granite	Rb-Sr	WR	495 ± 16	Frank et al., 1977
	Khadrala Granite	Rb-Sr	WR	460 ± 18	Rai et al., 1993
Tibet	Kangmar Granite	Rb-Sr	WR	485 ± 6	Wang et al., 1981
	Pingda (Baoshan)	U–Pb	Zirc	472 ± 5	Chen et al., 2007
	Pingda (Baoshan)	U–Pb	Zirc	498 ± 4.6	Liu et al., 2009
	Gaoligong	U–Pb	Zirc	487 ± 7	Wang et al., 2013

WR = whole rock; Mnz = monazite; Zirc = zircon

Most of the lesser Himalayan granites show Cambro-Ordovician ages (Table 6.4), yet Singh et al. (2002) reported that the Chor Granitoids from lesser Himalayan granitic belt in NW India which yield SHRIMP U-Pb age of 823 ± 5 Ma. They relate this pluton with ~825 Ma ultramafic to mafic magmatism and the associated extensive granite magmatism in the Yangtze block, SE China (Li, 1999). However, tectonic reconstructions do not affiliate the Yangtze block with the Himalayan region in the Neoproterozoic and early Paleozoic span (Metcalfe, 1996). Similar age range of Chor Granitoids to the studied zircon cores, Black Mountain Complex and Chingalai Gneisses, however, further support to the small scale magmatism during the late Proterozoic time in the northern margin of Indian plate.

The inherited zircons as indicated by the older age of certain cores (mostly between 813-893 Ma with few older analyses including 1143 Ma, 1315 Ma, 1683 Ma, 1993 Ma) are most likely represent their derivation from granite protolith (mostly likely older Proterozoic metasedimentary rocks). The Tanawal Formation hosting the currently studied Utla granites and Mansehra Granite is Proterozoic in age (LeFort et al., 1980; Pogue et al., 1992a). The sediments for Tanawal formation are most likely derived from Proterozoic basement rocks of Besham group (Baig et al., 1988, 1989). This group includes Shang orthogneisses and rocks from Kotla complex which have the ages of 1864 ± 4 Ma and 1836 ± 1 Ma respectively (DiPietro and Isachsen, 2001). The deposition of Tanawal formation, the likely protolith of Utla granite, must post date the age of youngest inherited zircon i.e. 813 Ma (from current study), which suggest its Neoproterozoic age.

CHAPTER 7

Petrographic features as an effective indicator for the variation in strength of granites

Published as:

Sajid, M., Coggan, J., Arif, M., Andersen, J., Rollinson, G., 2016. Petrographic features as an effective indicator for the variation in strength of granites. *Engineering Geology,* 202, 44–54

DOI: http://dx.doi.org/10.1016/j.enggeo.2016.01.001

Co-authors contribution:

J. Coggan, M. Arif, J. Andersen were involved in discussion during writing the paper. J. Coggan was also involved in interpretation of strength test results. Arif, M also helped in samples selection during the field trip. Rollinson, G. processed the QEMSCAN analysis and further interpretation.

Abstract

The textural characteristics of four different granites from the lower Himalayan regime in north-western Pakistan have been examined in relation to their effect on the mechanical nature of rock. Detailed petrographic examination and subsequent quantitative QEMSCAN analysis provide better understanding of the difference between their textures. Three of the granite types are slightly altered (Grade-II) whereas the other has a higher degree of alteration and corresponds to alteration Grade-III. The mechanical properties determined for each granite type include: unconfined compressive and tensile strength, elastic modulus, P-wave velocity, Schmidt hardness and dry density. Statistical analyses, combined with post-test petrography, demonstrate textural control on mechanical properties. The important petrographic characteristics influencing mechanical behaviour include modal concentration and grain size of individual minerals, mean grain size of rock and distribution of grain size within a rock. Recrystallization of minerals along boundaries has a pronounced effect on increased strength of granites. Texture, however, has a significant influence on the variation of strength of granites with similar alteration grade.

7.1. Introduction

Evaluation of the physical and mechanical characteristics of granites is essential when considering their industrial use and/or application e.g. for use as dimension stone or building material. Alteration of granites can have a detrimental effect on engineering behaviour and significantly change the behaviour of granites in different environments/conditions e.g. exposure to moisture/temperature, mechanical load etc. A number of researchers have previously described the cataloguing of granites based on their weathering and alteration (Brown, 1981; Hencher et al., 1990; Hencher and McNicholl, 1995; Anon, 1995; Irfan, 1996; Momeni et al., 2014). Several researchers have shown an inverse relationship between the strength of granite and increasing degree of alteration. Coggan et al. (2013) presented increasing kaolinization/alteration and associated changes in mineralogy to be responsible for a marked reduction in strength of granites from south-west England. Sousa (2013) evaluated the effect of mineral characteristics on the behaviour of different Portuguese granites including mineral weakening, quartz fissuration and type of contact between quartz with quartz and other mineral groups. He showed that evaluation of textural characteristics of quartz were vital for understanding the mechanical behaviour of granites. The influence of mineralogical composition and water content on the mechanical behaviour of argillite is described by Hu et al. (2014). The strength and elastic moduli was found to be significantly affected by increasing clay and water content. Rigopoulos et al. (2014) investigated ultrabasic and basic rocks from Greece to establish the relationship between mechanical and petrographic features. They revealed that strength tended to improve as the ratio between soft to hard minerals, ratio between secondary to primary phases and the degree of serpentinization decreased. Basu et al. (2009) assessed the engineering characteristics of altered granites from Brazil. They noticed that several alteration features, including mineralogical reform, disruption of existing textures and initiation of new cracks caused a reduction of strength of granites. The effect of weathering/ alteration on porosity and compressive strength of various rock types from Turkey was presented by Tugrul (2004). He proposed that micro-textures in relation to weathering of rocks were the controlling factors that influenced their physical and mechanical properties. Sajid and Arif (2015) investigated the effect of textural varieties on the mechanical behaviour of Utla granites from north-west Pakistan. They found that increased porosity and water absorption due to extensive recrystallization and associated mineralogical changes to be responsible for reduced strength of fine grained granites.

From the literature, researchers have observed a change in the mechanical behaviour with increased alteration grade; however, significant variation in strength is also observed in granites with similar alteration grade. The major objective of the current study is to describe the possible factors related to textural differences that are responsible for this mechanical variation in granites with analogous alteration. Pre- and post-test petrographic characteristics are compared to examine the influence of textural parameters (grain size, grain boundary recrystallization, modal concentration) on fracture propagation and engineering behaviour. Four texturally different granites types (Mansehra Granite: MG, Malakand Granite: SG, Utla Granite: UG, Ambela Granite: AG) from the lower Himalayan regime of north western Pakistan (Fig. 7.1) have been used to investigate this phenomena.

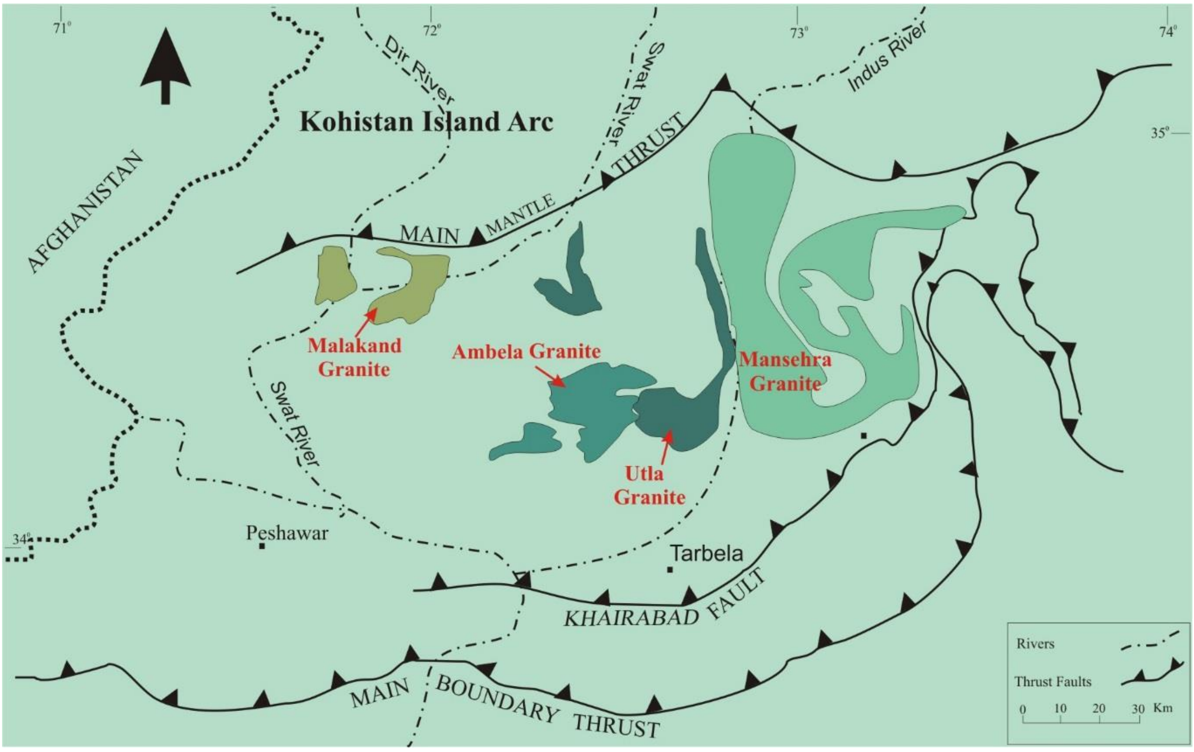

Fig. 7.1. Geological map of north-west Pakistan showing location of studied granites (after Pogue et al., 1999; Khattak et al., 2005).

7.2. Geology of Studied granites

The Kohistan Island arc is separated from the Indian plate in north Pakistan by a regional fault known as the Main Mantle Thrust (Burg, 2011) (Fig. 7.1). The Khairabad Fault divides the Indian plate into the northern internal metamorphosed zone and the southern external un-metamorphosed or low-grade metamorphic zone (Treloar et al., 1989a) (Fig. 7.1). All the granitic bodies in this study (MG, SG, UG and AG) lie towards the north of the Khairabad Fault, but represent different magmatic episodes. UG and MG exhibit similar mineralogical and chemical characteristics (Sajid et al., 2014) but texturally different varieties can be found in both of these plutons. MG yields whole-rock Rb–Sr age of 516 ± 16 Ma and intrudes pre-Cambrian Tanawal Quartzite (Le Fort et al., 1980). AG has an alkaline signature and can be related to Permian rifting in the northern margin of the Indian plate. The detailed petrography of AG is presented in Rafiq and Jan (1988). Le Bas et al. (1987) and Khattak et al. (2008) suggested that the alkaline magmatism occurred in two episodes; one in the Permian followed by another during the Paleogene (Oligocene) resulting in the formation of SG. However, Jan and Karim (1990) oppose episodic magmatism and suggest both SG and AG are the product of a single magmatic event during the Permian. The geochronological account of the alkaline rocks and other related suites are presented in more detail in Ahmed et al. (2013).

7.3. Methodology

Fresh bulk samples from all the four granite types were collected, processed, prepared and tested according to International Society of Rock Mechanics (2007) guidelines. All the tested samples were free of any kind of visible fracture. Strength tests were conducted using the MTS servo-controlled hydraulic testing machine at the Camborne School of Mines, University of Exeter, UK. A LVDT (Linear Variable Displacement Transformer) was used to record the axial displacement. In addition, an electric resistance 2.54 mm long strain gauges were used for measurement of lateral strain. Care was taken to avoid any feldspar mega-cryst while fixing strain gauges on the samples tested. A pulse generator unit with two transducers (a transmitter and a receiver) with a frequency of 55kHz was used for determination of ultrasonic velocities of five representative samples of each type of granite tested.

A texturally representative thin section from each granite type was also processed with a QEMSCAN-4300 in the analytical facility at the Camborne School of Mines. QEMSCAN is a widely applied technique to acquire quantitative mineralogical data for analysis of mineral association, micro-textures, textural connections and quantitative mineralogy of rock specimens (Gottlieb et al., 2000). Each thin section was measured using field scan mode at a resolution of 10 microns, and data was processed as described by Rollinson et al. (2011). Petrographic studies were performed using a Nikon Eclipse E600 polarizing microscope with attached 5MP digital camera on polished thin sections obtained from each granite type. Polished thin sections were also taken from failed samples that had been subjected to strength testing to observe the propagation of newly formed fractures and their relation to grain boundaries. Failed core samples were mounted in epoxy resin for three days to preserve the new fractures and to avoid disturbance of samples during thin section preparation. The micro-petrographic index (I_p) defined as the ratio between unaltered minerals to altered minerals and fractures (Irfan, 1996; Irfan and Dearman, 1978) was also determined from twelve representative thin sections obtained from the studied samples.

7.4. Petrographic characteristics of studied granites

Core specimens and mineral maps (generated through field scan analyses via QEMSCAN) of the studied granites are presented in Figures 7.2 and 7.3 respectively. Petrographic characterization based on quantitative mineralogical data from QEMSCAN and microscopy was undertaken. The modal concentration of minerals and their mean grain sizes are presented in Tables 7.1 and 7.2 respectively. The detailed petrographic characteristics of each granite type are described as:

7.4.1. Utla Granite (UG)

UG is a megacrystic granite with K-feldspar and plagioclase constituting most of the phenocrysts. Plagioclase ranges in alteration from fresh to partially altered grains; however, completely altered feldspar megacrysts are also observed in some thin sections (Fig. 7.4A). Sericite, kaolinite and fine grained epidote are the most common alteration products observed. Quartz is mostly anhedral and displays undulose extinction due to its strained nature (Fig. 7.4B). The ground mass is mostly fine grained and contains recrystallized fresh quartz grains (Fig. 7.4C) with significantly increased concentration of fine grained minerals along grain boundaries. The shape of major minerals ranges from euhedral to subhedral. Non-aligned micaceous minerals including biotite and muscovite are common accessories. Minor concentrations of tourmaline, apatite, zircon and ilmenite are also observed.

7.4.2. Mansehra Granite (MG)

MG is also megacrystic but a greater degree of alteration of major minerals makes it distinct from UG. Feldspar phenocrysts are mostly dull and cloudy showing their conversion to clay minerals and fine grained epidote grains (Fig. 7.4D, E). The groundmass is medium to coarse grained and exhibit some recrystallization features in the form of fine-grained quartz. Biotite, muscovite, tourmaline, apatite and ore minerals are common accessories.

Biotite is mostly well-developed and coarse grained, showing a variable degree of alteration to chlorite and muscovite.

7.4.3. Ambela Granite (AG)

AG is equigranular and very coarse grained, consisting predominantly of K-feldspar and quartz. Discrete plagioclase is uncommon. K-feldspar is subhedral to euhedral and shows limited alteration in comparison to other minerals. Most grains are perthitic and show well developed albite exsolution (Fig. 7.4F). Concentration of micaceous minerals is less when compared to UG and MG. Fine grained and fresh recrystallized quartz is very common and occurs along grain boundaries (Fig. 7.4G).

7.4.4. Malakand Granite (SG)

SG is petrographically more distinct due to its very fresh and equigranular nature (Fig. 7.4H, I). SG is holocrystalline, coarse grained and contains almost equal amounts of major minerals including quartz, plagioclase and K-feldspar. Feldspars are mostly fresh and display their typical optical properties with very delicate signs of alteration to other minerals. Quartz ranges from subhedral to anhedral and exhibits undulose extinction. Grain boundary recrystallization is lacking in SG when compared to UG, MG and AG. Concentration of micaceous minerals is less when compared to MG and UG. Epidote, allanite, sphene and apatite are other common accessory minerals present.

Fig. 7.2. Representative cylindrical core samples of studied granites.

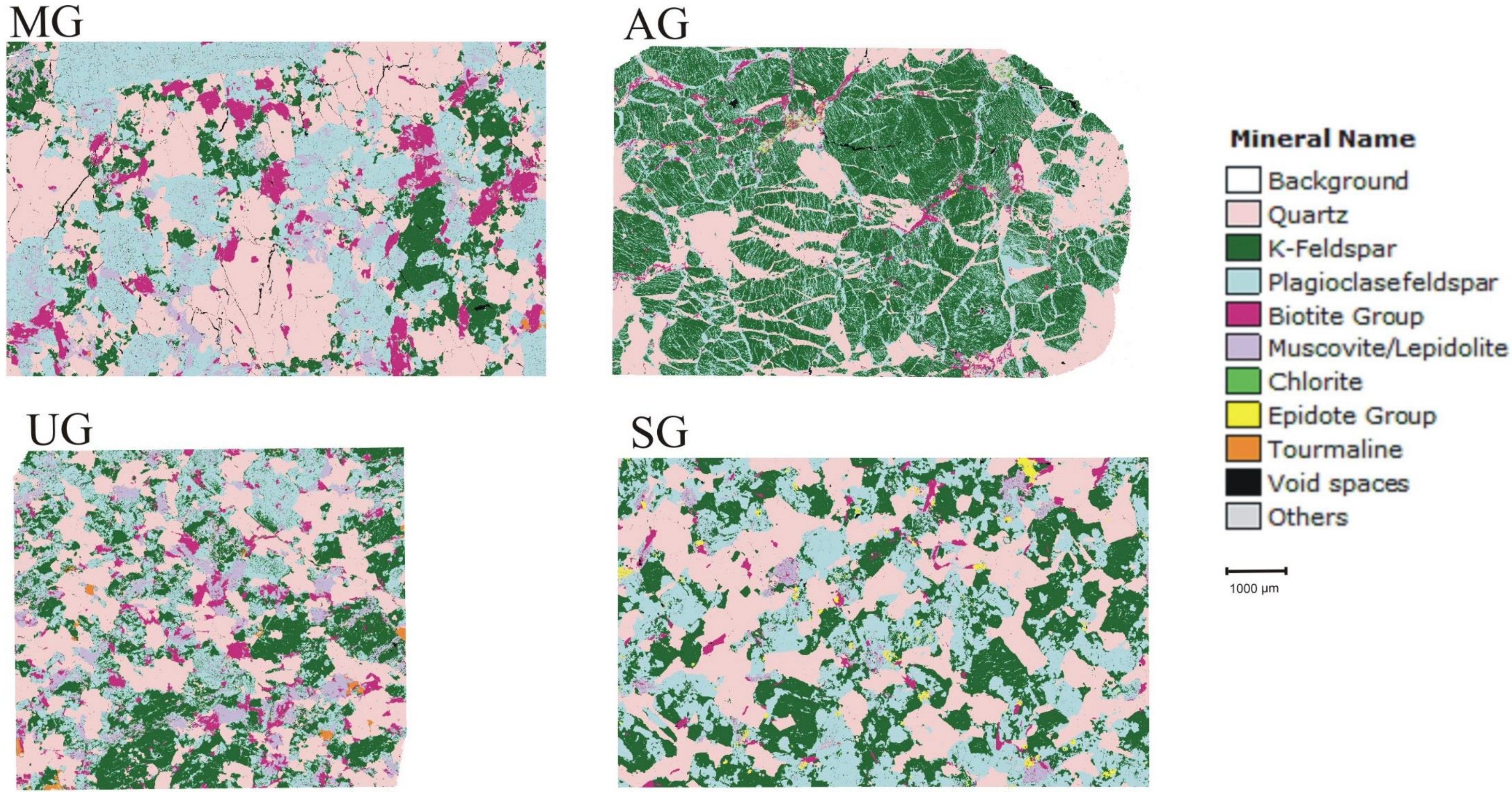

Fig. 7.3. Representative mineral maps of studied granites generated via QEMSCAN analysis.

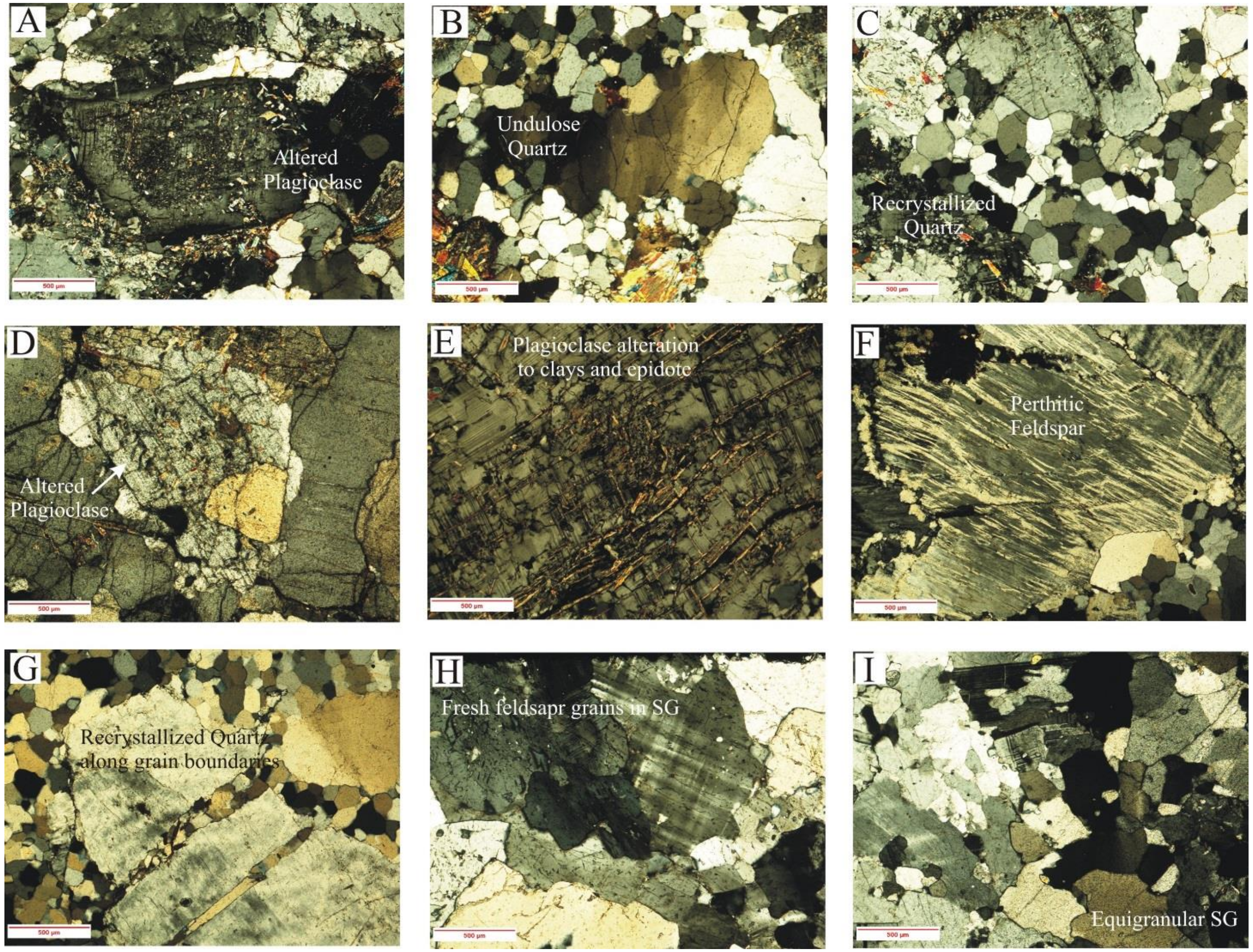

Fig. 7.4. Micrographs illustrating A) alteration of Plagioclase feldspar, B) quartz showing undulose extinction, C) fresh recrystallized quartz grain in ground mass, D–E) plagioclase alteration to clay minerals and epidote, F) perthitic alkali feldspar, G) grain boundary recrystallization of quartz, H–I) fresh and equigranular quartz and feldspar grains.

Table 7.1. Modal mineralogical concentration of studied rocks

	Qtz %	**K-Feldspar%**	**Pl%**	**Bt %**	**Ms%**	**Tur %**	**Others %**	**Voids %**
UG-1	35.12	26.23	21.98	5.49	9.65	0.59	0.94	1.0
UG-2	33.39	27.2	22.84	5.73	8.99	1.09	0.76	0.8
UG-3	35.42	25.12	22.69	6.11	9.21	0.95	0.5	0.8
MG-1	38.62	13.26	32.64	6.98	7.09	1.11	0.3	2.5
MG-2	39.12	14.18	31.21	7.89	6.54	1.03	0.03	2.8
SG-1	35.21	28.22	31.02	2.21	3.02	0	0.32	0.9
SG-2	35.11	28.21	30.64	3.12	2.33	0	0.59	0.9
AG-1	25.21	46.93	24.53	3.05	0.08	0	0.2	0.5
AG-2	23.26	47.65	24.64	2.13	0.12	0	2.2	0.5
AG-3	24.09	48.12	23.89	2.65	0.16	0	1.09	0.4

Qtz = quartz, Pl = plagioclase, Bt = biotite, Ms = muscovite, Tur = Tourmaline

Table 7.2. Grain size distribution of studied granites

	Qtz (mm)		Pl (mm)		K-feldspar (mm)		Bt (mm)	Ms (mm)	Mean grain size (mm)	
	Mean	Max	Mean	Max	Mean	Max	Mean	Mean	Rock forming minerals	cleaved minerals
UG-1	7	14	5.5	29	6	26	0.9	0.8	5.4	5.2
UG-2	7.5	15	4.5	26	6	25	0.9	0.9	5.3	4.3
UG-3	9	17	6	27	7	28	0.9	0.9	6.5	5.1
MG-2	9	18	16	33	4	27	2.4	1.2	9.6	10.0
MG-3	11	19	8	32	8	29	2.2	1.1	8.3	9.4
SG-1	14	19	6	11	5	18	0.4	0.2	8.2	5.1
SG-2	17	19	10	12	5	17	0.4	0.1	9.1	6.9
AG-1	6.5	13	4	5	9	15	0.4	0.1	6.9	6.1
AG-3	8.1	14	3.5	5	7	14	0.4	0.1	6.2	5.6
AG-4	7.2	11	3	6	7	16	0.4	0.1	5.9	4.9

Qtz = quartz, Pl = plagioclase, Bt = biotite, Ms = muscovite

7.5. Alteration grade of studied granites

Different schemes recommended for classification of granites based on their degree of weathering and alterations are presented in Table 7.3. These systems highlight the use of Schmidt hardness, discoloration and disintegration as the classifying criteria in field/hand specimens. The results of various mechanical properties determined during the current investigation are presented in Table 7.4. Schmidt hardness values of AG, UG and SG (>45) represent values associated with alteration Grade-II, however MG falls within Grade-III, as its hardness is < 45 i.e. 41 (Table 7.4). No staining related to alteration of minerals is observed in the SG samples; however, AG and UG portray slight discoloration, particularly along grain boundaries (Fig. 7.2). The degree of yellowish-brown staining on the MG sample is slightly more than other granites, which suggests a higher degree of alteration. Figure 7.5 shows an image taken from the QEMSCAN analysis that depicts the nature of the void spaces within the studied granitic samples. Quantitative analysis suggests that void spaces constitute more than one percent of area for the MG sample (Table 7.1). AG also contain considerable void area but it is inconsistent relative to MG (Fig. 7.5). Voids in MG are more regular and mostly follow intra-granular fractures and cleavages which are more distinct due to the altered and strained nature of mineral grains (mostly feldspar and quartz) (Fig. 7.5). The relationship of alteration degree with void space and dry density of the studied samples is depicted in Figure 7.6, which emphasis the higher degree of alteration of MG.

Heidari et al. (2013) described the classification of granitic rocks from western Iran on the basis of degree of weathering using different physical and mechanical properties including porosity, tensile strength, ultrasonic velocities etc. According to these classifications, MG samples exhibit higher alteration grade due to higher voids spaces, lower tensile strength and lower p-wave velocity than other studied granites (Table 7.4). Olona et al. (2010) related seismic velocities and other geotechnical properties to the grade of weathering of granitic rocks from Spain. They concluded that ultrasonic velocities are significantly reduced with increasing degree of alteration. Comparing their results with values of P-wave velocities (V_p) of granitic rock from the current study shows that UG, AG and SG belong to alteration Grade-II because of having higher V_p values whilst MG has a much lower V_p, which is more typical of Grade-III (Table

7.4). The results of micro-petrographic index presented in Table 5.5 suggests and confirms considerably lower I_p values for MG relative to the other granite types. This illustrates that UG, AG and SG granite types belong to similar alteration grade (Grade-II); however, MG portrays a slightly higher degree of alteration and corresponds to alteration Grade-III.

Table 7.3. Weathering classification systems of granitic rocks

Grade	**Rock description**	**Hencher et al. 1990; Anon 1995**	**Brown 1981**	**P-wave velocity (m/sec) Olona et al. 2010**
I	Fresh rock	No visible alteration.	No visible sign of rock material Weathering	3320–4315
II	Slightly altered	Slight discoloration and weakening. Schmidt Hammer ‘N’ > 45.	Discolouration indicates weathering of rock materials and discontinuity surfaces	2000-2450
III	Moderately altered	Considerable weakening. Penetrative. Discoloration. Schmidt Hammer ‘N’ 25–45.	Less than half of the rock material is decomposed and/or disintegrated to soil	
IV	Highly altered	Large pieces broken by hand. Schmidt Hammer ‘N’ 0–25.	More than half of the rock material is discomposed and/or disintegrated to soil	518-900
V	Completely altered	Considerably weakened. Geological pick penetrates. Original texture preserved. Slakes readily in water. Hand penetrometer, 50–250 kPa.	All rock material is decomposed and/or disintegrated to soil. The original mass structure is still largely intact	
VI			All rock material is converted to soil. The mass structure and material fabric are destroyed	

Table 7.4. Results of various mechanical properties of studied rocks

	Density Dry (kg/m^3)	Dry P-wave Velocity (m/s)	Schmidt Hardness	UCS (MPa)	UTS (MPa)	Modulus (GPa)
UG-1	2615	2601	59	98.6	6.1	25
UG-2	2630	3153	60	139.7	6.3	22
UG-3	2617	2866	58	84.3	5.6	24
MG-1	2561	1570	42	35.0	1.9	5
MG-2	2547	1656	43	35.5	2	6
SG-1	2562	2279	46	105.2	6.7	28
SG-2	2561	2173	48	95.0	6.5	23
AG-1	2573	3227	66	131.0	6.1	38
AG-2	2569	3371	68	137.9	6.5	40
AG-3	2551	3553	69	177.3	6.8	39

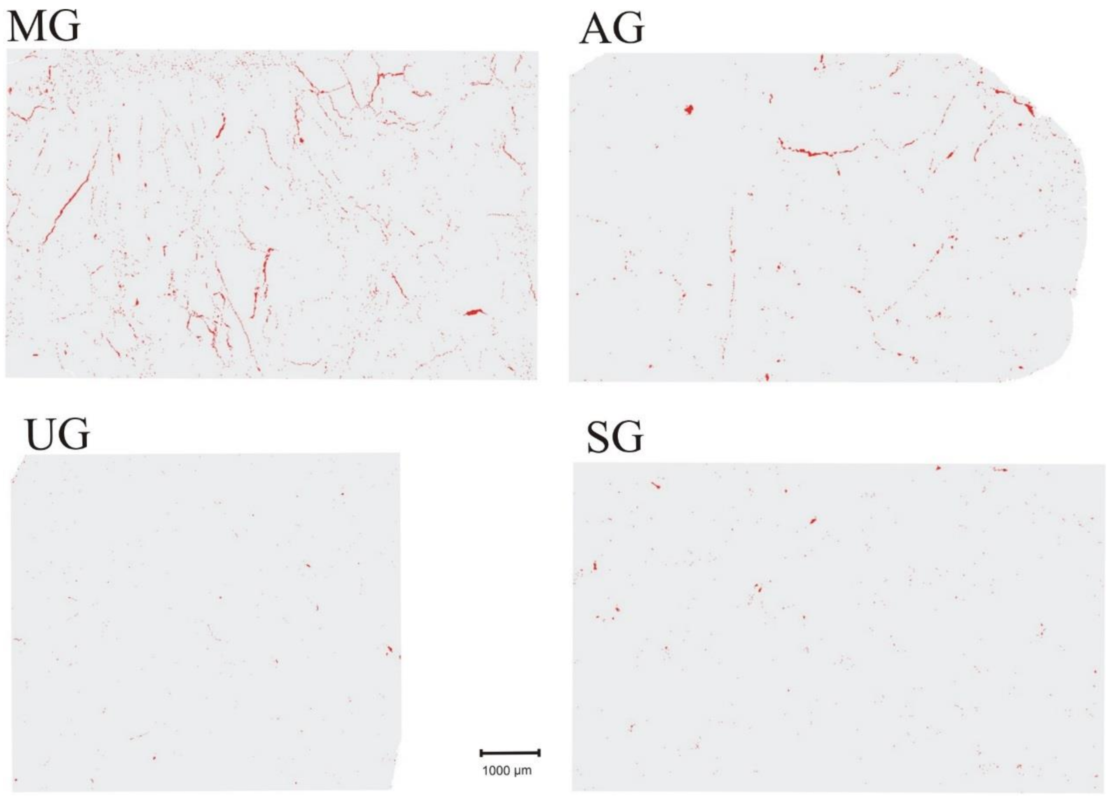

Fig. 7.5. Distribution of void spaces (represented by red colour) in studied granites. Image generated via QEMSCAN analysis.

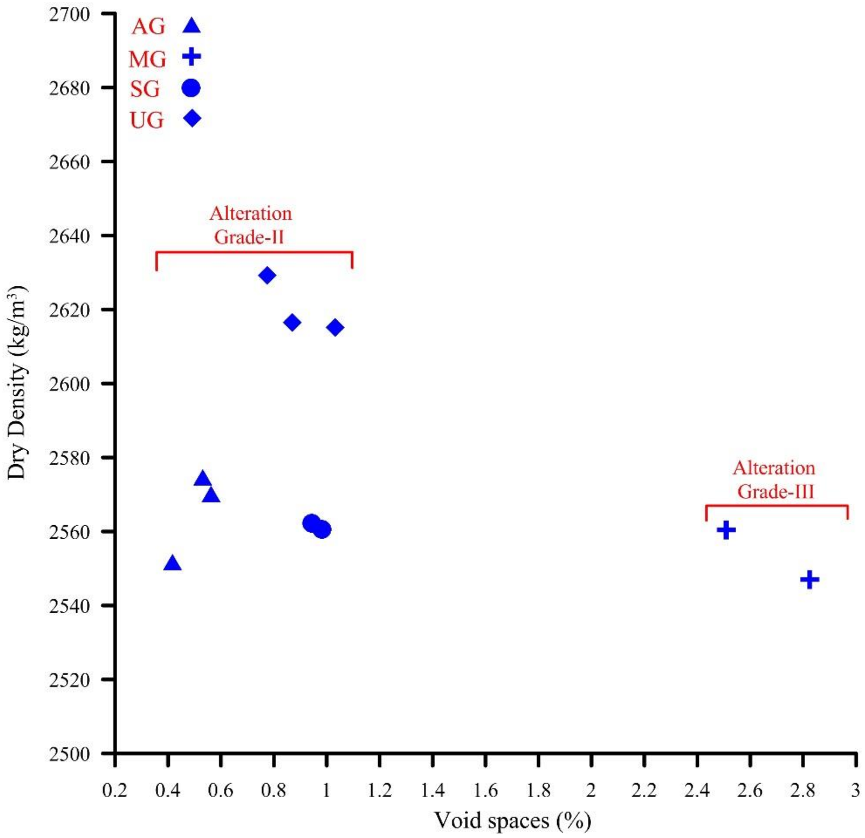

Fig. 7.6. Plot representing decrease in dry density with increasing void spaces.

7.6. Mechanical behaviour of studied granites

The mechanical properties tested include uniaxial compressive strength (UCS), uniaxial tensile strength (UTS) using an indirect Brazillian test, ultrasonic p-wave velocity, Schmidt hardness, elastic modulus and dry density. The corresponding results are presented in Table 7.4. These results show that MG, assigned Grade III from petrographic and mineralogical analysis, has the lowest strength. Significant changes in the mechanical behaviour of AG, UG and SG is observed despite their similar alteration grade (Table 7.4). The axial stress against axial and lateral strain response for the granites types tested are presented in Fig. 7.7. This highlights not only differences in UCS but also deformability or stiffness of the studied granites. AG shows higher strength followed by UG and SG respectively. Reduction in elastic moduli with increasing alteration grade is observed (Fig. 7.8). UCS exhibits positive relationships with UTS, Schmidt hardness and P-wave velocity (Fig. 7.9). The lower strength of MG resulting from the corresponding higher degree of alteration is consistent with previous work described by Coggan et al. (2013), but variations in mechanical behaviour that occur in samples with analogous alteration (SG, UG and AG) can be attributed to the observed textural changes which are described in more detail below.

Table 7.5. Calculation of micro-petrographic (I_p) index for studied rocks

	Altered minerals (Am) (%)	Fractures (f) (%)	Sound minerals (Sm) (%)	Ip = Sm/(f+Am)
MG	10.1	0.5	89.4	8.4
MG	9.8	0.9	89.3	8.3
MG	9.2	0.6	90.2	9.2
SG	3.2	0.2	96.6	28.4
SG	2.4	0.1	97.5	39.0
SG	2.7	0.3	97.0	32.3
UG	6.7	0.5	92.8	12.9
UG	5.9	0.4	93.7	14.9
UG	5.7	0.3	94.0	15.7
AG	3.3	0.1	96.6	28.4
AG	3.9	0.1	96.0	24.0
AG	2.7	0.4	96.9	31.2

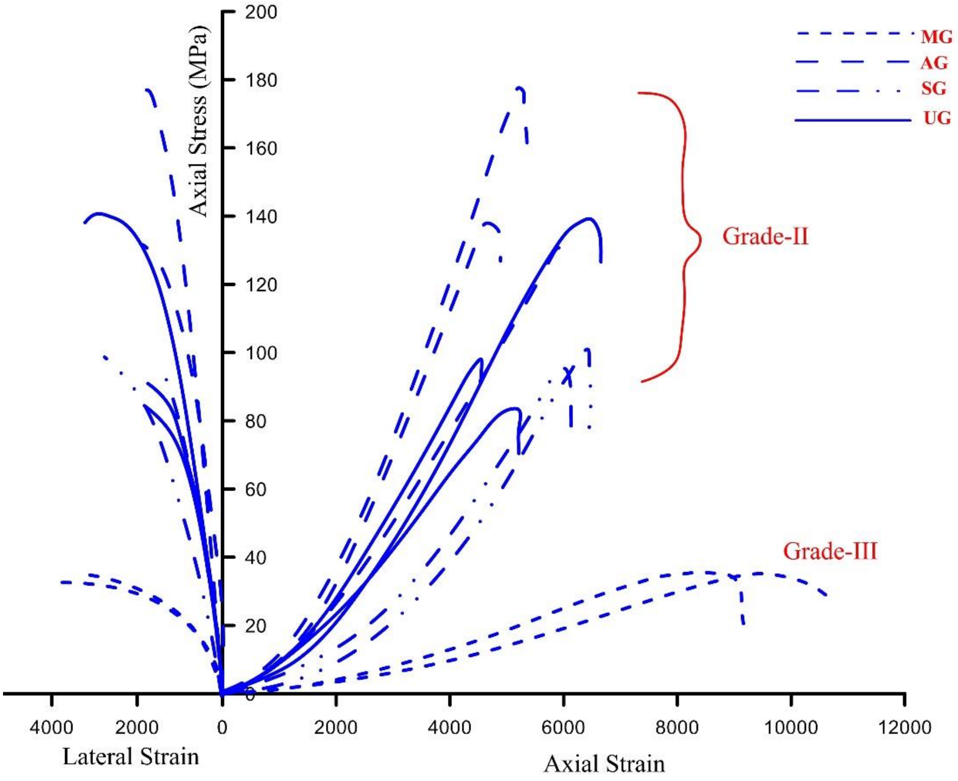

Fig. 7.7. Response of axial stress versus axial and lateral strain of studied granites.

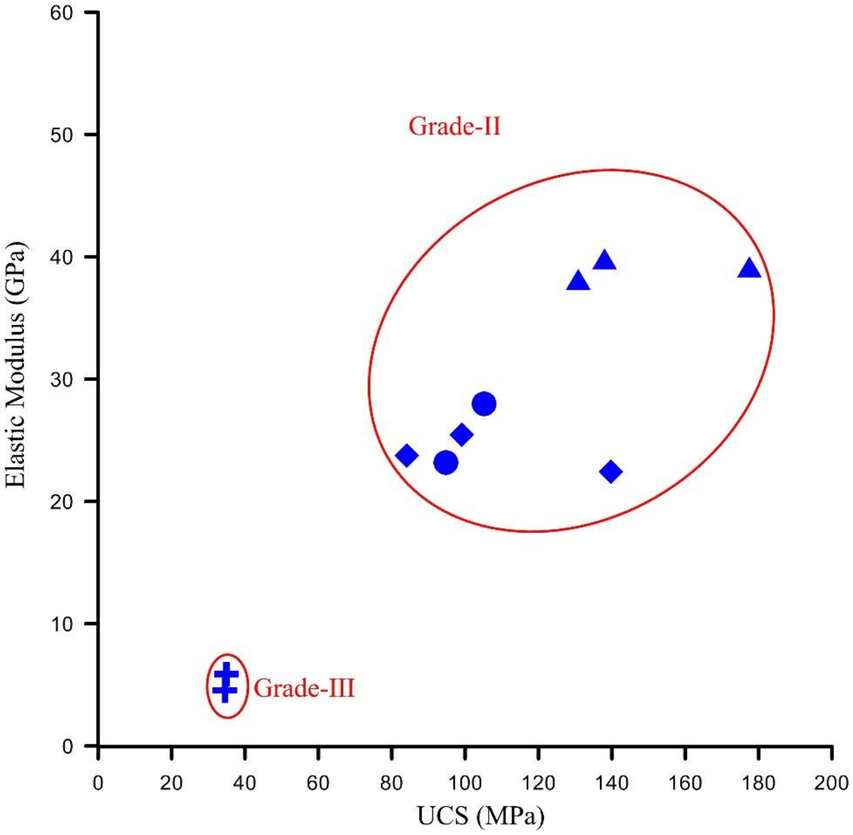

Fig. 7.8. Relationship between elastic modulus and uniaxial compressive strength for samples with different alteration grades. Symbols are same as in Fig. 7.6.

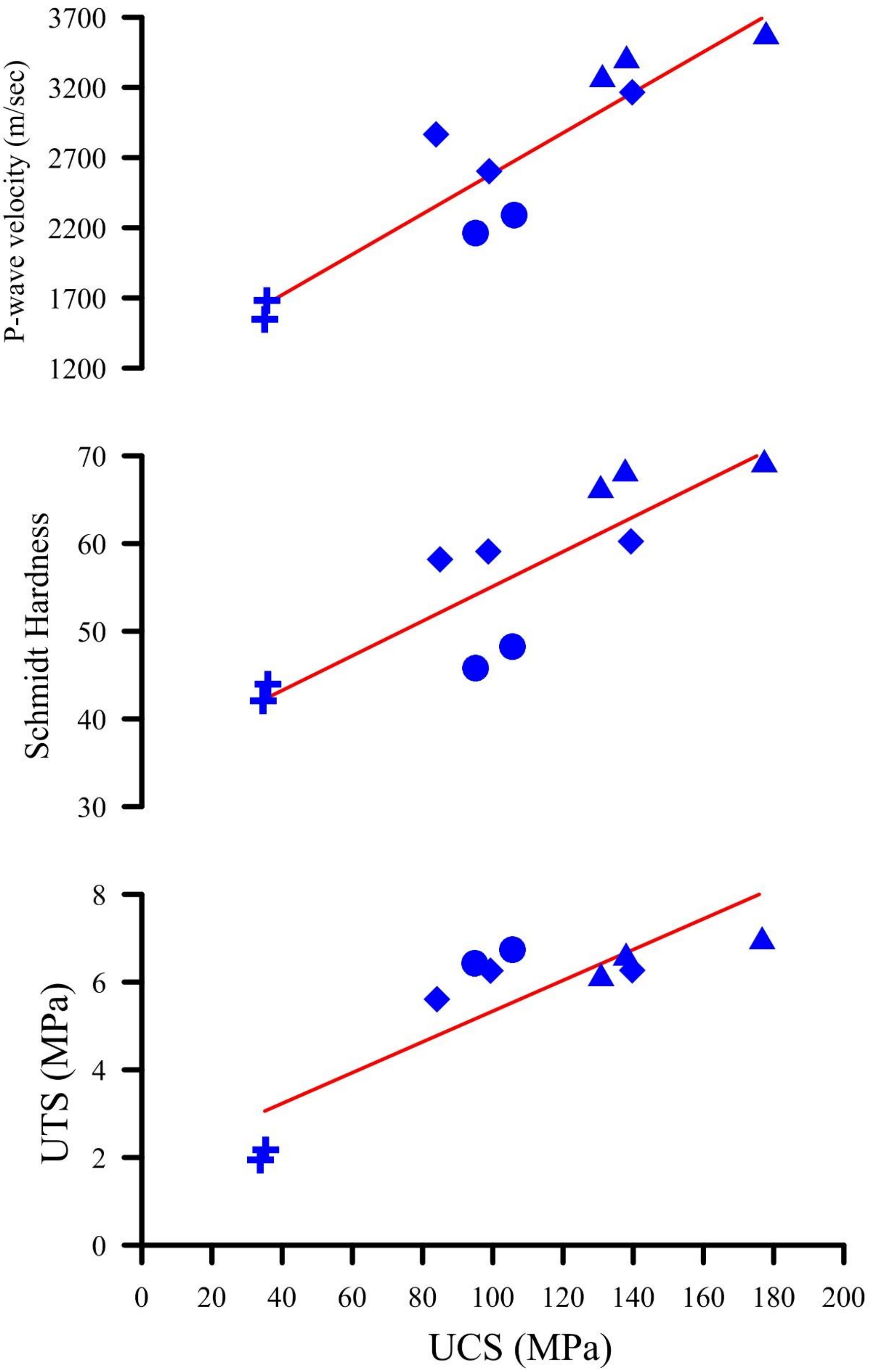

Fig. 7.9. Plots showing positive relationship of UCS with UTS, Schmidt hardness and ultrasonic velocities. Symbols are same as in Fig. 7.6.

7.7. Discussion

In order to describe the important relationships between petrographic features and mechanical behaviour of the granites studied, textural features including mean grain size and modal concentration of individual major mineral (Quartz, K-feldspar, plagioclase) and mean grain size of rocks have been plotted against corresponding UCS values.

Simple linear regression analysis has been applied to determine the coefficients of determination (r^2) which best describe the relationship between the variables. The values are verified by execution of the t-test method. A critical t-test value of 2.23 was obtained with 10 degrees of freedom and a 95 % confidence limit. The calculated t values for given data were significantly higher than the critical value, confirming the statistical significance of the relationships.

A strong positive relationship exists between the modal concentrations of K-feldspar with UCS but results suggest that increasing amounts of quartz and plagioclase results in decreasing UCS (Fig. 7.10). This is in direct contrast to work by Sajid and Arif (2015) and Tugrul and Zarif (1999) who suggest a direct correlation with increasing quartz content and UCS. Gunes-Yilmaz et al. (2011) concluded an inverse relation of quartz grain size with UCS but its concentration did not yield any significant relation. In agreement with present observation, Sousa (2013) described inverse relation of quartz content and quartz to feldspar ratio with strength of different Portuguese granites. He also described other textural features of quartz including quartz-quartz contact, quartz-feldspar contacts and quartz deterioration that can negatively influence the strength of granites despite its highest mechanical strength. This may be because of the decrease in rock capacity to accommodate deformation and increase in quartz-quartz contact.

The maximum grain size of quartz, orthoclase and plagioclase display an inverse relationship with UCS (Fig. 7.11). A similar relationship is also reported by Gunes-Yilmaz et al. (2011) for granites from various other parts of world. Fig. 7.12 suggests a clear relationship between mean grain size of plagioclase although this relationship is not as obvious with grain size of both quartz and K-feldspar. Strong negative correlations exist when plotting mean grain size of major rock forming minerals (combining quartz, feldspars and micas) and mean size of cleaved minerals (feldspars and micas) against UCS (Fig. 7.13). The comparison of Fig. 7.12 and 7.13 shows that mean grain size of rock is more important in assessing the mechanical behaviour of rock relative to individual grain size of constituent minerals.

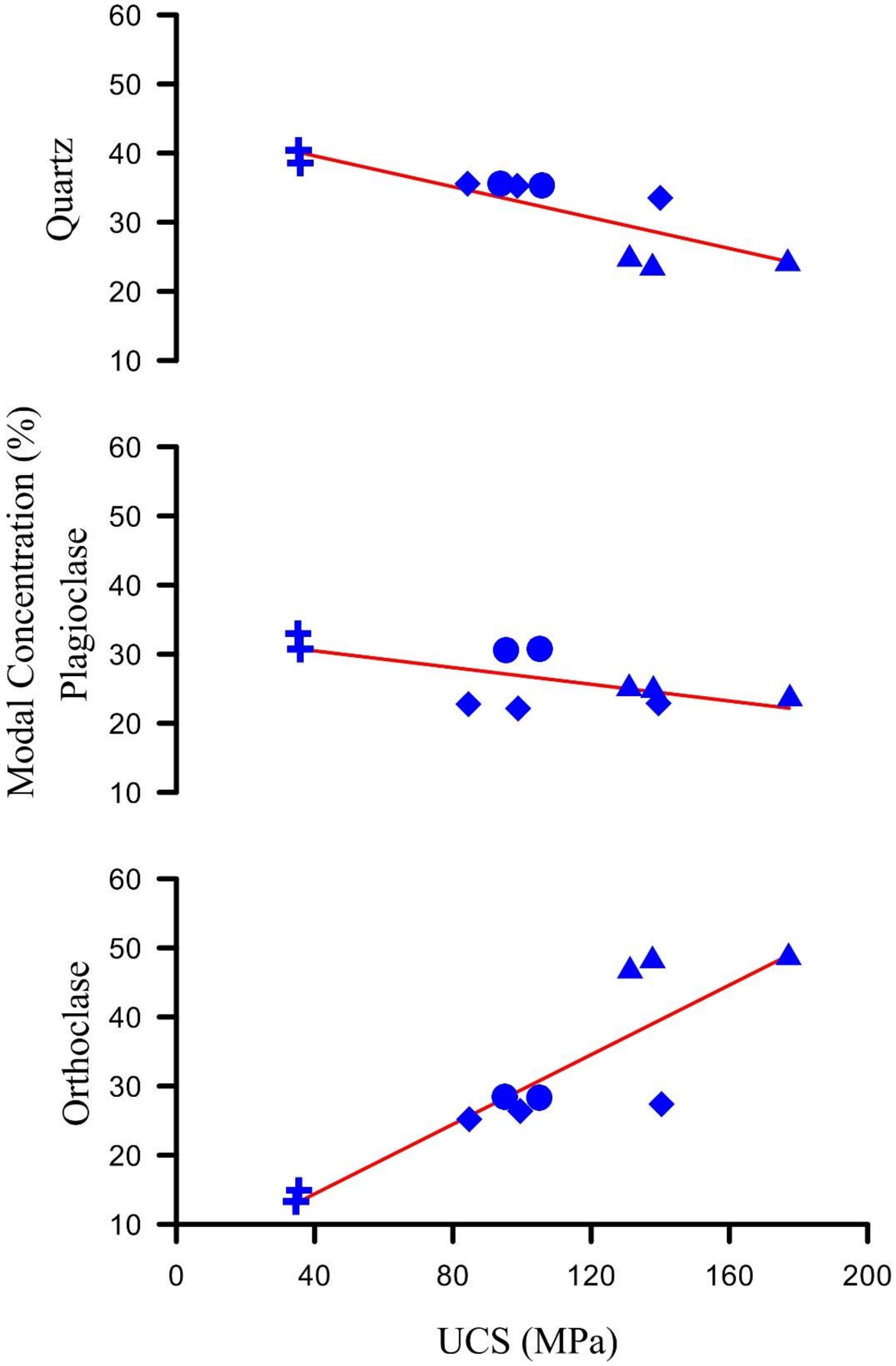

Fig. 7.10. Relationship of modal abundance of quartz, K-feldspar and plagioclase with UCS. Symbols are same as in Fig. 7.6.

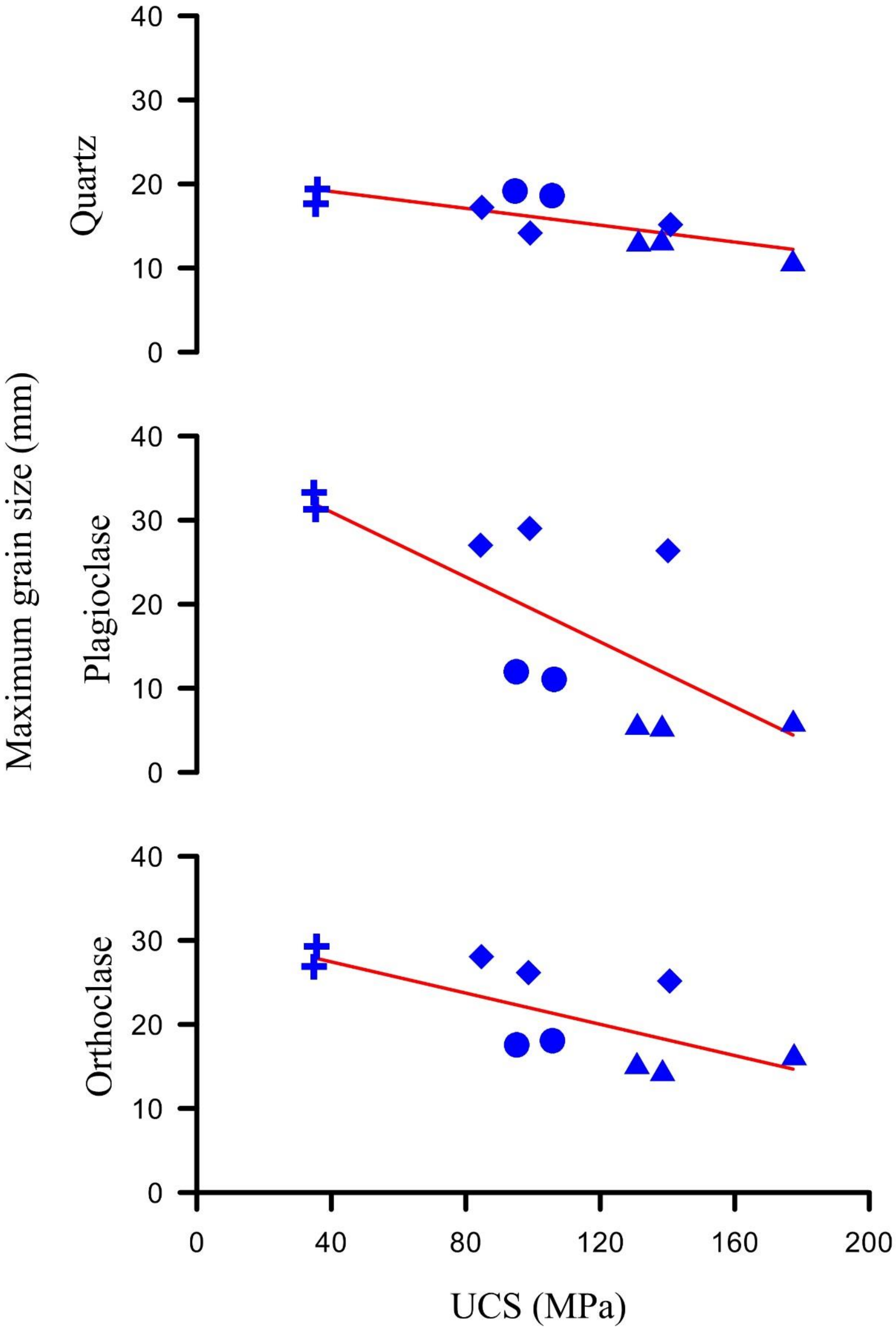

Fig. 7.11. Relationship of maximum grain size of quartz, K-feldspar and plagioclase with UCS. Symbols are same as in Fig. 7.6.

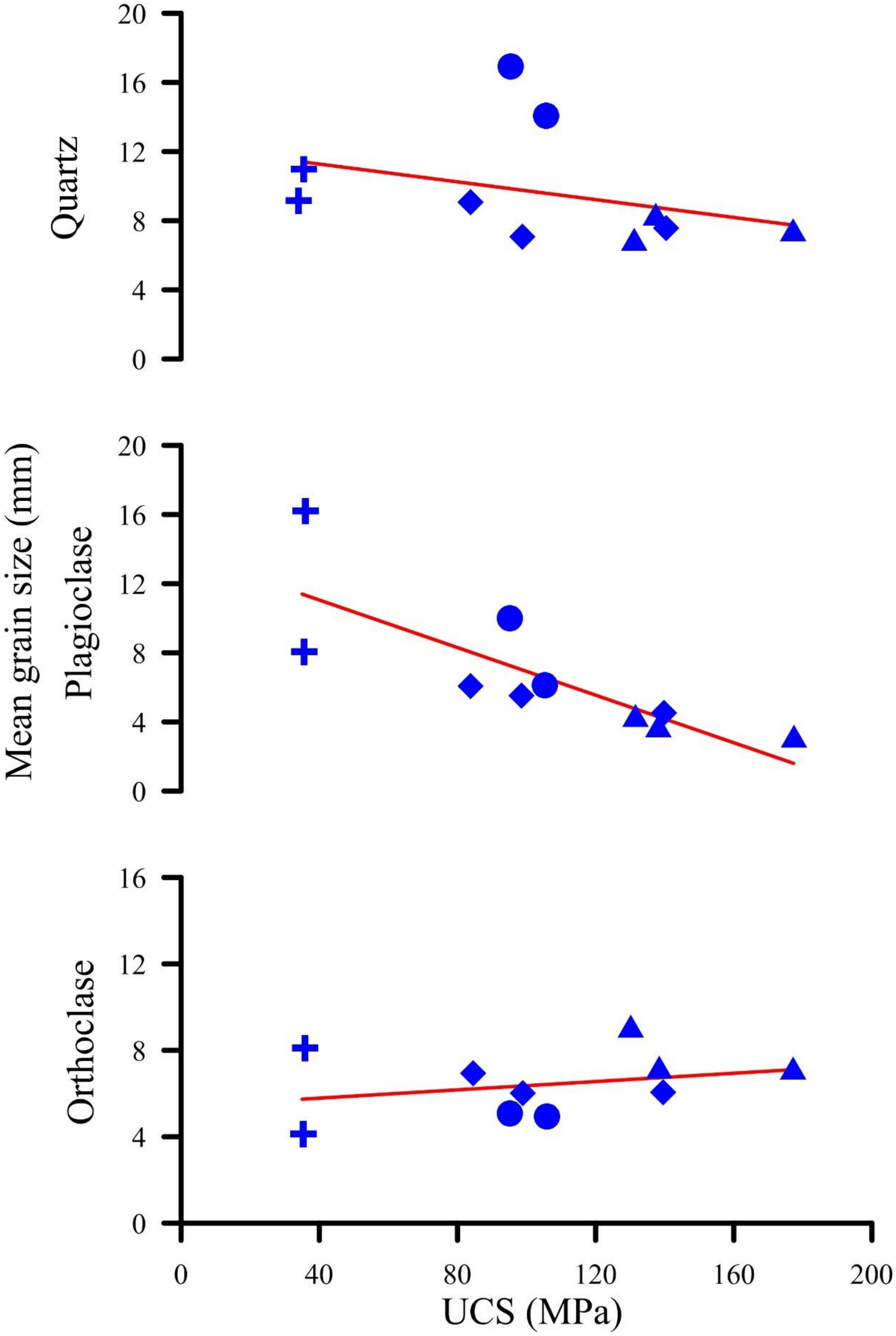

Fig. 7.12. Relationship of mean grain size of quartz, K-feldspar and plagioclase with UCS. Symbols are same as in Fig. 7.6.

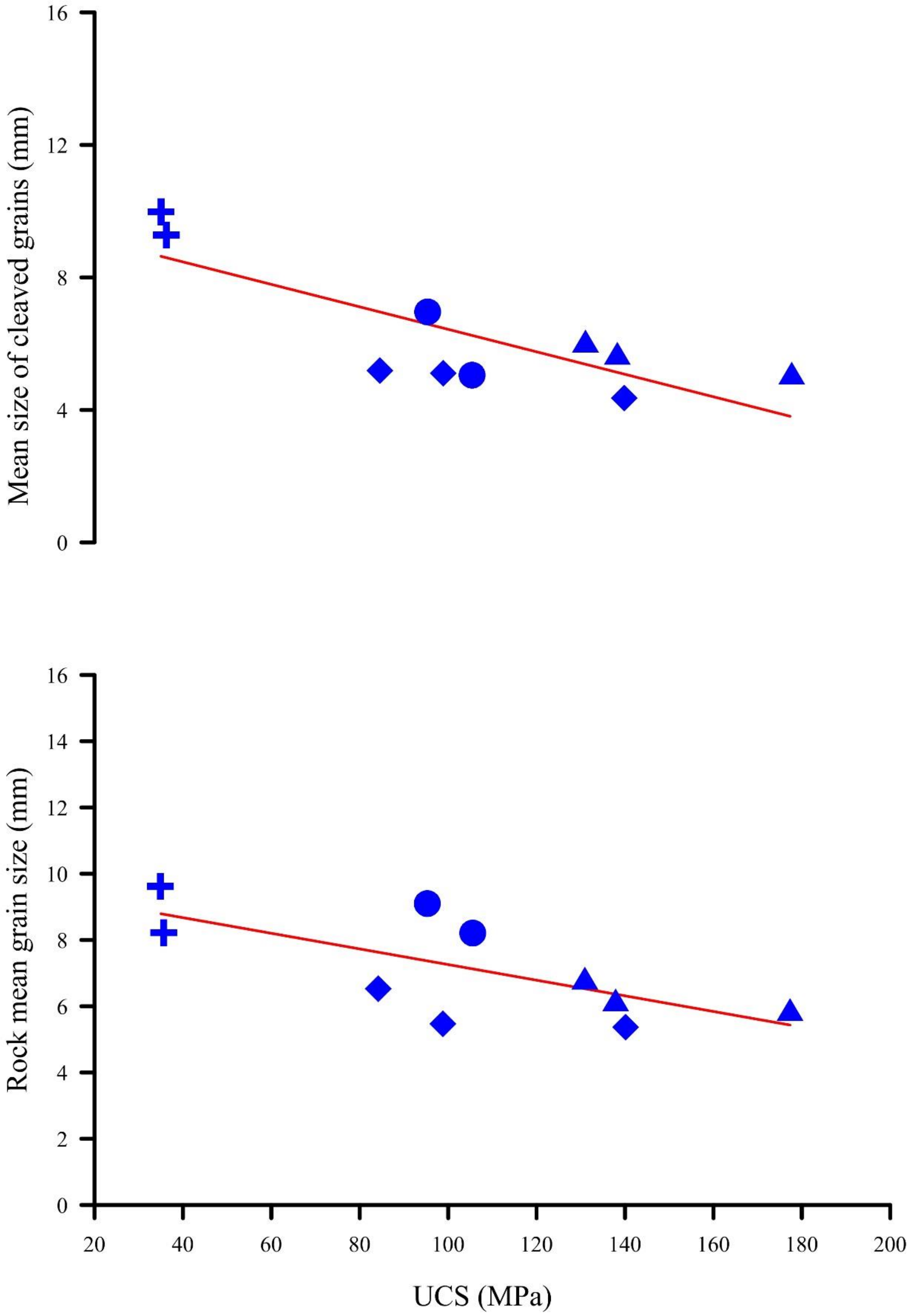

Fig. 7.13. UCS against mean grain size of rock and mean grain size of cleaved minerals. Symbols are same as in Fig. 7.6.

Fujii et al. (2007) presented the characteristics of fracture surfaces produced during the tensile strength tests of granite from Japan. According to the authors, pre-existing weak zones and preferred orientation are the most likely areas for fracture dissemination. The appearance and scatter of newly formed fractures and its relation to minerals and mineral boundaries via petrographic observation of post-failure samples (previously subjected to uniaxial loading conditions) are presented in Figure 7.14. As feldspars in MG are mostly altered, they are more susceptible to propagation of new fractures. An example is presented in Figure (7.14A) which displays propagation of fractures along the altered zones of an orthoclase mega-cryst. Systematic exsolution can also be targeted for fracturing during compressional loading conditions, as shown in Figure (7.14B), where K-feldspar develops fractures along the albite exsolution lamellae. Figure (7.14C) presents a K-feldspar megacryst, where newly formed fractures connect various altered zones across the cleavage planes. Similar observations about the fracture propagation and its relation to alteration zones and cleavage planes has been described in Rigopoulos et al. (2013) for diorite and troctolite rock types from ophiolites in Greece. They observed random failure in plagioclase from diorites because of higher degree of alteration while microcraks in fresh plagioclase from troctolite are formed parallel to cleavage planes. It can also be interpreted from this observation that alteration zones can provide more likely areas for fracture initiation relative to pre-existing discontinuities in the form of cleavages in minerals but direction of the applied stress can be a limiting or controlling factor.

Sousa (2014) investigated the petrographic features, modal mineralogy and physico-mechanical properties of different Portuguese granites used as dimension stones. The encouraging and better mechanical behaviour is shown by granites having lower porosity and lesser deformational features for their used as dimension stone. Similar results are obtained for the granites from the present study i.e. samples of MG exhibit significantly higher void spaces and lower strength values (Fig. 7.5; Table 7.1 and 7.4) as compared to other granites (AG, SG and UG) where the voids percentage is considerably lower.

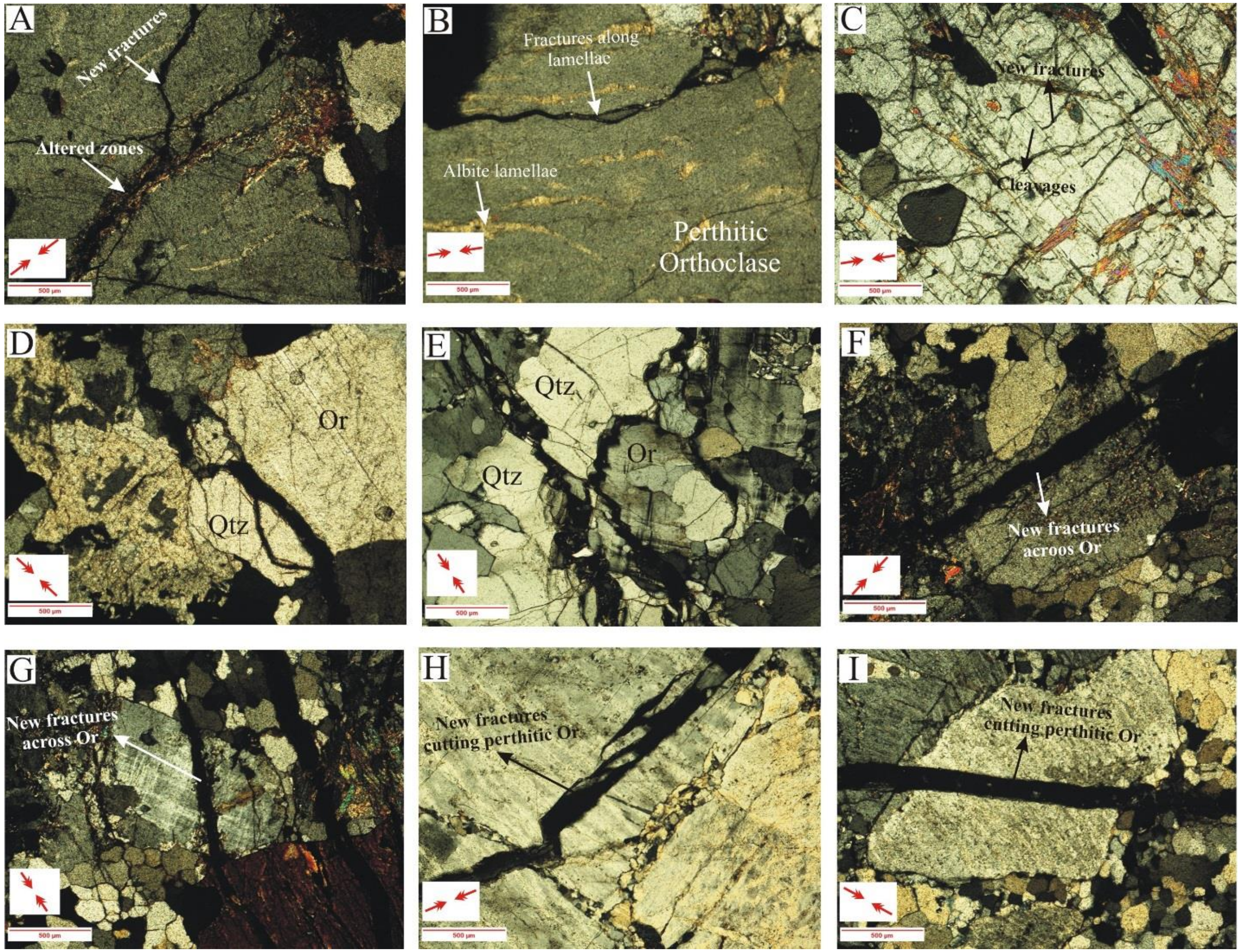

Fig. 7.14. Post-test micrographs illustrating A) fracture propagation along the altered zones of K-feldspar, B) fracture development along exsolution lamellae, C) fracturing of mineral across the cleavages connecting the altered zones, D-E) fracture spread along the grain boundaries, F-I) fracturing of minerals across the mineral grain. Arrows point towards the direction of compressional stress during strength tests.

The fracturing behaviour of four different granites types during different cycles of freeze-thaw tests was presented in Freire-Lista et al. (2015). They described the development of different types of fractures during different series of tests. Inter-crystalline fractures were developed during the initial series of testing followed by intra-crystalline fractures in later tests. Quartz and feldspars are the common minerals associated with these fractures. It shows that inter-crystalline fracturing is most likely to occur during compressional conditions; however, grain size seems to be the limitation to this observation as inequigranular rocks are less likely to develop the inter-crystalline fracturing. The presence of fresh cracks along grain boundaries in the failed coarse grained SG sample is clearly demonstrated in Figure 7.14 (D-E). In contrast, crack propagation in the AG and UG samples is mostly across the mineral grain rather than along grain boundaries (Fig. 7.14F-I). This indicates greater resistance shown by grain boundary recrystallization marked by the presence of fresh fine grained quartz grains to compression which ultimately increases the strength of these granites.

As a general observation from thin sections, hand specimen and data presented in Table 7.2, all studied granites are categorised as coarse grained granites; however, their grain size distribution varies. SG and AG are equigranular, although grain boundary recrystallization in the form of fine grained fresh quartz in AG makes it distinct from SG (Fig. 7.4). MG and UG are inequigranular with evident mega-crystic nature (Fig. 7.2 and 7.4). Equigranular rocks tend to be weaker in comparison to rock with a greater distribution in grain size (Raisanen, 2004; Lindqvist et al., 2007). The lower strength of SG than UG would support this observation. However, despite the inequigranular nature, the lower UCS of MG than SG would suggest that the higher degree of alteration has a significant influence on the strength characteristics of samples tested.

Fractures tend to propagate more easily in rocks with larger grain boundaries and fine-grained rocks are regarded as stronger than coarse grained rocks. Results from the present study (Table 7.4) for MG, SG and UG further support this observation. In spite of its coarser grain size, AG is stronger than UG. However, this can be explained using the post-test petrographic observation that intense grain boundary recrystallization in AG has a significant influence on the strength of the granite.

The reliance of mechanical behaviour on textural characteristics has also been described for other rock types apart from granites. Rigopoulos et al. (2010), for example, described the negative effect of the alteration on the mechanical behaviour of dolerites from northern Greece. Secondary minerals e.g. chlorite, formed as a result of alteration can contribute towards higher water absorption and porosity values and hence decrease the strength of dolerites. Diamantis et al. (2014) described the mineralogical control of ultrabasic rocks (peridotites and serpentinites) from central Greece on its mechanical behaviour. The degree of serpentinization has pronounced negative effect on strength and elastic moduli of ultrabasic rocks. Similar observations were made for the Callovo-Oxfordian argillite by Hu et al. (2014) where they observed a negative effect on elastic moduli with increasing clay and water content. Sajid et al. (2009) compared the strength of gabbronorite and amphibolites from northern Pakistan on textural grounds. Amphibolites yielded higher strength than gabbronorites due to a finer grain size and inequigranular nature. All these studies indicate that mineralogical and textural changes due to weathering/ alteration process and increase in the porosity have pronounce negative effect on the mechanical behaviour of rocks irrespective of its composition. Current observations and previous work on granites and other rock types highlight the importance of textural parameters in relation to their mechanical and engineering properties.

7.8. Conclusions

The relationship between textural features and variation in strength of granites has been investigated for four different granites from northern Pakistan. Three of the studied granites (AG, UG and SG) are associated with alteration Grade-II, while MG is more altered and representative of Grade-III. A series of petrographic, mineralogical and strength tests, together with statistical analyses demonstrate that textural characteristics have a dominant effect on changing the mechanical behaviour of granites. The main conclusions can be summarized as:

1. The mean grain size of feldspars, mean size of main rock forming minerals and mean size of cleaved minerals have a significant negative effect on UCS, UTS, ultrasonic velocity and Schmidt hardness of granites. The results confirm similar interpretations of Gunes-Yilmaz et al. (2011) for granites from various other parts of the world. This study suggests a negative correlation between

concentrations of quartz and UCS, which is in direct contrast with the studies conducted on granitic rocks from Turkey (Tugrul and Zarif, 1999). Textural relations of quartz with other minerals would appear more important than concentration alone.

2. From petrographic analysis of failed samples that had previously been subjected to uniaxial loading, fractures generally propagate through connecting grain boundaries in coarse grained rock (e.g. SG). However, recrystallization of minerals along boundaries can have a pronounced positive effect on the strength of granites (e.g. AG).
3. Alteration of granites has a controlling influence on their strength and engineering behaviour. However, textural characteristics have a significant impact on the observed variation in strength for granites with similar alteration grade. Despite the considerable variation in grain size MG yields a low strength due to its higher degree of alteration. The observed variation in strength of UG, SG and AG, with similar alteration grade, can be attributed to differences in their textural characteristics.
4. The petrological features such as exsolution in mineral phases can be potential sources for preferential fracture propagation during compressional loading conditions (Fig. 7.14B). Altered areas of minerals can also provide preferential locations for fracture initiation/propagation when compared with already present weaker zones in the form of cleavage planes in minerals.

CHAPTER 8

Discussion

The project aimed to describe the origin and tectonic relationships of early Paleozoic peraluminous granites and rift related Permian dykes in northern Indian plate, NW Pakistan with other pertinent rock suites from Himalayan and northern Gondwana regions. The extensive mineralogical, geochemical (Chapter 4 and 5) and geochronological (Chapter 6) data has been generated to investigate their petrogenetic and regional tectonic implications. In addition, the relatively new approach has been adopted of using the petrologically important textural features of granites to address the change in their mechanical properties (Chapter 7).

8.1. The Utla granites

8.1.1. Research Outcomes and Evaluation

Detailed mineralogy and geochemistry divide the granitic rocks from Utla area into megacrystic unit (MPG) forming the bulk of magmatic body and intruding aplite dykes (AMG). Tourmaline bearing cross cutting quartz rich veins are also present. MPG is regarded as two mica granite which also contains minor amount of tourmaline, apatite and zircon. The composition of biotite changes from magnesium siderophyllite in MPG to siderophyllite in AMG (Fig. 4.4) which represent decrease in Mg, Fe and Ti via fractionation during evolution of melt. Similar effect on mica composition due to fractional crystallization is noticed in peraluminous granites from Cornubian batholith (Simons et al., 2016). The differentiation trend in Utla granitoids is supported by major and trace element whole rock geochemistry (Fig. 4.11) and changes in composition of other mineral phases e.g. plagioclase. The gradual decrease of An content from core to margin in zoned plagioclase megacryst is noticed (Appendix-1). The drastic drop is An content of plagioclase from MPG to AMG further support the fractionation of melt during evolutionary process of Utla granitoids.

The studied granitoids also show the evidences of post-crystallization alteration by residual hydrothermal fluids. These include differences in the tourmaline composition, replacement textures in tourmaline nodules (Fig. 4.2F) and secondary growth of garnet (Fig. 4.6). Different tourmaline modes have been recognized in Utla granitoids (chapter 4 discussion). Tourmaline rich veins cross cutting both MPG and AMG (Fig. 4.2E) show their derivation from evolved residual magmatic fluids due to their similar Fe^{2+}/Mg ratio and higher silica content from tourmaline in MPG groundmass (Fig. 4.9). The nodular tourmaline seems to have crystallized from B-rich residual fluids derived from same magmatic system due to their analogous composition to other magmatic tourmaline and absence of any channel (e.g. fractures, veins) connecting them to any external source (Sinclair and Richardson, 1992; Trumbull et al., 2008; Drivenes et al., 2015). The QRV tourmalines have markedly different composition (foitite) (Fig. 4.8) from other tourmaline which most likely represent their crystallization from melt arising from external source. The systematic difference of $[Fe^{2+}/(Fe^{2+}+Mg)]$ is observed in different tourmaline modes. It gradually increases from MPG tourmaline to late stage tourmaline (i.e. tourmaline nodules and QRV tourmaline) (Fig. 4.9). Similar variation is also observed in different tourmaline generations from San Rafael Sn-related granitoids (Mlynarcz and Williams, 2006). In addition, they also noticed the parallel behaviour of Sn to Fe in tourmaline. Ore bearing granites have tourmaline with elevated Fe and Sn concentration whereas barren granites contain tourmaline with higher Mg content (Mlynarczyk and Williams, 2006). Tin has not been analysed in tourmaline during current investigation, however, trace element analysis of a sample from tourmaline rich veins show elevated Sn concentration in comparison to rest of the granitoids (Appendix 2) which might indicate the higher concentration of Sn hosted in vein tourmalines. Variation of Fe in tourmaline is also related to the proximity of source of mineralizing fluid in granite related Sn-W deposits from different localities including New Zealand, South Africa and Namibia (Pirajno and Smithies, 1992).

Garnet can occur as magmatic mineral in granite (du Bray, 1988; Dahlquist et al., 2007; René and Stelling, 2007) or as xenocrystic mineral derived from source rock (Jung and Mezger, 2001; Lackey et al., 2011). Garnet-bearing magmas are peraluminous and produced by the melting of metasedimentary protolith (Vielzeuf and Montel, 1994; Patino Douce and Beard, 1995). Several approaches have been used to describe the magmatic nature of garnet e.g. major element zoning (e.g. Dahlquist et al., 2007; Yang et al., 2013), trace element pattern and oxygen isotopes (e.g. Taylor and Stevens, 2010; Lackey et al., 2011; Xu et al., 2013). Spessartine and almandine are the dominant constituents of magmatic garnets in peraluminous granites with lesser abundance of other members (Miller and Stoddard, 1981; du Bray, 1988). The magmatic garnets in peraluminous granitic rocks have characteristic “inverse bell-shaped profile" spessartine zoning (du Bray, 1988; Dahlquist et al., 2007). Zoned grains with higher Sp content in core surrounded by Gr rich margin has been recognized in Utla granitoids (Fig. 4.6). The large variance in composition of rim from core suggest growth of outer garnet over already present garnet. The core composition is interpreted to be magmatic in origin due to inverse bell-shaped Sp profile and significantly high Sp content than margin (Fig. 4.6) (Dahlquist et al., 2007). The compositional difference from garnets in host metasedimentary rocks exclude their possibility to be xenocrystic (Appendix 1). The Gr-rich garnet is most likely to be secondary in origin formed due to hydrothermal process due to their crystallization along fractures in magmatic garnet (Fig. 4.6).

The Utla granitoids exhibit strongly peraluminous and sub-alkaline character (Fig. 4.10). Their fractionated nature is shown by strong negative Ba, Sr, Nb, Eu and Ti anomalies (Fig. 4.12). The samples from Mansehra granites also exhibit similar geochemical behaviour to Utla granitoids showing their comagmatic nature (Chapter 4). The origin of strongly peraluminous granites is related to different petrogenetic models including melting of meta-sedimentary (meta-pelite or meta-greywacke) source (Petford and Atherton, 1996; Springer and Seck, 1997; Sylvester, 1998) and lesser melting fractions of meta-aluminous meta-igneous source e.g. amphibolite or orthogneiss (Beard et al., 1993; Patino Douce and Beard, 1995; Springer and Seck, 1997). The molar $Al_2O_3/(MgO + FeO_T)$ vs molar $CaO/(MgO + FeO_T)$ (Fig. 4.13) confirms the meta-sedimentary protolith for the Utla and Mansehra granitoids. Moreover, their affinity towards a meta-pelite source is shown by lower CaO/Na_2O (<0.3) and Rb/Sr vs Rb/Ba plot (Fig. 4.13). REE modelling represent 30% partial melting of similar source rock i.e. metapelite for the generation of melt having approximate composition to MPG (Fig. 4.14). The modelling further suggests the evolution of MPG to AMG via fractionation of mineral assemblage containing feldspars, biotite, muscovite, apatite, garnet, ilmenite and zircon from the melt. The negative trend of MgO, CaO, Al_2O_3 and Fe_2O_3 against silica also support the fractionation of plagioclase, orthoclase, biotite and garnet (Fig. 4.11). The evolved nature of AMG is also favoured by their higher silica content and change in plagioclase composition. The U-Pb zircon systematics show the emplacement of MPG in 475.7 ± 4.5 Ma followed by intrusion of AMG in 471.3 ± 2.6 Ma. The Mansehra granite, towards the eastern extremity of Utla, yielded 479.5 ± 6.4 Ma which indicate their coeval magmatism.

The emplacement of peraluminous granitic suites around the Cambrian-Ordovician period is one of the most widespread event in the northern end of Gondwana (LeFort et al., 1986). In the Himalayan terrane, this event is marked by the exposures of independent granitic plutons with similar chemical properties that extend from Nepal in the east towards NW Pakistan in the west (LeFort et al., 1986; Miller et al., 2001; Wang et al., 2013). Similar aged granites are also found in Baoshan and Shan-Thai block in SW China, associated with parallel magmatic event (Dong et al., 2013; Wang et al., 2013). These early Paleozoic plutons share common petrographical (e.g. megacrystic) and geochemical (e.g. peraluminous) characteristics (Girard and Bussy, 1999; Kwatra et al., 1999; Dong et al., 2013; Wang et al., 2013) and have been deformed during the Himalayan orogenic episodes (Miller et al., 2001). The corresponding data of representative plutons from different region of northern India (Tso Morari and Mandi) and SW China (Baoshan and Shan-Thai) is presented in certain plots for comparison (Fig. 4.10, 4.13). The parallel mineralogical and geochemical details (Fig. 4.10), analogous age range, similar tectonic position and host rock characteristics (Fig. 4.13) of the Utla and Mansehra granites reveal their coeval origin to the other Cambro-Ordovician granites from northern Gondwana.

8.1.2. Tectono-magmatic Implications

The major research focus in the Himalayas is towards the Cenozoic uplift and related tectonism, metamorphism and magmatism, since the pre-Himalayan events are mostly veiled by extreme Tertiary tectonism. However, recent research has highlighted the magmatism related to widespread tectonothermal activity during early Paleozoic in the Himalayan terranes and other regions of northern Gondwana (Fig. 8.1). The Himalayas was part of the northern Gondwana supercontinent during late Precambrian and Paleozoic time and constituted the Indian passive continental margin prior to collision with Eurasian continent in early Cenozoic (Brookfield, 1993; Cawood et al., 2007; Wang et al., 2013). The large volume of Cambro-Ordovician (~530-470 Ma) granitoids intruding in LHS and GHS (DeCelles et al., 1998, 2000, 2004; Godin et al., 2001; Gehrels et al., 2003; Booth et al., 2004; Lee and Whitehouse, 2007; Quigley et al., 2008) indicate an early Paleozoic orogenic event in Himalayan terrane.

8.1.2.1. Evidence of early Paleozoic orogenesis

The existence of this orogeny is supported by break in the stratigraphic records (Garzanti et al., 1986; Le Fort et al., 1994; Valdiya, 1995; Liu et al., 2002; Zhou et al., 2004), detrital zircon chronology from sedimentary strata (Hodges, 2000; Kusky et al., 2003; Zhang et al., 2008a, b; Dong et al., 2009; Myrow et al., 2010; Spencer et al., 2012) and coeval metamorphism (e.g. Argles et al., 1999; Catlos et al., 2000, 2002; Foster, 2000; Godin et al., 2001; Gehrels et al., 2003, 2006a, 2006b; Kohn et al., 2004) across wide areas of the Himalayas.

The unconformable contact marked by conglomeratic beds between the Cambro-Ordovician strata with older rocks in Himalayan terrane is the evidence of erosion and uplift associated with orogenic event during early Paleozoic (e.g. Garzanti et al., 1986; Brookfield, 1993). The lower Ordovician basal conglomerate unconformably overly the Cambrian strata in Kathmandu, Nepal (Kumar et al., 1978; Funakawa, 2001; Gehrels et al., 2003). Similarly in Spiti and Zanskar region of NW India, the Cambrian lithologies are unconformably overlain by coarse Ordovician conglomerates (Hughes, 2002; Myrow et al., 2006a, b). The U-Pb chronology and Hf isotopes of detrital zircons from sedimentary strata led Spencer et al. (2011, 2012) to propose that sediment input in GHS was prompted during orogenic event in early Paleozoic. Similar interpretation was also made by the comparison of U-Pb age of detrital zircons representing particular time span from the broad geographic range covering around 2000km along the length of Himalayan orogen from Pakistan to Bhutan (Myrow et al., 2010). Early Paleozoic deformation and metamorphic evidences include regional folding and metamorphism (up to garnet grade) of Neoproterozoic Bhimphedi group rocks prior to the deposition of overlying Ordovician strata (Gehrels et al., 2006a). All these indications show the early Paleozoic orogenesis in northern Gondwana extending from NW India to Namche Barwa region in southern China at least (Wang et al., 2013).

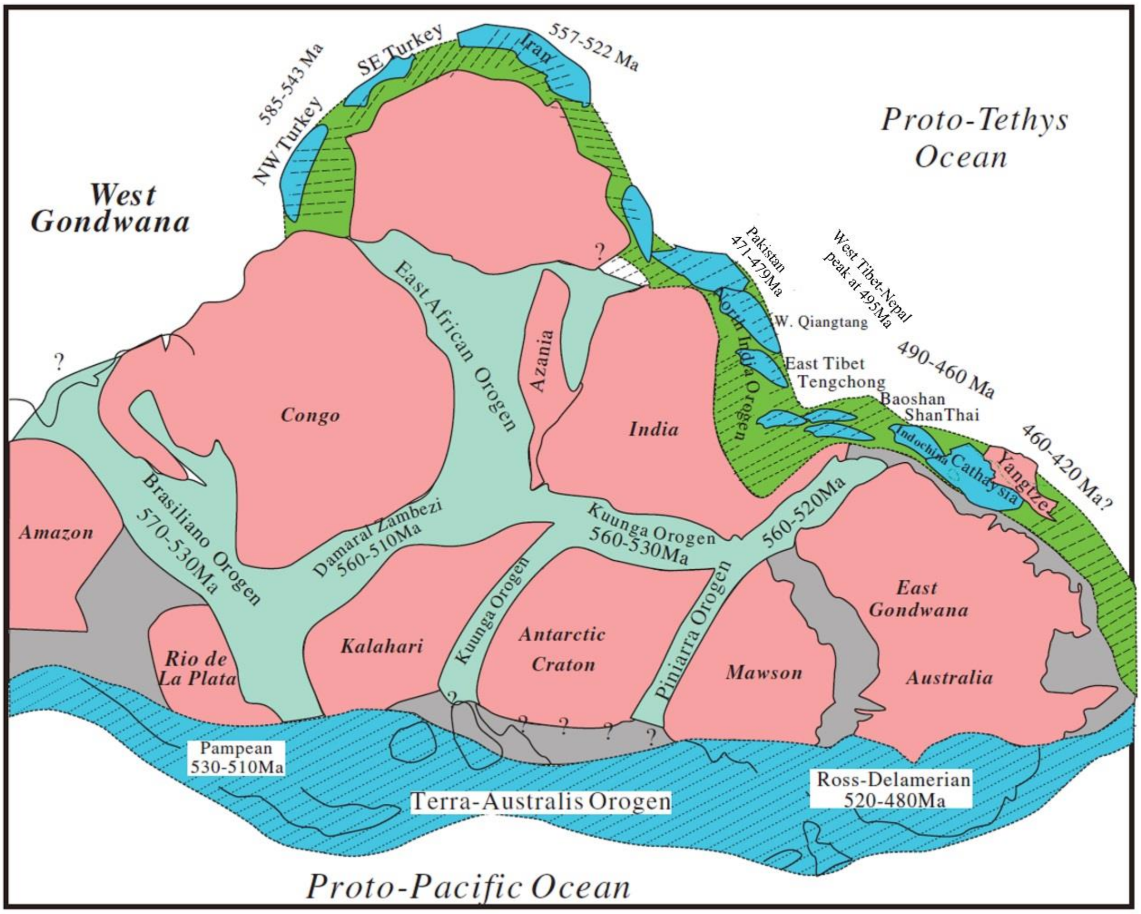

Fig. 8.1. Location of major orogens in early Paleozoic reconstruction map of Gondwana supercontinent (modified after Cawood et al., 2007; Wang et al., 2010, 2013). North Indian orogeny (Bhimphedian) is shown by several granitic plutons having similar age range. Paleogeographic locations of outboard microcontinents is shown along the Prototethyan margin.

The early Paleozoic stratigraphy of eastern Peshawar basin in NW Pakistan is summarized (Fig. 8.2). The Precambrian Tanawal Formation is unconformably overlain by Cambrian Ambar Formation. The contact is marked by angular pebble conglomerate containing quartzite clasts from Tanawal Formation (Pogue et al., 1992; 1999). In certain regions i.e. northern Swabi closer to Utla area, Ambar Formation is completely eroded and Tanawal Formation is directly overlain by Ordovician Misri Banda Quartzites (Pogue et al., 1999). Abbottabad formation is lateral equivalent of Ambar formation in Hazara region towards east of the Indus river (Fig. 4.1). The unconformable contact between Abbottabad and Tanawal Formation is noticed, however, in certain regions, Tanawal Formation is eroded and Abbottabad Formation directly overlain the Precambrian Hazara Formation through an angular unconformity marked by conglomeratic bed containing angular clasts (Calkins et al., 1975; Baig et al., 1988; Pogue et al., 1999). The growth of new metamorphic mica and evident cleavage has been noticed in the Hazara Formation which is metamorphosed up to the greenschist facies (Baig et al., 1988). No evidence of deformation and metamorphism is observed in conglomeratic bed marking the unconformity and above lying Abbottabad Formation. These indications show a tectonothermal orogenic event during the early Paleozoic times which have deformed and metamorphosed the Precambrian strata. The intrusion of early peraluminous Utla and Mansehra granites (475.7 ± 4.5 Ma and 479.5 ± 6.4 Ma respectively) in this region support the existence of this event.

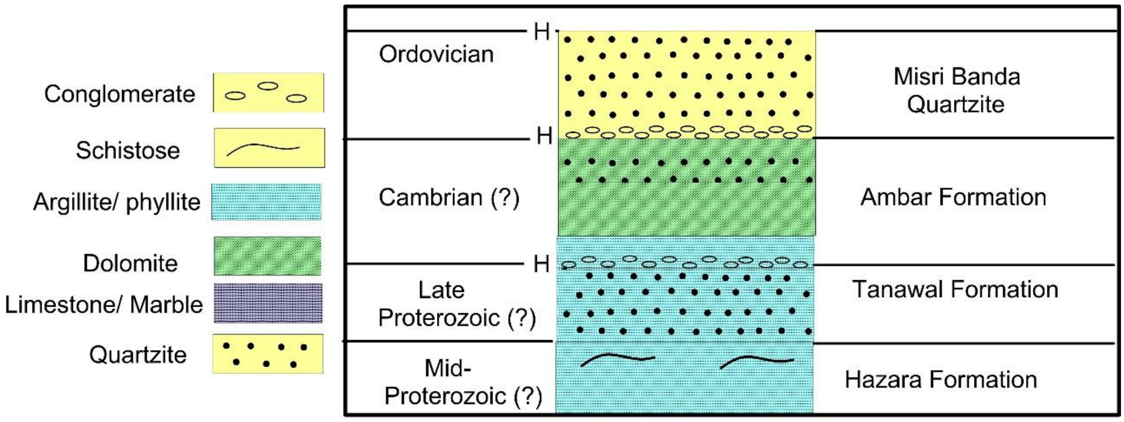

Figure 8.2. Precambrian and early Paleozoic stratigraphy of Peshawar basin after Pogue et al. (1992b; 1999). H = Major Hiatus.

8.1.2.2. Tectonic model

The emplacement of the peraluminous Utla and Mansehra granites occurs between 470 and 480 Ma on the basis of U-Pb zircon radiometric dating (Fig. 6.6, 6.17). Similar aged rocks are also present in other Himalayan regions including NW India (e.g. Miller et al., 2001) and Nepal (e.g. Gehrels et al., 2006a). Similar tectonic position, age range, geochemistry and earlier mentioned indications of orogenesis suggest an early Paleozoic magmatism resulting in the formation of these granitoids. The magmatism is the result of collision of northern margin of Gondwana continents with southward subducted oceanic lithosphere of proto-Tethys (Cawood et al., 2007; Dong et al., 2013).

However, such large scale crustal anatexis, causing magmatism along broader traverse (around 700 km, Cawood et al., 2007) of Himalayan orogen, cannot be the effect of simple magmatic arc. It suggests a large back-arc region with high amount of heat flow inducing crustal melting. The evidence of coeval mafic magmatism is highlighted in certain investigations (e.g. Miller et al., 2001). The Mandi mafic rocks in GHS of NW India yielded 496 ± 14 Ma age and exhibit convergent margin geochemical signature (Miller et al., 2001). The cumulated gabbros (473 ± 3.8 Ma) from Baoshan block (Wang et al., 2012) and associated synchronous I-type granites are believed to be the product of subduction of Prototethyan Ocean (e.g. Zhang et al., 2008; Liu et al., 2009; Zhu et al., 2012). The similar aged basic magmatism in the region indicates the heat input, from the mafic magma underplating the lower crust, might be responsible for the large scale anatexis.

The integration of current geochemical and geochronological data with existing data set indicate the convergent margin setting of northern Indian plate triggered Bhimphedian orogenic event (Cawood et al., 2007) during early Paleozoic. The Prototethyan oceanic crust is subducted beneath the northern Gondwana (Fig. 8.3) which produced the extended back-arc basin due to roll-back of subducted plate (Wang et al., 2013). The sediment accumulation is hosted by the back-arc basin (Fig. 8.3). The orogenesis is either related to ongoing subducted plate or accretion of an isolated block with continental margin (Fig. 8.3). Different terranes or geological blocks including Lhasa, Qiantang and Helmand along the Indian plate margin were recognized during the reconstruction of northern Gondwana in early Paleozoic (Sengor et al., 1988; Metcalfe, 1996). Detrital zircon ages of early Paleozoic strata from western Qiangtang also indicate its juxtaposition to Himalayan terrane in early Paleozoic (Zhu et al., 2013). The vicinity of these block to Indian plate is also shown by convincing paleoclimatic and palaeontological records presented in Metcalfe (1996). The peraluminous signature of most of granitic plutons in the northern Indian plate (e.g. Girard and Bussy, 1999; Miller et al., 2001; Wang et al., 2013; current study) support the accretion of outboard block with continental margin that induces the significant crustal and sediment thickness in back arc basin, which along with the mafic underplating, is responsible for crustal melting and generation of granitic melt. The prime factor for generating the peraluminous S-type granite is the melting of meta-sedimentary source most likely due to deep burial caused by continent-continent collision (Harris et al., 1986; Tingyu et al., 1995). The collision of outboard block with continental margin provide similar environment that led to the formation of peraluminous melt (Fig. 8.3).

However, the partial melting and roll back of subducted oceanic lithosphere also cause mantle convection which result in the formation of coeval calc-alkaline volcanic rocks (Miller et al., 2001; Visona et al., 2010). The existence of Cambrian volcanic rocks includes volcanic tuffs, basalts, andesites and felsic volcanic rocks in the western Tethyan Himalaya (e.g., Brookfield, 1993; Garzanti et al., 1986; Valdiya, 1995). The occurrence of an extensive subduction zone magmatism along the Indian margin of Gondwana is shown due to the presence of basalts and basaltic andesites from different regions of GHS including Mandi pluton, western Himalayas (Miller et al., 2001) and Kharta region, central-eastern Himalayas (Visona et al., 2010). Late Cambrian (~492 Ma) bimodal volcanic rocks have been identified in the central Lhasa block which relate to the active continental margin (Ji et al., 2009; Zhu et al., 2012). Subduction related late Cambrian (499.2 ± 2.1 Ma) mafic lavas have also been reported in Gongyanghe Group in Baoshan block (Yang et al., 2012) overlain by lower Ordovician basal conglomerate (Wang, 2000).

The described tectonic model based on novel geochemical and radiometric age data firmly support the concept of Bhimphedian orogeny initiated due to the subduction of Prototethyan oceanic lithosphere beneath the Indian plate margin (Cawood et al., 2007). Due the analogous peraluminous character of the granites (e.g. Girard and Bussy, 1999; Dong et al., 2013; Wang et al., 2013) associated with this tectonic event, the collision of the outboard continental block is emphasized in the proposed model as it supports the tectonic conditions that most likely cause the generation of peraluminous melts (Tingyu et al., 1995). The geochemical data suggest the metapelitic source for generation of the melt while REE modelling implies the melt segregation via muscovite-dominated dehydration melting with certain input of dehydration melting of biotite (Chapter 4). The temperature ranging from 750^{0}C to 800^{0}C is suggested for such melting condition (Le Breton and Thompson, 1988) as further increase in temperature will triggered extensive biotite dehydration melting which yields to segregate granodioritic rather than granitic melt.

The U-Pb geochronology data set revealed the emplacement of majority of granitic plutons during 470-490 Ma span (e.g. Debon et al., 1981; Trivedi et al., 1986;

Girard and Bussy, 1999; Gehrels et al., 2006a) which marks the active span for crustal melting and granitic magmatism. However, relatively few ages have been reported between 500-530 Ma (e.g. Lee et al., 2004, 2006) which most probably indicate the initial stage of tectonic evolution (Cawood et al., 2007). The petrological data of studied granites in combination with presented model, the Andean type orogeny along the northern of Gondwana supercontinent is proposed in early Paleozoic.

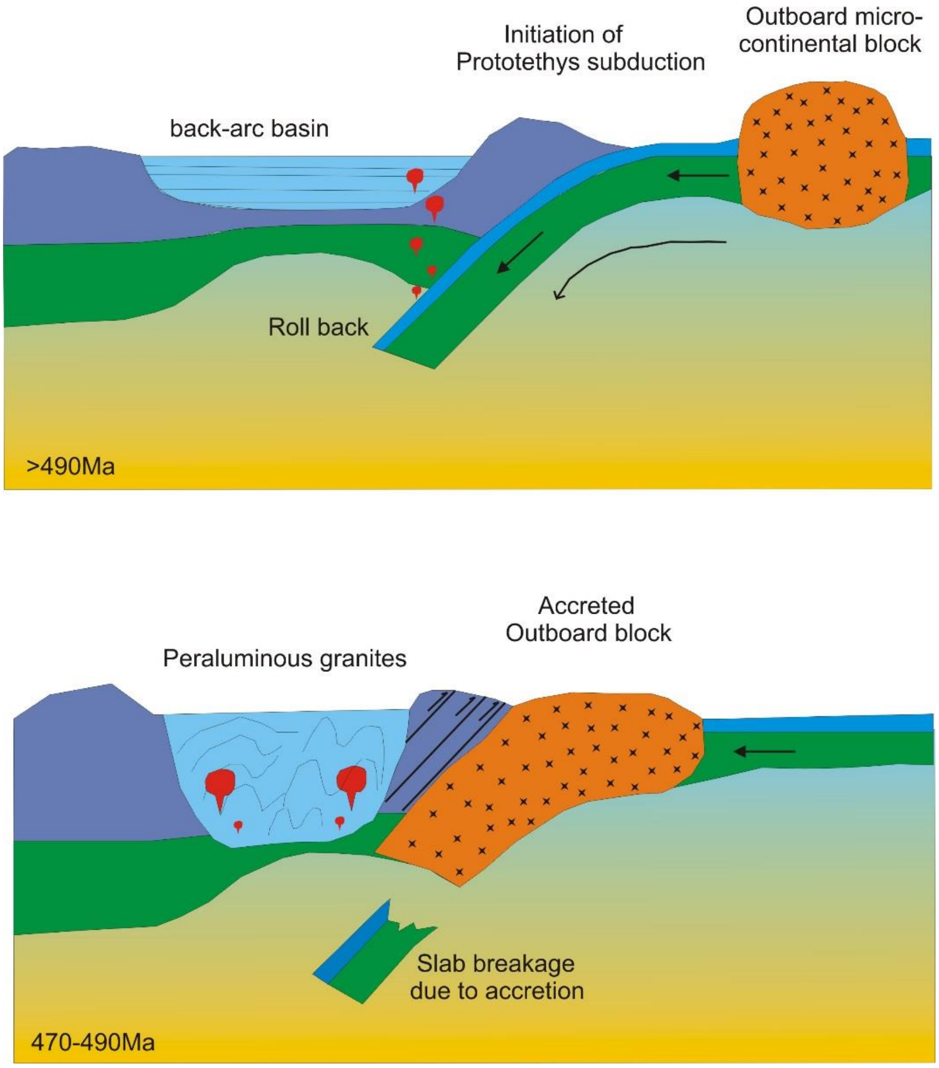

Figure 8.3. Sketch showing the tectonic model of early Paleozoic orogenesis, A) subduction of Prototethyan oceanic lithosphere beneath northern margin of Indian plate (Cawood et al., 2007). Initiation of extended back-arc basin due to mantle convection and slab bending for sediment accumulation. Mafic and calc-alkaline subduction related magmatism also initiate with slab bending (Garzanti et al., 1986; Miller et al., 2001; Visona et al., 2010), (B) Collision of external geological block with continental margin resulting in crustal thickening along with mafic underplating cause partial melting of lower crust to generate peraluminous melt.

8.1.2.3. Other Tectonic models

On the basis of available Rb-Sr and K-Ar ages of rock suites in Africa, Kennedy (1964) for the first time introduced the concept of Pan-African orogeny. This includes thermo-tectonic events during which several mobile belts formed surrounding the older cratons around 500 Ma. This concept was extended to all the regions in Gondwana continents which also include the Indian plate. The western end of Indian plate was attached to present day Somalia and Kenya with Madagascar in between (Smith et al., 1981; Dalziel, 1992; Unrug, 1996). The existence of analogous geological features confirms the Pan-African events in Madagascar and Southern India which includes the occurrence of major shear zone having >100 km sinistral displacement and analogous podiform chromite deposits in ultramafic lenses (Kroner and Stern, 2004).

However, the nearly similar aged magmatism in northern Indian plate and their relation with the Pan-African is unclear. Girard and Bussy (1999) relate the A-type magmatism in Kaghan Granite (Pakistan) and Rupshu Granite (Ladakh, India) with the youngest A-type activity from Arabian-Nubian shield in Pan-African belt. This comparison seems uncertain due the subtle age differences (Trivedi et al., 1986; Windley et al., 1996) in both events. Kwatra et al. (1999) described the geochemical and geochronological features of early Paleozoic Rakcham granitoids from Sutlej valley in NW India. They include the Cambro-Ordovician granitic suites (including Mansehra Granite) for northern Indian plate in the Pan-African magmatic belt due to similar tectonic settings based to trace element discrimination diagrams.

In contrast, Stern (1994) clearly illustrates that early Paleozoic granites in NW Himalayas post-date the collision and major thermal events of the Pan-African belt. Only southern part of Indian plate is effected by these events as revealed by their paleogeographic reconstruction (Stern, 1994). Furthermore, in most of the Pan-African suites (e.g Mali, southern Brazil) a general magmatic evolutionary trend is observed with subduction related rocks (Bonin et al., 1998). The alkaline magmatism during similar time span also form a common observation in these belts. Although having roughly similar crystallization age of Utla-Mansehra granites (and other Cambro-Ordovician GHS and LHS granites), the convincing evidence for their association with Pan-African event is lacking due to the absence of any evolutionary imprints from mafic magma and lack of synchronous alkaline magmatism.

The early Paleozoic magmatism was related to non-arc extensional settings by Miller et al. (2001). The studied granites fall in the field of syn-collisional to volcanic arc settings on Nb vs Y and Rb vs Y+Nb tectonic discrimination diagrams (Fig. 4.13). Moreover, the granites are depleted in Ba, Nb and Sr but enriched in Rb, Th and U (Fig. 4.12) which is indicative of continental volcanic arc settings (Brown et al., 1984). These geochemical evidences contradict the extensional non-arc settings and favour the magmatic arc environment for the studied granites which is most probably associated with subduction and collision along the northern margin of Gondwana. This interpretation is supported by the widespread existence of volcanic rocks including acid and basic tuffs and andesites in the western Tethyan Himalayas (Garzanti et al., 1986; Valdiya, 1995) and Lhasa terrane (Zhu et al., 2012).

8.2. Basic Dykes

8.2.1. Summary of Research Findings

The basic dykes cross cutting the different pre-Permian rock suites in northern Indian plate, NW Pakistan are divided in to dolerites and amphibolites on the basis of their distinctive field features, mineralogy and geochemistry. Dolerites mainly consist plagioclase and clinopyroxene with lesser concentration of olivine, amphibole and oxide phases. The evidence of fractional crystallization in host melt is indicated by variation in composition of plagioclase and olivine (Appendix 4), Pearce element ratios (Fig. 5.12) and major oxides trends against silica (Fig. 5.9). Their REE concentration is relatively low and show roughly flat chondrite normalized trend (Fig. 5.10). Trace element modelling suggest their derivation via <10% partial melting of spinel lherzolite mantle (Fig. 5.13). Certain degree of crustal contamination of their host melt originated from subcontinental lithospheric mantle is shown by lower Nb/Ta, Nb/La and higher $(Th/Nb)_{PM}$ (Fig. 5.14). The amphibolites are fragile and contain amphibole as a major phase with subordinate amount of plagioclase, titanite and ore minerals. Trace element ratios and REE represent relative deeper mantle source for amphibolite with negligible crustal input (Fig. 5.10, 5.14). Trace element discrimination diagrams suggest within plate tectonic settings from both dyke types (Fig. 5.11).

8.2.2. Tectonic Association of Basic Dykes

The Permian aged rift related magmatism in the Himalayan domains of Pakistan, India and China is widely considered as large igneous province (Chaudry and Ashraf, 1980; Bhat et al., 1981; Vannay and Spring, 1993; Spencer et al., 1995; Garzanti et al., 1999; Ernst and Buchan, 2001; Zhu et al., 2010; Shellnutt et al., 2011, 2012, 2014; Ali et al., 2012; Zhai et al., 2013; Wang et al., 2014). The Panjal Traps (e.g. Papritz and Rey, 1989; Chauvet et al., 2008; Shellnutt et al., 2014), Abor volcanics (Bhat, 1984; Ali et al., 2012) and Qiangtang dykes (Zhu et al., 2013; Xu et al., 2015) are the few examples of early to middle Permian basaltic rocks in the Himalayas which are the result of plate separation and initiation of new oceanic basin i.e. Neotethys (Sengor, 1987; Bhat et al., 1981; Shellnutt et al., 2014). The uncertainty exists whether the regional extensive rock suites are petrogenetically connected or they represent fragmented events as a result of single large scale extensional regime.

The Panjal Traps has been reported widely from northern Pakistan (e.g. Papritz and Rey, 1989; Pogue et al., 1992) and Indian terranes (e.g. Garzanti et al., 1999; Chauvet et al., 2008). The source of Panjal Traps is linked with the deep mantle plume originated within the Qiangtang block causing the plate separation (Chauvet et al., 2008; Zhai et al., 2013). However, Shellnutt et al. (2011, 2014) relate them with partial melting of enriched subcontinental lithospheric mantle. The geochemically similar and synchronous basic magmatism has also been reported in the southern Qiantang regime of Tibet (e.g. Zhai et al., 2013; Zhu et al., 2013). Xu et al. (2015) proposed a tectonic model which describe the origination of Panjal Traps and mafic dykes of Qiangtang, Tibet as single Large Igneous Province (LIP) in around 290 Ma. The analogous geochemical and geochronological results and paleogeographic reconstruction formed the basis of this model. The emplacement of LIP is followed by the breakup of Tibet from Indian plate during the opening of Neotethys. Using the evidence of regular and systematic depositional processes in sedimentary strata, Zhang et al. (2012) propose the separation of the Qiangtang terrane from Indian plate during the Artinskian.

The present investigation shows two texturally, mineralogically and chemically different dykes that intrudes Permian and pre-Permian rocks suites in Peshawar basin and Hazara region in NW Pakistan. The geochemical similarities of these dykes with Permian basalts from other pertinent tectonic regimes (e.g. NW India and Tibet) support their emplacement during Permian. The 284 ± 4 Ma (hornblende) and 262 ± 1 Ma (biotite) $^{39}Ar/^{40}Ar$ age of similar dykes intruding Mansehra granites (Baig, 1990) further confirms their emplacement in Permian. However, the deformed imprint of amphibolites indicate an intense tectonic event that might predates the emplacement of dolerites. The region is mainly effected by regional metamorphism caused by collision of the Indian plate with KIA in Tertiary time (Treloar et al., 1989b; Searle and Treloar, 2010), however, an early Paleozoic pre-Himalayan tectonism has also been identified (e.g. Baig et al., 1988; Gehrels et al., 2006a, b; current study). The deformation of amphibolites due to early Paleozoic event seems unlikely due to the intrusion of both dyke types in early Permian rocks which show their younger emplacement time. Hence, metamorphism of amphibolite is most likely caused by tertiary tectonism which also effect other rock types in the region. The limited distribution of dolerites relative to amphibolites and their restriction to granitic host rocks (chapter 5) indicate the probability of their relict nature that survive during deformation.

8.2.3. Comparison with dykes from other locations

Though both the dyke types belong to similar within plate tectonic setting (5.11), significant geochemical variations have been observed in them which points towards the different depth and composition of the source mantle. The amphibolites are mostly alkaline while dolerites show sub-alkaline character (Fig. 5.8). Different trace element ratios and modelling (e.g. Nb/Ta, La/Sm) show the origination of dolerites from subcontinental lithospheric mantle (SLM). In contrast, amphibolites show relatively deeper asthenospheric source due to their higher Ti, Nb/La, Nb/Y and lower $(Th/Nb)_N$ ratios (Fig. 5.14). The significant crustal input during the evolution of melt parental to dolerites is also observed (Fig. 5.14) which is further supported by the U-Pb geochronological data of zircons recovered from the dolerites (Section 6.4; Fig. 6.15). The age data suggest their derivation from the host rocks of dolerite dykes which strongly advocate the crustal involvement in their parental melt. In contrast, amphibolites lack any contamination cyphers (Fig. 5.14). The Nb/Ta ratio of amphibolites is similar to typical OIB arising from deep mantle via mantle plume and is higher relative to dolerites. All these geochemical differences suggest that both of the dykes originate from distinct source mantle via different pulses during the coeval rifting event (Fig. 8.4). The high-Ti melt, represented by amphibolite dykes, originate via mantle plume which has cause significant increase in temperature to melt the overlying SLM. This results in the evolution of relatively low-Ti basalt represented by dolerite dykes from SLM.

The chemical composition (major elements, REE and trace element ratios) of studied dykes have been compared with well-studied Panjal traps from other regions in Pakistan and India (e.g. Papritz and Rey, 1989; Pogue et al., 1992, Chauvet et al., 2008; Shellnutt et al., 2014). The comparison revealed similar source composition i.e. subcontinental lithospheric mantle, of dolerites to other Panjal dykes which endorse their petrogenetic connection. Further support is ascertained due to similar trace element ratios which indicate significant crustal contamination of host melt (Fig. 5.14). The amphibolites, however, are Ti-rich (>3%) and show relatively different composition. Trace element ratio indicate deeper mantle source with negligible crustal contamination which make them resemble high-Ti mafic dykes from Qiangtang region (Fig. 5.14). These differences inferred multiple mantle source for the magmatism during Permian rifting that cause separation of Himalayan terrane from Cimmeria (Fig. 8.4). Xu et al. (2015) show the presence of plume originated High-Ti dykes in Qiangtang block that has been separated from Himalayan terrane due to continental rifting (Fig. 5.15). The chemical composition of studied dykes, however, indicate their sporadic existence with Panjal traps in Himalayan terrane (Fig. 8.4). Further support to their existence in Himalayan terrane is extended by Papritz and Rey (1989) and Pogue et al. (1992a) who report geochemically similar dykes from other parts of northern Pakistan.

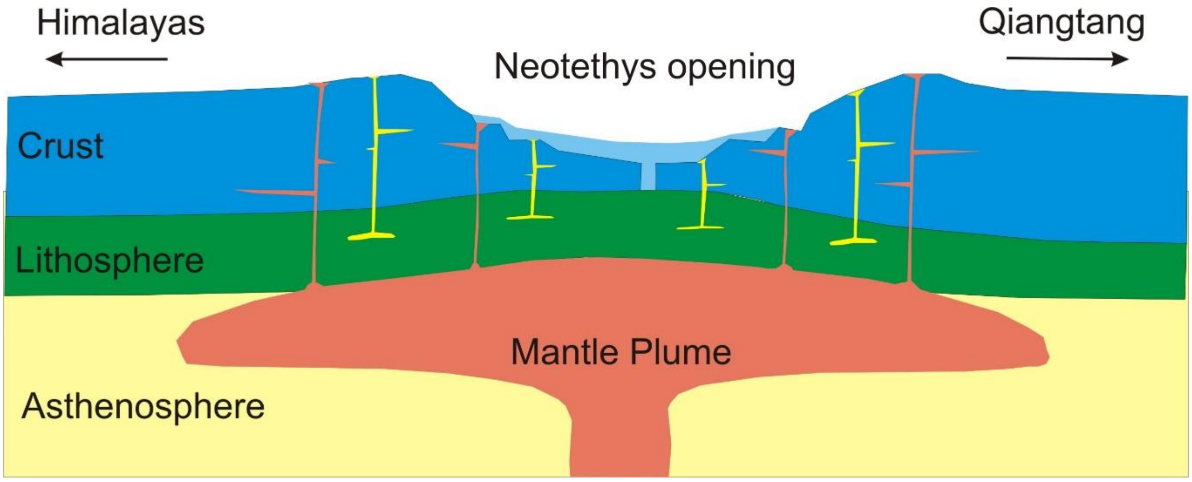

Figure 8.4. Sketch showing the generation of High-Ti dykes via deep mantle plume (Chauvet et al., 2008; Zhai et al., 2013; Xu et al., 2015) and SLM derived Panjal traps (Shellnutt et al., 2014) as a single large igneous province during late Paleozoic rifting event. The distinct source composition is interpreted on the basis of geochemical differences between the dykes described in text. Opening of Neotethys separate the Qiangtang block from Himalayan terrane (Zhang et al., 2012).

8.3. Controls of textural features on rock mechanics

Several studies have been conducted to describe the reliance of physico-mechanical properties of granites on textural and petrographic characteristics (i.e. Yildiz et al., 2010; Yilmaz et al., 2011; Basu et al., 2012; Coggan et al., 2013; Sousa, 2014; Sajid and Arif, 2015). Different textural properties have been described in these studies which have controlling role on mechanical nature of granites. These features include grain size, grain shape, scope of grain size variation within a rock, mineral alignment, concentration of individual mineral etc. The weathering grade of granite is also one of the important feature to be considered for the description of mechanical nature of granite. Increasing degree of weathering has pronounced negative impact on mechanical properties of granite (Gupta and Rao, 2001; Fahimifar and Soroush, 2007; Ceryan et al., 2008; Coggan et al., 2013). The pre- and post-compressional test petrographic observations of four texturally different granites have been described in current investigation to see their relationship with fractures propagation. Most of the approaches outlined above have described the strength variation in granites with different alteration grade; however, erratic strength of granite with similar alteration has not been considered. In the current investigation, three granite samples i.e. AG, SG and UG with analogous weathering (grade-II) have been chosen to properly address the changes in their strength in relation to their textural differences. The fourth granite sample (MG) has higher weathering degree (grade-III) and has been used to compare the effects of weathering grade against the textural properties on rock mechanics.

8.3.1. Variation in granite strength with similar weathering grade

Different weathering classification schemes based on Schmidt hardness, ultrasonic velocity, surface discoloration, tensile strength and micro-petrographic indices (chapter 7) show the analogous weathering degree of AG, UG and SG. Obvious variation in their strength is observed (Fig. 8.5). These granites have greater differences in their textural and petrographic observations (chapter 7; Fig. 7.2). Post-failure textural characteristics show the different response of minerals grains and mineral boundaries among the granite types to newly formed fractures during compression which demonstrate the petrographic controls on strength variation (Fig. 7.14, 8.6).

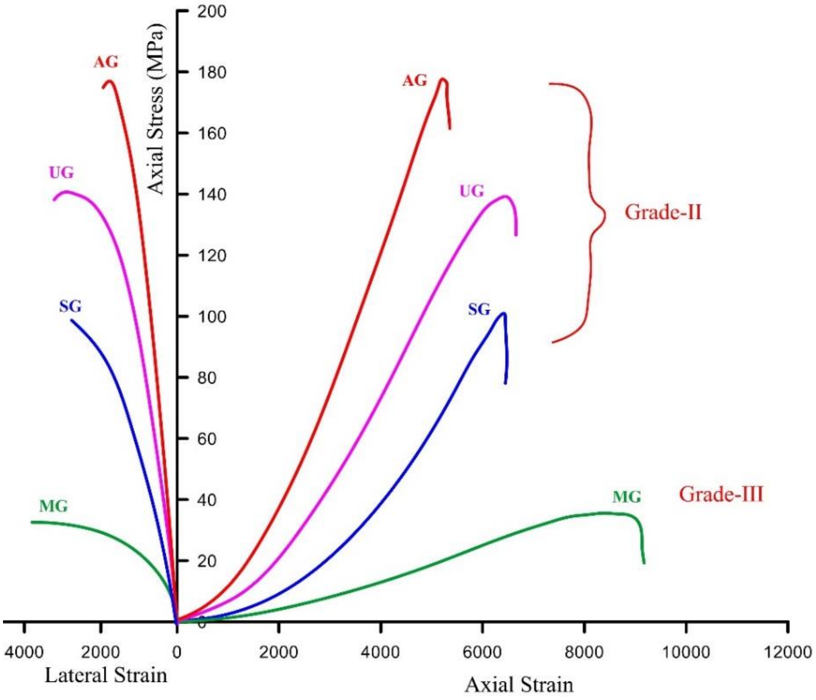

Fig. 8.5. Stress-strain curves of representative samples showing difference in their respective strength and weathering grade.

Fractures generally spread easily in coarse grained rocks via connecting the larger grain boundaries of minerals during compression (Bell, 2007; Lindqvist et al., 2007). SG samples are coarse grained, equigranular and having lower strength than AG and UG due to very evident and larger mineral contacts and boundaries which tend to initiate fracturing readily during compressional testing. Inequigranular rocks are usually stronger than equigranular as the grain size distribution within a sample increases grain boundaries interlocking and interrupting the long grain boundaries which eventually resist the applied stresses (Raisanen, 2004). UG samples are inequigranular containing megacrystic feldspars and groundmass containing quartz, feldspar, biotite, muscovite and tourmaline. The plagioclase in UG show more alteration to fine grained sericite and clay minerals relative to fresh plagioclase of SG (Fig. 8.6 A-B). Despite the relatively higher alteration of feldspars in UG, it exhibits higher strength than SG which is attributed to inequigranular nature and greater distribution in grain size of former. AG samples are also coarse grained and have higher strength than UG and SG which is credited to extensive grain boundary recrystallization observed along mineral contacts (Fig. 8.6C). Post-test petrographic observation reveals the fracture propagation across the minerals in AG (Fig. 8.6D), avoiding the grains boundaries due to fine grained quartz recrystallization which is the strong indication of their resistance to stresses during testing.

MG samples exhibit more or less analogous petrographic character to UG i.e. megacrystic, inequigranular, greater grain size distribution. However, they yielded lower strength relative to other granite types (Fig. 8.5). It can be explained due to their higher weathering grade (Fig. 8.5). From the above description, it is inferred that textural characteristics are vital in expressing the variation in mechanical nature of rocks with analogous alteration, however, higher weathering degree of granites pointedly restrain their mechanics and minimize the petrographic effects.

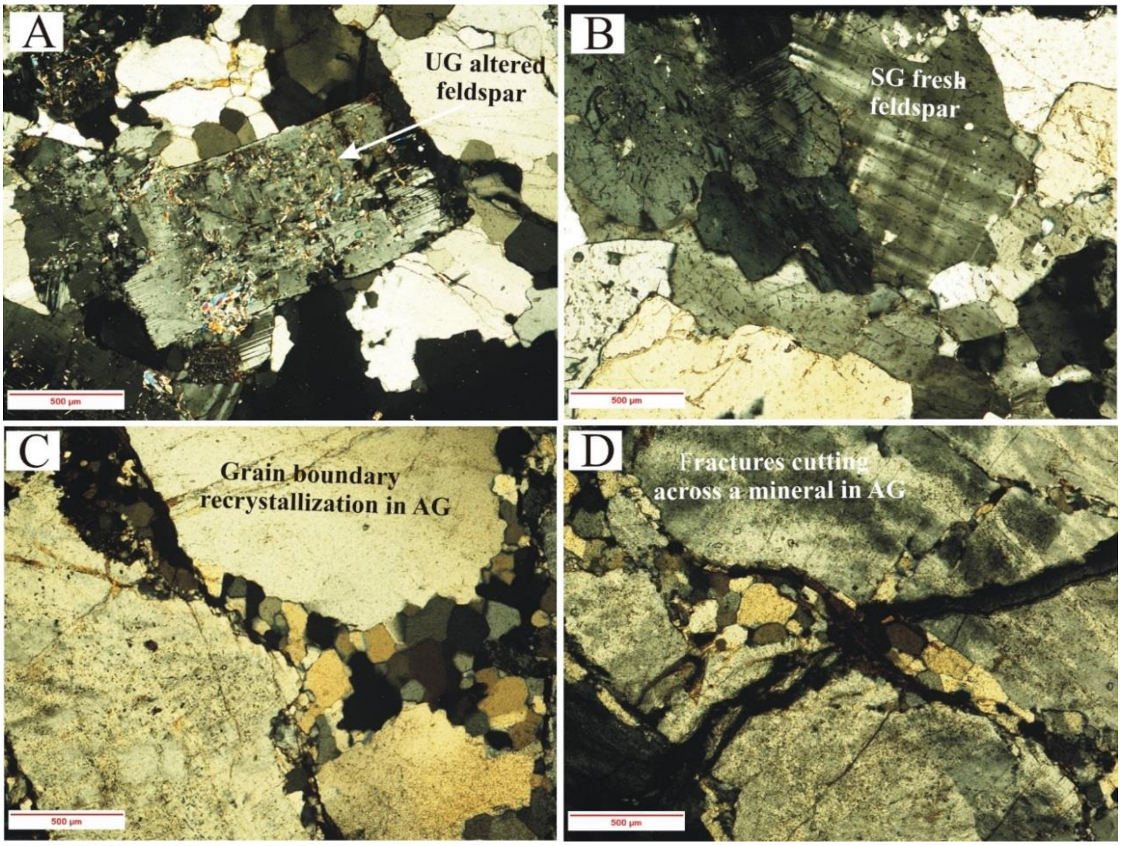

Fig. 8.6. Micrographs, A-B) showing the difference between feldspar alteration in SG and UG samples, C) grain boundary recrystallization in AG, D) fracture cutting across the mineral grain rather than following grain boundaries.

8.3.2. Important textural features

The recrystallization of minerals along grain boundaries (Fig. 8.6C) and its effect on the mechanical properties has been identified for the first time as one of the effective controlling factor. Lindqvist et al. (2007) described that fractures tends to propagate more easily along the larger and smooth grain boundaries (typical in fresh plutonic rocks). The recrystallization apparently increases the irregularity along the grain boundaries which can significantly resist the fracture to propagate. The bonding strength with adjacent grains escalates as the complexity in grain boundary geometry increase. The rocks with inequigranular texture are stronger than equigranular rocks (Raisanen, 2004). The minerals recrystallization not only increase the irregularity along grain contacts but also contribute towards the greater distribution of grain sizes within a rock which eventually have a positive impact on its mechanical nature.

The individual modal concentration of major rock forming mineral e.g. quartz and feldspar in granite, is considered as important controlling factor. Quartz, one of the hardest mineral, has been studied in different granitic rocks across the world to see the relationship between its modal concentration and strength of its host granite. The positive trend between the two parameters is documented by Tugrul and Zarif (1999), Khalil et al. (2015) and Sajid and Arif (2015). In contrast, Sousa (2013) and current investigation yields negative relation. Yilmaz et al. (2011) reported no significant relation between the parameters. These contrasting relations show that the concentration of mineral alone is not a sufficient approach towards describing the mechanical behaviour of rock unless tied to other parameters e.g. textural characteristics. The concentration alone may produce some good and positive interpretations as mentioned above but not in all the cases. The different textural relations of individual mineral (e.g. quartz) include investigation of its contact relations i.e. between quartz-quartz, quartz-feldspar and other rock forming minerals.

CHAPTER 9

CONCLUSIONS

9.1. The Utla Granites

- The Utla granites intrude Precambrian metasedimentary rocks in the northern Indian plate, NW Pakistan. The granites are megacrystic and containing biotite, muscovite, tourmaline, garnet, epidote and apatite as accessory phases. Fine to medium grained aplite dykes and coarse grained quartz rich veins cross cut the megacrystic granites.
- The granitoids are S-type and strongly peraluminous (A/CNK values > 1.11). Fractional crystallization as the dominant evolutionary process is indicated due to the change in composition of plagioclase from megacrystic granite to aplite dykes, zoned plagioclase megacryst and higher silica content of aplite dykes. Major and trace elements geochemistry showed the origin of granites related to melting of pelitic source. REE modelling revealed up to 30% partial melting of metapelites for the generation of similar melt, however, aplite dykes evolve via 20-25% fractional crystallization of feldspars, biotite, muscovite, apatite, ilmenite and zircon from the melt.
- Post magmatic alteration of Utla granites via different hydrothermal fluids is revealed from the varied tourmaline occurrence with specific chemical composition and textural characteristics. Nodular tourmaline and tourmaline rich veins seems to crystallized from fluids belonging to similar magmatic system due to their analogous composition to tourmaline hosted in ground mass of megacrystic granite. The coarse tourmalines with distinct chemical composition in quartz rich veins points towards the derivation of crystallizing fluids from external source.
- Different trace elements ratios used in exploration geochemistry indicates strong mineralization potential of Utla granitoids. This interpretation is further supported by the enriched Sn concentration in certain alteration zones.
- The early Paleozoic 475.7 ± 4.5 Ma emplacement age of megacrystic Utla granites is shown by U-Pb zircon geochronology followed by the intrusion of aplite dykes in 471 ± 2.6 Ma. The mineralogically and geochemically similar Mansehra granites show synchronous emplacement time i.e. 479.5 ± 6.4 Ma.
- The analogous composition and geochronology represent their regional association with other early Paleozoic granitoids from northern Gondwana. The origination of these granitoids in arc setting related to subduction of Proto-Tethys

Ocean beneath the northern Gondwana supercontinent in early Paleozoic has been interpreted which is supported by the several metamorphic and stratigraphic evidences and trace element characteristics.

9.2. Basic Dykes

- The dykes of basic composition intrude early Permian and pre-Permian rocks of northern Indian plate in NW Pakistan. Textural, mineralogical and geochemical distinctions divide the dykes into dolerites and amphibolites. Intra-plate tectonic setting, alkaline to sub-alkaline nature and intrusion in pre-Permian lithologies inferred their tectonic relation to regional scale Permian rifting event in the northern Gondwana.
- Dolerites consist plagioclase and clinopyroxene as major minerals with subordinate amount of olivine, amphibole and oxide phases. Their evolution via fractional crystallization is shown by trends of major elements oxides against silica, PER, zoned plagioclase and variation in olivine composition. Trace and REE ratios indicate their origination from spinel bearing subcontinental lithospheric mantle via <10% partial melting. Significant crustal contamination of crystallizing melt is also indicated. All these features make them resemble the Panjal trap magmatism reported on regional scale from other part of NW Himalayas in Pakistan and India.
- Amphibolites contain amphibole as a dominant phase with lesser concentration of feldspar, titanite and ore minerals. They are mostly foliated with fragile appearance in the field. Geochemically these rocks are TiO_2 rich (> 3%) and trace element ratios suggest relatively deeper asthenospheric mantle source with negligible crustal contribution during their evolution. These characteristics show their association to High-Ti Qiangtang mafic dykes from southern Tibet.
- Both of dyke types originate from compositionally distinct mantle in two separate but synchronous magmatic pulses as indicated by their intrusion in similar aged rocks. Their sporadic distribution in similar host rocks from Himalayan terrane and Qiangtang block show their origination as single magmatic event.

9.3. Textural controls on geotechnical properties

- The combined petrographical, mineralogical and mechanical observations of granites revealed that textural properties are vital in evaluating the variations in mechanical behaviour of granites with similar weathering grade. Upsurge in weathering intensity of rock most likely disguised the textural effects as it increases the voids area and moisture content of rocks that have an abrupt negative effect on rock mechanics.

- The important textural characteristics which effect the mechanical nature of rock include average grain size of rock, maximum grain size of major rock forming minerals, mean grain size of cleaved minerals, variation of mineral grain size within a rock and grain boundary recrystallization. Modal concentration of minerals is also important but it needs to be tied with respective textural characteristics for their better assessment. The irregularity along grain boundaries and suturing with adjacent grains increases with recrystallization of minerals. This eventually raise the inter-grains bonding strength which can efficiently resist the stresses and increase the rock strength.
- Exsolution textures in the form of perthitic or antiperthitic relations are important for petrogenetic information however, their systematic imprint is likely to be susceptible for fractures initiation during their exposure to compressional stress conditions. Pre-existing weak zones of rocks in the form of mineral cleavages are most likely to initiate the fracturing, however, altered zones of megacrystic minerals are also the plausible areas of fracture initiation.

9.4. Recommendations for further studies

- Variation in major elements composition of tourmaline and their mode of occurrence revealed important information about the secondary magmatic processes and differences in their crystallizing fluids (Chapter 4). Strong association of fluids precipitating tourmaline and ore minerals e.g. cassiterite from the similar source is noticed (e.g. Rozendaal and Bruwer 1995; Perugini and Poli 2007; Drivenes et al., 2015). The detailed investigation of B isotopes of different tourmaline types and their respective trace element concentration e.g. Sn, Sr, Rb, Y, Ta and W, via LA ICPMS is important to examine the role of their crystallization in interpreting the mineralization prospects of studied granitoids.
- Major and trace elements characteristics show distinct comparison of the studied dykes with other similar dykes from Himalayan terrane (Chapter 5). However, the geochronological approach using amphibole K-Ar systematics from different dyke

types will aid some further interesting insights to their origin. The Sr, Nd or Hf isotopic compositions of different dykes will also be beneficial for further understandings of the mantle behaviour during the rifting event.

- Grain boundary recrystallization is recognized as efficient controlling factor regarding rock mechanics (Chapter 7). The corresponding observations from other studied granitoids are limited and needed to be thoroughly examined. The strength of granitoids with similar characteristics is valuable to test under different orientations to see the response of fractures to grain boundaries. Similarly, the applicability of this approach also need to be extended to other rocks used primarily in engineering operations e.g. marble. Suturing of grain boundaries is a common textural observation in marble which is also most likely to be affecting its mechanical nature and hence need to be appropriately investigated.

References

Abdel-Fattah, M.A., 1994. Nature of biotites from alkaline, calc-alkaline, and peraluminous magmas. Journal of Petrology 35, 525–541

Ahmed, M., Ali, K.S.S., Khan, B., Shah, M.A., Ullah, I., 1969. The geology of the Warsak area, Peshawar, West Pakistan. Geological Bulletin, University of Peshawar 4, 44–78

Ahmad, I., Hamidullah, S., Jehan, N., 1990. Petrology of the Shewa–Shahbaz Garhi complex, Mardan North Pakistan. Geological Bulletin, University of Peshawar 23, 135–159

Ahmad, I., Jan, M.Q., DiPietro, J.A., 2003. Age and Tectonic implications of granitoids rocks from the Indian plate of Northern Pakistan. Journal of Virtual Explorer 11, 13–34

Ahmad, I., Khan, S., Lapen, T., Burke, K., Jehan, N., 2013. Isotopic Ages for Alkaline Igneous Rocks, Including a 26 Ma Ignimbrite, from the Peshawar Plain of Northern Pakistan and Their Tectonic Implications. Journal of Asian Earth Sciences 62, 414–424

Akesson, U., Stigh, J., Lindqvist, J.E. and Goransson, M., 2003. The influence of foliation on the fragility of granitic rocks, image analysis and quantitative microscopy. Engineering Geology, 68, 275–288

Ali, J.R., Aitchison, J.C., Chik, S.Y.S., Baxter, A.T., Bryan, S.E., 2012. Paleomagnetic data support Early Permian age for the Arbor volcanics in the lower Siang Valley, NE India: Significance for Gondwana break-up models: Journal of Asian Earth Sciences 50, 105–115

Altherr R., Holl A., Hegner E., Langer C., Kreuzer H., 2000. High-potassium, calc-alkaline I-type plutonism in the European Variscides: Northern Vosges (France) and northern Schwarzwald (Germany). Lithos 50, 51–73

Anczkiewicz, R., Burg, J.P., Hussain, S.S., Dawood, H., Ghanzanfar, M. Chaudhry, M. N. 1998. Stratigraphy and structure of the Indus Suture in the Lower Swat, Pakistan, NW Himalaya. Journal of Asian Earth Sciences 16, 225-238

Anczkiewicz, R., Oberli, F., Burg, J.P., Villa, I.M., Gunther, D., Meier, A., 2001. Timing of normal faulting along the Indus Suture in Pakistan Himalaya and a case of major 231Pa/235U initial disequilibrium in zircon. Earth and Planetary Science Letters 191, 101-114

Anon, 1995. The description and classification of weathered rocks for engineering purposes. Geological Society working Party Report. The Quarterly Journal of Engineering Geology 28, 207–242

Argles, T.W., Prin, C.I., Foster, G.L., Vance, D., 1999. New garnets for old? Cautionary tales from young mountain belts. Earth and Planetary Science Letters 172, 301–309

Arif, M., 1996. Chemical characteristics of chrome spinel in the magnesite-rich rocks from Swat, northwestern Pakistan. Geological Bulletin University of Peshawar 29, 9–15

Arif, M., Henry, D.J., Moon C.J., 2011. Host rock characteristics and source of chromium and beryllium for emerald mineralization in the ophiolitic rocks of the Indus Suture Zone in Swat, NW Pakistan. Ore Geology Reviews 39, 1–20

Arif, M, Bukhari, W.H., Muhammad, N., Sajid, M., 2013. Petrography and physicomechanical properties of rocks from the Ambela granitic complex, NW Pakistan. Scientific World Journal, ID: 349381. DOI:10.1155/2013/349381

Aydin, A., Basu, A., 2005. The Schmidt hammer in rock material characterization. Engineering Geology 81, 1–14

Baig, M.S., Lawrence, R.D., Snee, L.W., 1988. Evidence for late Precambrian to early Cambrian orogeny in northwest Himalaya, Pakistan, Geological Magazine 125, 83–86

Baig, M.S., Snee, L.W., La Fortune, J.R., Lawrence, R.D., 1989, Timing of pre-Himalayan orogenic events in the north-west Himalaya: Ar/Ar constraints. Kashmir Journal of Geology 6-7, 29-40

Baig, M.S., 1990. Structure and geochronology of pre-Himalayan and Himalayan orogenic events in the northwest Himalaya, Pakistan, with special reference to the Besham area. Ph.D. dissertation, 300pp. Oregon state University, Corvallis

Baker, T., Pollard, P., Mustard, R., Mark, G., Grahan, J., 2005. A comparison of granite related tin, tungsten and gold–bismuth deposits: implications for exploration. SEG Newsletter 61, 9–17

Baksi, A.K., 2001. Search for a deep-mantle component in mafic lavas using a Nb–Y–Zr plot. Canadian Journal of Earth Sciences 38, 813–824

Barth, M.G., McDonough, W.F., Rudnick, R.L., 2000. Tracking the budget of Nb and Ta in the continental crust. Chemical Geology 165, 197–213

Basu, A., Celestino, T.B., Bortolucci, A.A., 2009. Evaluation of rock mechanical behaviours under uniaxial compression with reference to assessed weathering grades. Rock Mechanics Rock Engineering 42, 73–93

Beard, J.S., Abirz, R.J., Lofgren, G.E., 1993. Experimental melting of crustal xenoliths from Kilbourne Hole, New Mexico and implications for the contamination and genesis of magmas. Contributions to Mineralogy and Petrology 115, 88–102

Bell, F. G., 2007. Engineering Geology, 2nd edition. Butterworth-Heinemann: an imprint of Elsevier, United Kingdom

Bhanot, V.B., Bhandari, A.K., Singh, V.P., Kansal, A.K., 1979. Geochronological and geological studies on a granite of Higher Himalaya, northeast of Manikaran, Himachal Pradesh. Journal of the Geological Society of India 20, 90–4

Bhat, M.I., Zainuddin, S.M., Rais, A., 1981, Panjal Trap chemistry and the birth of Tethys: Geological Magazine 118 (4), 367–375

Bhat, M.I., 1984. Abor Volcanics: further evidence for the birth of the Tethys Ocean in the Himalayan segment: Journal of the Geological Society London 141 (4), 763–775

Black, L.P., Kamo, S.L., Allen, C.M., Davis, D.W., Aleinikoff, J.N., Valley, J.W., Mundil, R., Campbell, I.H., Korsch, R.J., Williams, I.S., Foudoulis, C., 2004. Improved Pb-206/U-218 microprobe geochronology by the monitoring of a trace-element-related matrix effect; SHRIMP, ID-TIMS, ELA-ICP-MS and oxygen isotope documentation for a series of zircon standards. Chemical Geology 205, 115-140

Bonin, B., Azzouni-Sekkal, A., Bussy, F., Ferrag, S., 1998. Alkali-calcic and alkaline post-orogenic (PO) granite magmatism: petrologic constraints and geodynamic settings. Lithos 45, 45–70

Booth, A.L., Zeitler, P.K., Kidd, W.S.F., Wooden, J., Liu, Y.P., Idleman, B., Hren, M., Chamberlain, C.P., 2004. U–Pb zircon constrains on the tectonic evolution of south eastern Tibet, Namche Barwa area. American Journal of Science 304, 889–929

Brandon, A.D., Creaser, R.A., Chacko, T., 1996. Constraints on rates of granitic magma transport from epidote dissolution kinetics. Science 271, 1845–1848

Brookfield, M.E., 1993. The Himalayan passive margin from Precambrian to Cretaceous times. Sedimentary Geology 84, 1–35

Broska, I., Uher, P., Lipka, J., 1998. Brown and blue schorl from the Spiš-Gemer granite, Slovakia: composition and genetic relations. Journal of Czech Geological Society 43(1/2), 9-16

Brown, E.T., 1981. Rock Characterization, Testing and Monitoring: ISRM Suggested Methods. Pergamon, New York

Brown, G.C., Thope, R.S., Webb, P.C., 1984. The geochemical characteristics of granitoids in contrasting arc and comments on magma sources. Journal of the Geological Society of London 141, 411–426

Burg, J.P., Nievergelt, P., Oberli, F., Seward, D.,Davy, P., Maurin, J.C., Diao, Z., Meier, M., 1998. The Namche Barwa syntaxis: Evidence for exhumation related to compressional crustal folding: Journal of Asian Earth Sciences 16, 239–252

Burg, J.P., 2011. The Asia-Kohistan-India Collision: Review and Discussion, *In:* Brown, D., Ryan, P.D. (eds.), Arc-Continent Collision, Frontiers in Earth Sciences, DOI 10.1007/978-3-540-88558-0_10, Springer-Verlag Berlin Heidelberg, 279-309

Butt, K.A., Arif, A.Z., Ahmed, J., Ahmed, A., Qadir, A., 1989. Chemistry and petrography of the Sillai Patti carbonatite complex, North Pakistan. Geological Bulletin, University of Peshawar 22, 197-215

Calkins, J.A., Offield, T.W., Ali, S.T., 1969. Geology and mineral resources of southern Hazara District, West Pakistan, and parts of western Azad Kashmir: Ibid., Professional Report (IR) PK-43, 92p

Calkins, J.A., Offield, T.W., Abdullah, S.K.M., Ali, S.T., 1975. Geology of southern Himalaya in Hazara, Pakistan and adjacent areas. US Geological Survey Professional paper 716-C, 29p

Campbell, I.H., 2002. Implications of Nb/U, Th/U and Sm/Nd in plume magmas for the relationship between continental and oceanic crust formation and the development of the depleted mantle. Geochimica et Cosmochimica Acta 66, 1651–1661

Catlos, E.J., Sorenson, S.S., Harrison, T.M., 2000. Th–Pb ion microprobe dating of allanite. American Mineralogist 85, 633–648

Catlos, E.J., Harrison, T.M., Manning, C.E., Grove, M., Rai, S.M., Hubbard, M.S., Upreti, B.N., 2002. Records of the evolution of the Himalayan orogeny from in-situ Th–Pb ion microprobe dating of monazite: Eastern Nepal and Western Garhwal. Journal of Asian Earth Sciences 20, 459–479

Cawood, P. A., Buchan, C., 2007. Linking accretionary orogenesis with supercontinent assembly. Earth Science Reviews 82, 217–256

Cawood, P.A., Johnson, M.R.W., Nemchin, A.A., 2007. Early Paleozoic orogenesis along the Indian margin of Gondwana: tectonic response to Gondwana assembly. Earth and Planetary Science Letters 255, 70–84

Ceryan, S., Tudes, S., Ceryan, N., 2008. Influence of weathering on the engineering properties of Harsit granitic rocks. Bulletin of Engineering Geology and Environment 67, 97–104

Chappell, B.W., 1999. Aluminium Saturation in I- and S-Type Granites and the Characterization of Fractionated Haplogranites. Lithos 46, 535–551

Chappell, B.W., White, A.J.R., 1992. I- and S-type granites in the Lachlan Fold Belt. Transactions of the Royal Society of Edinburgh: Earth Sciences 83, 1–26

Chaudhry, M.N., Ashraf, M., 1980. The volcanic rocks of Poonch District, Azad Kashmir: Proceedings of the International Committee of Geodynamics Group 6, Kashmir Special issue, Geological Bulletin of the University of Peshawar 13, 121–128

Chauvet, F., Lapierre, K., Bosch, D., Guillot, S., Mascle, G., Vannay, J.C., Cotten, J., Brunet, P., Keller, F., 2008, Geochemistry of the Panjal Traps basalts (NW Himalaya): records of the Pangea Permian break-up: Bulletin de la Societe Geologique de France 179 (4), 383–395

Chauvet, F., Dumont, T., Basile, C., 2009. Structures and timing of Permian rifting in the central Oman Mountains (Saih Hatat). Tectonophysics 475, 563–574

Chen, F.K., Li, X.H., Wang, X.L., Li, Q.L., Siebel, W., 2007. Zircon age and Nd–Hf isotopic composition of the Yunnan Tethyan belt, southwestern China. International Journal of Earth Sciences 96, 1179–1194

Class, C., Goldstein, S.L., Altherr, R., Bachelery, P., 1998. The process of plume-lithosphere interactions in the ocean basins — the case of the Grand Comore. Journal of Petrology 39, 881–903

Clemens, J.D. 2012. Granitic magmatism, from source to emplacement: a personal view. Applied Earth Science 121 (3), 107-136

Clemens, J.D., Vielzeuf, D., 1987. Constraints on melting and magma production in the crust. Earth and Planetary Science Letters 86, 287–306

Coggan, J.S., Stead, D., Howe, J.H., Faulks, C.I., 2013. Mineralogical controls on the engineering behaviour of hydrothermally altered granites under uniaxial compression. Engineering Geology 160, 89–102

Colchen, M., Le Fort, P., Pêcher, A., 1986. Annapurna–Manaslu–Ganesh Himal: Paris, Centre National de la Recherche Scientifique, 136p

Coleman, M.E., 1996. Orogen-parallel and orogen-perpendicular extension in the central Nepalese Himalayas: Geological Society of America Bulletin 108, 1594–1607

Coward, M.P., Windley, B.F., Broughton, R., Luff, I.W., Petterson, M.G., Pudsey, C., Rex, D., Khan, M. A., 1986. Collision tectonics in the NW Himalayas. *In:* Coward, M. P., Ries, A. C., eds., Collision tectonics: Geological Society London Special Publication 19, 203–219

Coward, M.P., Butler, R.W.H., Khan, M. A., Knipe, R.J., 1987. The tectonic history of Kohistan and its implications for Himalayan structure: Geological Society London Journal 144, 377–391

Crawford, A.R., Davies, R.G., I975. Ages of Pre-Mesozoic of the Lesser Himalaya, Hazara district, Northern Pakistan. Geological Magazine I12 (5), 509-514

Crawford, M.B., Searle, M.P., 1992. Field relations and geochemistry of pre-collisional (India-Asia) granitoid magmatism in the central Karakoram, northern Pakistan. Tectonophysics 206, 171-192

Cui, X., Jiang, X., Wang, J., Wang, X., Zhuo, J., Deng, Q., Liao, S., Wu, H., Jiang, A., Wei, Y., 2015. Mid-Neoproterozoic diabase dykes from Xide in the western YangtzeBlock, South China: New evidence for continental rifting related to the breakup of Rodinia supercontinent. Precambrian Research 268, 339–356

Dahlquist J.A., Galindo, C., Pankhurst, R.J., Rapela, C.W., Alasino, P.H., Saavedra, J., Fanning, C.M., 2007. Magmatic evolution of the Peñón Rossado granite: petrogenesis of garnet-bearing granitoid. Lithos 95,177–207

DallAgnol, R., Lafon, J.M., Macambira, M.J.B., 1994. Proterozoic and orogenic magmatism in the Central Amazonian Province, Amazonian Craton: geochronological, petrological and geochemical aspects. Mineralogy and Petrology 50, 113–138

Dalziel, I.W.D., 1992. Antarctica; a tale of two supercontinents. Annual review Earth and Planetary Sciences 20, 501-526

Debon, F., LeFort, P., Sonet, J., Liu, G.H., Jin, C.W., Xu, R.H., 1981. About the lower Paleozoic age of the Kangmar granite (Lhagoi Kangri Plutonic belt, South Tibet, China). Terra Cognita 14, 67–68 (Special Issue)

DeCelles, P.G., Gehrels, G.E., Quade, J., Ojha, T.P., 1998. Neogene foreland basin deposits, erosional unroofing, and kinematic history of the Himalayan fold-thrust belt, western Nepal. Geological Society of America Bulletin 110, 2–21

DeCelles, P., Gehrels, G.E., Quade, J., La Reau, B., Spurlin, M., 2000. Tectonic implications of U–Pb zircon ages of the Himalayan orogenic belt in Nepal. Science 288, 497–499

DeCelles, P.G., Gehrels, G.E., Najman, Y., Martin, A.J., Carter, A., Garzanti, E., 2004. Detrital geochronology and geochemistry of Cretaceous-Early Miocene strata of Nepal: implications for timing and diachroneity of initial Himalayan orogenesis. Earth and Planetary Science Letters 227, 313–330

Dhuime, B., Bosch, D., Bodinier, J.L., Garrido, C.J., Bruguier, O., Hussain, S.S., Dawood, H., 2007. Multistage evolution of the Jijal ultramafic–mafic complex (Kohistan, N Pakistan): implications for building the roots of island arcs. Earth Planetary Science Letters 261, 179–200. DOI:10.1016/j.epsl.2007.06.026

Diamantis, K., Gartzos, E., Migiros, G., 2014. Influence of petrographic characteristics on physico-mechanical properties of ultrabasic rocks from central Greece. Bulletin of Engineering Geology and Environment 73, 1273-1292. DOI: 10.1007/s10064-014-0584-x

Dilles, J.H., Snee, L.W., Laurs, B.M., 1994. Geology, Ar-Ar age, and stable isotope geochemistry of suture-related emerald mineralization, Swat, Pakistan Himalaya. Geological Society of America Abstracts with Programs 26 (7), 311

DiPietro, J.A., Pogue, K.R., Lawrence, R.D., Baig, M.S., Hussain, A., Ahmad, I., 1993. Stratigraphy south of the Main Mantle thrust, Lower Swat, Pakistan. *In:* Treloar, P.J., Searle, M.P., eds. Himalayan Tectonics, Geological Society of London Special Publication 74, 207-220

DiPietro, J.A., Pogue, K.A., Hussain, A. and Ahmed, I., 1998. Geologic map of Indus syntaxis and surrounding area, northwest Himalaya, Pakistan. Geological society of America, Special paper, 328, plate-1

DiPietro, J.A., Hussain, A., Ahmad, I., Khan, M.A., 2000. The Main Mantle thrust in Pakistan: Its character and extent. *In*: Khan, M.A., Treloar, P.J., Searle, M.P., Jan, M.Q., eds., Tectonics of the Nanga Parbat Syntaxis and the Western Himalaya, Geological Society of London Special Publication 170, 375-393

DiPietro, J.A., Isachsen, C.E., 2001. U-Pb zircon ages from the Indian Plate in northwest Pakistan and their significance to Himalayan and pre-Himalayan geologic history. Tectonics, 20, 510 – 525

DiPietro, J.A., Pogue, K.R., 2004. Tectonostratigraphic subdivisions of the Himalaya: A view from the west. Tectonics 23, TC5001, DOI:10.1029/2003TC001554 20

DiPietro, J.A., 2008. Addressing Tectonic and Metamorphic Controversy in the Pakistan Himalaya. Himalayan Journal of Sciences 5 (7), 45-46

Dong, X., Zhang, Z.M., Wang, J.L., Zhao, G.C., Liu, F., Wang, W., Yu, F., 2009. Provenance and formation age of the Nyingchi Group in the southern Lhasa terrane, Tibetan Plateau: petrology and zircon U–Pb geochronology. Acta Petrologica Sinica 25, 1678–1694 (in Chinese with English abstract)

Dong, M.L., Dong, G.C., Mo, X.X., Santosh, M., Zhu, D.C., Yu, J.C., Nie, F., Hu, Z.C., 2013. Zircon U–Pb geochronology, Hf isotopes, and geochemistry of leucogranites in the Baoshan Block, western Yunnan: implications for Early Paleozoic arc magmatism along Gondwana margin. Lithos 179, 36–47

Drivenes, K., Larsen R.B., Müller A., Sørensen B.E., Wiedenbeck M., Raanes M.P., 2015. Late‑magmatic immiscibility during batholith formation: assessment of B isotopes and trace elements in tourmaline from the Land’s End granite, SW England. Contributions to Mineralogy and Petrology 169, 56, DOI: 10.1007/s00410-015-1151-6

du Bray, E.A., 1988. Garnet compositions and their use as indicators of peraluminous granitoid petrogenesis south eastern Arabian Shield. Contributions to Mineralogy and Petrology 100, 205–212

Ehlen, J., 2002. Some effects of weathering on joints in granitic rocks. Catena 49, 91–109

Einfalt, H.C., Hoehndorf, A.F., Kaphle, K.P., 1993. Radiometric age determination of the Dadeldhura granite, Lesser Himalaya, Far Western Nepal. Schweizerische Mineralogische and Petrographische Mitteilungen 73, 97–106

Ernst, R.E., Buchan, K.L., 2001, Large mafic magmatic events through time and links to mantle plume-heads, *In:* Ernst, R.E., Buchan, K.L., (eds) Mantle Plumes: Their Identification Through Time: Geological Society of America Special Papers 352, 483–57

Ernst, R.E., Buchan, K.L., Campbell, I.H., 2005. Frontiers in large igneous province research. Lithos 79, 271–297

Ertl, A., Hughes, J.M., Prowatke, S., Ludwig, T., Prasad, P.S.R., Brandstätter, F., Körner, W., Schuster, R., Pertlik, F., Marschall, H., 2006.Tetrahedrally coordinated boron in tourmalines from the liddicoatite-elbaite series from Madagascar: structure, chemistry, and infrared spectroscopic studies. American Mineralogist 91, 1847–1856

Evans, B.W., Vance, J.A., 1987. Epidote phenocrysts in dacitic dikes, Boulder County, Colorado. Contributions to Mineralogy and Petrology 96, 178–185

Fahimifar, A., Soroush, H., 2007. A moisture index classification system for rocks (MiC System). Rock Mechanics Rock Engineering 40(1), 63–79

Ferla, P., Meli, C., 2007. Petrogenesis of tourmaline rocks associated with Fe-carbonate–graphite metapelite, metabasite and strata-bound polymetallic sulphide mineralisation, Peloritani Mountains, Sicily, Southern Italy. Lithos, 99, 266–288

Ferreira, V.P., Sial, A.N., Pimentel, M.M., Armstrong, R., Spicuzza, M., Guimaraes, I.P., Silva Filho, A.F., 2011. Contrasting sources and P-T crystallization conditions of epidote-bearing granitic rocks, northeastern Brazil: O, Sr, and Nd Isotopes. Lithos 121, 189-201

Fitton, J.G., Saunders, A.D., Norry, M.J., Hardarson, B.S., Taylor, R.N., 1997. Thermal and chemical structure of the Iceland plume. Earth and Planetary Science Letters 153, 197–208

Fogliata, A.S., Báez, M.A., Hagemann, S.G., Santos, J.O., Sardi, F., 2012. Post-orogenic, Carboniferous granite-hosted Sn–W mineralization in the Sierras Pampeanas Orogen, North western Argentina. Ore Geology Reviews 45, 16–32

Foster, G.L., 2000. The Pre-Neogene thermal history of the Nanga Parbat Haramosh massif and the NW Himalaya. The Open University, United Kingdom. 345pp

Frank, W., Thoni, M., Purtscheller, F., 1977. Geology and Petrography of Kulu-South Lahularea. Colloques Intenatioanux du Centre National de la Recerche Scientifique 286, 147–172

Freire-Lista, D.M., Fort, R., Varas-Muriel, M.J., 2015. Freeze–thaw fracturing in building granites. Cold Regions Science and Technology 113, 40–51

Frey, F.A., Weis, D., Borisova, A.Y., Xu, G., 2002. Involvement of continental crust in the formation of the Cretaceous Kerguelen Plateau: new perspectives from ODP Leg 120 sites. Journal of Petrology 43, 1207–1239

Fujii, Y., Takemura, T., Takahashi, M., Lin, W., 2007. Surface features of uniaxial tensile fractures and their relation to rock anisotropy in Inada granite. International Journal of Rock Mechanics and Mining Sciences, 44, 98-107

Funakawa, S., 2001. Lower Paleozoic Tethys sediments from the Kathmandu nappe, Phulchauki area, central Nepal. Journal of Nepal Geological Society 25, 123–134

Gaetani, M., Casnedi, R., Garzanti, E., Jadoul, F., Nicora, A., Tintori, A., 1985. Stratigraphy of the Tethys Himalaya in Zanskar, Ladakh. Rivista Italiana di Paleontologie e Stratigraphia 91, 443–478

Gaetani, M., Garzanti, E., Tintori, A., 1990. Permo-Carboniferous stratigraphy in SE Zanskar and NW Lahul (NW Himalaya, India). Eclogae Geologicae Helvetiae 83, 143-161

Gaetani, M., Garzanti, E., 1991. Multicyclic history of the northern India continental margin (Northwestern Himalaya). American Association of Petroleum Geologists Bulletin 75, 1427–1446

Gansser, A., 1964, Geology of the Himalayas: London, Wiley Inter-science, 289p

Garzanti, E., Casnedi, R., Jadoul, F., 1986. Sedimentary evidence of a Cambro-Ordovician orogenic event in the Northwestern Himalaya. Sedimentary Geology 48, 237–265

Garzanti, E., LeFort, P., Sciunnach, D., 1999, First report of Lower Permian basalts in south Tibet: tholeiitic magmatism during break-up and incipient opening of Neotethys: Journal of Asian Earth Sciences 17 (4), 533–546

Gehrels, G.E., Decelles, P.G., Martin, A., Ojha, T.P., Pinhassi, G., Upreti, B.N., 2003. Initiation of the Himalayan orogeny as an Early Paleozoic thin-skinned thrust belts. GSA Today 13, 4–9

Gehrels, G.E., DeCelles, P.G., Ojha, T.P., Upreti, B.N., 2006a. Geological and U–Pb geochronologic evidence for early Paleozoic tectonism in the Dadeldhura thrust sheet, far-west Nepal Himalaya. Journal of Asian Earth Sciences 28, 385–408

Gehrels, G.E., Decelles, P.G., Ojha, T.P., Upreti, B.N., 2006b. Geologic and U–Th–Pb geochronologic evidence for early Paleozoic tectonism in the Kathmandu thrust sheet, central Nepal Himalaya. Geological Society of American Bulletin 118, 185–198

Girard, M., Bussy, F., 1999. Late Pan-African magmatism in the Himalaya: new geochronological and geochemical data from the Ordovician Tso Morari metagranites (Ladakh, NW India). Schweizerische Mineralogische und Petrographische Mitteilungen 79, 399–418

Godin, L., Parrish, R.R., Brown, R.L., Hodges, K.V., 2001. Crustal thickening leading to exhumation of the Himalayan metamorphic core of central Nepal: insight from U–Pb geochronology and 40Ar/39Ar thermochronology. Tectonics 20, 729–747

Gottlieb, P., Wilkie, G., Sutherland, D., Ho-Tun, E., Suthers, S., Perera, K., Jenkins, B., Spencer, S., Butcher, A., Rayner, J., 2000. Using quantitative electron microscopy for process mineralogy applications. JOM, 24–25.

Greco, A., Spencer, D.A., 1993. A section through the Indian Plate, Kaghan Valley, NW Himalaya, Pakistan. *In:* Treloar, P.J., Searle, M.P., (eds), Himalayan Tectonics. Geological Society of London, Special Publication 74, 221-236

Gupta, A.S., Rao, K.S., 2001.Weathering indices and their applicability for crystalline rocks. Bulletin of Engineering Geology and Environment 60, 201–221

Guynn, J., Kapp, P., Gehrels, G.E., Ding, L., 2012. U–Pb geochronology of basement rocks in central Tibet and paleogeographic implications. Journal of Asian Earth Sciences 43, 23–50

Haapala, I., 1977. Petrography and geochemistry of the Eurajoki stock a rapakivi-granite complex with greisen type mineralization in south-western Finland. Geological survey of Finland Bulletin 286, 1-128

Halsey, D.P., Mitchell, D.J., Dews, S.J., 1998. Influence of climatically induced cycles in physical weathering. Quarterly Journal of Engineering Geology and Hydrogeology 31, 359–367

Harris, N.B.W., Pearce, J.A., Tindle, A.G., 1986. Geochemical characteristics of collision-zone magmatism. *In*: Coward, M. P., Ries, A. C., (eds), Collision Tectonics, Geological Society Special Publication 19, 67-81

Harrison, T.M., McKeegan, K.D., LeFort, P., 1995. Detection of inherited monazite in the Manaslu leucogranite by ^{208}Pb/^{232}Th ion microprobe dating: Crystallization age and tectonic implications: Earth and Planetary Science Letters 133, 271–282

Hawthorne, F.C., Oberti, R., Harlow, G.E, Maresch, W.V., Martin, R.F., Schumacher, J.C., Welch, M.D., 2012. Nomenclature of the amphibole supergroup. American Mineralogist 97, 2031–2048

Hecht, C.A., Bonsch, C., Bauch, E., 2005. Relations of rock structure and composition to petrophysical and geomechanical rock properties: examples from Permocarboniferous Red-Beds. Rock Mechanics Rock Engineering 38(3), 197–216

Healy, B., Collins, W.J., Richards, S.W., 2004. A hybrid origin for Lachlan S-type granites: the Murrumbidgee batholith example. Lithos 79, 197–216

Heidari, M., Momeni, A.A., Naseri, F., 2013. New weathering classifications for granitic rocks based on geomechanical parameters. Engineering Geology 166, 65-73

Heim, A., Gansser, A., 1939, Central Himalaya–Geological observations of Swiss expedition, 1936: Mémoire, Société Helvetique Science Naturelle 73, 1–245

Hencher, S.R., McNicholl, D.P., 1995. Engineering in weathered rock. The Quarterly Journal of Engineering Geology, 28 253–266

Hencher, S.R., Ebuk, E.J., Abrams, J.H., Lumsden, A.C., 1990. Field description and classification of hydrothermally altered granite of SW England. 10th Southeast Asian Geotechnical Conference, 16-20 April, Taipei, 303–308

Henry, D.J., Novák, M., Hawthorne, F.C., Ertl, A., Dutrow, B.L., Uher, P., Pezzotta, F., 2011. Nomenclature of the tourmaline-supergroup minerals. American Mineralogist 96, 895–913. DOI: 10.2138/am.2011.3636

Hodges, K. V., Parrish, R. R., Searle, M. P., 1996. Tectonic evolution of the central Annapurna Range, Nepalese Himalayas: Tectonics 15, 1264–1291

Hodges, K.V., 2000. Tectonics of the Himalaya and southern Tibet from two perspectives. Geological Society of American Bulletin 112, 324–350

Honegger, K., Dietrich, V., Frank, W., Gansser, A., Thoeni, M., Trommsdorff, V., 1982. Magmatism and metamorphism in the Ladakh Himalayas (The Indus - Tsangpo Suture Zone). Earth and Planetary Science Letters 60, 253-292

Howarth, D.F., 1988. Experimental study on the relationship between rock texture and mechanical performance. Transactions of the Institution of Mining and Metallurgy (Sect A Mining industry) 95, 41–5

Hu, D.W., Zhang, F., Shao, J.F., Gatmiri, B., 2014. Influences of Mineralogy and Water Content on the Mechanical Properties of Argillite. Rock Mechanics and Rock Engineering 47:157–166. DOI 10.1007/s00603-013-0413-8

Huang, L.C., Jiang, S.Y., 2014. Highly fractionated S-type granites from the giant Dahutang tungsten deposit in Jiangnan Orogen, Southeast China: geochronology, petrogenesis and their relationship with W-mineralization. Lithos 202–203, 207–226

Hudec, P.P., 1998. Rock properties and physical processes of rapid weathering and deterioration. *In:* Moore, D.P., Hungr, O. (Eds.), Proceeding of 8th International Congress of IAEG, Balkema 1, 335– 341

Hughes, N.C., 2002. Late Middle Cambrian trace fossils from the Lejopyge armata horizon, Zanskar Valley, India, and the use of Precambrian/Cambrian isochronostratigraphy in the Indian subcontinent. Special Papers in Palaeontology 67, 135–151

Hughes, H.S.R., McDonald, I., Goodenough, K.M., Ciborowski, T.J.R., Kerr, A.C., Davies, J.H.F.L., Selby, D., 2014. Enriched lithospheric mantle keel below the Scottish margin of the North Atlantic Craton: Evidence from the Palaeoproterozoic Scourie Dyke Swarm and mantle xenoliths. Precambrian Research 250, 97–126

Hussain, A., Dipietro, J.A., Pogue, K.A., Ahmed, I., 2004. Geologic map of 43-B degree sheet of NWFP Pakistan. Geologic map series, Geological survey of Pakistan, Map No. 11

Irfan, T.Y., 1996. Mineralogy, fabric properties and classification of weathered granite in Hong Kong. The Quarterly Journal of Engineering Geology 29, 5–35

Irfan, T.Y., Dearman, W.R., 1978. The engineering petrography of a weathered granite in Cornwall, England. The Quarterly Journal of Engineering Geology 11, 233-244

International Society for Rock Mechanics (ISRM), 2007. The complete ISRM Suggested Methods for rock characterization, testing and monitoring: 1974–2006. *In:* Ulusay, R., Hudson J.A., (eds) Suggested Methods prepared by the Commission on Testing Methods, International Society for Rock Mechanics, compilation arranged by the ISRM Turkish National Group, Kozan Ofset, Ankara, Turkey

Islam, R., Gururajan, N.S., 1997. Geochemistry and petrogenesis of Lower Paleozoic meta-granites of Lahaul–Spiti region, Himachal Pradesh, India. Geochemical Journal 31, 1-16

Jagoutz, O., Muntener, O., Burg, J.P., Ulmer, P., Jagoutz, E., 2006. Lower continental crust formation through focused flow in km-scale melt conduits: The zoned ultramafic bodies of the Chilas Complex in the Kohistan island arc (NW Pakistan). Earth and Planetary Science Letters 242 (3-4), 320–342

Jagoutz, O., Müntener, O., Schmidt, M.W., Burg, J.P., 2011. The roles of flux- and decompression melting and their respective fractionation lines for continental crust formation: Evidence from the Kohistan arc. Earth and Planetary Science Letters 303, 25–36

Jan, M.Q., Khan, M.A., Tahirkheli, T., 1981. The Geology and Petrology of the Tarbela Alkaline Complex. Geological Bulletin, University of Peshawar 14, 1-28

Jan, M.Q., Karim, A., 1990. Continental Magmatism Related to Late Paleozoic–Early Mesozoic Rifting in North Pakistan and Kashmir. Geological Bulletin, University of Peshawar 23, 1–25

Ji, W.H., Chen, S.J., Zhao, Z.M., Li, R.S., He, S.P., Wang, C., 2009. Discovery of the Cambrian volcanic rocks in the Xainza area, Gangdese orogenic belt, Tibet, China and its significance. Geological Bulletin of China 9, 1350–1354 (in Chinese with English abstract)

Jung, S., Mezger, K., 2001. Geochronology in migmatites-a Sm–Nd, U–Pb and Rb–Sr study from the Proterozoic Damara belt (Namibia): implications for polyphaser development of migmatites in high-grade terranes. Journal of Metamorphic Geology 19, 77–97

Jung, S., Hellebrand, E., 2006. Trace element fractionation during high-grade metamorphism and crustal melting-constraints from ion microprobe data of metapelitic, migmatitic and igneous garnets and implications for Sm–Nd garnet chronology. Lithos 87, 193–213

Kapoor, H.M., 1977: Lower Gondwana of Nishatbagh, Kashmir and its significance. Geophytology 7/2,188-196

Kazmi, A.H., Lawrence, R.D., Dawood, H., Snee, L.W., Hussain, S., 1984. Geology of the Indus suture zone in the Mingora-Shangla area of Swat, N. Pakistan. Geological Bulletin, University of Peshawar 17, 127-144

Kebede, T., Koeberl, C., Koller, F., 2001. Magmatic Evolution of the Siqii-Wagga Garnet Bearing Two Mica Granite, Wallagga Area, Western Ethopia. Journal of African Earth Sciences 32, 193–221

Kempe, D.R.C., 1973. The Petrology of the Warsak Alkaline granites, Pakistan, and their relationship to other alkaline rocks of the region. Geological Magazine 110, 385-404

Kempe, D.R.C., Jan, M.Q., 1970. An Alkaline Igneous Province in North West Frontier Province, West Pakistan. Geological Magazine 107, 395-398

Kempe, D.R.C., Jan, M. Q., 1980. The Peshawar Plain Alkaline Igneous Province, NW Pakistan. Geological Bulletin, University of Peshawar 13, 71-77

Kempe, D.R.C., 1986. A note on the ages of the alkaline rocks of the Peshawar plain alkaline igneous province, NW Pakistan Geological Bulletin, University of Peshawar 19, 113-119

Kennedy, W.Q., 1964. The structural differentiation of Africa in the Pan-African (±500m.y.) tectonic episode. Annual Reports of the Institute of African Geology University of Leeds 8, 48-49

Kerr, A.C., Khan, M., Mahoney, J.J., Nicholson, K.N., Hall, C.M., 2010. Late Cretaceous alkaline sills of the south Tethyan suture zone, Pakistan: Initial melts of the Réunion hotspot? Lithos 117, 161–171

Khalil, Y.S., Arif, M., Bangash, H.A., Sajid, M., Muhammad, N., 2015. Petrographic and structural controls on geotechnical feasibility of dam sites: implications from investigation at Sher Dara area (Swabi), north-western Pakistan. Arabian Journal of Geosciences 8, 5067-5079

Khan, S.R., Khan, M.A., Nawaz, R., Karim, T., 1990. Stratigraphic control for the age of Peshawar Plain magmatism, north Pakistan. Geological Bulletin, University of Peshawar 23, 253–263

Khan, S.R., Khan, M.A., 1994. Late Proterozoic stratigraphy of the Swabi area, N.W.F.P., N. Pakistan. Geological Bulletin, University of Peshawar 27, 57-68

Khan, M.A., Stern, R.J., Gribble, R.F., Windley, B.F., 1997. Geochemical and isotopic constraints on subduction polarity, magma sources and palaeogeography of the Kohistan Arc, northern Pakistan. Journal of the Geological Society of London, 154, 935–946

Khattak, N.U., Qureshi, A.A., Akram, M., Ullah, K., Azhar, M., Khan, M.A., 2005. Unroofing histories of the Jambil and Jawar Carbonatite Complexes from NW Pakistan: Constraints from Fission- Track Dating of Apatite. Journal of Asian Earth Sciences 25, 643-652

Khattak, N.U., Akram, M., Khan, M.A., Khan, H.A., 2008. Emplacement of Loe Shilman carbonatite from NW Pakistan: Constraints from fission track dating. Radiation Measurements 43, S313–S318

Kieffer, B., Arndt, N., Lapierre, H., Bastien, F., Bosch, D., Pecher, A., Yirgu, G., Ayalew, D., Weise, D., Jerram, D.A., Keller, F., Meugniot, C., 2004. Flood and shield basalts from Ethiopia: magmas from the African superswell. Journal of Petrology 45, 793–834

King, B.H., 1964. The structure and petrology of part of lower Swat, West Pakistan, with special reference to the origin of the granitic gneisses, Ph.D. thesis, 130 pp., University of London, England

King, J., Harris, N., Argles, T., Parrish, R., Zhang, H., 2011. Contribution of crustal anatexis to the tectonic evolution of Indian crust beneath southern Tibet. Geological Society of America Bulletin 123, 218–239

Kohn, M.J., Widland, M.S., Parkinson, C.D., Upreti, B.N., 2004. Miocene faulting at plate tectonic velocity in the Himalaya of central Nepal. Earth and Planetary Science Letters 228, 299–310

Kohn, M.J., Paul, S.K., Corrie, S.L., 2010. The lower Lesser Himalayan sequence: A Paleoproterozoic arc on the northern margin of the Indian plate. GSA Bulletin 122, 323–335

Kohn, M.J, 2014, Himalayan metamorphism and its tectonic implications. Annual Review of Earth and Planetary Sciences 42, 381–419

Kroner, A., Stern, R.J., 2004. Pan-African Orogeny North African Phanerozoic Rift Valley. Encyclopaedia of Geology 1, Elsevier, Amsterdam

Kwatra, S.K., Singh, S., Singh, V.P., Sharma, R.K., Rai, B., Kishor, N., 1999. Geochemical and geochronological characteristics of the Early Paleozoic granitoids from Sutlej-Baspa Valleys, Himachal Himalaya. Gondwana Research Group Memoirs 6, 145–58

Kumar, R., Shah, A.N., Bingham, D.K., 1978. Positive evidence of a Precambrian tectonic phase in central Nepal, Himalaya. Journal of the Geological Society of India 19, 519–522

Kusky, T.M., Abdelsalam, M., Stern, R.J., Tucker, R.D., 2003. Evolution of the east African and related orogens, and the assembly of the Gondwana. Precambrian Research 123, 81–85

Lackey, J.S., Dramann, S., Hark, J.S., Nowak, R.M., 2011. Tracing garnet origins in granitoids rocks by oxygen isotope analysis: examples from the South Mountain batholith, Nova Scotia. Canadian Mineralogist 49, 417–439

Le Bas, M.J., Mian, I., Rex, D.C., 1987. Age and nature of carbonatites emplacement in north Pakistan. Geologische Rundschau 76 (2), 317–323

Le Breton, N., Thompson, A.B., 1988. Fluid-absent (dehydration) melting of biotite in metapelites in the early stages of crustal anatexis. Contribution to Mineralogy and Petrology 99, 226-237

Le Fort, P., 1986. Metamorphism and magmatism during the Himalayan collision. *In*: Coward, M.P., Ries, A.C., (eds.) Collision tectonics: Geological Society London Special Publication 19, 159–172

Le Fort, P., Debon, F., Sonet, J., 1980. The “lessor Himalayan” cordierite granite belt, typology and age of the pluton of Mansehra, Pakistan. Geological Bulletin, University of Peshawar 13, 51-62.

Le Fort, P., Debon, F., Sonet, J., 1983. The lower Paleozoic “lesser Himalayan” granite belt: Emphasis on Simchar pluton of central Nepal. *In:* Shams, F.A., (eds.) Granite of Himalayas, Karakoram and Hindukush, Institute of Geology, Punjab University, Lahore, 235-256

Le Fort, P., Debon, F., Pêcher, A., Sonet, J., Vidal, P., 1986. The 500 Ma magmatic event in Alpine southern Asia, a thermal episode at Gondwana scale. Sciences de la Terre, Mémoire 47, 191–209

Le Fort, P., Tongiorgi, M., Gaetani, M., 1994. Discovery of a crystalline basement and Early Ordovician marine transgression in the Karakorum mountain range, Pakistan. Geology 22, 941–944

Le Maitre, R.W., 2002. Igneous rocks: a classification and glossary of terms, 2nd edition. Cambridge University Press

Lee, J., Hacker, B.R., Wang, Y., 2004. Evolution of North Himalayan gneiss domes: structural and metamorphic studies in Mabja Dome, southern Tibet. Journal of Structural Geology 26, 2297–2316

Lee, J., McClelland, W., Wang, Y., Blythe, A.E., McWilliams, M., 2006. Oligocene-Miocene middle crustal flow in southern Tibet: geochronology of Mabja Dome. *In:* Law, R.D., Searle, M.P., Godin, L., (eds) Channel Flow, Ductile Extrusion and

Exhumation in Continental Collision Zones, Geological Society of London Special Publications 268, 445–469

Lee, J., Whitehouse, M.J., 2007. Onset of mid-crustal extensional flow in southern Tibet: evidence from U/Pb zircon ages. Geology 35, 45–48

Lehmann, B., 1987. Tin granites, geochemical heritage, magmatic differentiation. Geologische Rundschau 76, 177–185

Leterrier, J., Maury, R.C., Thonon, P., Girard, D., Marchal, M., 1982. Clinopyroxene composition as a method of identification of the magmatic affinities of paleo-volcanic series. Earth and Planetary Science Letters 59, 139-154

Li, X.H., 1999. U-Pb zircon ages of granites from the southern margin of Yangtze block and the timing of Neoproterozoic sinning orogeny in SE China: termination of Rodinia assembly. Precambrian Research 97, 43-57

Li, X.W., Mo, X.X., Huang, X.F., Dong, G.C., Yu, X.H., Luo, M.F., Liu, Y.B., 2015. U–Pb zircon geochronology, geochemical and Sr–Nd–Hf isotopic compositions of the Early Indosinian Tongren Pluton in West Qinling: Petrogenesis and geodynamic implications. Journal of Asian Earth Sciences 97, 38–50

Lindqvist, J.E., Akesson, U., Malaga, K., 2007. Microstructure and functional properties of rock materials. Material Characterization 58, 1183–1188

Liu, W.C., Liang, D.Y., Wang, K.Y., Zhou, Z.G., Li, G.B., Zhang, X.X., 2002. The discovery of the Ordovician and its significance in the Kangmar area, southern Tibet. Earth Science Frontiers 9, 247–248 (in Chinese with English abstract)

Liu, S., Hu, R.Z., Gao, S., Feng, C.X., Huang, Z., Lai, S., Yuan, H., Liu, X., Coulson, I.M., Feng, G., 2009. U–Pb zircon, geochemical and Sr–Nd–Hf isotopic constraints on the age and origin of Early Palaeozoic I-type granite from the Tengchong–Baoshan Block, Western Yunnan Province, SW China. Journal of Asian Earth Sciences 36, 168–182

Locock, A.J., 2014. An Excel spreadsheet to classify chemical analyses of amphiboles following the IMA 2012 recommendations. Computers & Geosciences 62, 1–11. DOI: http://dx.doi.org/10.1016/j.cageo.2013.09.011

Ludwig, K.R., 2012. Isoplot 3.75: A Geochronological Toolkit for Microsoft Excel. Berkeley Geochronology Center, Special Publication No. 5, pp. 75

Lumb, P., 1962. The properties of decomposed granites. Geotechnique 12, 226-243

Lydekker, R., 1883. Geology of Kashmir and Chamba territories and the British district of Khagan. Memoirs of the Geological Society of India 22, 211–224

Maluski, H., Matte, P., 1984. Ages of Alpine tectono-metamorphic events in the northwestern Himalaya (northern Pakistan) by ^{39}Ar/^{40}Ar methods. Tectonics 3, 1–18

Majid, M., Danishwar, S., Hamidullah, S., 1991. Petrographic and Chemical Variations in the Rift-Related Basic Dykes of the Malka Area (Lower Swat), NWFP, Pakistan. Geological Bulletin, University of Peshawar 24, 1-23

Maniar, P.D., Piccoli, P.M., 1989. Tectonic discrimination of granitoids. Geological society of America bulletin 101, 635-643

Manning, D.A.C., 1982. Chemical and morphological variation in tourmalines from the Hub Kapong batholith of peninsular Thailand. Mineralogical Magazine 45, 139-147

McDonough, W.F., Sun, S.S., Ringwood, A.E., Jagoutz, E., Hofmann, A.W., 1992. Potassium, Rubidium and Cesium in the Earth and Moon and the evolution of the mantle of the Earth. Geochimica et Cosmochimica Acta 56, 1001-1012. DOI: 10.1016/0016-7037(92)90043-I

McDonough, W.F., Sun, S., 1995. The composition of the Earth. Chemical Geology 120, 223–253

Mendes, F.M., Aires-Barros, L., Rodrigues, F.P., 1966. The use of modal analysis in the mechanical characterization of rock masses. Proc. 1st Int. Cong. ISRM, Lisbon 2 (20), 217–223

Metcalfe, I., 1996. Pre-Cretaceous evolution of SE Asian terranes. Geological Society, London, Special Publications 106, 97–122

Metcalfe, I., 2006. Paleozoic and Mesozoic tectonic evolution and palaeogeography of East Asian crustal fragments: the Korean Peninsula in context. Gondwana Research 9 (1–2), 24–46

Middlemiss, C.S., 1910. Revision of Silurian–Trias sequence in Kashmir. Records of the Geological Survey of India 40, 206–260

Miller, C.F., Stoddard, E.F., 1981. The role of manganese in the paragenesis of magmaticgarnet: an example from the Old Woman Piute Range, California. Journal of Geology 89, 233–246

Miller, C.F., 1985. Are strongly peraluminous magmas derived from pelitic sedimentary sources? Journal of Geology 93, 673–689

Miller, C., Thoni, M., Frank, W., Grasemann, B., Klotzli, U., Guntli, P., Draganits, E., 2001. The early Palaeozoic magmatic event in the Northwest Himalaya, India: source, tectonic setting and age of emplacement. Geological Magazine 138, 237–251

Miyashiro, A., 1973. Metamorphism and metamorphic belts. George Allen and Unwin, London

Mlynarczyk, M.S.J., Williams-Jones, A.E., 2006. Zoned tourmaline associated with cassiterite: implications for fluid evolution and tin mineralization in the San Rafael Sn–Cu deposit, south eastern Peru. The Canadian Mineralogist 44, 347-365

Molina, E., Cultrone, G., Sebastian, E., Alonso, F.J., Carrizo, L., Gisbert, J., Buj, O., 2011. The pore system of sedimentary rocks as a key factor in the durability of building materials. Engineering Geology 118,110–121

Momeni, A.A., Khanlari, G.R., Heidari, M., Sepahi, A.A., Bazvand, E., 2015. New engineering geological weathering classifications for granitoid rocks. Engineering Geology 185, 43–51. DOI: 10.1016/j.enggeo.2014.11.012

Müller, A., Seltmann, R., Halls, C., Siebel, W., Dulski, P., Jeffries, T., Spratt, J., Kronz, A., 2006. The magmatic evolution of the Land's End pluton, Cornwall, and associated pre-enrichment of metals. Ore Geology Reviews 28, 329–367

Mustafa, S., Khan, M.A., Khan, M.R., Sousa, L.M.O., Hameed, F., Mughal, M.S., Niaz, A., 2016. Building stone evaluation - A case study of the sub-Himalayas, Muzaffarabad region, Azad Kashmir, Pakistan. Engineering Geology 209, 56- 69

Myrow, P.W., Snell, K.E., Hudges, N.C., Paulsen, T.S., Heim, N.A., Parcha, S.K., 2006a. Cambrian depositional history of the Zanskar Valley region of the Indian Himalaya: tectonic implications. Journal of Sedimentary Research 76, 364–381

Myrow, P.W., Thompson, K.R., Hughes, N.C., Paulsen, T.S., Sell, B.K., Parcha, S.K., 2006b. Cambrian stratigraphy and depositional history of the northern Indian Himalaya, Spiti Valley, north-central India. Geological Society of America Bulletin 118, 491–510

Myrow, P.M., Hughes, N.C., Goodge, J.W., Mark Fanning, C., Williams, I.S., Peng, S.C., Bhargava, O.N., Parcha, S.K., Pogue, K.R., 2010. Extraordinary transport and mixing of sediment across Himalayan central Gondwana during the Cambrian–Ordovician. Geological Society of American Bulletin 122, 1660–1670

Nabelek, P.I., Russ-Nabelek, C., Denison, J.R., 1992. The generation and crystallization conditions of the Proterozoic Harney Peak leucogranite, Black Hills, South Dakota, USA: Petrologic and geochemical constraints. Contribution to Mineralogy and Petrology 110, 173-191

Nabelek, P.I., Bartlett, C.D., 1999. Fertility of metapelites and metagreywackes during leucogranite generation: an example from the Black Hills, USA. *In:* Barbarin, B., Stephens, W.E., Bonin, B., Bouchez, J.L., Clarke, D.B., Cuney, M., Martin, H. (eds.), Fourth Hutton Symposium: The Origin of Granites and Related RocksProceedings of a symposium held in Clermont-Ferrand, France, 20–25 September, 1999. GSA Books, USA

Nakazawa, K., Kapoor, H.M., Ishii, K.I., Bando, Y., Okimura, Y., Tokuoka, T., Murata, M., Nakamura, K., Nogami, Sakagami, S., Shimizu, D., 1975. The upper Permian and the lower Triassic in Kashmir, India. Memoirs of the Faculty of Science, Kyoto University, Series of Geology and Mineralogy 42, 1–106

Nicholls, J., Russell, J.K., 1990. Pearce element ratios — an overview, example and bibliography. *In:* Russell, J.K., Stanley, C.R. (eds.), Theory and Application of

Pearce Element Ratios to Geochemical Analysis. Geological Association of Canada Short Course 8, 11–21

Noble, S.R., Searle, M.P., Walker, C.B., 2001. Age and Tectonic Significance of Permian Granites in Western Zanskar, High Himalaya. The Journal of Geology, 109, 127–135

Olade, M.A., 1980. Geochemical characteristics of tin bearing and tin-barren granites, Northern Nigeria. Economic Geology 75, 71–82

Onodera, T.F., Yoshinaka, R., Oda, M., 1974. Weathering and Its Relation to Mechanical Properties of Granite. Proceedings 3rd Congress International Society of Rock Mechanic, Denver 2A, 71–78

Onodera, T.F., Asoka, K.H.M., 1980. Relation between petrographic characteristics, engineering index properties and mechanics properties of selected sandstone. Bulletin of the International Association of Engineering Geology 28, 55–71

Olona, J., Pulgar, J.A., Fernández-Viejo, G., López-Fernández, C., González-Cortina, J.M., 2010. Weathering variations in a granitic massif and related geotechnical properties through seismic and electrical resistivity methods. Near Surface Geophysics 8, 585-599. DOI: 10.3997/1873-0604.2010043.

Pan, G.Q., Ding, J., Yao, D.S., Wang, L.Q., 2004. Geological Map of the Qinghai-Xizang (Tibet) Plateau and Adjacent Areas. Chengdu Cartographic Publishing House

Pandit, D., Panigrahi, M.K., Moriyama, T., 2014. Constrains from magmatic and hydrothermal epidotes on crystallization of granitic magma and sulfide mineralization in Paleoproterozoic Malanjkhand Granitoid, Central India. Chemie der Erde 74, 715–733

Papritz, K., Rey, R., 1989, Evidence for the occurrence of Permian Panjal trap basalts in the Lesser- and Higher-Himalayas of the western syntaxis area, NE Pakistan: Eclogae Geologicae Helvetiae 82, 603–627

Parrish, R.R., Tirrul, R., 1989. U-Pb age of the Baltoro granite, northwest Himalaya, and implications for zircon inheritance and monazite U-Pb systematics. Geology 17, 1076-1079

Patiňo Douce, A.E., Humphreys, E.D., Johnston, A.D., 1990. Anatexis and metamorphism in tectonically thickened continental crust exemplified by the Sevier hinterland, western North America. Earth and Planetary Science Letters 97, 290–315

Patiňo Douce, A.E., Johnston, A.D., 1991. Phase equilibria and melt productivity in thepelitic system: implications for the origin of peraluminous granitoids and aluminous granulites. Contributions to Mineralogy and Petrology 107, 202–218

Patiño Douce, A.E., Beard, J.S., 1995. Dehydration-melting of biotite gneiss and quartz amphibolite from 3 to 15 kbar. Journal of Petrology 36, 707–738

Patiño Douce, A.E., Harris, N.B.W., 1998. Experimental constraints on Himalayan anatexis. Journal of Petrology 39, 689–710

Pearce, T.H., 1968. A contribution to the theory of variation diagrams. Contributions to Mineralogy and Petrology 19, 142–157

Pearce, T.H., Gorman, B.E., Birkett, T.C., 1977. The relationship between major element chemistry and tectonic environment of basic and intermediate volcanic rocks. Earth and planetary science letters 36, 121-132

Pearce, J.A., Harris, N.B.W., Tindle, A.G., 1984. Trace element discrimination diagrams for the tectonic interpretation of granitic rocks. Journal of Petrology 25, 956–983

Peate, D.W., Hawkesworth, C.J., Mantovani, M.S.M., 1992. Chemical stratigraphy of magma types and their spatial distribution. Bulletin of Volcanology 55, 119–139

Perugini, D., Poli, G., 2007. Tourmaline nodules from Capo Biancoaplite (Elba Island, Italy): an example of diffusion limited aggregation growth in a magmatic system. Contributions to Mineralogy and Petrology 153, 493–508. DOI: 10.1007/s00410-006-0167-3

Petford, N., Atherton, M., 1996. Na-rich partial melts from newly under plated basaltic crust: the Cordillera Blanca Batholith, Peru. Journal of Petrology 37, 1491–1521

Petterson, M.G., Windley, B.F., 1991. Changing source regions of magmas and crustal growth in the Trans-Himalayas: Evidence from the Chalt volcanics and

Kohistan batholith, Kohistan, N. Pakistan, Earth Planetary Science Letters 102, 326-346

Petterson, M.G., 2010. A Review of the geology and tectonics of the Kohistan island arc, north Pakistan. *In*: Kusky, T. M., Zhai, M.G., Xiao, W. (eds) The Evolving Continents: Understanding Processes of Continental Growth. Geological Society, London, Special Publications 338, 287–327

Pirajno, F., Smithies, R.H., 1992. The FeO/(FeO+MgO) ratio of tourmaline: a useful indicator of spatial variations in granite-related hydrothermal mineral deposits. Journal of Geochemical Exploration 42, 371-381

Pognante, U., Lombardo, B., 1989. Metamorphic evolution of the High Himalayan Crystallines in SE Zanskar, India. Journal of metamorphic Geology 7, 9-17

Pognante, U., Castelli, D., Benna, P., Genovese,G., Oberli, F., Meir,M., and Tonarini, S., 1990, The crystalline units of the High Himalayas in the Lahul-Zanskar region (northwest India): Metamorphic-tectonic history and geochronology of the collided and imbricated Indian plate. Geological Magazine 127, 101–116

Pogue, K.R., Hussain, A., 1986. New light on the stratigraphy of the Nowshera area and the discovery of Early to Middle Ordovician trace fossils in N.W.F.P., Pakistan, Geological Survey of Pakistan Information Release 135, pp. 15

Pogue, K.R., DiPietro, J.A., Khan, S.R., Hughes, S.S., Dilles, J.H., Lawrence, R.D., 1992a. Late Paleozoic rifting in northern Pakistan. Tectonics 11 (4), 871-883

Pogue, K.R., Wardlaw, B.R., Harris, A.G., Hussain, A., 1992b. Paleozoic and Mesozoic stratigraphy of Peshawar basin, Pakistan; Correlations and implications. Geological Society of America Bulletin 104, 915-927

Pogue, K.R., Hylland, M.D., Yeats, R.S., Khattak, W.U., Hussain, A., 1999. Structural framework of the Himalayan foothills, northern Pakistan. Geological Society of America Special Paper 328, 259–274

Pudsey, C.J., 1986. The Northern Suture, Pakistan: Margin of a Cretaceous island arc. Geological Magazine 123, 405-423

Quigley, M.C., Yu, L.J., Gregory, C., Corvino, A., Sandiford, M., Wilson, C.J.L., Liu, X.H., 2008. U–Pb SHRIMP zircon geochronology and T-t-d history of the Kampa Dome, southern Tibet. Tectonophysics 446, 97–113

Rafiq, M., Jan, M.Q., 1988. Petrography of Ambela granitic complex, NW Pakistan. Geological Bulletin, University of Peshawar 21, 27-48

Rafiq, M., Jan, M.Q., 1989. Geochemistry and petrogenesis of Ambela granitic complex, NW Pakistan. Geological Bulletin, University of Peshawar 22, 159-179

Rai, B., Kwatra, S.K., Singh, V.P., Sharma, N.K., 1993. Whole rock Rb–Sr age for granitic rocks of Khadrala area, district Shimla, Himachal Pradesh, India. Preprint Volume 6th National Symposium Mass Spectrometry 8, 1–4

Raisanen, M., 2004. Relationships between texture and mechanical properties of hybrid rocks from the Jaala–Iitti complex, southeastern Finland. Engineering Geology 74, 197–211

Rene, M., Stelling, J., 2007. Garnet-bearing granite from the Trebic Pluton, Bohemian Massif (Czech Republic). Mineralogy and Petrology 91, 55–69

Rigopoulos, I., Tsikouras, B., Pomonis, P., Hatzipanagiotou, K., 2010. The influence of alteration on the engineering properties of dolerites: the examples from the Pindos and Vourinos ophiolites (northern Greece). International Journal of Rock Mechanics and Mining Sciences 47, 69–80

Rigopoulos, I., Tsikouras, B., Pomonis, P., Hatzipanagiotou, K., 2013. Petrographic investigation of microcrack initiation in mafic ophiolitic rocks under uniaxial compression. Rock Mechanics and Rock Engineering 46, 1061–1072

Rigopoulos, I., Tsikouras, B., Pomonis, P., Hatzipanagiotou, K., 2014. Correlations between petrographic and geometrical properties of ophiolitic aggregates from Greece. Bulletin of Engineering Geology and Environment 73, 1–12

Ringuette, L., Martignole, J., Windley, B.F., 1999. Magmatic crystallization, isobaric cooling, and decompression of the garnet-bearing assemblages of the Jijal Sequence (Kohistan Terrane, western Himalayas). Geology 27, 139–142

Rollinson, G.K., Stickland, R.J., Andersen, J.C., Fairhurst, R., Boni, M., 2011. Characterisation of Supergene Non-Sulphide Zinc Deposits using QEMSCAN. Minerals Engineering 24, 778-787

Rollinson, H.R., 1993. Using geochemical data: evaluation, presentation, interpretation. Longman group limited, England

Rozendaal, A., Bruwer, L., 1995. Tourmaline nodules: indicators of hydrothermal alteration and Sn–Zn–(W) mineralization in the Cape Granite Suite, South Africa. Journal of African Earth Sciences 21, 141–155

Rudnick, R.L., Gao, S., 2003. The composition of the continental crust. *In:* Rudnick, R.L., Holland, H.D., Turekian, K.K. (eds.), The Crust Treatise on Geochemistry 3, Elsevier, Oxford, 1–64

Ruiz, C., Fernández-Leyva, C., Locutura, J., 2008. Geochemistry, geochronology and mineralisation potential of the granites in the Central Iberian Zone: The Jalama batholith. Chemie der Erde 68, 413-429

Russell, J.K., Nicholls, J., 1988. Analysis of petrological hypothesis with Pearce element ratios. Contributions to Mineralogy and Petrology 99, 25–35

Sajid, M., Arif, M., Muhammad, N., 2009. Petrographic characteristics and mechanical properties of rocks from Khagram-Razagram area, Lower Dir, NWFP, Pakistan. Journal of Himalayan Earth Sciences 42, 25-36

Sajid, M., Arif, M., 2010. Field features and petrography of igneous rocks from Utla (Gadoon), NW Pakistan: Preliminary investigation. Journal of Himalayan Earth Sciences 43, 75-76

Sajid, M., Arif, M., Shah, M.T., 2014. Petrogenesis of granites from the Utla area of Gadoon, north-west Pakistan: Implications from Petrography and Geochemistry. Journal of Earth Science 25, 445-459

Sajid, M., Arif, M., 2015. Reliance of physico-mechanical properties on petrographic characteristics: consequences from the study of Utla granites, north-west Pakistan. Bulletin of Engineering Geology and Environment 74, 1321–1330. DOI 10.1007/s10064-014-0690-9

Sajid, M., Coggan, J., Arif, M., Andersen, J.C., Rollinson, G., 2016. Petrographic features as an effective indicator for the variation in strength of granites. Engineering Geology 202, 44-54

Saunders, A.D., Storey, M., Kent, R.W., Norry, M.J., 1992. Consequences of plume-lithosphere interactions. *In:* Storey, B.C., Alabaster, T., Pankhurst, R.J. (eds.), Magmatism and the Causes of Continental Break-up. Geological Society of London Special Publication 68, 41–60

Schaltegger, U., Zeilinger, G., Frank, M., Burg, J.P., 2002. Multiple mantle sources during island arc magmatism: U–Pb and Hf isotopic evidence from the Kohistan arc complex, Pakistan. Terra Nova 14, 461–468

Schärer, U., Allègre, C.J., 1983. The Palung granite (Himalaya): high resolution U–Pb systematics in zircon and monazite. Earth and Planetary Science Letters 63, 423–432

Schelling, D., 1992. The tectonostratigraphy and structure of the eastern Nepal Himalaya: Tectonics 11, 925–943

Schelling, D., 1999. Geological map of eastern Nepal Himalaya at 1:650,000 scale. Journal of Asian Earth Sciences AD9-AD20

Schmidt, M.W., Poli, S., 2004. Magmatic epidote. Reviews in Mineralogy and Geochemistry 56, 399–430

Searle, M.P., 1983, Stratigraphy, structure and evolution of the Tibetan Tethys zone in Zanskar and the Indus suture zone in the Ladakh Himalaya. Royal Society of Edinburgh Transactions, Earth Sciences 73, 203–217

Searle, M.P., 1986. Structural evolution and sequence of thrusting in the High Himalayan, Tibetan-Tethys and Indus suture zones of Zanskar and Ladakh, Western Himalaya. Journal of Structural Geology 8 (8), 923-936

Searle, M.P., 1999. Extensional and compressional faults in the Everest-Lhotse massif, Khumbu Himalaya, Nepal. Journal of the Geological Society London 156, 227–240

Searle, M.P., Rex, A.J., Tirrul, R., Rex, D.C., Bamicoat, A., Windley, B.F., 1989. Metamorphic, magmatic and tectonic evolution of the Central Karakoram in the

Biafo-Baltoro-Hushe regions of north Pakistan. Geological Society of America special paper 232, 47-73

Searle, M.P., Tirrul, R., 1991. Structural and thermal evolution of the Karakoram crust. Journal of the Geological Society London 148, 65-82

Searle, M.P., Crawford, M.B., Rex, A.J., 1992. Field relations, geochemistry, origin and emplacement of the Baltoro granite, Central Karakoram. Royal Society of Edinburgh Transactions, Earth Sciences 83, 519-538

Searle, M.P., Khan, M.A., Fraser, J.E., Gough, S.J., Jan, M.Q., 1999. The tectonic evolution of the Kohistan–Karakoram collision belt along the Karakoram Highway transect, North Pakistan. Tectonics 18, 929–949

Searle, M.P., Law, R.D., Godin, L., Larson, K., Streule, M.J., Cottle, J.M., Jessup, M. J., 2008. Defining the Himalayan Main Central Thrust in Nepal. Journal of the Geological Society London 165, 523–34

Searle, M.P., Cottle, J.M., Streule, M.J., Waters, D.J., 2009. Crustal melt granites and migmatites along the Himalaya: melt source, segregation, transport and granite emplacement mechanisms. Transactions of the Royal Society of Edinburgh 100, 1–15. DOI:10.1017/S175569100901617X

Searle, M.P., Treloar, P.J., 2010. Was late Cretaceous – Palaeocene obduction of ophiolite complexes the primary cause of crustal thickening and regional metamorphism in the Pakistan Himalaya? *In:* Kusky, T.M., Zhai, M.G., Xiao, W., (eds.), The evolving continents: Understanding processes of continental growth. Geological Society London Special Publication 338, 345–359

Sengor, A.M.C., 1979. Mid-Mesozoic closure of Permo-Triassic Tethys and its implications. Nature 279 (5714), 590–593

Sengör, A.M.C., 1987. Tectonics of the Tethysides: orogenic collage development in a collisional setting: Annual Review of Earth and Planetary Sciences 15, 213–244

Sengör, A.M.C., Altner, D., Cin, A., Ustaömer, T., Hsu, K.J., 1988. Origin and assembly of the Tethyside orogenic collage at the expense of Gondwanaland. *In:* Audley-Charles, M.G., Hallam, A., (eds.), Gondwana and Tethys. Geological Society of London Special Publication 37, 119–181

Shah, S.M.I., Siddique, R.A., Talent, J.A., 1980. Geology of eastern Khyber agency, NWFP Pakistan. Geological survey of Pakistan records 44, pp. 31

Shah, S.M.I., 2009. Stratigraphy of Pakistan. Geological Survey of Pakistan Memorial, Volume 22

Shellnutt, J.G., Bhat, G.M., Brookfield, M.E., Jahn, B.M., 2011. No link between the Panjal Traps (Kashmir) and the Late Permian mass extinctions. Geophysical Research Letters-Solid Earth 38, L19308

Shellnutt, J.G., Bhat, G.M., Wang, K.L., Brookfield, M.E., Dostal, J., Jahn, B.M., 2012. Origin of the silicic volcanic rocks of the Early Permian Panjal Traps, Kashmir, India. Chemical Geology 334, 154–170

Shellnutt, J.G., Bhat, G.M., Wang, K.L., Brookfield, M.E., Jahn, B.M., Dostal, J., 2014. Petrogenesis of the flood basalts from the Early Permian Panjal Traps, Kashmir, India: Geochemical evidence for shallow melting of the mantle. Lithos 204, 159–171

Sial, A.N., Toselli, A.J., Saavedra, J., 1999. Emplacement, petrological and magnetic susceptibility characteristics of diverse magmatic epidote-bearing granitoid rocks in Brazil, Argentina and Chile. Lithos 46, 367–392

Sial, A.N., Vasconcelos, P.M., Ferreira, V.P., Pessoa, R.R., Brasilino, R.G., Morais Neto, J.M., 2008. Geochronological and mineralogical constraints on depth of emplacement and ascencion rates of epidote-bearing magmas from north-eastern Brazil. Lithos 105, 225–238

Silva, T.T., Ferreira, V.P., Lima, M.M.C., Sial, A.N., Silva, J.M.R., 2015. Synkinematic emplacement of the magmatic epidote bearing MajorIsidorotonalite-granite batholith: Relicts of an Ediacaran continental arc in the Pernambucoe Alagoas domain, Borborema Province, NE Brazil. Journal of South American Earth Sciences 64, 1-13

Simons, B., Shail, R.K., Andersen, J.C., 2016. The petrogenesis of the Early Permian Variscan granites of the Cornubian Batholith: Lower plate post-collisional peraluminous magmatism in the Rhenohercynian Zone of SW England. Lithos 260, 76–94

Sinclair, W.D., Richardson, J.M., 1992. Quartz–tourmaline orbicules in the Seagull Batholith, Yukon Territory. Canadian Mineralogist 30, 923–935

Singh, M.P, Nanda, M.M., Sinha. P.K. 1976: The Ralakung Volcanics of the Zanskar Valley, Ladakh - Its Geological Settings Petrography, Petrochemistry and a Comparative Study with the Panjal Volcanics of the Northwestern Himalayas. Geological Survey of India misc. Publication 41, 218-228

Singh, S., Barley, M.E., Brown, S.J., Jain, A.K., Manickavasagam, R.M., 2002. SHRIMP U-Pb in zircon geochronology of the Chor granitoid: evidence for Neoproterozoic magmatism in the Lesser Himalayan granite belt of NW India. Precambrian Research 118, 285-292

Skjerlie, K.P., Johnston, A.D., 1996. Vapour-absent melting from 10 to 20 kbar of crustal rocks that contain multiple hydrous phases: implications for anatexis in the deep to very deep continental crust and active continental margins. Journal of Petrology 37, 661–691

Slack, J.F., Coad, P.R., 1989. Multiple hydrothermal and metamorphic events in the Kidd Creek volcanogenic massive sulphide deposit, Timmins, Ontario: evidence from tourmalines and chlorites. Canadian Journal of Earth Sciences 26, 694-715

Smith, A.G., Hurley, A.M., Briden, J.C., 1981. Phanerozoic Paleo-continental world maps. Cambridge University Press. pp. 102

Smith, H.A., Chamberlain, C.P., Zeitler, P.K., 1994. Timing and Duration of Himalayan Metamorphism within the Indian Plate, Northwest Himalaya, Pakistan. Journal of Geology 102, 493–508

Solomovich, L.I., Trifonov, B.A., Sabelnikov, S.E., 2012. Geology and mineralization of the Uchkoshkon tin deposit associated with a breccia pipe, Eastern Kyrgyzstan. Ore Geology Reviews 44, 59–69

Sousa, L.M.O., Suarez del Rio, L.M., Calleja, L., Ruiz de Argandona, V., Rey, A.R., 2005. Influence of microfractures and porosity on the physico-mechanics properties and weathering of ornamental granites. Engineering Geology 77, 153–168

Sousa, L.M.O., 2013. The influence of the characteristics of quartz and mineral deterioration on the strength of granitic dimensional stones. Environmental Earth Sciences 69 (4), 1333–1346

Sousa, L.M.O., 2014. Petrophysical properties and durability of granites employed as building stone: a comprehensive evaluation. Bulletin of Engineering Geology and Environment 73, 569–588

Spencer, D.A., Tonarini, S., Pognante, U., 1995, Geochemical and Sr-Nd isotopic characterisation of Higher Himalayan eclogites (and associated metabasites): European Journal of Mineralogy 7 (1), 89–102

Spencer, C.J., Harris, R.A., Sachan, H.K., Saxena, A., 2011. Depositional provenance of the Greater Himalayan Sequence, Garhwal Himalaya, India: implications for tectonic setting. Journal of Asian Earth Sciences 41, 344–354

Spencer, C.J., Harris, R.A., Dorais, M.J., 2012. Depositional provenance of the Himalayan metamorphic core of Garhwal region, India: constrained by U–Pb and Hf isotopes in zircons. Gondwana Research 22, 26-35

Springer, W., Seck, H.A., 1997. Partial fusion of basic granulites at 5 to 15 kbar: implications for the origin of TTG magmas. Contributions to Mineralogy and Petrology 127, 30–45

Srivastava, P.K., Sinha, A.K., 1997. Geochemical characterization of tungsten-bearing granites from Rajasthan, India. Journal of Geochemical Exploration 60, 173–184

Stacey, J.S., Kramers, J.D., 1975. Approximation of terrestrial lead isotope evolution by a two-stage model. Earth and Planetary Science Letters 26, 207-221

Steiger, R.H., Jäger, E., 1977. Subcommission on geochronology: convention on the use of decay constants in geo- and cosmochronology. Earth and Planetary Science Letters 36, 359-362

Stern, R.J., 1994. Arc assembly and continental collision in the Neoproterozoic East African Orogen: implications for the consolidation of Gondwana. Annual Review of Earth and Planetary Sciences 22, 319–51

Sun, S.S., McDonough, W.F., 1989. Chemical and isotopic systematics of ocean basalts: implications for mantle composition and processes. *In:* Saunders, A.D., Norry, M.J. (eds.), Magmatism in the Ocean Basins, Geological Society London Special Publications 42, 313-345

Sylvester, P.J., 1998. Post-Collisional Strongly Peraluminous Granites. Lithos 45, 29–44

Taylor, S.R., McLennan, S.M., 1985. The continental crust: Its composition and evolution. Blackwell, Oxford, pp. 312

Taylor, J., Stevens, G., 2010. Selective entrainment of peritectic garnet into S-type granitic magmas: evidence from Archaean mid-crustal anatectites. Lithos 120, 277–292

Tingyu, C., Guiying, S., Yupeng, Y., Huilan, C., 1995. Peraluminous granites of East Tethys and their implication in Gondwana dispersion and Asian accretion. Journal of Southeast Asian Earth Sciences 11 (3), 243-251

Tischendorf, G., Förster, H.J., Gottesmann, B., 2001. Minor- and trace-element composition of trioctahedral micas: a review. Mineralogical Magazine 65, 249–276

Tindle, A.G., Breaks, F.W., Selway, J.B., 2002. Tourmaline in petalite-subtype granitic pegmatites: Evidence of fractionation and contamination from the Pakeagama lake and separation lake areas of northwestern Ontario, Canada. The Canadian Mineralogist 40, 753-788

Treloar, P.J., 1997. Thermal controls on early-Tertiary, short-lived, rapid regional metamorphism in the NW Himalaya, Pakistan. Tectonophysics 273, 77-104

Treloar, P.J., Broughten, R.D., Coward, M.P., Williams, M.P., Windley, B.F., 1989a. Deformation, metamorphism and imbrication of the Indian plate south of MMT, north Pakistan. Journal of Metamorphic Geology 7, 111-127

Treloar, P.J., Williams, M.P. Coward, M.E, 1989b. Metamorphism and crustal stacking in the north Indian Plate, North Pakistan. Tectonophysics 165, 167-184

Treloar, P.J., Coward, M.E, Williams, M.E., Khan, M.A., 1989c. Basement-cover imbrication south of the Main Mantle Thrust, North Pakistan. Geological Society of America, Special Paper 232, 137-152

Treloar, P.J., Rex, D.C., Guise, P.G., Coward, M.P., Searle, M.P., Windley, B.F. Petterson, M.G., Jan, M.Q., Luff, I.W., 1989d. K-Ar and Ar-Ar Geochronology of the Himalayan Collision in NW Pakistan: Constraints on the Timing of Suturing, Deformation, Metamorphism and Uplift. Tectonics 8 (4), 881-909

Treloar, P.J., Rex, D.C., 1990. Cooling and uplift histories of the crystalline thrust stack of the Indian Plate internal zones west of Nanga Parbat, Pakistan Himalaya. Tectonophysics 180, 323-349

Treloar, P.J., Petterson, M.G., Jan, M.Q., Sullivan, M.A., 1996, A re-evaluation of the stratigraphy and evolution of the Kohistan arc sequence, Pakistan Himalaya: Implications for magmatic and tectonic arc-building processes. Journal of Geological Society London 153, 681–693

Trivedi, J.R., Sharma, K.K., Gopalan, K.S., 1986. Widespread Caledonian magmatism in Himalaya and its significance. Terra Cognita 6, 144

Trivedi, J.R., 1990. Geochronological studies of Himalayan granitoids. Unpublished Ph.D. Thesis, Physical Research Laboratory, Ahmedabad, pp. 170

Trumbull, R.B., Krienitz, M.S., Gottesmann, B., Wiedenbeck, M., 2008. Chemical and boron-isotope variations in tourmalines from an S-type granite and its source rocks: the Erongo granite and tourmalinites in the Damara Belt, Namibia. Contributions to Mineralogy and Petrology 155, 1–18

Tugrul, A., Zarif, I.H., 1999. Correlation of mineralogical and textural characteristics with engineering properties of selected granitic rocks from Turkey. Engineering Geology 51, 303–317

Tugrul, A., 2004. The effect of weathering on pore geometry and compressive strength of selected rock types from Turkey. Engineering Geology 75, 215–227

Tullborg, E.L., Larson, S.A., 2006. Porosity in crystalline rocks: a matter of scale. Engineering Geology 84, 75–83

Tulloch, A., 1979. Secondary Ca–Al silicates as low-grade alteration products of granitoid biotite. Contributions to Mineralogy and Petrology 69, 105–117

Tulloch, A., 1986. Comment on “Implications of magmatic epidote-bearing plutons on crustal evolution in the accreted terranes of northwestern North America” and “Magmatic epidote and its petrologic significance”. Geology 14, 186–187

Turner, S., Hawkesworth, C., 1995. The nature of the sub-continental mantle: constraints from the major-element composition of continental flood basalts. Chemical Geology 120, 295–314

Undul, O., Tugrul, A., 2012. The influence of weathering on the engineering properties of dunites. Rock Mechanics Rock Engineering 45, 225–239

Unrug, R., 1996. The assembly of Gondwanaland. Episodes 19 (1-2), 11-20

Valdiya, K.S., 1980. Geology of the Kumaun Lesser Himalaya: Dehra Dun, Wadia Institute of Himalayan Geology 291

Valdiya, K.S., 1995. Proterozoic sedimentation and Pan-African geodynamic development in the Himalaya, the northern frontier of east Gondwanaland. Gondwana Research 1, 3–9

Vannay, J.C., Spring, L., 1993, Geochemistry of the continental basalts within the Tethyan Himalaya of Lahul-Spiti and SE Zanzkar (NW India), in Trelor, P. J., and Searle, M., editors, Himalayan Tectonics: Geological Society London Special Publications 74, 237–249

Vielzeuf, D., Montel, J.M., 1994. Partial melting of metagreywackes. Part I. Fluid absent experiments and phase relationships. Contributions to Mineralogy and Petrology 117, 375–393

Villaros, A., Stevens, G., Buick, I.S., 2009. Tracking S-type granite from source to emplacement: clues from garnet in the Cape Granite Suite. Lithos 112, 217–235

Visonà, D., Rubatto, D., Villa, I.M., 2010. The mafic rocks of Shao La (Kharta, S. Tibet): Ordovician basaltic magmatism in the greater Himalayan crystallines of central eastern Himalaya. Journal of Asian Earth Sciences 38, 14–25

Wadia, D.N., 1961. Geology of India. McMillan and Company, London, pp. 536

Wang, Y.Z., 2000. Tectonics and Mineralization of Southern Sanjiang Area. Geology Press, Beijing 45–49 (in Chinese with English abstract)

Wang, J.W., Cheng, Z.L., Gui, X.T., Xu, R.H., Rage, Y.Q., 1981. Rb–Sr isotopic studies on some intermediate-acid plutons in Southern Xizang. Geochemistry 3, 242–246 (in Chinese with English abstract)

Wang, M., Li, C., Zhai, Q.G., Xie, C.M., Wu, Y.W., 2009.Magma homology of mafic dyke and basalt in southern Qiangtang, northern Tibet, China. Geological Bulletin of China 28 (9), 1281–1289 (in Chinese with English abstract)

Wang, Y.J., Zhang, F.F., Fan, W.M., Zhang, G.W., Chen, S.Y., Cawood, P.A., Zhang, A.M., 2010. Tectonic setting of the South China Block in the early Paleozoic: resolving intracontinental and ocean closure models from detrital zircon U–Pb geochronology. Tectonics 29, TC6020

Wang, B.D., Wang, L.Q., Pan, G.T., Yin, F.G., Wang, D.B., Tang, Y., 2012. U–Pb zircon dating of early Paleozoic gabbro from the Nantinghe ophiolite in the Changning–Menglian suture zone and its geological implication. Chinese Science Bulletin 58, 344–354

Wang, Y.J., Xing, X.W., Cawood, P.A., Lai, S.C., Xia, X.P., Fan, W.M., Liu, H.C., Zhang, F.F., 2013. Petrogenesis of early Paleozoic peraluminous granite in the Sibumasu Block of SW Yunnan and diachronous accretionary orogenesis along the northern margin of Gondwana. Lithos 182–183, 67–85

Wang, M., Li, C., Wu, Y.W., Xie, C.M., 2014a. Geochronology, geochemistry, Hf isotopic compositions and formation mechanism of radial mafic dikes in northern Tibet. International Geology Review 56 (2), 187–205

Wang, X.C., Li, Z.X., Li, J., Pisarevsky, S.A., Wingate, M.T.D., 2014b. Genesis of the 1.21Ga Marnda Moorn large igneous province by plume-lithosphere interaction. Precambrian Research 241, 85–103

Wazir, K., Arif, M., Sajid, M., 2015. Controls and Implications of Geo-Technical Variation in Quartzose Rocks from Peshawar Basin, North-Western Pakistan. Geomaterials 5, 85-98

Weaver, B.L., 1991. The origin of ocean island basalt end member compositions: trace element and isotopic constraints. Earth and Planetary Science Letters 104, 381–397

Weinert, H.N., 1964. Basic igneous rocks in road foundations. National Institute Road Research Bulletin, Pretoria, South Africa 5, 1-47

White, L.T., Ireland, T.R., 2012. High-uranium matrix effect in zircon and its implications for SHRIMP U–Pb age determinations. Chemical Geology 306-307, 78–91

Wiedenbeck, M., 1995. An example of reverse discordance during ion microprobe zircon dating: An artifact of enhanced ion yields from a radiogenic labile Pb. Chemical Geology 125, 197-218

Wiedenbeck, M., Alle, P., Corfu, F., Griffin, W.L., Meier, M., Oberli, F., Von Quart, A., Roddick, J.C., Spiegel, W., 1995. Three natural zircon standards for U–Th–Ph, Lu–Th, trace element and REE analyses. Geostandards Newsletter 19(1), 1–23

Williams, M.P., Treloar, P.J., Coward, M.P., 1988. More evidence of pre-Himalayan orogenesis in northern Pakistan. Geological Magazine 125, 651-652

Williams, I.S., Hergt, J.M., 2000. U–Pb dating of Tasmanian dolerites: a cautionary tale of SHRIMP analysis of high-U zircon. *In:* Woodhead, J.D., Hergt, J.M., Noble, W.P. (eds.), Beyond 2000: New Frontiers in Isotope Geoscience. Lorne, Abstract Proceedings, 185–188

Winchester, J.A., Floyd, P.A., 1977. Geochemical discrimination of different magma series and their differentiation products using immobile elements. Chemical Geology 20, 325–343

Windley, B.F., Whitehouse, M.J., Ba-Bttat, M.A.O., 1996. Early Precambrian gneiss terranes and Pan-African island arcs in Yemen: crustal accretion of eastern Arabian shield. Geology (Boulder) 24 (2), 131-134

Winter J.D., 2010. Principles of igneous and metamorphic petrology, 2nd Edition. Pearson Education Incorporation

Wood, D.A., 1980. The application of a Th-Hf-Ta diagram to problems of tectonomagmatic classification and to establishing the nature of crustal contamination of basaltic lavas of the British Tertiary volcanic province. Earth and planetary science letters 50, 11-30

Wu, F.Y., Jahn, B.M., Wilde, S.A., Lo, C.H., Yui, T.F., Lin, Q., Ge, W.C., Sun, D.Y., 2003. Highly fractionated I-type granites in NE China (I): geochronology and petrogenesis. Lithos 66, 241–273

Xia, L., Xia, Z., Xu, X., Li, X., Ma, Z., 2013. Late Paleoproterozoic rift-related magmatic rocks in the North China Craton: Geological records of rifting in the Columbia supercontinent, Earth-Science Reviews 125, 69–86

Xia, L.Q., Xia, Z.C., Xu, X.Y., Li, X.M., Ma, Z.P., 2007. The discrimination between continental basalt and island arc basalt based on geochemical method. Acta Petrologica et Mineralogica 26, 77–89

Xiao, L., Xu, Y.G., Mei, H.J., Zheng, Y.F., He, B., Pirajno, F., 2004. Distinct mantle sources of low-Ti and high-Ti basalts from the western Emeishan large igneous province, SW China: implications for plume–lithosphere interaction. Earth and Planetary Science Letters 228, 525–546

Xu, Y.G., Chung, S.L., Jahn, B.M., Wu, G.Y., 2001. Petrologic and geochemical constraints on the petrogenesis of Permian–Triassic Emeishan flood basalts in southwestern China. Lithos 58, 145–168

Xu, L., Xiao, Y., Wu F., Li, S., Simon K., Wörner, G., 2013. Anatomy of garnets in a Jurassic granite from the south-eastern margin of the North China Craton: Magma sources and tectonic implications. Journal of Asian Earth Sciences 78, 198–221

Xu, W., Dong, Y., Zhang, X., Deng, M., Zhang, L., 2015. Petrogenesis of high-Ti mafic dykes from Southern Qiangtang, Tibet: Implications for a ca. 290 Ma large igneous province related to the early Permian rifting of Gondwana. Gondwana Research, DOI: http://dx.doi.org/10.1016/j.gr.2015.07.016

Yang, X.J., Jia, X.C., Xiong, C.L., Bai, X.Z., Huang, B.X., Luo, G., Yang, C.B., 2012. LA-ICP-MS zircon U–Pb age of metamorphic basic volcanic rock in Gongyanghe Group of southern Gaoligong Mountain, western Yunnan Province, and its geological significance. Geological Bulletin of China 31, 264–276 (in Chinese with English abstract)

Yang, J., Peng, J., Hu, R., Bi, X., Zhao, J., Fu, Y., Shen, N.P., 2013. Garnet geochemistry of tungsten-mineralized Xihuashan granites in South China. Lithos 177, 79–90

Yeats, R.S., Hussain, A., 1987. Time of structural events in Himalayan foothills of northwestern Pakistan. Geological society of America bulletin 99, 161-176

Yildiz, A., Kuscu, M., Dumlupunar, I., Aritan, A.E., Bagcı, M., 2010. The determination of the mineralogical alteration index and the investigation of the efficiency of the hydrothermal alteration on physico-mechanical properties in volcanic rocks from Koprulu, Afyonkarahisar, West Turkey. Bulletin of Engineering Geology and Environment 69, 51–61

Yilmaz, N.G., Goktan, R.M., Kibici, Y., 2011. Relations between some quantitative petrographic characteristics and mechanical strength properties of granitic building stones. International Journal of Rock Mechanics and Mining Science 48, 506–513

Yu, Z., Robinson, P., McGoldrick, P., 2001. An evaluation of methods for the chemical decomposition of geological materials for trace element determination using ICP-MS. Geostandards Newsletter 25, 199–217

Zeitler, P.K., 1988. Ion microprobe dating of zircon from the Malakand granite, NW Himalaya, Pakistan. A constraint on the timing of Tertiary metamorphism in the region. Geological Society of America Abstracts Programs 20, 323

Zeitler, P.K., Chamberlain, C.P., Smith, H.A., 1993. Synchronous anatexis, metamorphism and rapid denudation at Nanga Parbat (Pakistan Himalaya): Geology 21, 347–350

Zen, E., 1985. Implications of magmatic epidote-bearing plutons on crustal evolution in the accreted terranes of northwestern North-America. Geology 13, 266–269

Zen, E., Hammarstrom, J.M., 1984. Magmatic epidote and its petrologic significance. Geology 12, 515–518

Zhai, Q.G., Jahn, B.M., Su, L., Ernst, R.E., Wang, K.L., Zhang, R.Y., Wang, J., Tang, S., 2013, SHRIMP zircon U-Pb geochronology, geochemistry and Sr-Nd-Hf isotopic compositions of a mafic dyke swarm in the Qiangtang terrane, northern Tibet and geodynamic implications: Lithos 174, 28–43

Zhang, Z.M., Wang, J.L., Shen, K., Shi, C., 2008a. Paleozoic circun-Gondwana orogens: petrology and geochronology of the Namche Barwa Complex in the eastern Himalayan syntaxis, Tibet. Acta Petrologica Sinica 24, 1627–1637 (in Chinese with English abstract)

Zhang, Z.M., Wang, J.L., Zhao, G.C., Shi, C., 2008b. Geochronology and Precambrian tectonic evolution of the Namche Barwa complex from the eastern Himalayan syntaxis. Acta Petrologica Sinica 24, 1477–1487 (in Chinese with English abstract)

Zhang, Y.C., Shen, S.Z., Shi, G.R.,Wang, Y., Yuan, D.X., Zhang, Y.J., 2012. Tectonic evolution of the Qiangtang Block, northern Tibet during the Late Cisuralian (Late Early Permian): evidence from fusuline fossil records. Palaeogeography, Palaeoclimatology, Palaeoecology 350–352, 139–148

Zhang, L., Ding, X., Budhu, M., 2012. A rock expert system for the evaluation of rock properties. International Journal of Rock Mechanics and Mining Sciences 50,124–132

Zhao, J.H., Asimow, P.D., 2014. Neoproterozoic boninite-series rocks in South China: a depleted mantle source modified by sediment-derived melt. Chemical Geology 388, 98–111

Zhou, Z.G., Liu, W.C., Liang, D.Y., 2004. Discovery of the Ordovician and its basal conglomerate in the Kangmar area, southern Tibet-with a discussion of the relation of the sedimentary cover and unifying basement in the Himalayas. Geological Bulletin of China 23, 655–663 (in Chinese with English abstract)

Zhu, D.C., Mo, X.X., Zhao, Z.D., Niu, Y., Wang, L.Q., Chu, Q.H., Pan, G.T., Xu, J.F., Zhou, C.Y., 2010. Presence of Permian extension- and arc-type magmatism in southern Tibet: paleogeographic implications: Geological Society of America Bulletin 122(7–8), 979–993

Zhu, D.C., Zhao, Z.D., Niu, Y.L., Dilek, Y., Wang, Q., Ji, W.H., Dong, G.C., Sui, Q.L., Liu, Y.S., Yuan, H.L., Mo, X.X., 2012. Cambrian bimodal volcanism in the Lhasa

Terrane, southern Tibet: record of an early Paleozoic Andean-type magmatic arc in the Australian proto-Tethyan margin. Chemical Geology 328, 290–308

Zhu, D.C., Zhao, Z.D., Niu, Y.L., Dilek, Y., Hou, Z.Q., Mo, X.X., 2013. The origin and pre-Cenozoic evolution of the Tibetan Plateau. Gondwana Research 23 (4), 1429-1454

Zorlu, K., Gokceoglu, C., Ocakoglu, F., Nefeslioglu, H.A., Acikalin, S., 2008. Prediction of uniaxial compressive strength of sandstones using petrography-based models. Engineering Geology 96, 141–158

APPENDIX-1

Major element chemistry of major and accessory minerals in studied granites. Concentration is in “%age”

Plagioclase

Point	UT-69_5	UT-69_5	UT-69_5	UT-69_5	UT-69_5	UT-69_5	UT-69_5	UT-69_5	UT-69_5	UT-69_5	UT-69_5	UT-65-45	UT-65-46	UT-65-47	UT-65-48	UT-65-49
Type	MPG	MPG	MPG	MPG	MPG	MPG	MPG	MPG	MPG	MPG	MPG	MPG	MPG	MPG	MPG	MPG
Comment	Plg	Plg	Plg	Plg	Plg	Plg	Plg	Plg	Plg	Plg	Plg	Plg-core	Plg-core	Plg-mar	Plg-mar	Plg-mar
SiO_2	65.24	64.70	64.25	63.88	64.05	65.07	65.30	65.47	65.79	62.72	64.15	59.20	60.46	66.41	62.68	61.40
Al_2O_3	22.08	22.69	22.33	22.12	22.24	22.40	22.38	21.94	21.58	23.77	23.20	24.76	23.77	19.46	22.22	23.12
CaO	2.90	3.38	3.42	3.77	3.11	3.15	3.08	2.44	2.45	4.96	4.02	6.51	5.88	3.44	4.14	4.82
Na_2O	10.46	10.46	10.28	9.94	10.63	10.86	10.38	10.72	10.83	9.45	9.92	7.85	8.44	8.62	9.29	8.85
K_2O	0.10	0.10	0.11	0.11	0.11	0.09	0.11	0.08	0.09	0.18	0.15	0.57	0.14	0.09	0.15	0.27
Total	100.77	101.33	100.39	99.82	100.14	101.58	101.26	100.64	100.74	101.07	101.42	98.89	98.69	98.03	98.48	98.46
Formula (8 O apfu)																
Si	2.85	2.82	2.83	2.83	2.83	2.83	2.85	2.87	2.88	2.76	2.80	2.67	2.72	2.96	2.81	2.77
Al	1.14	1.17	1.16	1.15	1.16	1.15	1.15	1.13	1.11	1.23	1.19	1.32	1.26	1.02	1.18	1.23
Ca	0.14	0.16	0.16	0.18	0.15	0.15	0.14	0.11	0.11	0.23	0.19	0.32	0.28	0.16	0.20	0.23
Na	0.89	0.88	0.88	0.85	0.91	0.92	0.88	0.91	0.92	0.80	0.84	0.69	0.74	0.75	0.81	0.77
K	0.005	0.006	0.006	0.006	0.006	0.005	0.006	0.004	0.005	0.010	0.008	0.033	0.008	0.005	0.008	0.015
Ab	86.73	84.84	84.46	82.69	86.08	86.18	85.90	88.82	88.89	77.50	81.70	68.57	72.20	81.93	80.24	76.87
An	13.27	15.16	15.54	17.31	13.92	13.82	14.10	11.18	11.11	22.50	18.30	31.43	27.80	18.07	19.76	23.13

Plagioclase (continued)

Point	UT-65-50	UT-65-51	UT-65-52	UT-65-53	UT-65-54	UT-65-57	UT-65-58	UT-44-5	UT-44-6	UT-44-6	UT-44-6	UT-44-6	UT-44-6	UT-44-6	UT-24-3	UT-24-3
Type	MPG	MPG	MPG	MPG	MPG	MPG	MPG	AMG	AMG	AMG	AMG	AMG	AMG	AMG	AMG	AMG
Comment	Plg-mar	Plg-mar	Plg-core	Plg-core	Plg-core	Plg	Plg	Plg	Plg	Plg	Plg	Plg	Plg	Plg	Plg	Plg
SiO_2	62.06	63.46	59.51	60.32	58.02	60.62	61.34	67.93	68.33	69.09	68.37	68.37	68.73	68.74	67.44	67.71
Al_2O_3	22.68	21.83	24.83	23.67	25.21	23.30	22.93	19.39	19.53	19.79	19.66	19.52	19.53	19.83	19.58	19.92
CaO	4.62	3.48	5.42	5.72	7.74	5.57	4.96	0.27	0.10	0.09	0.06	0.05	0.09	0.09	0.99	0.27
Na_2O	9.13	9.85	7.44	8.54	7.30	8.58	8.85	11.73	11.60	12.27	12.44	12.19	12.10	12.44	12.66	12.15
K_2O	0.24	0.17	1.18	0.11	0.13	0.22	0.21	0.09	0.06	0.06	0.07	0.07	0.08	0.08	0.22	0.12
Total	98.73	98.79	98.70	98.36	98.40	98.29	98.29	99.41	99.62	101.30	100.60	100.20	100.53	101.17	100.89	100.17
Formula (8 O apfu)																
Si	2.79	2.84	2.69	2.73	2.64	2.74	2.77	2.99	2.99	2.98	2.98	2.99	2.99	2.98	2.95	2.96
Al	1.20	1.15	1.32	1.26	1.35	1.24	1.22	1.01	1.01	1.01	1.01	1.00	1.00	1.01	1.01	1.03
Ca	0.22	0.17	0.26	0.28	0.38	0.27	0.24	0.01	0.005	0.004	0.003	0.002	0.004	0.004	0.05	0.01
Na	0.79	0.85	0.65	0.75	0.64	0.75	0.77	1.00	0.99	1.03	1.05	1.03	1.02	1.04	1.07	1.03
K	0.014	0.010	0.068	0.006	0.007	0.013	0.012	0.005	0.003	0.003	0.004	0.004	0.005	0.004	0.01	0.01
Ab	78.15	83.67	71.30	72.99	63.06	73.60	76.35	98.76	99.51	99.61	99.72	99.78	99.59	99.61	95.86	98.80
An	21.85	16.33	28.70	27.01	36.94	26.40	23.65	1.24	0.49	0.39	0.28	0.22	0.41	0.39	4.14	1.20

Plagioclase (continued)

Point	UT-24_3	UT-24_3	UT-24_3	UT-24_3	UT-24_3	UT-24_3	UT-24_3	UT-24_3	UT-24_3	UT-24_3	U-19_4	U-19_4	U-19_4	U-19_4	U-19_4	U-19_4	U-19_4	U-19_4
Type	AMG	AMG	AMG	AMG	AMG	AMG	AMG	AMG	AMG	AMG	AMG	AMG	AMG	AMG	AMG	AMG	AMG	AMG
Comment	Plg	Plg	Plg	Plg	Plg	Plg	Plg	Plg	Plg	Plg	Plg	Plg	Plg	Plg	Plg	Plg	plg	Plg
SiO_2	68.47	67.19	66.86	66.38	67.06	68.46	65.47	67.34	69.73	69.52	67.79	68.38	67.61	66.56	68.28	67.34	66.92	68.26
Al_2O_3	19.83	19.75	19.64	19.66	19.72	20.24	21.71	19.68	20.57	20.23	20.58	19.91	20.39	21.27	20.50	20.71	20.75	19.98
CaO	0.17	0.40	0.36	0.32	0.30	0.32	0.22	0.15	0.13	0.25	0.99	0.41	0.94	2.10	0.77	1.21	1.33	0.93
Na_2O	12.23	11.95	12.50	11.50	11.02	12.29	10.20	13.25	12.14	12.16	11.77	12.01	12.30	11.36	12.09	11.42	11.40	11.83
K_2O	0.10	0.09	0.11	0.15	0.19	0.18	1.73	0.11	0.49	0.08	0.10	0.10	0.09	0.12	0.07	0.10	0.12	0.08
Total	100.79	99.38	99.47	98.01	98.39	101.49	100.15	100.53	103.19	102.24	101.24	100.81	101.32	101.41	101.71	100.78	100.51	101.08
Formula (8 O apfu)																		
Si	2.98	2.96	2.95	2.97	2.98	2.96	2.90	2.95	2.97	2.98	2.94	2.97	2.94	2.89	2.95	2.93	2.92	2.96
Al	1.02	1.03	1.02	1.03	1.03	1.03	1.13	1.02	1.03	1.02	1.05	1.02	1.04	1.09	1.04	1.06	1.07	1.02
Ca	0.01	0.02	0.02	0.02	0.01	0.01	0.01	0.01	0.01	0.01	0.05	0.02	0.04	0.10	0.04	0.06	0.06	0.04
Na	1.03	1.02	1.07	1.00	0.95	1.03	0.88	1.13	1.00	1.01	0.99	1.01	1.04	0.96	1.01	0.96	0.97	1.00
K	0.01	0.01	0.01	0.01	0.01	0.01	0.10	0.01	0.03	0.00	0.01	0.01	0.00	0.01	0.00	0.01	0.01	0.00
Ab	99.22	98.17	98.45	98.49	98.54	98.59	98.83	99.37	99.43	98.88	95.55	98.16	95.95	90.73	96.61	94.47	93.93	95.86
An	0.78	1.83	1.55	1.51	1.46	1.41	1.17	0.63	0.57	1.12	4.45	1.84	4.05	9.27	3.39	5.53	6.07	4.14

Orthoclase

Point	UT-69_4	UT-69_4	UT-69_4	UT-69_4	UT-69_4	UT-69_4	UT-69_4	UT-69_4	UT-44_4	UT-44_4	UT-44_4	UT-44_4	UT-44_4	U-19_4	U-19_4	U-19_4	U-19_4
Type	MPG	MPG	MPG	MPG	MPG	MPG	MPG	MPG	AMG	AMG	AMG	AMG	AMG	AMG	AMG	AMG	AMG
Comment	Or	Or	Or	Or	Or	Or	Or	Or	Or	Or	Or	Or	Or	Or	Or	Or	Or
SiO_2	64.75	64.39	65.10	64.48	64.48	64.87	63.62	64.29	63.57	63.75	64.46	65.46	66.23	64.59	63.63	64.32	65.03
Al_2O_3	18.61	18.46	18.69	18.34	18.75	18.49	18.19	18.39	18.14	18.34	18.33	18.48	18.69	18.61	18.29	18.41	18.63
CaO				0.09				0.08	0.12	0.06						0.45	0.06
Na_2O	0.85	0.88	0.71	0.87	1.22	0.77	0.81	1.19	0.36	0.54	0.84	0.55	1.69	0.78	0.64	0.57	0.54
K_2O	14.84	14.67	14.89	14.66	14.38	15.07	14.78	14.40	15.38	15.15	14.56	15.50	12.69	15.13	15.64	15.46	15.41
BaO	0.10	0.09	0.09	0.09	0.13	0.09	0.12	0.10			0.04						
Total	99.15	98.49	99.48	98.52	98.94	99.29	97.53	98.44	97.57	97.84	98.23	99.99	99.30	99.13	98.20	99.21	99.68
Formula (8 O apfu)																	
Si	3.00	3.00	3.00	3.00	2.99	3.00	3.00	3.00	3.00	3.00	3.01	3.01	3.02	3.00	2.99	2.99	3.00
Al	1.02	1.01	1.02	1.01	1.02	1.01	1.01	1.01	1.01	1.02	1.01	1.00	1.01	1.02	1.01	1.01	1.01
Ca	0.00	0.00	0.00	0.00	0.00	0.00	0.00	0.00	0.01	0.00	0.00	0.00	0.00	0.00	0.00	0.02	0.00
Na	0.08	0.08	0.06	0.08	0.11	0.07	0.07	0.11	0.03	0.05	0.08	0.05	0.15	0.07	0.06	0.05	0.05
K	0.88	0.87	0.88	0.87	0.85	0.89	0.89	0.86	0.93	0.91	0.87	0.91	0.74	0.90	0.94	0.92	0.91
Ba	0.00	0.00	0.00	0.00	0.00	0.00	0.00	0.00	0.00	0.00	0.00	0.00	0.00	0.00	0.00	0.00	0.00

Orthoclase (continued)

Point	U-19_4	U-19_4	U-19_4	U-19_4	UT-24_3	UT-24_3	UT-24_3	UT-24_3	UT-24_3	UT-24_3	UT-24_3	UT-24_3	UT-24_3	UT-24_3	UT-24_3	UT-24_3	UT-24_3
Type	AMG	AMG	AMG	AMG	AMG	AMG	AMG	AMG	AMG	AMG	AMG	AMG	AMG	AMG	AMG	AMG	AMG
Comment	Or	Or	Or	Or	Or	Or	Or	Or	Or	Or	Or	Or	Or	Or	Or	Or	Or
SiO_2	64.35	64.59	63.09	64.34	61.20	62.12	64.32	63.79	63.35	63.02	62.56	60.78	63.35	64.79	62.98	54.65	64.78
Al_2O_3	18.35	18.54	18.61	18.83	17.60	17.92	18.39	18.12	18.10	18.02	17.80	17.58	18.18	18.72	18.31	24.83	19.01
CaO			0.24		0.12	0.06				0.30	0.05				0.07	0.10	0.10
Na_2O	0.50	0.77	0.63	0.80	0.47	0.51	0.51	0.65	0.55	0.53	0.56	0.32	0.60	0.48	0.41	2.47	2.15
K_2O	15.92	15.37	14.86	15.42	15.41	15.78	15.88	15.78	15.66	15.80	15.90	15.44	16.08	15.64	16.14	4.67	13.32
BaO																	
Total	99.12	99.28	97.43	99.39	94.79	96.39	99.10	98.35	97.66	97.67	96.87	94.13	98.20	99.64	97.91	89.13	99.36
Formula (8 O apfu)																	
Si	3.00	3.00	2.98	2.98	2.99	2.98	3.00	3.00	2.99	2.99	1.49	2.99	2.99	2.99	2.98	2.76	2.98
Al	1.01	1.01	1.04	1.03	1.01	1.01	1.01	1.00	1.01	1.01	0.67	1.02	1.01	1.02	1.02	1.48	1.03
Ca	0.00	0.00	0.01	0.00	0.01	0.00	0.00	0.00	0.00	0.02	0.02	0.00	0.00	0.00	0.00	0.01	0.00
Na	0.05	0.07	0.06	0.07	0.04	0.05	0.05	0.06	0.05	0.05	0.10	0.03	0.05	0.04	0.04	0.24	0.19
K	0.95	0.91	0.90	0.91	0.96	0.97	0.94	0.95	0.94	0.96	1.91	0.97	0.97	0.92	0.97	0.30	0.78
Ba	0.00	0.00	0.00	0.00	0.00	0.00	0.00	0.00	0.00	0.00	0.00	0.00	0.00	0.00	0.00	0.00	0.00

Biotite

Point	UT-69_2	UT-69_2	UT-69_2	UT-69_2	UT-69_2	UT-69_2	UT-69_2	UT-69_2	UT-65_2	UT-65_2	UT-65_2	UT-65_2	UT-65_2	UT-65_2	UT-24_1	UT-24_1	UT-24_2
Type	MPG	MPG	MPG	MPG	MPG	MPG	MPG	MPG	MPG	MPG	MPG	MPG	MPG	MPG	AMG	AMG	AMG
Comment	Bt	Bt	Bt	Bt	Bt	Bt	Bt	Bt	Bt	Bt	Bt	Bt	Bt	Bt	BTS	BTS	Bt
SiO_2	36.83	36.16	37.00	36.12	35.88	35.80	36.35	36.25	35.40	35.49	34.80	35.05	34.57	34.93	35.33	36.39	36.81
TiO_2	2.39	2.34	2.38	2.80	2.72	2.71	2.41	2.46	2.92	2.98	3.00	2.69	2.69	2.71	2.22	2.24	2.10
Al_2O_3	17.28	17.28	17.31	17.20	17.55	17.40	17.28	17.06	16.51	16.86	16.56	16.96	16.83	16.65	16.30	16.81	17.28
FeO	23.12	22.78	22.85	23.36	22.53	23.08	22.41	23.62	23.99	24.49	24.34	23.94	24.35	24.29	24.61	24.18	25.51
MnO	0.52	0.54	0.52	0.52	0.57	0.54	0.52	0.53	0.33	0.36	0.33	0.31	0.35	0.32	0.40	0.41	0.50
MgO	6.54	6.56	6.52	6.11	6.15	6.16	6.44	6.62	6.96	7.14	6.91	6.98	6.98	7.03	4.07	4.03	4.44
CaO	0.11	0.09	0.06	0.08	0.08	0.10	0.10	bd	bd	bd	bd	bd	bd	bd	0.35	0.26	0.16
Na_2O	bd	bd	bd	bd	0.15	bd	bd	bd	0.13	bd	bd	bd	0.13	0.13	0.22	0.21	0.48
K_2O	8.24	8.29	8.39	8.31	8.05	8.11	8.18	8.66	9.01	9.30	9.17	9.14	9.26	9.19	8.08	8.20	6.85
F	0.36	0.63	0.56	0.55	0.50	0.83	0.19	0.59	0.37	0.53	0.67	0.64	0.29	0.37	0.52	0.36	0.28
Cl	0.13	0.11	0.12	0.12	0.12	0.11	0.10	0.10	0.11	0.12	0.12	0.23	0.24	0.21	0.10	0.10	0.17
Li_2O*	0.46	0.46	0.46	0.57	0.56	0.55	0.48	0.44	0.38	0.35	0.39	0.38	0.38	0.37	0.48	0.86	0.98
Subtotal	95.96	95.24	96.16	95.74	94.86	95.39	94.46	96.33	96.11	97.60	96.28	96.31	96.07	96.19	92.68	94.04	95.56
O=F,Cl	0.18	0.29	0.26	0.26	0.24	0.37	0.10	0.27	0.18	0.25	0.31	0.32	0.18	0.20	0.24	0.17	0.16
Total	95.78	94.95	95.90	95.48	94.62	95.01	94.36	96.06	95.93	97.36	95.97	95.99	95.89	95.99	92.44	93.87	95.41
Formula																	
Si	5.64	5.60	5.66	5.58	5.56	5.55	5.63	5.58	5.50	5.45	5.43	5.45	5.40	5.44	5.69	5.72	5.68
Al iv	2.36	2.40	2.34	2.42	2.44	2.45	2.37	2.42	2.50	2.55	2.57	2.55	2.60	2.56	2.31	2.28	2.32
Al vi	0.76	0.76	0.78	0.71	0.77	0.74	0.79	0.68	0.52	0.50	0.48	0.56	0.50	0.50	0.79	0.84	0.82
Ti	0.28	0.27	0.27	0.33	0.32	0.32	0.28	0.29	0.34	0.34	0.35	0.32	0.32	0.32	0.27	0.26	0.24
Fe	2.96	2.95	2.92	3.02	2.92	2.99	2.90	3.04	3.11	3.14	3.18	3.11	3.18	3.17	3.32	3.18	3.29
Mn	0.07	0.07	0.07	0.07	0.07	0.07	0.07	0.07	0.04	0.05	0.04	0.04	0.05	0.04	0.05	0.05	0.07
Mg	1.49	1.51	1.49	1.41	1.42	1.43	1.49	1.52	1.61	1.63	1.61	1.62	1.63	1.63	0.98	0.95	1.02
Li*	0.28	0.28	0.29	0.35	0.35	0.34	0.30	0.27	0.24	0.22	0.24	0.23	0.24	0.23	0.31	0.54	0.61
Ca	0.02	0.01	0.01	0.01	0.01	0.02	0.02	0.00	0.00	0.00	0.00	0.00	0.00	0.00	0.06	0.04	0.03
Na	0.00	0.00	0.00	0.00	0.05	0.00	0.00	0.00	0.04	0.00	0.00	0.00	0.04	0.04	0.07	0.06	0.14
K	1.61	1.64	1.64	1.64	1.59	1.61	1.62	1.70	1.78	1.82	1.83	1.81	1.85	1.83	1.66	1.65	1.35
F	0.17	0.31	0.27	0.27	0.25	0.41	0.09	0.29	0.18	0.26	0.33	0.32	0.14	0.18	0.27	0.18	0.14
Cl	0.03	0.03	0.03	0.03	0.03	0.03	0.03	0.03	0.03	0.03	0.03	0.06	0.06	0.06	0.03	0.03	0.04
Y total	5.84	5.85	5.82	5.88	5.86	5.89	5.83	5.87	5.86	5.88	5.90	5.89	5.91	5.89	5.72	5.83	6.04
X total	1.63	1.65	1.65	1.65	1.65	1.62	1.63	1.70	1.82	1.82	1.83	1.81	1.89	1.87	1.79	1.75	1.52
Al total	3.12	3.16	3.12	3.13	3.21	3.18	3.16	3.10	3.02	3.05	3.05	3.11	3.10	3.06	3.10	3.12	3.14
Fe/Fe+Mg	0.66	0.66	0.66	0.68	0.67	0.68	0.66	0.67	0.66	0.66	0.66	0.66	0.66	0.66	0.77	0.77	0.76
Mg-Li	1.21	1.23	1.20	1.05	1.07	1.08	1.19	1.25	1.38	1.42	1.37	1.38	1.39	1.40	0.67	0.40	0.41
Fe+Mn+Ti-Al	2.54	2.54	2.48	2.70	2.54	2.65	2.46	2.72	2.98	3.04	3.09	2.91	3.04	3.02	2.85	2.66	2.78

Biotite (continued)

Point	UT-24_2	UT-24_2	UT-24_2	UT-24_2	UT-24_2	UT-24_2	UT-24_1	UT-24_1	UT-24_1	UT-24_1	UT-24_1	UT-24_1
Type	AMG	AMG	AMG	AMG	AMG	AMG	AMG	AMG	AMG	AMG	AMG	AMG
Comment	Bt	Bt	Bt	Bt	Bt	Bt	BTS	BTS	BTS	BTS	BTS	BTS
SiO_2	37.52	34.05	37.28	35.33	36.47	36.08	36.12	36.30	35.26	36.13	35.68	34.56
TiO_2	2.21	2.04	2.13	2.15	2.16	2.33	2.16	2.17	2.09	2.21	2.19	2.16
Al_2O_3	17.21	15.49	17.54	15.77	17.23	16.03	16.99	16.87	17.24	16.25	16.73	16.56
FeO	25.03	24.63	23.72	25.68	25.75	23.57	24.81	24.86	24.81	24.60	25.15	25.65
MnO	0.47	0.35	0.40	0.44	0.40	0.36	0.44	0.37	0.44	0.42	0.42	0.44
MgO	4.30	3.72	3.82	3.88	4.15	4.02	3.96	4.01	4.02	4.10	4.07	3.91
CaO	0.19	0.70	0.17	0.19	0.33	0.25	0.26	0.26	0.49	0.38	0.29	0.32
Na_2O	0.35	0.18	0.32	0.17	0.36	0.23	0.27	0.26	0.38	0.26	0.25	0.41
K_2O	8.20	7.50	8.04	8.00	7.88	8.66	8.27	8.34	7.31	7.88	8.10	7.68
F	0.23	0.39	0.28	0.38	0.35	0.48	0.28	0.47	0.39	0.56	0.43	0.24
Cl	0.12	0.11	0.12	0.11	0.12	0.08	0.11	0.11	0.10	0.10	0.10	0.12
Li_2O*	1.18	0.53	1.12	0.51	0.88	0.77	0.78	0.83	0.49	0.78	0.48	0.50
Subtotal	97.01	89.68	94.92	92.63	96.08	92.86	94.45	94.85	93.01	93.69	93.88	92.55
O=F,Cl	0.12	0.19	0.14	0.19	0.17	0.22	0.14	0.22	0.19	0.26	0.21	0.13
Total	96.89	89.49	94.78	92.44	95.91	92.64	94.30	94.63	92.82	93.43	93.67	92.42
Formula												
Si	5.70	5.68	5.76	5.72	5.64	5.77	5.68	5.69	5.63	5.73	5.67	5.59
Al iv	2.30	2.32	2.24	2.28	2.36	2.23	2.32	2.31	2.37	2.27	2.33	2.41
Al vi	0.79	0.73	0.95	0.73	0.78	0.79	0.83	0.81	0.87	0.77	0.81	0.75
Ti	0.25	0.26	0.25	0.26	0.25	0.28	0.26	0.26	0.25	0.26	0.26	0.26
Fe	3.18	3.44	3.06	3.48	3.33	3.15	3.26	3.26	3.31	3.27	3.34	3.47
Mn	0.06	0.05	0.05	0.06	0.05	0.05	0.06	0.05	0.06	0.06	0.06	0.06
Mg	0.97	0.93	0.88	0.94	0.96	0.96	0.93	0.94	0.96	0.97	0.96	0.94
Li*	0.72	0.36	0.69	0.33	0.55	0.50	0.49	0.53	0.31	0.50	0.31	0.33
Ca	0.03	0.12	0.03	0.03	0.05	0.04	0.04	0.04	0.08	0.06	0.05	0.05
Na	0.10	0.06	0.10	0.05	0.11	0.07	0.08	0.08	0.12	0.08	0.08	0.13
K	1.59	1.60	1.58	1.65	1.55	1.77	1.66	1.67	1.49	1.60	1.64	1.59
F	0.11	0.20	0.14	0.20	0.17	0.24	0.14	0.23	0.20	0.28	0.22	0.12
Cl	0.03	0.03	0.03	0.03	0.03	0.02	0.03	0.03	0.03	0.03	0.03	0.03
Y total	5.98	5.76	5.88	5.79	5.93	5.73	5.83	5.84	5.77	5.83	5.74	5.82
X total	1.72	1.78	1.71	1.74	1.72	1.88	1.78	1.79	1.69	1.74	1.77	1.77
Al total	3.08	3.05	3.19	3.01	3.14	3.02	3.15	3.12	3.24	3.04	3.14	3.16
Fe/Fe+Mg	0.77	0.79	0.78	0.79	0.78	0.77	0.78	0.78	0.78	0.77	0.78	0.79
Mg-Li	0.25	0.57	0.19	0.61	0.41	0.46	0.43	0.41	0.64	0.47	0.66	0.61
Fe+Mn+Ti-Al	2.71	3.01	2.41	3.07	2.85	2.69	2.75	2.75	2.75	2.81	2.85	3.04

Muscovite

Point	UT-69_3	UT-69_3	UT-69_3	UT-69_3	UT-69_3	UT-69_3	UT-69_3	UT-69_3	UT-69_3	UT-69_3	UT-44_3	UT-44_3	UT-44_3	UT-44_3	UT-44_3	UT-24_4	UT-24_4
Type	MPG	MPG	MPG	MPG	MPG	MPG	MPG	MPG	MPG	MPG	AMG	AMG	AMG	AMG	AMG	AMG	AMG
Comment	Mus	Mus	Mus	Mus	Mus	Mus	Mus	Mus	Mus	Mus	Mus	Mus	Mus	Mus	Mus	Mus	Mus
SiO_2	47.14	47.32	47.20	47.84	45.69	46.03	45.89	45.75	45.40	45.66	47.07	46.12	46.33	45.99	46.72	45.53	46.02
TiO_2	0.19	0.63	0.93	0.65	0.42	0.40	0.51	0.42	0.46	0.46	0.09	0.09		0.08	0.05		
Al_2O_3	31.85	31.02	29.95	30.82	34.78	34.87	34.77	33.65	34.31	34.52	35.68	35.06	34.85	34.99	35.03	35.57	35.39
FeO	3.37	3.61	3.37	3.09	2.08	2.02	1.84	2.43	2.59	2.19	1.99	1.35	1.90	1.36	1.33	1.32	1.46
MgO	1.35	1.51	1.52	1.55	0.55	0.58	0.56	0.71	0.63	0.57	0.74	0.55	0.78	0.53	0.63	0.62	0.66
Na_2O	0.24	0.22	0.26	0.27	0.47	0.43	0.45	0.35	0.39	0.50	0.82	0.68	0.87	0.89	0.57	1.03	1.01
K_2O	10.19	10.44	10.37	10.35	10.12	10.43	10.28	10.37	10.30	10.35	10.15	10.02	9.79	9.87	10.39	10.00	10.03
F	0.40	0.71	0.39	0.15	0.15	0.19	0.19	0.16	0.04	0.24	0.13	0.27	0.03	0.04	0.06	0.18	0.18
Li_2O*	0.12	0.25	0.11	0.03	0.03	0.04	0.04	0.03	0.01	0.06	0.03	0.07	0.00	0.01	0.01	0.04	0.04
Subtotal	94.83	95.69	94.09	94.74	94.12	95.00	94.54	93.88	94.12	94.55	96.71	94.22	94.56	93.76	94.78	94.29	94.78
O=F	0.17	0.30	0.16	0.06	0.08	0.08	0.08	0.07	0.02	0.10	0.06	0.11	0.01	0.02	0.02	0.07	0.07
Total	94.66	95.39	93.93	94.68	94.04	94.92	94.46	93.81	94.10	94.45	96.65	94.10	94.55	93.74	94.76	94.22	94.71
Formula																	
Si	6.38	6.38	6.45	6.46	6.17	6.17	6.18	6.22	6.16	6.17	6.18	6.21	6.21	6.21	6.24	6.13	6.16
Al iv	1.62	1.62	1.55	1.54	1.83	1.83	1.82	1.78	1.84	1.83	1.82	1.79	1.79	1.79	1.76	1.87	1.84
Al vi	3.45	3.32	3.28	3.36	3.70	3.69	3.69	3.62	3.64	3.66	3.71	3.77	3.72	3.77	3.76	3.77	3.75
Ti	0.02	0.06	0.10	0.07	0.04	0.04	0.05	0.04	0.05	0.05	0.01	0.01	0.00	0.01	0.00	0.00	0.00
Fe	0.38	0.41	0.39	0.35	0.23	0.23	0.21	0.28	0.29	0.25	0.22	0.15	0.21	0.15	0.15	0.15	0.16
Mg	0.27	0.30	0.31	0.31	0.11	0.12	0.11	0.14	0.13	0.11	0.15	0.11	0.16	0.11	0.13	0.13	0.13
Li*	0.06	0.14	0.06	0.02	0.00	0.02	0.02	0.02	0.00	0.03	0.01	0.04	0.00	0.00	0.00	0.02	0.02
Na	0.06	0.06	0.07	0.07	0.12	0.11	0.12	0.09	0.10	0.13	0.21	0.18	0.23	0.23	0.15	0.27	0.26
K	1.76	1.80	1.81	1.78	1.74	1.78	1.77	1.80	1.78	1.78	1.70	1.72	1.67	1.70	1.77	1.72	1.71
F	0.17	0.30	0.17	0.06	0.07	0.08	0.08	0.07	0.02	0.10	0.06	0.12	0.01	0.02	0.02	0.08	0.07
Y total	4.19	4.23	4.13	4.11	4.09	4.09	4.09	4.10	4.11	4.10	4.10	4.08	4.09	4.04	4.04	4.07	4.07
X total	1.82	1.85	1.88	1.85	1.87	1.90	1.88	1.89	1.88	1.91	1.91	1.90	1.90	1.93	1.92	1.99	1.98
Al total	5.08	4.93	4.83	4.90	5.53	5.51	5.52	5.39	5.48	5.49	5.52	5.56	5.51	5.56	5.52	5.64	5.59
Fe/Fe+Mg	0.58	0.57	0.55	0.53	0.68	0.66	0.65	0.66	0.70	0.68	0.60	0.58	0.58	0.59	0.54	0.54	0.55
Mg-Li	0.21	0.17	0.25	0.29	0.11	0.09	0.09	0.13	0.12	0.08	0.13	0.07	0.15	0.10	0.12	0.10	0.11
Fe+Mn+Ti-Al	-3.05	-2.85	-2.80	-2.95	-3.42	-3.42	-3.43	-3.30	-3.30	-3.37	-3.48	-3.61	-3.50	-3.61	-3.60	-3.62	-3.59

Muscovite (continued)

Point	UT-24_4	UT-24_4	UT-24_4	UT-24_4	UT-24_4	UT-24_4	UT-24_4	UT-24_4	UT-24_4	UT-24_4	UT-24_4	UT-24_4	UT-24_4	UT-24_4	UT-24_4	UT-24_4	UT-24_4
Type	AMG	AMG	AMG	AMG	AMG	AMG	AMG	AMG	AMG	AMG	AMG	AMG	AMG	AMG	AMG	AMG	AMG
Comment	Mus	Mus	Mus	Mus	Mus	Mus	Mus	Mus	Mus	Mus	Mus	Mus	Mus	Mus	Mus	Mus	Mus
SiO_2	45.30	45.50	45.76	46.62	46.39	46.88	45.91	45.17	46.47	45.78	44.94	45.98	46.79	46.01	45.76	45.96	45.95
TiO_2																0.07	0.08
Al_2O_3	34.72	35.36	35.00	34.68	35.80	36.36	34.54	33.74	34.29	35.38	33.62	34.20	34.70	35.06	35.04	34.15	35.83
FeO	1.57	1.48	1.34	2.13	1.81	1.78	1.75	2.10	2.36	1.58	2.08	1.71	2.30	1.62	1.62	2.07	1.50
MgO	0.66	0.64	0.52	0.81	0.67	0.67	0.72	0.76	0.76	0.64	0.71	0.69	0.86	0.59	0.63	0.64	0.52
Na_2O	0.93	0.99	0.73	0.79	0.88	0.72	0.82	0.55	0.48	1.09	0.60	0.83	0.88	0.65	0.81	0.82	0.82
K_2O	10.08	10.13	10.41	10.25	10.03	9.37	9.78	9.21	10.23	9.95	10.63	10.10	10.20	10.21	10.15	10.02	10.22
F	0.07	0.09	0.16	0.16	0.17	0.27	0.15	0.19	0.02	0.13	0.02	0.19	0.05	0.19	0.11	0.33	0.25
Li_2O*	0.01	0.02	0.03	0.03	0.04	0.07	0.03	0.04	0.00	0.03	0.00	0.04	0.01	0.04	0.02	0.09	0.06
Subtotal	93.34	94.22	93.97	95.48	95.82	96.13	93.71	91.80	94.60	94.60	92.60	93.73	95.81	94.37	94.14	94.17	95.25
O=F	0.03	0.04	0.07	0.07	0.07	0.12	0.06	0.09	0.01	0.06	0.01	0.08	0.02	0.08	0.05	0.14	0.11
Total	93.31	94.18	93.90	95.41	95.74	96.01	93.64	91.71	94.59	94.54	92.60	93.65	95.79	94.29	94.09	94.03	95.14
Formula																	
Si	6.17	6.13	6.19	6.22	6.15	6.16	6.21	6.23	6.25	6.15	6.20	6.24	6.22	6.19	6.17	6.22	6.13
Al iv	1.83	1.87	1.81	1.78	1.85	1.84	1.79	1.77	1.75	1.85	1.80	1.76	1.78	1.81	1.83	1.78	1.87
Al vi	3.74	3.75	3.77	3.67	3.75	3.80	3.73	3.72	3.68	3.75	3.66	3.70	3.66	3.75	3.75	3.68	3.77
Ti	0.00	0.00	0.00	0.00	0.00	0.00	0.00	0.00	0.00	0.00	0.00	0.00	0.00	0.00	0.00	0.01	0.01
Fe	0.18	0.17	0.15	0.24	0.20	0.20	0.20	0.24	0.27	0.18	0.24	0.19	0.26	0.18	0.18	0.23	0.17
Mg	0.13	0.13	0.11	0.16	0.13	0.13	0.15	0.16	0.15	0.13	0.15	0.14	0.17	0.12	0.13	0.13	0.10
Li*	0.01	0.01	0.02	0.02	0.02	0.04	0.02	0.02	0.00	0.01	0.00	0.02	0.00	0.02	0.01	0.05	0.03
Na	0.24	0.26	0.19	0.20	0.23	0.18	0.21	0.15	0.12	0.28	0.16	0.22	0.23	0.17	0.21	0.22	0.21
K	1.75	1.74	1.79	1.74	1.70	1.57	1.69	1.62	1.75	1.70	1.87	1.75	1.73	1.75	1.75	1.73	1.74
F	0.03	0.04	0.07	0.07	0.07	0.11	0.07	0.08	0.01	0.06	0.01	0.08	0.02	0.08	0.05	0.14	0.11
Y total	4.06	4.06	4.04	4.09	4.10	4.16	4.09	4.15	4.10	4.07	4.05	4.06	4.09	4.08	4.07	4.09	4.08
X total	1.99	2.00	1.98	1.95	1.92	1.76	1.90	1.77	1.88	1.99	2.03	1.97	1.96	1.92	1.96	1.95	1.95
Al total	5.57	5.62	5.58	5.45	5.60	5.63	5.51	5.49	5.43	5.60	5.47	5.47	5.44	5.56	5.57	5.45	5.64
Fe/Fe+Mg	0.57	0.56	0.59	0.60	0.60	0.60	0.57	0.61	0.64	0.58	0.62	0.58	0.60	0.61	0.59	0.65	0.62
Mg-Li	0.13	0.12	0.09	0.14	0.11	0.09	0.13	0.13	0.15	0.11	0.15	0.12	0.17	0.09	0.12	0.08	0.07
Fe+Mn+Ti-Al	-3.56	-3.59	-3.61	-3.43	-3.54	-3.60	-3.53	-3.48	-3.41	-3.57	-3.42	-3.51	-3.40	-3.57	-3.56	-3.43	-3.60

Tourmaline (GM = discrete tourmaline from MPG groundmass; VT = tourmaline veins; OT = Nodular tourmaline; QRVT = tourmaline from QRV)

Point	UT-69_1	UT-69_1	UT-69_1	UT-69_1	UT-69_1	UT-69_1	UT-69_1	UT-69_1	UT-69_1	UT-69_1	UT-69_1	UT-69_1	UT-69_1	UT-69_1	UT-69_1	UT-69_1	UT-69_1
Type	MPG	MPG	MPG	MPG	MPG	MPG	MPG	MPG	MPG	MPG	MPG	MPG	MPG	MPG	MPG	MPG	MPG
Tour type	GM	GM	GM	GM	GM	GM	GM	GM	GM	GM	GM	GM	GM	GM	GM	GM	GM
SiO_2	36.26	36.11	36.34	36.49	36.46	36.63	36.65	36.86	36.67	37.20	36.32	36.42	36.68	36.85	36.64	36.77	36.49
TiO_2	0.83	0.72	0.87	0.81	0.73	0.74	0.78	0.80	0.72	0.38	0.49	0.81	1.02	0.96	0.31	0.53	0.65
Al_2O_3	34.86	34.47	35.21	33.62	34.47	34.69	34.96	34.90	34.84	35.54	35.37	34.81	33.02	33.71	34.77	35.23	34.55
FeO	9.62	9.77	9.68	9.74	9.30	9.41	9.39	9.32	9.33	9.06	9.05	9.18	8.95	9.03	9.25	9.10	9.18
MgO	3.74	4.06	3.61	4.20	4.04	3.77	3.89	3.92	3.79	3.38	3.57	3.87	4.68	4.40	4.25	3.75	3.81
CaO	0.42	0.45	0.44	0.52	0.58	0.39	0.35	0.37	0.38	0.19	0.34	0.45	0.30	0.28	0.41	0.33	0.40
MnO														0.09	0.09		
Na_2O	1.91	2.05	1.88	1.94	1.90	1.96	1.85	1.83	1.78	1.49	1.80	1.88	2.01	1.84	1.96	1.80	1.96
K_2O	0.04	0.05	0.03	0.06	0.04	0.05	0.04	0.04	0.05		0.04	0.06	0.05	0.05	0.06	0.04	0.05
F	0.08	0.44	0.25	0.21	0.41	0.19	0.31	0.28	0.35	0.32	0.19	0.09	0.28	0.36	0.36	0.28	0.15
Li_2O*	0.39	0.33	0.40	0.36	0.42	0.44	0.37	0.40	0.40	0.40	0.41	0.42	0.37	0.35	0.32	0.41	0.45
Subtotal	88.14	88.44	88.71	87.93	88.35	88.26	88.59	88.72	88.29	87.95	87.58	87.99	87.34	87.92	88.42	88.23	87.69
O=F	0.03	0.19	0.10	0.09	0.17	0.08	0.13	0.12	0.15	0.13	0.08	0.04	0.12	0.15	0.15	0.12	0.06
Total	88.11	88.25	88.60	87.84	88.17	88.18	88.46	88.60	88.15	87.82	87.50	87.95	87.22	87.77	88.27	88.11	87.63
Formula																	
Si	5.84	5.83	5.83	5.91	5.87	5.89	5.87	5.89	5.89	5.96	5.86	5.86	5.96	5.95	5.89	5.90	5.90
Ti	0.10	0.09	0.10	0.10	0.09	0.09	0.09	0.10	0.09	0.05	0.06	0.10	0.12	0.12	0.04	0.06	0.08
Al^T	0.16	0.17	0.17	0.09	0.13	0.11	0.13	0.11	0.11	0.04	0.14	0.14	0.04	0.05	0.11	0.10	0.10
Al^Z	6.00	6.00	6.00	6.00	6.00	6.00	6.00	6.00	6.00	6.00	6.00	6.00	6.00	6.00	6.00	6.00	6.00
Al^Y	0.46	0.40	0.48	0.33	0.42	0.46	0.48	0.47	0.49	0.68	0.59	0.47	0.28	0.36	0.48	0.56	0.47
Mg	0.90	0.98	0.86	1.01	0.97	0.90	0.93	0.93	0.91	0.81	0.86	0.93	1.13	1.06	1.02	0.90	0.92
Mn	0.00	0.00	0.00	0.00	0.00	0.00	0.00	0.00	0.00	0.00	0.00	0.00	0.00	0.01	0.01	0.00	0.00
Fe^{2+}	1.30	1.32	1.30	1.32	1.25	1.26	1.26	1.25	1.25	1.21	1.22	1.24	1.22	1.22	1.24	1.22	1.24
Li*	0.25	0.22	0.26	0.24	0.27	0.28	0.24	0.26	0.26	0.26	0.27	0.27	0.24	0.23	0.21	0.26	0.29
Ca	0.07	0.08	0.08	0.09	0.10	0.07	0.06	0.06	0.07	0.03	0.06	0.08	0.05	0.05	0.07	0.06	0.07
Na	0.60	0.64	0.59	0.61	0.59	0.61	0.57	0.57	0.55	0.46	0.56	0.59	0.63	0.58	0.61	0.56	0.62
K	0.01	0.01	0.01	0.01	0.01	0.01	0.01	0.01	0.01	0.00	0.01	0.01	0.01	0.01	0.01	0.01	0.01
r	0.32	0.27	0.33	0.29	0.30	0.31	0.36	0.36	0.37	0.51	0.37	0.33	0.31	0.36	0.31	0.38	0.31
OH	3.96	3.77	3.88	3.89	3.79	3.90	3.84	3.86	3.82	3.84	3.91	3.95	3.86	3.82	3.82	3.86	3.92
F	0.04	0.23	0.12	0.11	0.21	0.10	0.16	0.14	0.18	0.16	0.09	0.05	0.14	0.18	0.18	0.14	0.08
B	3.00	3.00	3.00	3.00	3.00	3.00	3.00	3.00	3.00	3.00	3.00	3.00	3.00	3.00	3.00	3.00	3.00
Mg/Mg+Fe	0.41	0.43	0.40	0.43	0.44	0.42	0.42	0.43	0.42	0.40	0.41	0.43	0.48	0.46	0.45	0.42	0.43
r/r+Na+K	0.35	0.29	0.36	0.32	0.33	0.34	0.38	0.39	0.40	0.52	0.39	0.35	0.32	0.38	0.33	0.40	0.33

Tourmaline (continued)

Point	UT-69_1	UT-69_1	UT-69_1	UT-69_1	UT-69_1	UT-69_1	UT-69_1	UT-65_3	UT-65_3	UT-65_3	UT-65_3	U-24_1	U-24_2	U-24_2	U-24_1	U-24_2	U-24_1
Type	MPG	MPG	MPG	MPG	MPG	MPG	MPG	MPG	MPG	MPG	MPG	MPG-AMG	MPG-AMG	MPG-AMG	MPG-AMG	MPG-AMG	MPG-AMG
Tour type	GM	GM	GM	GM	GM	GM	GM	GM	GM	GM	GM	VT	VT	VT	VT	VT	VT
SiO_2	36.65	37.37	36.92	37.66	36.60	36.92	36.65	36.03	36.42	36.40	36.63	36.91	37.40	38.15	36.15	36.18	36.65
TiO_2	0.43	0.34	0.79		0.71	0.79	0.90	1.05	1.04	0.88	0.21	0.31	0.33	0.33	0.92	0.94	0.32
Al_2O_3	33.56	35.87	34.06	34.43	34.92	34.05	33.71	33.60	33.80	34.56	35.74	32.93	33.02	33.34	32.51	32.48	32.86
FeO	8.77	8.98	9.18	7.65	9.24	9.59	9.56	8.67	9.14	8.59	7.95	11.63	9.92	8.91	12.77	12.49	12.05
MgO	4.76	3.32	4.00	5.48	3.84	4.34	4.23	4.62	4.38	4.44	4.43	2.85	4.57	5.24	2.78	2.69	2.89
CaO	0.47	0.19	0.37	0.23	0.37	0.46	0.44	0.52	0.50	0.42	0.29	0.09	0.32	0.47	0.32	0.34	0.13
MnO												0.10	0.10		0.16	0.12	0.12
Na_2O	2.08	1.53	1.88	2.05	1.86	2.02	1.87	1.91	1.87	2.05	2.09	2.09	2.33	2.31	2.03	1.84	1.96
K_2O	0.06		0.04		0.05	0.04	0.05				0.06		0.04	0.04			
F	0.34	0.18	0.21	0.49	0.05	0.18	0.44	0.17	0.16	0.17	0.06	0.03	0.10	0.28	0.22	0.21	0.11
Li_2O*	0.37	0.43	0.44	0.32	0.40	0.37	0.36	0.37	0.37	0.41	0.41	0.46	0.40	0.51	0.27	0.30	0.33
Subtotal	87.48	88.21	87.88	88.31	88.04	88.77	88.20	86.93	87.69	87.90	87.86	87.39	88.52	89.57	88.13	87.58	87.39
O=F	0.14	0.08	0.09	0.21	0.02	0.08	0.18	0.07	0.07	0.07	0.02	0.01	0.04	0.12	0.09	0.09	0.05
Total	87.34	88.13	87.79	88.10	88.02	88.69	88.01	86.86	87.62	87.83	87.84	87.38	88.48	89.45	88.04	87.49	87.35
Formula																	
Si	5.95	5.96	5.95	6.01	5.88	5.91	5.92	5.87	5.89	5.86	5.86	6.04	6.02	6.04	5.95	5.97	6.03
Ti	0.05	0.04	0.10	0.00	0.09	0.10	0.11	0.13	0.13	0.11	0.02	0.00	0.00	0.00	0.05	0.03	0.00
Al^T	0.05	0.04	0.05	0.00	0.12	0.09	0.08	0.13	0.11	0.14	0.14	6.00	6.00	6.00	6.00	6.00	6.00
Al^Z	6.00	6.00	6.00	6.00	6.00	6.00	6.00	6.00	6.00	6.00	6.00	0.36	0.26	0.22	0.25	0.29	0.37
Al^Y	0.36	0.70	0.42	0.47	0.49	0.34	0.34	0.33	0.34	0.41	0.59	0.04	0.04	0.04	0.11	0.12	0.04
Mg	1.15	0.79	0.96	1.30	0.92	1.04	1.02	1.12	1.06	1.06	1.06	0.70	1.09	1.24	0.68	0.66	0.71
Mn	0.00	0.00	0.00	0.00	0.00	0.00	0.00	0.00	0.00	0.00	0.00	0.01	0.01	0.00	0.02	0.02	0.02
Fe^{2+}	1.19	1.20	1.24	1.02	1.24	1.28	1.29	1.18	1.24	1.16	1.06	1.59	1.34	1.18	1.76	1.72	1.66
Li*	0.24	0.28	0.28	0.21	0.26	0.24	0.23	0.24	0.24	0.26	0.26	0.30	0.26	0.33	0.18	0.20	0.22
Ca	0.08	0.03	0.06	0.04	0.06	0.08	0.08	0.09	0.09	0.07	0.05	0.02	0.06	0.08	0.06	0.06	0.02
Na	0.65	0.47	0.59	0.63	0.58	0.63	0.59	0.60	0.59	0.64	0.65	0.66	0.73	0.71	0.65	0.59	0.62
K	0.01	0.00	0.01	0.00	0.01	0.01	0.01	0.00	0.00	0.00	0.01	0.00	0.01	0.01	0.00	0.00	0.00
r	0.25	0.49	0.34	0.33	0.35	0.29	0.33	0.31	0.33	0.29	0.29	0.32	0.21	0.20	0.30	0.35	0.35
OH	3.82	3.91	3.89	3.75	3.97	3.91	3.78	3.91	3.92	3.92	3.96	3.99	3.95	3.86	3.89	3.89	3.94
F	0.18	0.09	0.11	0.25	0.03	0.09	0.22	0.09	0.08	0.08	0.03	0.01	0.05	0.14	0.11	0.11	0.06
B	3.00	3.00	3.00	3.00	3.00	3.00	3.00	3.00	3.00	3.00	3.00	3.00	3.00	3.00	3.00	3.00	3.00
Mg/Mg+Fe	0.49	0.40	0.44	0.56	0.43	0.45	0.44	0.49	0.46	0.48	0.50	0.46	0.49	0.50	0.51	0.51	0.51
r/r+Na+K	0.28	0.51	0.37	0.34	0.37	0.31	0.36	0.34	0.36	0.31	0.30	0.40	0.35	0.33	0.33	0.27	0.30

Tourmaline (continued)

Point	U-24_1	U-24_1	U-24_1	U-24_1	U-24_1	U-24_1	U-24_1	U-24_1	U-24_1	U-24_1	U-24_1	U-24_1	U-24_1	U-24_1	U-24_1	U-24_1	U-24_1
Type	MPG-AMG	MPG-AMG	MPG-AMG	MPG-AMG	MPG-AMG	MPG-AMG	MPG-AMG	MPG-AMG	MPG-AMG	MPG-AMG	MPG-AMG	MPG-AMG	MPG-AMG	MPG-AMG	MPG-AMG	MPG-AMG	MPG-AMG
Tour type	VT	VT	VT	VT	VT	VT	VT	VT	VT	VT	VT	VT	VT	VT	VT	VT	VT
SiO_2	37.49	37.09	37.03	36.99	37.21	37.28	37.28	37.00	36.76	36.82	37.11	37.08	37.05	37.00	37.18	36.92	37.10
TiO_2	0.18	0.20	0.22	0.23	0.25	0.25	0.27	0.25	0.26	0.24	0.25	0.25	0.26	0.26	0.25	0.25	0.24
Al_2O_3	33.75	33.33	33.06	33.19	33.28	33.00	32.99	33.32	33.18	33.25	33.27	33.42	33.42	33.66	33.35	33.53	33.83
FeO	9.48	9.06	8.86	8.79	8.91	8.88	8.78	9.32	9.10	9.13	9.23	9.45	9.54	9.49	9.68	9.60	9.72
MgO	4.45	4.83	4.98	5.07	5.22	5.24	5.14	5.13	5.02	4.87	4.75	4.71	4.64	4.54	4.52	4.48	4.46
CaO	0.33	0.37	0.40	0.41	0.45	0.47	0.45	0.49	0.47	0.41	0.43	0.40	0.40	0.41	0.35	0.36	0.34
MnO	0.10	0.11	0.11														
Na_2O	1.81	1.94	1.98	1.97	2.16	2.04	2.16	2.20	2.12	2.10	1.98	2.22	2.07	2.19	2.17	2.10	2.04
K_2O									0.03		0.04					0.04	0.04
F		0.09	0.08	0.15	0.20	0.48	0.28	0.30	0.17	0.34	0.36	0.51	0.22	0.04	0.33	0.28	0.31
Li_2O*	0.35	0.31	0.33	0.31	0.31	0.35	0.41	0.28	0.30	0.31	0.34	0.34	0.31	0.35	0.35	0.32	0.30
Subtotal	87.93	87.34	87.05	87.12	87.98	87.97	87.75	88.28	87.41	87.48	87.76	88.37	87.91	87.94	88.18	87.87	88.38
O=F	0.00	0.04	0.03	0.06	0.08	0.20	0.12	0.13	0.07	0.14	0.15	0.21	0.09	0.02	0.14	0.12	0.13
Total	87.93	87.31	87.02	87.05	87.90	87.77	87.63	88.16	87.34	87.33	87.61	88.15	87.82	87.92	88.04	87.75	88.25
Formula																	
Si	6.03	6.01	6.02	6.01	6.00	6.02	6.02	5.97	5.97	5.98	6.01	5.98	5.99	5.97	6.00	5.98	5.98
Ti	0.00	0.00	0.00	0.00	0.00	0.00	0.00	0.03	0.03	0.02	0.00	0.02	0.01	0.03	0.00	0.02	0.02
Al^T	6.00	6.00	6.00	6.00	6.00	6.00	6.00	6.00	6.00	6.00	6.00	6.00	6.00	6.00	6.00	6.00	6.00
Al^Z	0.40	0.37	0.33	0.35	0.32	0.28	0.28	0.30	0.32	0.35	0.35	0.34	0.36	0.37	0.35	0.38	0.40
Al^Y	0.02	0.02	0.03	0.03	0.03	0.03	0.03	0.03	0.03	0.03	0.03	0.03	0.03	0.03	0.03	0.03	0.03
Mg	1.07	1.17	1.21	1.23	1.25	1.26	1.24	1.23	1.22	1.18	1.15	1.13	1.12	1.09	1.09	1.08	1.07
Mn	0.01	0.02	0.01	0.00	0.00	0.00	0.00	0.00	0.00	0.00	0.00	0.00	0.00	0.00	0.00	0.00	0.00
Fe^{2+}	1.27	1.23	1.20	1.19	1.20	1.20	1.19	1.26	1.24	1.24	1.25	1.28	1.29	1.28	1.31	1.30	1.31
Li*	0.23	0.20	0.22	0.20	0.20	0.23	0.26	0.18	0.19	0.20	0.22	0.22	0.20	0.23	0.23	0.21	0.19
Ca	0.06	0.06	0.07	0.07	0.08	0.08	0.08	0.08	0.08	0.07	0.07	0.07	0.07	0.07	0.06	0.06	0.06
Na	0.56	0.61	0.62	0.62	0.67	0.64	0.68	0.69	0.67	0.66	0.62	0.70	0.65	0.68	0.68	0.66	0.64
K	0.00	0.00	0.00	0.00	0.00	0.00	0.00	0.00	0.01	0.00	0.01	0.00	0.00	0.00	0.00	0.01	0.01
r	0.38	0.32	0.31	0.31	0.25	0.28	0.25	0.23	0.25	0.27	0.30	0.24	0.28	0.24	0.26	0.27	0.30
OH	4.00	3.95	3.96	3.92	3.90	3.76	3.85	3.84	3.91	3.83	3.82	3.74	3.89	3.98	3.83	3.86	3.84
F	0.00	0.05	0.04	0.08	0.10	0.24	0.15	0.16	0.09	0.17	0.18	0.26	0.11	0.02	0.17	0.14	0.16
B	3.00	3.00	3.00	3.00	3.00	3.00	3.00	3.00	3.00	3.00	3.00	3.00	3.00	3.00	3.00	3.00	3.00
Mg/Mg+Fe	0.51	0.50	0.50	0.49	0.48	0.47	0.46	0.46	0.45	0.45	0.45	0.45	0.45	0.44	0.45	0.44	0.44
r/r+Na+K	0.27	0.25	0.27	0.29	0.32	0.25	0.30	0.26	0.28	0.29	0.31	0.31	0.34	0.33	0.36	0.42	0.40

Tourmaline (continued)

Point	U-24_1	U-24_1	U-24_1	U-24_1	U-24_1	U-24_1	U-24_1	U-24_1	U-24_2	U-24_2	U-24_2	U-24_2	U-24_2	U-24_2	U-24_2	U-24_2	U-24_2
Type	MPG-AMG	MPG-AMG	MPG-AMG	MPG-AMG	MPG-AMG	MPG-AMG	MPG-AMG	MPG-AMG	MPG-AMG	MPG-AMG	MPG-AMG	MPG-AMG	MPG-AMG	MPG-AMG	MPG-AMG	MPG-AMG	MPG-AMG
Tour type	VT	VT	VT	VT	VT	VT	VT	VT	VT	VT	VT	VT	VT	VT	VT	VT	VT
SiO_2	37.25	37.37	37.21	37.31	37.51	37.48	37.48	37.40	36.79	36.71	36.88	36.96	36.74	36.80	36.69	37.04	37.08
TiO_2	0.25	0.24	0.24	0.24	0.24	0.24	0.24	0.24	0.15	0.16	0.15	0.15	0.15	0.14	0.15	0.15	0.14
Al_2O_3	33.74	33.98	33.74	33.88	34.05	34.28	34.01	34.06	33.66	33.82	33.72	33.78	33.50	33.69	33.85	33.91	33.77
FeO	9.65	9.64	9.76	9.69	9.87	9.85	9.82	9.79	9.65	9.95	9.77	10.00	9.96	9.93	10.17	10.15	10.07
MgO	4.37	4.41	4.38	4.37	4.30	4.30	4.22	4.24	3.93	3.91	3.85	3.75	3.71	3.71	3.75	3.75	3.70
CaO	0.33	0.32	0.32	0.31	0.29	0.31	0.29	0.30	0.25	0.23	0.22	0.23	0.22	0.22	0.22	0.22	0.20
MnO									0.10			0.11	0.10				0.11
Na_2O	2.08	2.01	2.03	1.92	1.75	1.83	1.79	1.76	2.22	2.21	2.11	2.17	2.12	2.23	2.01	2.07	1.94
K_2O				0.04	0.04			0.04				0.04					0.03
F	0.29	0.39	0.38		0.41	0.23	0.20	0.21	0.36	0.14	0.19	0.30	0.05	0.16	0.15	0.04	0.10
Li_2O*	0.34	0.32	0.31	0.31	0.29	0.27	0.33	0.30	0.39	0.36	0.38	0.39	0.38	0.41	0.32	0.36	0.38
Subtotal	88.31	88.67	88.36	88.07	88.75	88.79	88.37	88.32	87.50	87.49	87.28	87.85	86.94	87.28	87.32	87.68	87.53
O=F	0.12	0.16	0.16	0.00	0.17	0.10	0.09	0.09	0.15	0.06	0.08	0.12	0.02	0.07	0.06	0.02	0.04
Total	88.19	88.51	88.20	88.07	88.58	88.69	88.29	88.23	87.34	87.43	87.20	87.73	86.92	87.21	87.25	87.66	87.49
Formula																	
Si	6.00	6.00	6.00	6.00	6.01	5.99	6.02	6.01	5.99	5.97	6.00	5.99	6.00	5.99	5.98	6.00	6.02
Ti	0.00	0.00	0.00	0.00	0.00	0.01	0.00	0.00	0.01	0.03	0.00	0.01	0.00	0.01	0.02	0.00	0.00
Al^T	6.00	6.00	6.00	6.00	6.00	6.00	6.00	6.00	6.00	6.00	6.00	6.00	6.00	6.00	6.00	6.00	6.00
Al^Z	0.40	0.42	0.40	0.42	0.43	0.45	0.43	0.45	0.44	0.45	0.47	0.45	0.45	0.46	0.48	0.47	0.46
Al^Y	0.03	0.03	0.03	0.03	0.03	0.03	0.03	0.03	0.02	0.02	0.02	0.02	0.02	0.02	0.02	0.02	0.02
Mg	1.05	1.05	1.05	1.05	1.03	1.03	1.01	1.02	0.95	0.95	0.93	0.91	0.90	0.90	0.91	0.91	0.90
Mn	0.00	0.00	0.00	0.00	0.00	0.00	0.00	0.00	0.01	0.00	0.00	0.01	0.01	0.00	0.00	0.00	0.02
Fe^{2+}	1.30	1.29	1.32	1.30	1.32	1.32	1.32	1.32	1.31	1.35	1.33	1.36	1.36	1.35	1.39	1.37	1.37
Li*	0.22	0.21	0.20	0.20	0.19	0.18	0.21	0.19	0.26	0.23	0.25	0.25	0.25	0.27	0.21	0.23	0.25
Ca	0.06	0.06	0.05	0.05	0.05	0.05	0.05	0.05	0.04	0.04	0.04	0.04	0.04	0.04	0.04	0.04	0.04
Na	0.65	0.62	0.63	0.60	0.55	0.57	0.56	0.55	0.70	0.70	0.67	0.68	0.67	0.70	0.64	0.65	0.61
K	0.00	0.00	0.00	0.01	0.01	0.00	0.00	0.01	0.00	0.00	0.00	0.01	0.00	0.00	0.00	0.00	0.01
r	0.29	0.32	0.31	0.34	0.40	0.38	0.39	0.39	0.26	0.26	0.30	0.27	0.29	0.26	0.33	0.31	0.35
OH	3.85	3.80	3.81	4.00	3.79	3.88	3.90	3.90	3.81	3.93	3.90	3.85	3.98	3.92	3.92	3.98	3.95
F	0.15	0.20	0.19	0.00	0.21	0.12	0.10	0.10	0.19	0.07	0.10	0.15	0.02	0.08	0.08	0.02	0.05
B	3.00	3.00	3.00	3.00	3.00	3.00	3.00	3.00	3.00	3.00	3.00	3.00	3.00	3.00	3.00	3.00	3.00
Mg/Mg+Fe	0.43	0.44	0.42	0.41	0.41	0.40	0.40	0.40	0.40	0.40	0.40	0.41	0.40	0.40	0.40	0.41	0.40
r/r+Na+K	0.41	0.41	0.27	0.27	0.31	0.28	0.30	0.27	0.34	0.32	0.36	0.32	0.34	0.32	0.36	0.32	0.34

Tourmaline (continued)

Point	UT-28_1	UT-28_1	UT-28_1	UT-28_1	UT-28_1	UT-28_2	UT-28_2	UT-28_2	UT-28_2	UT-82_1	UT-82_1	UT-82_1	UT-82_1	UT-82_1	UT-82_1	UT-82_1	UT-82_1
Type	AMG	AMG	AMG	AMG	AMG	AMG	AMG	AMG	AMG	QRV	QRV	QRV	QRV	QRV	QRV	QRV	QRV
Tour type	OT	OT	OT	OT	OT	OT	OT	OT	OT	QRVT	QRVT	QRVT	QRVT	QRVT	QRVT	QRVT	QRVT
SiO_2	36.08	36.29	36.02	36.08	36.30	34.94	35.01	34.94	35.21	37.09	37.01	37.07	37.16	37.01	36.92	37.22	36.92
TiO_2	0.56	0.60	0.65	0.63	0.54	0.45	0.39	0.33	0.27	0.11	0.10	0.10	0.10	0.11	0.10	0.11	0.11
Al_2O_3	33.82	33.92	34.46	33.79	33.82	35.27	33.83	35.60	35.57	36.03	36.13	35.87	35.88	36.01	35.72	35.72	35.90
FeO	12.53	12.77	13.18	12.21	12.50	13.81	14.81	13.63	13.88	11.68	11.56	11.45	11.95	11.60	11.54	11.50	11.42
MgO	2.25	2.11	1.64	2.21	2.31	0.68	0.81	0.86	0.75	1.39	1.33	1.34	1.43	1.39	1.37	1.37	1.39
CaO	0.07	0.10	0.13	0.09	0.10	0.29	0.20	0.25	0.24								
MnO	0.12		0.11	0.11	0.12	0.22	0.17	0.21	0.20		0.10		0.09				0.13
Na_2O	2.09	1.99	1.96	1.89	2.03	1.92	1.97	1.82	2.01	1.28	1.30	1.26	1.21	1.22	1.29	1.31	1.24
K_2O	0.05	0.04	0.05	0.07	0.07	0.07	0.07	0.04									
F	0.33	0.56	0.39	0.36	0.37	0.32	0.30	0.40	0.50	0.20	0.08	0.18	0.16	0.13		0.09	0.31
Li_2O*	0.30	0.32	0.32	0.32	0.31	0.34	0.24	0.27	0.32	0.37	0.38	0.42	0.32	0.37	0.39	0.46	0.37
Subtotal	88.18	88.67	88.93	87.76	88.47	88.29	87.79	88.35	88.94	88.15	88.00	87.67	88.31	87.83	87.32	87.77	87.77
O=F	0.14	0.23	0.17	0.15	0.15	0.13	0.12	0.17	0.21	0.08	0.03	0.07	0.07	0.06	0.00	0.04	0.13
Total	88.04	88.44	88.76	87.61	88.32	88.16	87.67	88.18	88.72	88.07	87.97	87.60	88.24	87.77	87.32	87.73	87.64
Formula																	
Si	5.91	5.93	5.87	5.93	5.93	5.76	5.84	5.75	5.77	5.98	5.97	6.00	5.99	5.98	6.00	6.02	5.98
Ti	0.09	0.07	0.13	0.07	0.07	0.24	0.16	0.25	0.23	0.02	0.03	0.00	0.01	0.02	0.00	0.00	0.02
Al^T	6.00	6.00	6.00	6.00	6.00	6.00	6.00	6.00	6.00	6.00	6.00	6.00	6.00	6.00	6.00	6.00	6.00
Al^Z	0.45	0.46	0.50	0.48	0.44	0.62	0.50	0.66	0.65	0.83	0.84	0.84	0.81	0.85	0.83	0.80	0.84
Al^Y	0.07	0.07	0.08	0.08	0.07	0.06	0.05	0.04	0.03	0.01	0.01	0.01	0.01	0.01	0.01	0.01	0.01
Mg	0.55	0.51	0.40	0.54	0.56	0.17	0.20	0.21	0.18	0.33	0.32	0.32	0.34	0.33	0.33	0.33	0.34
Mn	0.02	0.00	0.02	0.02	0.02	0.03	0.02	0.03	0.03	0.00	0.01	0.00	0.01	0.00	0.00	0.00	0.02
Fe^{2+}	1.72	1.74	1.80	1.68	1.71	1.91	2.07	1.88	1.90	1.58	1.56	1.55	1.61	1.57	1.57	1.55	1.55
Li*	0.20	0.21	0.21	0.21	0.20	0.22	0.16	0.18	0.21	0.24	0.25	0.27	0.21	0.24	0.26	0.30	0.24
Ca	0.01	0.02	0.02	0.02	0.02	0.05	0.04	0.04	0.04	0.00	0.00	0.00	0.00	0.00	0.00	0.00	0.00
Na	0.66	0.63	0.62	0.60	0.64	0.61	0.64	0.58	0.64	0.40	0.41	0.39	0.38	0.38	0.40	0.41	0.39
K	0.01	0.01	0.01	0.01	0.02	0.01	0.01	0.01	0.00	0.00	0.00	0.00	0.00	0.00	0.00	0.00	0.00
r	0.31	0.35	0.34	0.37	0.32	0.32	0.31	0.36	0.32	0.60	0.59	0.61	0.62	0.62	0.60	0.59	0.61
OH	3.83	3.71	3.80	3.81	3.81	3.83	3.84	3.79	3.74	3.90	3.96	3.91	3.92	3.93	4.00	3.95	3.84
F	0.17	0.29	0.20	0.19	0.19	0.17	0.16	0.21	0.26	0.10	0.04	0.09	0.08	0.07	0.00	0.05	0.16
B	3.00	3.00	3.00	3.00	3.00	3.00	3.00	3.00	3.00	3.00	3.00	3.00	3.00	3.00	3.00	3.00	3.00
Mg/Mg+Fe	0.24	0.23	0.18	0.24	0.25	0.08	0.09	0.10	0.09	0.18	0.17	0.17	0.18	0.18	0.17	0.17	0.18
r/r+Na+K	0.32	0.35	0.35	0.37	0.33	0.34	0.32	0.38	0.33	0.60	0.59	0.61	0.62	0.62	0.60	0.59	0.61

Tourmaline (continued)

Point	UT-82_1	UT-82_1	UT-82_1	UT-82_1	UT-82_1	UT-82_1	UT-82_1	UT-82_1	UT-82_1	UT-82_1	UT-82_1	UT-82_1	UT-82_1	UT-82_1	UT-82_1	UT-82_1
Type	QRV	QRV	QRV	QRV	QRV	QRV	QRV	QRV	QRV	QRV	QRV	QRV	QRV	QRV	QRV	QRV
Tour type	QRVT	QRVT	QRVT	QRVT	QRVT	QRVT	QRVT	QRVT	QRVT	QRVT	QRVT	QRVT	QRVT	QRVT	QRVT	QRVT
SiO_2	37.11	36.90	37.02	37.14	37.21	37.07	37.04	37.07	37.08	37.28	37.05	37.21	37.19	37.16	37.27	37.14
TiO_2	0.11	0.10	0.09	0.10	0.10	0.11	0.10	0.11	0.09	0.10	0.10	0.10	0.10	0.10	0.10	0.11
Al_2O_3	35.91	35.53	35.78	35.83	35.88	35.85	35.77	35.75	35.37	35.73	35.79	35.79	35.70	35.69	35.79	35.53
FeO	11.65	11.25	11.46	11.65	11.62	11.60	11.59	11.66	11.68	11.54	11.61	11.74	11.54	11.38	11.61	11.71
MgO	1.36	1.38	1.36	1.41	1.39	1.40	1.37	1.35	1.44	1.36	1.36	1.37	1.34	1.40	1.42	1.35
CaO																
MnO						0.10	0.10				0.12	0.12			0.10	
Na_2O	1.34	1.29	1.22	1.12	1.13	1.26	1.25	1.26	1.29	1.22	1.23	1.19	1.16	1.24	1.25	1.22
K_2O																
F	0.01	0.01		0.02		0.21	0.06	0.11	0.06	0.34	0.07			0.03	0.42	0.01
Li_2O*	0.40	0.46	0.41	0.37	0.39	0.37	0.38	0.39	0.44	0.46	0.37	0.38	0.44	0.46	0.41	0.43
Subtotal	87.88	86.91	87.33	87.63	87.71	87.97	87.66	87.71	87.43	88.04	87.68	87.88	87.47	87.46	88.35	87.50
O=F	0.00	0.00	0.00	0.01	0.00	0.09	0.03	0.05	0.02	0.14	0.03	0.00	0.00	0.01	0.18	0.00
Total	87.88	86.90	87.33	87.62	87.71	87.88	87.63	87.66	87.40	87.90	87.66	87.88	87.47	87.44	88.17	87.49
Formula																
Si	5.99	6.01	6.01	6.01	6.01	5.99	6.00	6.00	6.02	6.02	6.00	6.01	6.02	6.02	6.01	6.02
Ti	0.01	0.00	0.00	0.00	0.00	0.01	0.00	0.00	0.00	0.00	0.00	0.00	0.00	0.00	0.00	0.00
Al^T	6.00	6.00	6.00	6.00	6.00	6.00	6.00	6.00	6.00	6.00	6.00	6.00	6.00	6.00	6.00	6.00
Al^Z	0.82	0.82	0.84	0.83	0.83	0.83	0.83	0.82	0.77	0.80	0.83	0.81	0.81	0.81	0.80	0.79
Al^Y	0.01	0.01	0.01	0.01	0.01	0.01	0.01	0.01	0.01	0.01	0.01	0.01	0.01	0.01	0.01	0.01
Mg	0.33	0.34	0.33	0.34	0.34	0.34	0.33	0.33	0.35	0.33	0.33	0.33	0.32	0.34	0.34	0.33
Mn	0.00	0.00	0.00	0.00	0.00	0.01	0.01	0.00	0.00	0.00	0.02	0.02	0.00	0.00	0.01	0.00
Fe^{2+}	1.57	1.53	1.55	1.58	1.57	1.57	1.57	1.58	1.59	1.56	1.57	1.59	1.56	1.54	1.57	1.59
Li*	0.26	0.30	0.27	0.24	0.25	0.24	0.25	0.26	0.28	0.30	0.24	0.24	0.29	0.30	0.26	0.28
Ca	0.00	0.00	0.00	0.00	0.00	0.00	0.00	0.00	0.00	0.00	0.00	0.00	0.00	0.00	0.00	0.00
Na	0.42	0.41	0.38	0.35	0.35	0.39	0.39	0.40	0.40	0.38	0.39	0.37	0.36	0.39	0.39	0.38
K	0.00	0.00	0.00	0.00	0.00	0.00	0.00	0.00	0.00	0.00	0.00	0.00	0.00	0.00	0.00	0.00
r	0.58	0.59	0.62	0.65	0.65	0.61	0.61	0.60	0.60	0.62	0.61	0.63	0.64	0.61	0.61	0.62
OH	4.00	4.00	4.00	3.99	4.00	3.89	3.97	3.94	3.97	3.82	3.97	4.00	4.00	3.98	3.79	4.00
F	0.00	0.00	0.00	0.01	0.00	0.11	0.03	0.06	0.03	0.18	0.03	0.00	0.00	0.02	0.21	0.00
B	3.00	3.00	3.00	3.00	3.00	3.00	3.00	3.00	3.00	3.00	3.00	3.00	3.00	3.00	3.00	3.00
Mg/Mg+Fe	0.17	0.18	0.17	0.18	0.18	0.18	0.17	0.17	0.18	0.17	0.17	0.17	0.17	0.18	0.18	0.17
r/r+Na+K	0.58	0.59	0.62	0.65	0.65	0.61	0.61	0.60	0.60	0.62	0.61	0.63	0.64	0.61	0.61	0.62

Garnet (OZ =outer zone; CZ = central zone; FZ = fracture zone; NZ= un-zoned; HR =Garnet from metasedimentary host rock)

Point	U-19_1	U-19_1	U-19_1	U-19_1	U-19_1	U-19_1	U-19_1	U-19_1	U-19_1	U-19_1	U-19_1	U-19_1	U-19_1	U-19_1	U-19_1	U-19_1	U-19_1
Granite type	AMG	AMG	AMG	AMG	AMG	AMG	AMG	AMG	AMG	AMG	AMG	AMG	AMG	AMG	AMG	AMG	AMG
Comment	Zoned Gt line	Zoned Gt line	Zoned Gt line	Zoned Gt line	Zoned Gt line	Zoned Gt line	Zoned Gt line	Zoned Gt line	Zoned Gt line	Zoned Gt line	Zoned Gt line	Zoned Gt line	Zoned Gt line	Zoned Gt line	Zoned Gt line	Zoned Gt line	Zoned Gt line
zoned/unzoned	OZ	OZ	OZ	OZ	OZ	OZ	OZ	CZ	CZ	CZ	CZ	CZ	CZ	CZ	CZ	CZ	CZ
SiO_2	37.63	37.56	37.44	37.57	37.77	37.56	37.77	37.04	37.35	36.53	36.80	37.02	36.92	36.99	36.86	37.03	36.82
TiO_2	0.23	0.22	0.18	0.18	0.22	0.23	0.18	0.10	0.07	0.06	0.06	0.08	0.09	0.08	0.09	0.10	0.11
Al_2O_3	20.92	20.74	20.68	20.78	21.08	20.78	21.28	20.83	20.79	20.88	20.95	20.71	20.83	20.76	20.85	20.85	20.97
Fe_2O_3	0.75	0.72	0.71	0.79	0.51	0.80	0.67	0.46	0.18	0.41	0.22	0.50	0.31	0.42	0.35	0.54	0.43
FeO	14.83	14.81	14.74	14.72	14.43	14.00	13.72	16.90	18.32	18.75	19.18	19.41	19.48	19.64	19.72	20.02	19.90
MnO	15.97	15.02	14.66	14.49	14.18	13.60	14.53	20.94	21.47	21.38	21.28	20.99	20.81	20.82	20.73	20.67	20.67
MgO	0.38	0.39	0.34	0.35	0.34	0.29	0.21	0.48	0.53	0.62	0.62	0.70	0.66	0.69	0.68	0.74	0.73
CaO	10.83	11.36	11.63	11.99	12.60	13.36	13.40	4.52	2.70	2.33	2.07	2.12	2.16	2.06	2.04	2.03	2.08
Total	101.56	100.81	100.38	100.86	101.12	100.61	101.75	101.27	101.42	100.96	101.18	101.52	101.26	101.46	101.33	101.98	101.71
Formula																	
Si	2.979	2.989	2.991	2.986	2.986	2.983	2.969	2.983	3.009	2.967	2.980	2.988	2.986	2.988	2.981	2.978	2.969
Al^{iv}	0.021	0.011	0.009	0.014	0.014	0.017	0.031	0.017	0.000	0.033	0.020	0.012	0.014	0.012	0.019	0.022	0.031
Al^{vi}	1.936	1.938	1.941	1.936	1.953	1.932	1.945	1.962	1.975	1.968	1.981	1.961	1.973	1.966	1.970	1.957	1.964
Ti	0.014	0.013	0.011	0.011	0.013	0.014	0.010	0.006	0.004	0.004	0.004	0.005	0.005	0.005	0.006	0.006	0.007
Fe^{3+}	0.045	0.043	0.043	0.047	0.030	0.048	0.040	0.028	0.011	0.025	0.014	0.030	0.019	0.025	0.021	0.033	0.026
Fe^{2+}	0.982	0.985	0.984	0.978	0.954	0.930	0.902	1.138	1.234	1.274	1.299	1.310	1.318	1.326	1.334	1.347	1.342
Mn	1.071	1.012	0.992	0.975	0.949	0.915	0.968	1.428	1.465	1.471	1.460	1.435	1.426	1.424	1.420	1.408	1.412
Mg	0.045	0.046	0.041	0.042	0.040	0.035	0.024	0.058	0.064	0.075	0.074	0.084	0.079	0.083	0.082	0.089	0.087
Ca	0.919	0.968	0.995	1.021	1.067	1.137	1.129	0.390	0.233	0.203	0.180	0.184	0.187	0.178	0.177	0.175	0.180
Almandine	31.678	32.058	32.040	31.750	31.131	30.063	28.582	37.103	40.803	41.065	42.492	43.026	43.324	43.594	43.668	43.867	43.458
Andradite	2.264	2.165	2.152	2.370	1.528	2.415	2.009	1.415	0.540	1.259	0.685	1.510	0.952	1.279	1.072	1.655	1.331
Grossular	28.578	30.299	31.198	31.823	34.207	35.693	35.998	11.660	7.300	5.578	5.340	4.632	5.315	4.679	4.852	4.216	4.721
Pyrope	1.521	1.547	1.369	1.393	1.342	1.159	0.825	1.936	2.142	2.534	2.500	2.811	2.653	2.781	2.766	2.979	2.943
Spessartine	35.959	33.930	33.241	32.664	31.793	30.670	32.586	47.886	49.216	49.564	48.984	48.022	47.756	47.667	47.641	47.282	47.546

Garnet (continued)

Point	U-19_1	U-19_1	U-19_1	U-19_1	U-19_1	U-19_1	U-19_1	U-19_1	U-19_1	U-19_1	U-19_1	U-19_1	U-19_1	U-19_1	U-19_1	U-19_1	U-19_1
Granite type	AMG	AMG	AMG	AMG	AMG	AMG	AMG	AMG	AMG	AMG	AMG	AMG	AMG	AMG	AMG	AMG	AMG
Comment	Zoned Gt line	Zoned Gt line	Zoned Gt line	Zoned Gt line	Zoned Gt line	Zoned Gt line	Zoned Gt line	Zoned Gt line	Zoned Gt line	Zoned Gt line	Zoned Gt line	Zoned Gt line	Zoned Gt line	Zoned Gt line	Zoned Gt line	Zoned Gt line	Zoned Gt line
zoned/unzoned	CZ	CZ	CZ	CZ	CZ	CZ	CZ	CZ	CZ	CZ	CZ	FZ	FZ	FZ	FZ	FZ	CZ
SiO_2	37.17	36.79	37.08	36.78	37.13	38.24	36.79	36.87	37.14	36.82	37.26	38.28	38.16	37.19	37.83	37.06	36.98
TiO_2	0.11	0.10	0.13	0.11	0.11	0.12	0.07	0.08	0.08	0.08	0.10	0.13	0.23	0.18	0.20	0.12	0.13
Al_2O_3	20.82	20.84	20.75	20.89	20.79	21.60	20.80	20.77	20.91	20.74	20.94	21.38	21.33	20.85	20.83	20.50	20.86
Fe_2O_3	0.60	0.35	0.17	0.26	0.45	0.00	0.20	0.15	0.18	0.32	0.17	0.08	0.03	0.66	0.60	0.78	0.27
FeO	20.02	20.08	19.73	19.87	19.83	20.15	19.38	19.14	19.30	18.78	18.88	16.45	16.13	15.68	14.76	14.76	17.35
MnO	20.70	20.37	20.73	20.76	20.95	20.59	21.13	21.16	21.40	21.80	20.47	16.56	15.47	15.98	14.10	17.36	21.57
MgO	0.74	0.72	0.71	0.72	0.73	0.74	0.65	0.60	0.60	0.59	0.54	0.37	0.45	0.49	0.35	0.33	0.48
CaO	2.10	1.95	1.82	1.78	1.86	1.81	1.80	1.99	1.96	1.89	3.17	9.13	10.00	9.68	12.24	9.23	3.50
Total	102.27	101.20	101.12	101.17	101.85	103.25	100.83	100.76	101.57	101.01	101.53	102.37	101.80	100.71	100.90	100.12	101.15
Formula																	
Si	2.981	2.979	3.001	2.979	2.988	3.008	2.989	2.995	2.995	2.988	2.997	3.007	3.005	2.975	2.998	2.988	2.987
Al^{iv}	0.019	0.021	0.000	0.021	0.012	0.000	0.011	0.005	0.005	0.012	0.003	0.000	0.000	0.025	0.002	0.012	0.013
Al^{vi}	1.952	1.970	1.980	1.975	1.963	2.008	1.982	1.985	1.983	1.974	1.982	1.980	1.980	1.944	1.948	1.940	1.973
Ti	0.007	0.006	0.008	0.007	0.007	0.007	0.004	0.005	0.005	0.005	0.006	0.007	0.013	0.011	0.012	0.007	0.008
Fe^{3+}	0.036	0.021	0.011	0.016	0.027	0.000	0.012	0.009	0.011	0.019	0.010	0.005	0.002	0.040	0.036	0.047	0.016
Fe^{2+}	1.342	1.360	1.335	1.346	1.335	1.355	1.317	1.301	1.301	1.275	1.270	1.081	1.062	1.049	0.978	0.995	1.172
Mn	1.406	1.398	1.421	1.424	1.428	1.372	1.454	1.456	1.462	1.499	1.394	1.102	1.032	1.082	0.947	1.185	1.475
Mg	0.089	0.087	0.085	0.087	0.087	0.087	0.079	0.073	0.072	0.072	0.065	0.043	0.053	0.059	0.042	0.040	0.058
Ca	0.180	0.169	0.158	0.155	0.161	0.153	0.157	0.173	0.169	0.164	0.273	0.768	0.844	0.830	1.039	0.797	0.303
Almandine	43.803	44.488	44.246	44.084	43.921	45.669	43.449	43.177	43.155	41.949	42.130	35.722	35.097	33.761	31.807	32.320	38.530
Andradite	1.834	1.071	0.529	0.798	1.353	0.000	0.607	0.449	0.558	0.969	0.509	0.249	0.098	1.996	1.814	2.365	0.828
Grossular	4.217	4.603	4.754	4.400	4.026	5.150	4.644	5.331	5.082	4.529	8.612	25.567	28.290	25.888	33.138	24.310	9.312
Pyrope	2.972	2.922	2.862	2.910	2.915	2.940	2.646	2.434	2.392	2.397	2.167	1.444	1.793	1.972	1.399	1.328	1.931
Spessartine	47.175	46.916	47.610	47.809	47.786	46.240	48.655	48.609	48.813	50.157	46.582	37.018	34.723	36.384	31.843	39.677	49.398

Garnet (continued)

Point	U-19_1	U-19_1	U-19_1	U-19_1	U-19_1	U-19_1	U-19_1	U-19_1	U-19_1	U-19_1	U-19_2	U-19_2	U-19_2	U-19_2	U-19_2	U-19	U-19
Granite type	AMG	AMG	AMG	AMG	AMG	AMG	AMG	AMG	AMG	AMG	AMG	AMG	AMG	AMG	AMG	AMG	AMG
Comment	Zoned Gt line	Zoned Gt line	Zoned Gt line	Zoned Gt line	Zoned Gt line	Zoned Gt line	Zoned Gt line	Zoned Gt line	Zoned Gt line	Zoned Gt line	Gt with incl	Gt with incl	Gt with incl	Gt with incl	Gt with incl	Fracture Gt	Fracture Gt
zoned/unzoned	CZ	CZ	CZ	CZ	CZ	CZ	CZ	CZ	CZ	NZ	NZ	NZ	NZ	NZ	NZ	NZ	NZ
SiO_2	36.93	36.89	36.87	36.81	36.88	36.95	36.70	36.78	36.95	37.58	37.48	37.25	37.56	37.53	37.60	37.49	37.32
TiO_2	0.11	0.12	0.12	0.10	0.10	0.12	0.11	0.10	0.12	0.10	0.00	0.00	0.00	0.00	0.00	0.00	0.28
Al_2O_3	20.74	20.80	20.75	20.49	20.74	20.61	20.66	20.82	20.54	20.95	21.39	21.28	21.22	21.21	21.50	20.95	20.79
Fe_2O_3	0.19	0.33	0.36	0.55	0.16	0.41	0.27	0.04	0.42	0.76	0.37	0.47	0.59	0.68	0.60	0.16	0.25
FeO	17.48	17.61	17.40	17.13	17.44	17.28	17.31	18.08	18.88	14.77	16.35	17.20	16.24	16.52	16.85	16.64	16.55
MnO	21.18	21.48	21.28	21.62	21.47	21.46	21.07	20.09	17.18	13.12	12.32	12.54	12.51	12.77	12.92	13.69	14.03
MgO	0.50	0.51	0.54	0.51	0.49	0.49	0.53	0.53	0.47	0.30	0.35	0.37	0.35	0.38	0.37	0.37	0.33
CaO	3.45	3.28	3.54	3.42	3.23	3.50	3.55	3.68	5.60	13.22	12.55	11.59	12.57	12.16	12.03	10.57	10.38
Total	100.56	101.01	100.84	100.63	100.51	100.82	100.21	100.11	100.15	100.79	100.81	100.70	101.03	101.24	101.87	99.86	99.93
Formula																	
Si	2.996	2.985	2.986	2.991	2.996	2.994	2.989	2.994	2.998	2.981	2.973	2.967	2.976	2.971	2.961	3.008	2.997
Al^{iv}	0.004	0.015	0.014	0.009	0.004	0.006	0.011	0.006	0.002	0.019	0.027	0.033	0.024	0.029	0.039	0.000	0.003
Al^{vi}	1.981	1.970	1.968	1.956	1.983	1.965	1.974	1.992	1.964	1.943	1.975	1.968	1.960	1.955	1.960	1.982	1.966
Ti	0.007	0.007	0.007	0.006	0.006	0.007	0.007	0.006	0.007	0.006	0.000	0.000	0.000	0.000	0.000	0.000	0.017
Fe^{3+}	0.011	0.020	0.022	0.033	0.010	0.025	0.017	0.002	0.025	0.045	0.022	0.028	0.035	0.040	0.036	0.009	0.015
Fe^{2+}	1.187	1.192	1.178	1.164	1.185	1.171	1.179	1.230	1.281	0.980	1.084	1.146	1.076	1.094	1.110	1.116	1.112
Mn	1.456	1.472	1.460	1.488	1.477	1.473	1.453	1.385	1.180	0.882	0.828	0.846	0.840	0.857	0.862	0.930	0.954
Mg	0.060	0.062	0.065	0.062	0.059	0.059	0.065	0.064	0.057	0.035	0.041	0.044	0.041	0.045	0.044	0.044	0.039
Ca	0.300	0.284	0.308	0.298	0.281	0.303	0.310	0.321	0.487	1.124	1.067	0.989	1.067	1.032	1.015	0.909	0.893
Almandine	39.320	39.092	38.647	38.242	39.297	38.609	38.850	40.869	42.220	31.524	34.889	36.661	34.556	34.953	35.145	36.940	36.587
Andradite	0.567	1.003	1.102	1.677	0.491	1.246	0.843	0.115	1.280	2.283	1.128	1.432	1.773	2.039	1.802	0.474	0.775
Grossular	9.454	8.509	9.199	8.283	8.906	8.902	9.521	10.608	15.036	35.425	34.745	31.901	34.078	32.681	32.479	29.958	29.248
Pyrope	2.001	2.073	2.167	2.057	1.966	1.975	2.161	2.148	1.913	1.190	1.392	1.481	1.369	1.498	1.475	1.470	1.309
Spessartine	48.658	49.323	48.886	49.740	49.340	49.268	48.625	46.260	39.551	29.579	27.846	28.525	28.224	28.830	29.099	31.158	32.080

Garnet (continued)

Point	M-23-1	M-23-2	M-23-3	M-23-4	M-23-25	M-23-26	M-23-27	M-23-28	M-23-29	M-23-30	M-23-31	M-23-32	M-23-33	M-23-34	M-23-35	M-23-36	M-23-37
Granite type	host	host	host	host	host	host	host	host	host	host	host	host	host	host	host	host	host
Comment	Garnet	Garnet	Garnet	Garnet	Garnet	Garnet	Garnet	Garnet	Garnet	Garnet	Garnet	Garnet	Garnet	Garnet	Garnet	Garnet	Garnet
zoned/unzoned	HR	HR	HR	HR	HR	HR	HR	HR	HR	HR	HR	HR	HR	HR	HR	HR	HR
SiO_2	37.85	38.40	38.46	38.75	37.97	38.32	38.63	38.35	37.89	38.05	38.17	38.33	38.33	38.41	38.10	38.34	38.27
TiO_2	0.09	0.11	0.08	0.05	0.11	0.09	0.09	0.18	0.16	0.13	0.14	0.12	0.11	0.15	0.09	0.09	0.16
Al_2O_3	21.19	21.36	21.25	21.57	20.85	21.18	21.38	21.11	21.05	20.99	21.20	21.17	21.16	21.14	21.18	21.20	21.10
Fe_2O_3	0.11	0.07	0.22	0.00	0.13	0.19	0.00	0.21	0.14	0.28	0.11	0.12	0.16	0.11	0.04	0.00	0.00
FeO	19.52	19.51	19.19	18.72	21.11	18.58	17.73	19.21	19.80	20.64	21.16	20.94	21.10	21.03	21.21	21.15	20.79
MnO	7.51	8.79	9.19	7.79	10.66	7.38	7.30	9.04	11.79	10.56	10.01	10.32	10.56	10.14	10.51	10.11	10.26
MgO	0.85	0.77	0.69	0.71	0.98	1.02	0.91	0.78	0.78	0.93	0.95	0.95	0.96	0.99	1.01	0.99	0.99
CaO	12.89	12.34	12.43	14.05	8.71	13.73	14.51	12.24	9.30	9.55	9.64	9.59	9.30	9.61	8.99	9.35	9.36
Total	100.01	101.36	101.51	101.64	100.52	100.49	100.55	101.12	100.91	101.13	101.37	101.55	101.68	101.58	101.13	101.23	100.93
Formula																	
Si	3.00	3.01	3.02	3.02	3.03	3.02	3.03	3.02	3.01	3.01	3.01	3.02	3.02	3.02	3.02	3.03	3.03
Al^{iv}	0.00	0.00	0.00	0.00	0.00	0.00	0.00	0.00	0.00	0.00	0.00	0.00	0.00	0.00	0.00	0.00	0.00
Al^{vi}	1.98	1.98	1.96	1.98	1.96	1.97	1.98	1.96	1.97	1.96	1.97	1.97	1.96	1.96	1.98	1.97	1.97
Ti	0.01	0.01	0.00	0.00	0.01	0.01	0.01	0.01	0.01	0.01	0.01	0.01	0.01	0.01	0.01	0.01	0.01
Fe^{3+}	0.01	0.00	0.01	0.00	0.01	0.01	0.00	0.01	0.01	0.02	0.01	0.01	0.01	0.01	0.00	0.00	0.00
Fe^{2+}	1.30	1.28	1.26	1.22	1.41	1.22	1.17	1.26	1.32	1.37	1.40	1.38	1.39	1.38	1.40	1.40	1.38
Mn	0.50	0.58	0.61	0.51	0.72	0.49	0.48	0.60	0.79	0.71	0.67	0.69	0.70	0.68	0.70	0.68	0.69
Mg	0.10	0.09	0.08	0.08	0.12	0.12	0.11	0.09	0.09	0.11	0.11	0.11	0.11	0.12	0.12	0.12	0.12
Ca	1.10	1.04	1.04	1.17	0.74	1.16	1.22	1.03	0.79	0.81	0.82	0.81	0.78	0.81	0.76	0.79	0.79
Almandine	42.97	42.37	41.47	40.44	46.44	40.30	38.93	41.58	43.50	45.07	46.23	45.59	45.91	45.70	46.54	46.50	45.88
Andradite	0.34	0.22	0.66	0.00	0.41	0.56	0.00	0.63	0.42	0.84	0.32	0.36	0.49	0.33	0.11	0.00	0.00
Grossular	36.40	34.71	34.55	39.48	24.81	38.51	41.13	34.29	26.24	26.51	27.16	26.99	26.01	27.13	25.58	26.73	26.88
Pyrope	3.37	3.02	2.73	2.78	3.95	4.03	3.58	3.11	3.12	3.69	3.75	3.79	3.79	3.94	4.01	3.93	3.94
Spessartine	16.92	19.67	20.58	17.30	24.39	16.60	16.36	20.39	26.72	23.90	22.55	23.27	23.79	22.90	23.75	22.85	23.30

Epidote

Point	U-26-Z1	U-26-Z1	U-26-Z1	U-26-Z1	U-26-Z1	U-26-Z1	U-26-Z1	U-26-Z1	U-26-Z1	U-26-Z2	U-26-Z2	U-26-Z2	U-26-Z2	U-26-Z2	U-26-Z2	U-26-Z2	U-26-Z2
Type	AMG	AMG	AMG	AMG	AMG	AMG	AMG	AMG	AMG	AMG	AMG	AMG	AMG	AMG	AMG	AMG	AMG
Comment	Center	Center	Center	Center	Center	Margin	Margin	Margin	Margin	Center	Center	Center	Center	Margin	Margin	Margin	Margin
SiO_2	37.86	37.57	37.83	38.28	38.06	38.46	38.31	38.20	37.57	37.82	37.86	37.91	37.68	38.54	38.23	38.08	38.75
Al_2O_3	24.49	24.48	25.30	25.37	25.88	26.06	25.97	26.15	25.17	24.58	24.22	24.16	24.29	26.55	26.53	26.28	26.58
Fe_2O_3	10.39	10.70	9.09	9.65	8.88	8.59	8.64	8.40	8.85	10.79	11.49	11.26	11.06	8.18	8.36	8.09	7.92
CaO	23.83	23.76	23.55	23.90	23.67	23.82	23.31	23.65	23.87	23.48	23.69	23.65	23.63	23.68	23.80	23.92	23.92
MnO	0.17	0.10	0.22	0.22	0.22	0.19	0.18	0.24	0.14	0.22	0.19	0.17	0.16	0.15	0.12	0.15	0.13
Total	97.17	96.62	96.01	97.41	96.71	97.12	96.40	96.65	96.18	96.89	97.45	97.15	96.82	97.10	97.04	96.52	97.31
Formula																	
Si	3.01	3.01	3.03	3.03	3.02	3.04	3.04	3.03	3.01	3.02	3.01	3.02	3.01	3.03	3.02	3.02	3.04
Al	2.30	2.31	2.39	2.36	2.42	2.42	2.43	2.44	2.38	2.31	2.27	2.27	2.29	2.46	2.47	2.46	2.46
Fe^{3+}	0.62	0.65	0.55	0.57	0.53	0.51	0.52	0.50	0.53	0.65	0.69	0.68	0.67	0.48	0.50	0.48	0.47
Ca	2.03	2.04	2.02	2.02	2.01	2.01	1.98	2.01	2.05	2.01	2.02	2.02	2.03	2.00	2.01	2.03	2.01
Mn	0.01	0.01	0.01	0.01	0.01	0.01	0.01	0.02	0.01	0.01	0.01	0.01	0.01	0.01	0.01	0.01	0.01
Ps	21.32	21.82	18.66	19.53	17.97	17.39	17.51	17.02	18.33	21.89	23.25	22.93	22.52	16.44	16.75	16.43	15.99

Epidote (continued)

Point	Ept in Gt	Ept in Gt	Ept in Gt	Ept in Gt	Ept in Gt	Ept in Gt	Ept in Gt	Ept in Gt	Ept in Gt	Ept in Gt	Ept in Gt	Ept in Gt	U-19	U-19	U-19	U-19	U-19
Type	AMG	AMG	AMG	AMG	AMG	AMG	AMG	AMG	AMG	AMG	AMG	AMG	AMG	AMG	AMG	AMG	AMG
Comment	Ept	Ept	Ept	Ept	Ept	Ept	Ept	Ept	Ept	Ept	Ept	Ept	Ept	Ept	Ept	Ept	Ept
SiO_2	38.79	38.53	38.37	38.22	38.51	38.45	38.39	38.07	38.37	38.02	37.73	37.95	37.81	37.80	38.20	38.35	38.07
Al_2O_3	27.00	26.58	26.86	26.51	26.96	27.05	26.67	27.17	27.59	27.35	27.14	27.07	25.78	26.10	26.17	26.29	26.77
Fe_2O_3	7.87	7.92	7.92	8.49	8.07	8.05	8.24	8.43	7.98	8.07	7.94	8.14	9.07	8.51	8.69	8.27	8.00
CaO	23.72	23.67	23.83	23.19	23.81	23.75	23.51	23.80	23.93	23.89	23.28	23.58	23.54	23.66	23.05	23.39	23.54
MnO	0.45	0.49	0.43	0.55	0.37	0.44	0.48	0.52	0.44	0.43	0.58	0.55	0.46	0.34	0.37	0.45	0.19
Total	97.82	97.20	97.41	96.98	97.72	97.73	97.28	97.98	98.31	97.76	96.68	97.28	96.66	96.42	96.48	96.75	96.57
Formula																	
Si	3.03	3.03	3.02	3.02	3.02	3.01	3.02	2.98	2.99	2.98	2.99	2.99	3.01	3.01	3.03	3.03	3.01
Al	2.49	2.47	2.49	2.47	2.49	2.50	2.47	2.51	2.53	2.53	2.53	2.51	2.42	2.45	2.45	2.45	2.50
Fe^{3+}	0.46	0.47	0.47	0.50	0.48	0.47	0.49	0.50	0.47	0.48	0.47	0.48	0.54	0.51	0.52	0.49	0.48
Ca	1.99	2.00	2.01	1.96	2.00	1.99	1.98	2.00	2.00	2.01	1.98	1.99	2.01	2.02	1.96	1.98	2.00
Mn	0.03	0.03	0.03	0.04	0.02	0.03	0.03	0.03	0.03	0.03	0.04	0.04	0.03	0.02	0.03	0.03	0.01
Ps	15.69	15.99	15.85	16.98	16.04	15.96	16.47	16.53	15.59	15.85	15.75	16.11	18.34	17.24	17.49	16.72	16.03

Epidote (continued)

Point	U-19	U-19	U-19	U-19	U-19	U-19	M-23-5	M-23-6	M-23-7	M-23-8	M-23-9	M-23-10	M-23-11	M-23-12	M-23-13	M-23-14	M-23-15
Type	AMG	AMG	AMG	AMG	AMG	AMG	host rock	host rock	host rock	host rock	host rock	host rock	host rock	host rock	host rock	host rock	host rock
Comment	Ept	Ept	Ept	Ept	Ept	Ept	Ept	Ept	Ept	Ept	Ept	Ept	Ept	Ept	Ept	Ept	Ept
SiO_2	38.25	38.42	38.16	38.02	38.28	38.36	38.81	38.98	38.97	39.24	39.20	38.93	39.15	39.12	39.20	39.03	39.25
Al_2O_3	26.47	26.25	25.99	26.09	26.07	25.97	28.64	28.55	29.02	29.83	28.78	28.33	28.70	29.13	28.92	29.91	30.17
Fe_2O_3	8.28	8.68	8.91	8.98	8.80	9.12	5.95	5.52	5.40	4.31	5.46	6.42	6.00	4.67	5.27	3.86	4.18
CaO	23.59	23.21	23.11	23.33	23.36	23.44	24.12	24.24	24.28	24.37	24.26	23.96	24.14	24.18	24.28	24.47	24.25
MnO	0.38	0.45	0.49	0.50	0.40	0.40	0.29	0.24	0.25	0.27	0.27	0.28	0.25	0.28	0.31	0.24	0.24
Total	96.97	97.01	96.67	96.92	96.91	97.29	97.81	97.53	97.92	98.02	97.97	97.92	98.24	97.38	97.98	97.51	98.09
Formula																	
Si	3.02	3.03	3.02	3.01	3.02	3.02	3.01	3.03	3.01	3.02	3.03	3.02	3.02	3.03	3.03	3.02	3.02
Al	2.46	2.44	2.42	2.43	2.43	2.41	2.62	2.62	2.64	2.71	2.62	2.59	2.61	2.66	2.63	2.72	2.73
Fe^{3+}	0.49	0.52	0.53	0.53	0.52	0.54	0.35	0.32	0.31	0.25	0.32	0.37	0.35	0.27	0.31	0.22	0.24
Ca	1.99	1.96	1.96	1.98	1.98	1.98	2.00	2.02	2.01	2.01	2.01	1.99	2.00	2.01	2.01	2.03	2.00
Mn	0.03	0.03	0.03	0.03	0.03	0.03	0.02	0.02	0.02	0.02	0.02	0.02	0.02	0.02	0.02	0.02	0.02
Ps	16.65	17.43	17.96	18.02	17.73	18.32	11.68	10.98	10.60	8.43	10.78	12.63	11.76	9.27	10.40	7.59	8.11

Epidote (continued)

Point	M-23-16	M-23-17	M-23-18	M-23-19	M-23-20	M-23-21	M-23-22	M-23-23	M-23-24	M-23-25	M-23-26
Type	host rock	host rock	host rock	host rock	host rock	host rock	host rock	host rock	host rock	host rock	host rock
Comment	Ept	Ept	Ept	Ept	Ept	Ept	Ept	Ept	Ept	Ept	Ept
SiO_2	39.04	38.54	38.85	38.78	39.17	39.04	38.89	39.14	38.97	39.24	39.12
Al_2O_3	28.45	28.39	29.01	29.39	28.99	29.15	28.54	28.64	28.69	28.87	28.91
Fe_2O_3	6.06	5.89	5.55	5.02	5.20	5.23	5.80	6.07	6.00	5.76	5.90
CaO	24.02	24.20	24.17	24.35	24.34	24.27	24.04	24.02	24.09	24.11	24.11
MnO	0.25	0.21	0.24	0.19	0.15	0.18	0.18	0.23	0.20	0.23	0.20
Total	97.81	97.23	97.82	97.73	97.85	97.87	97.45	98.10	97.95	98.21	98.25
Formula											
Si	3.02	3.01	3.01	3.00	3.03	3.02	3.02	3.02	3.01	3.02	3.02
Al	2.60	2.61	2.65	2.68	2.64	2.65	2.62	2.61	2.62	2.62	2.63
Fe^{3+}	0.35	0.35	0.32	0.29	0.30	0.30	0.34	0.35	0.35	0.33	0.34
Ca	1.99	2.02	2.00	2.02	2.02	2.01	2.00	1.99	2.00	1.99	1.99
Mn	0.02	0.01	0.02	0.01	0.01	0.01	0.01	0.02	0.01	0.01	0.01
Ps	11.95	11.68	10.86	9.82	10.26	10.27	11.47	11.90	11.76	11.27	11.51

APPENDIX-2

Calculations for REE models

- Batch melting equation used: $C_L/C_O = 1/\ [D(1-F)+F]$

  C_L = Weight concentration of a trace element liquid

  C_O = Concentration of trace element in the source

  D = Bulk distribution coefficient for residual solids

  F Weight fraction of melt produced

- REE modelling outcomes are summarized in following table for melts produced due to 20 to 30% partial melting:

	Bulk Partition coefficient (D)	**Source (LCC)**	**Target (UT-66)**	**(C_L) F = 0.2**	**(C_L) F = 0.3**
La	0.12	8.00	17.07	20.76	16.91
Ce	0.12	20.00	30.88	51.88	42.26
Pr*		2.40	4.55		
Nd	0.15	11.00	17.26	26.93	22.32
Sm	0.19	2.80	3.84	6.46	5.44
Eu	1.13	1.10	0.83	1.01	1.02
Gd	0.29	3.10	3.52	6.21	5.43
Dy	0.74	3.10	2.95	3.79	3.68
Ho*		0.68	0.56		
Er	0.65	1.90	1.48	2.52	2.41
Tm*		0.24	0.24		
Yb	1.01	1.50	1.37	1.49	1.49
Lu	0.97	0.25	0.26	0.26	0.25

* not determined due to limited partition coefficient data

- Partition coefficient used in current REE modelling:

	Quartz	**K-feld**	**Plg**	**Bt**	**Gt**	**Zr**	**Ala**	**Ap**	**Ilm**	**Mon**
La	0.02	0.08	0.38	0.06	0.39	16.90	2362	14.5	1.31	298
Ce	0.01	0.04	0.27	0.05	0.69	16.75	2063	21.1	1.19	277
Nd	0.02	0.04	0.2	0.08	0.60	13.30	1400	32.8	0.96	290
Sm	0.01	0.03	0.17	0.06	2.04	14.40	756	46	0.68	217
Eu	0.06	4.45	4.45	0.05	0.52	16.00	100	25.5	0.40	114
Gd	--	--	0.13	0.10	6.98	12.00	--	43.90	--	175
Dy	0.02	0.06	0.11	0.17	28.60	101.5	123	34.80	0.37	83
Er	--	0.03	0.08	0.22	25.00	135	--	22.70	--	44
Yb	0.02	0.03	0.09	0.12	43.48	527	24.5	15.40	0.55	18
Lu	0.01	0.03	0.09	0.20	39.78	641	22	13.80	0.74	13

- Rayleigh fractionation equation used: $C_L/C_O = F^{(D-1)}$

  C_L = Weight concentration of a trace element liquid
  C_O = Concentration of trace element in the source
  D = Bulk distribution coefficient for fractionated phases
  F = Weight fraction of remaining melt

- REE modelling outcomes are summarized in following table for remaining melt after 10 to 20% fractionation:

	Bulk Partition coefficient (D)	**Source (UT-65)**	**Target (UT-27)**	**(C_L) F = 0.9**	**(C_L) F = 0.8**
La	10.10	29.54	6.28	11.33	3.88
Ce	9.00	61.73	12.27	26.56	10.35
Pr		7.80	1.83		
Nd	7.17	29.65	6.90	15.48	7.49
Sm	4.71	6.19	1.85	4.19	2.71
Eu	4.87	0.90	0.13	0.60	0.38
Gd	2.28	5.27	1.73	4.61	3.96
Dy	2.95	3.59	2.03	2.92	2.32
Ho		0.54	0.40		
Er	2.00	1.27	1.20	1.14	1.02
Tm		0.15	0.18		
Yb	3.10	0.95	1.22	0.76	0.59
Lu	2.98	0.15	0.16	0.12	0.10

APPENDIX-3

Major element chemistry of major minerals in studied dykes. Concentration is in “%age”

Plagioclase

Sample	**Dolerite**	**Dolerite**	**Dolerite**	**Dolerite**	**Dolerite**	**Dolerite**	**Dolerite**	**Dolerite**	**Dolerite**	**Dolerite**	**Dolerite**	**Dolerite**	**Dolerite**	**Dolerite**	**Dolerite**
Comment	**UT-1_3**	**UT-1_3**	**UT-1_3**	**UT-1_3**	**UT-1_3**	**UT-1_3**	**UT-1_3**	**UT-1_3**	**UT-1_3**	**UT-1_3**	**UT-1_3**	**UT-1_3**	**UT-1_3**	**UT-1_3**	**UT-1_3**
SiO_2	52.66	52.05	54.04	53.41	52.27	57.47	52.82	52.80	57.14	56.57	53.92	52.29	52.80	54.69	56.74
Na_2O	4.72	4.41	4.85	4.90	4.54	7.03	4.59	4.77	6.61	6.43	5.33	4.53	4.62	5.55	6.52
FeO	0.56	0.65	0.69	0.84	0.68	0.47	0.57	0.61	0.68	0.66	0.76	0.67	0.65	0.66	0.57
K_2O	0.26	0.23	0.33	0.15	0.23	0.30	0.29	0.29	0.30	0.40	0.33	0.21	0.24	0.30	0.21
Al_2O_3	28.91	29.72	28.62	29.25	29.37	25.93	28.94	29.08	26.76	26.90	27.47	29.11	29.34	27.94	27.04
CaO	12.21	13.16	11.65	12.25	12.90	8.58	12.42	12.43	9.03	9.43	10.82	12.67	12.51	11.13	9.67
Total	99.32	100.21	100.26	100.95	100.05	99.77	99.75	100.09	100.51	100.39	98.82	99.49	100.25	100.34	100.75
Formula (8 O apfu)															
Si	2.41	2.37	2.45	2.41	2.38	2.59	2.41	2.41	2.56	2.54	2.48	2.39	2.40	2.47	2.54
Na	0.42	0.39	0.43	0.43	0.40	0.61	0.41	0.42	0.57	0.56	0.47	0.40	0.41	0.49	0.57
Fe	0.02	0.02	0.03	0.03	0.03	0.02	0.02	0.02	0.03	0.02	0.03	0.03	0.02	0.02	0.02
K	0.02	0.01	0.02	0.01	0.01	0.02	0.02	0.02	0.02	0.02	0.02	0.01	0.01	0.02	0.01
Al	1.56	1.59	1.53	1.56	1.58	1.38	1.56	1.56	1.41	1.43	1.49	1.57	1.57	1.49	1.43
Ca	0.60	0.64	0.57	0.59	0.63	0.41	0.61	0.61	0.43	0.45	0.53	0.62	0.61	0.54	0.46
An	58.86	62.23	57.02	58.00	61.09	40.27	59.91	59.01	42.99	44.76	52.90	60.72	59.95	52.57	45.02
Ab	41.14	37.77	42.98	42.00	38.91	59.73	40.09	40.99	57.01	55.24	47.10	39.28	40.05	47.43	54.98

Plagioclase (continued)

Sample	**Dolerite**	**Dolerite**	**Dolerite**	**Dolerite**	**Dolerite**	**Dolerite**	**Dolerite**	**Dolerite**	**Dolerite**	**Dolerite**	**Dolerite**	**Dolerite**	**Dolerite**	**Dolerite**	**Dolerite**
Comment	**M-14-5**	**M-14-6**	**M-14-7**	**M-14-8**	**M-14-9**	**M-14-10**	**M-14-11**	**M-14-12**	**M-14-13**	**UT_1_18**	**UT_1_22**	**UT_1_40**	**UT_1_41**	**UT_1_42**	**UT_1_43**
SiO_2	55.46	52.40	57.18	56.43	54.60	55.13	54.11	54.85	52.30	52.02	53.17	59.64	59.41	58.48	59.39
Na_2O	5.68	4.37	6.50	5.70	4.76	5.99	5.79	5.59	4.62	3.96	4.49	6.55	7.21	7.17	6.30
FeO		0.46			0.22	0.79	0.55	0.36	1.21	0.57	0.57	0.68	0.81	1.39	0.63
K_2O	0.15	0.11	0.30	1.01	0.16	0.20	0.23	0.16	0.15	0.26	0.28	1.39	0.26	0.17	1.60
Al_2O_3	27.02	28.60	25.43	26.05	27.99	26.27	25.89	26.92	28.22	29.46	28.54	25.08	25.08	24.64	25.13
CaO	9.88	12.21	8.40	8.73	10.87	9.40	9.26	9.99	11.67	12.78	11.82	7.13	6.95	6.54	7.10
Total	98.19	98.22	97.88	98.01	98.67	97.88	96.00	97.92	98.28	99.11	98.93	100.58	99.92	99.00	100.24
Formula (8 O apfu)															
Si	2.54	2.42	2.62	2.59	2.49	2.54	2.54	2.52	2.42	2.39	2.44	2.66	2.66	2.66	2.66
Na	0.50	0.39	0.58	0.51	0.42	0.54	0.53	0.50	0.41	0.35	0.40	0.57	0.63	0.63	0.55
Fe	0.00	0.02	0.00	0.00	0.01	0.03	0.02	0.01	0.05	0.02	0.02	0.03	0.03	0.05	0.02
K	0.01	0.01	0.02	0.06	0.01	0.01	0.01	0.01	0.01	0.02	0.02	0.08	0.01	0.01	0.09
Al	1.46	1.56	1.37	1.41	1.51	1.43	1.43	1.46	1.54	1.59	1.54	1.32	1.32	1.32	1.33
Ca	0.48	0.60	0.41	0.43	0.53	0.46	0.47	0.49	0.58	0.63	0.58	0.34	0.33	0.32	0.34
An	49.01	60.69	41.66	45.84	55.79	46.44	46.92	49.69	58.26	64.07	59.26	37.56	34.75	33.51	38.38
Ab	50.99	39.31	58.34	54.16	44.21	53.56	53.08	50.31	41.74	35.93	40.74	62.44	65.25	66.49	61.62

Clinopyroxene

Sample	**Dolerite**	**Dolerite**	**Dolerite**	**Dolerite**	**Dolerite**	**Dolerite**	**Dolerite**	**Dolerite**	**Dolerite**	**Dolerite**	**Dolerite**	**Dolerite**	**Dolerite**	**Dolerite**	**Dolerite**
Comment	**utp-1**	**utp-6**	**utp-9**	**utp-78**	**utp-21**	**utp-4**	**utp-7**	**utp-8**	**mp-63**	**mp-42**	**mp-22**	**utp-8**	**utp-15**	**utp-10**	**utp-18**
SiO_2	51.75	51.10	52.01	50.27	50.64	50.32	51.34	50.83	50.28	51.26	51.13	51.39	52.39	51.64	52.33
Na_2O	0.36	0.37	0.33	0.32	0.31	0.32	0.38	0.35	0.40	0.27	0.28	0.33	0.31	0.30	0.37
FeO	9.24	9.57	10.11	9.65	11.77	12.40	11.45	13.30	12.08	9.04	10.28	10.85	8.94	9.60	8.33
Al_2O_3	2.86	3.44	2.25	3.46	2.65	3.71	2.70	2.54	2.51	2.56	2.41	2.43	2.12	2.84	2.19
MnO	0.22	0.23	0.28	0.20	0.28	0.33	0.27	0.32	0.28	0.20	0.25	0.36	0.23	0.24	0.22
CaO	18.99	18.62	17.33	18.04	16.96	17.90	17.70	16.25	20.31	20.10	20.02	16.98	18.12	18.17	18.90
MgO	16.15	15.69	16.42	16.17	15.36	14.55	15.65	15.26	12.33	14.05	14.27	16.10	17.12	15.99	16.66
TiO_2	0.59	0.76	0.56	0.80	0.68	1.00	0.71	0.75	0.54	0.58	0.53	0.63	0.50	0.65	0.53
Total	100.17	99.77	99.28	98.90	98.63	100.52	100.20	99.59	98.73	98.06	99.18	99.08	99.72	99.43	99.53
Formula (6 O apfu)															
Si	1.92	1.90	1.94	1.89	1.92	1.88	1.91	1.92	1.93	1.94	1.93	1.93	1.94	1.92	1.94
Na	0.03	0.03	0.02	0.02	0.02	0.02	0.03	0.03	0.03	0.02	0.02	0.02	0.02	0.02	0.03
Fe^{2+}	0.29	0.30	0.32	0.30	0.37	0.39	0.36	0.42	0.39	0.29	0.32	0.34	0.28	0.30	0.26
Al	0.12	0.15	0.10	0.15	0.12	0.16	0.12	0.11	0.11	0.11	0.11	0.11	0.09	0.12	0.10
Mn	0.01	0.01	0.01	0.01	0.01	0.01	0.01	0.01	0.01	0.01	0.01	0.01	0.01	0.01	0.01
Ca	0.75	0.74	0.69	0.73	0.69	0.72	0.71	0.66	0.83	0.82	0.81	0.68	0.72	0.72	0.75
Mg	0.89	0.87	0.91	0.91	0.87	0.81	0.87	0.86	0.70	0.79	0.80	0.90	0.94	0.89	0.92
Ti	0.02	0.02	0.02	0.02	0.02	0.03	0.02	0.02	0.02	0.02	0.02	0.02	0.01	0.02	0.01
En	46.16	45.56	47.53	46.81	44.98	42.34	44.99	44.37	36.59	41.86	41.45	46.82	48.70	46.44	47.72
Fs	14.81	15.60	16.42	15.66	19.33	20.24	18.46	21.68	20.11	15.11	16.75	17.70	14.27	15.64	13.38
Wo	39.02	38.85	36.05	37.52	35.69	37.42	36.55	33.94	43.31	43.03	41.79	35.48	37.04	37.92	38.90

Clinopyroxene (continued)

Sample	**Dolerite**	**Dolerite**	**Dolerite**	**Dolerite**	**Dolerite**	**Dolerite**	**Dolerite**	**Dolerite**	**Dolerite**	**Dolerite**
Comment	**utp-24**	**utp-27**	**utp-31**	**utp-38**	**utp-64**	**utp-71**	**utp-69**	**utp-74**	**utp-52**	**utp-16**
SiO_2	51.39	51.33	51.35	51.38	50.97	51.12	51.44	51.18	50.82	51.46
Na_2O	0.32	0.28	0.35	0.32	0.39	0.41	0.35	0.38	0.38	0.37
FeO	9.17	8.99	9.11	9.22	8.79	8.71	8.98	9.20	9.09	9.04
Al_2O_3	3.16	3.30	3.18	3.29	3.23	3.17	3.17	3.25	3.24	3.21
MnO	0.22	0.21	0.17	0.22	0.21	0.19	0.22	0.23	0.16	0.22
CaO	18.91	18.98	19.10	19.01	19.01	19.20	19.01	19.09	18.92	18.90
MgO	15.82	15.84	15.92	15.89	15.96	15.84	15.82	16.00	15.76	15.82
TiO_2	0.70	0.68	0.68	0.69	0.68	0.70	0.69	0.70	0.68	0.67
Total	99.67	99.61	99.85	100.02	99.24	99.34	99.68	100.02	99.04	99.71
Formula (6 O apfu)										
Si	1.91	1.91	1.91	1.90	1.90	1.91	1.91	1.90	1.90	1.91
Na	0.02	0.02	0.03	0.02	0.03	0.03	0.02	0.03	0.03	0.03
Fe^{2+}	0.28	0.28	0.28	0.29	0.27	0.27	0.28	0.29	0.28	0.28
Al	0.14	0.14	0.14	0.14	0.14	0.14	0.14	0.14	0.14	0.14
Mn	0.01	0.01	0.01	0.01	0.01	0.01	0.01	0.01	0.00	0.01
Ca	0.75	0.76	0.76	0.75	0.76	0.77	0.76	0.76	0.76	0.75
Mg	0.88	0.88	0.88	0.88	0.89	0.88	0.88	0.89	0.88	0.88
Ti	0.02	0.02	0.02	0.02	0.02	0.02	0.02	0.02	0.02	0.02
En	45.79	45.88	45.81	45.77	46.20	45.88	45.83	45.88	45.74	45.89
Fs	14.88	14.61	14.70	14.90	14.28	14.15	14.59	14.79	14.80	14.71
Wo	39.33	39.51	39.49	39.33	39.53	39.97	39.58	39.33	39.46	39.40

Olivine

Comment	**ut1p1**	**ut1p7**	**ut1p12**	**ut1p24**	**ut4p59**	**ut4p33**	**ut4p67**	**ut4p77**	**ut4p12**	**dm1p4**	**dm1p9**	**dm1p67**	**dm1p22**	**dm1p34**	**dm1p45**	**dm1p25**	**dm1p33**
Color	**Brown**	**Brown**	**Brown**	**Brown**	**Brown**	**Brown**	**Brown**	**Brown**	**Brown**	**Colorless**	**Colorless**	**Colorless**	**Colorless**	**Colorless**	**Colorless**	**Colorless**	**Colorless**
SiO_2	37.52	36.63	36.46	37.01	37.22	36.09	37.04	35.90	35.96	33.63	33.27	32.96	33.21	32.36	32.38	32.35	32.29
FeO	29.45	31.60	36.48	32.28	32.19	37.54	32.72	37.21	37.20	51.86	51.80	51.09	51.75	52.71	52.17	52.70	52.15
CaO	0.29	0.25	0.29	0.38	0.27	0.25	0.22	0.25	0.32	0.05		0.05					
MnO	0.41	0.47	0.52	0.44	0.42	0.48	0.40	0.51	0.63	0.63	0.71	0.70	0.75	0.72	0.66	0.74	0.73
MgO	34.27	31.11	28.31	31.46	31.59	27.23	31.14	27.42	26.34	15.66	15.42	14.94	15.13	14.69	14.71	14.46	14.61
Total	101.93	100.05	102.05	101.58	101.70	101.59	101.52	101.29	100.45	101.82	101.25	100.06	100.84	100.50	99.93	100.25	99.78
Formula (4 O apfu)																	
Si	0.99	1.00	1.00	1.00	1.00	1.00	1.00	0.99	1.00	1.00	1.00	1.00	1.00	0.99	0.99	0.99	0.99
Fe^{2+}	0.65	0.72	0.83	0.73	0.72	0.87	0.74	0.86	0.87	1.29	1.30	1.30	1.30	1.34	1.33	1.35	1.34
Ca	0.01	0.01	0.01	0.01	0.01	0.01	0.01	0.01	0.01	0.00	0.00	0.00	0.00	0.00	0.00	0.00	0.00
Mn	0.01	0.01	0.01	0.01	0.01	0.01	0.01	0.01	0.01	0.02	0.02	0.02	0.02	0.02	0.02	0.02	0.02
Mg	1.35	1.26	1.15	1.26	1.26	1.12	1.25	1.13	1.10	0.69	0.69	0.68	0.68	0.67	0.67	0.66	0.67
Fo	67.47	63.70	58.04	63.47	63.63	56.39	62.92	56.78	55.80	34.99	34.66	34.27	34.27	33.20	33.45	32.84	33.31
Fa	32.53	36.30	41.96	36.53	36.37	43.61	37.08	43.22	44.20	65.01	65.34	65.73	65.73	66.80	66.55	67.16	66.69

Amphibole

Comment	**M-14-1**	**M-14-2**	**M-14-3**	**M-14-4**	**M-14-41**	**M-14-42**	**M-14-43**	**M-14-44**	**M-14-45**	**M-14-46**	**M-8-1**	**M-8-2**	**M-8-3**	**M-8-11**	**M-8-12**	**M-8-13**
Sample	**Dolerite**	**Dolerite**	**Dolerite**	**Dolerite**	**Dolerite**	**Dolerite**	**Dolerite**	**Dolerite**	**Dolerite**	**Dolerite**	**Amphibolite**	**Amphibolite**	**Amphibolite**	**Amphibolite**	**Amphibolite**	**Amphibolite**
SiO_2	43.27	43.08	43.14	43.35	43.31	46.08	43.00	42.85	43.40	44.40	43.26	43.73	42.32	43.89	42.34	44.22
TiO_2	2.27	2.36	2.36	2.39	2.19	1.84	2.22	2.30	2.45	1.70	0.53	0.48	0.52	0.54	0.47	0.61
Al_2O_3	10.22	10.09	10.09	10.04	10.46	8.57	10.09	10.24	10.36	9.19	14.96	14.02	15.82	14.15	15.93	13.50
MnO	0.21	0.14	0.19	0.21	0.15	0.15	0.21	0.20	0.19	0.20	0.16	0.21	0.22	0.23	0.16	0.15
FeO	17.14	16.88	17.54	17.11	17.79	17.85	18.12	17.78	18.05	17.55	13.35	13.08	13.01	12.97	13.38	13.14
Fe_2O_3	1.75	1.86	2.00	2.11	0.95	0.59	1.02	0.80	0.86	2.07	0.91	1.47	1.02	1.15	1.28	0.95
MgO	9.24	9.49	9.33	9.38	8.65	9.31	8.81	8.80	8.47	9.33	9.54	10.02	9.22	10.08	9.02	10.29
CaO	10.61	10.63	10.70	10.51	11.06	11.36	11.15	11.17	10.87	10.63	11.74	11.80	11.61	11.77	11.65	11.76
Na2O	1.76	1.72	1.80	1.70	1.44	1.16	1.74	1.65	1.60	1.37	1.24	1.12	1.28	1.22	1.28	1.22
K2O	0.91	0.93	0.96	0.90	1.00	0.96	0.93	0.94	0.98	0.97	0.56	0.51	0.62	0.52	0.50	0.58
F	0.03	0.10	0.00	0.12	0.05	0.01	0.06	0.00	0.09	0.07	0.00	0.00	0.07	0.00	0.04	0.03
Cl	0.02	0.02	0.02	0.02	0.01	0.02	0.02	0.03	0.02	0.02	0.04	0.02	0.04	0.03	0.05	0.04
O=F,Cl	0.02	-0.05	0.00	-0.05	-0.02	-0.01	-0.03	-0.01	-0.04	-0.03	-0.01	-0.01	-0.04	-0.01	-0.03	-0.02
Total	97.44	97.24	98.13	97.79	97.04	97.88	97.34	96.76	97.29	97.46	96.28	96.46	95.71	96.55	96.07	96.45
Formula (22 O apfu)																
Si	6.55	6.53	6.51	6.54	6.59	6.90	6.55	6.55	6.59	6.72	6.44	6.50	6.34	6.51	6.33	6.57
Al	1.82	1.80	1.79	1.79	1.88	1.51	1.81	1.84	1.85	1.64	2.63	2.46	2.80	2.47	2.81	2.36
Ti	0.26	0.27	0.27	0.27	0.25	0.21	0.25	0.26	0.28	0.19	0.06	0.05	0.06	0.06	0.05	0.07
Fe^{3+}	0.20	0.21	0.23	0.24	0.11	0.07	0.12	0.09	0.10	0.24	0.10	0.17	0.12	0.13	0.14	0.11
Fe^{2+}	2.08	2.04	2.11	2.05	2.22	2.23	2.27	2.25	2.26	2.11	1.65	1.61	1.63	1.60	1.65	1.62
Mg	2.09	2.15	2.10	2.11	1.96	2.08	2.00	2.01	1.92	2.10	2.12	2.22	2.06	2.23	2.01	2.28
Mn	0.03	0.02	0.03	0.03	0.02	0.02	0.03	0.03	0.02	0.03	0.02	0.03	0.03	0.03	0.02	0.02
Ca	1.72	1.73	1.73	1.70	1.80	1.82	1.82	1.83	1.77	1.72	1.87	1.88	1.87	1.87	1.87	1.87
Na	0.52	0.51	0.51	0.51	0.52	0.52	0.48	0.49	0.55	0.52	0.31	0.27	0.34	0.29	0.28	0.32
K	0.18	0.18	0.18	0.17	0.19	0.18	0.18	0.18	0.19	0.19	0.11	0.10	0.12	0.10	0.10	0.11
F	0.01	0.05		0.06	0.02	0.00	0.03		0.04	0.03			0.03		0.02	0.01
Cl	0.01	0.01	0.01	0.01	0.00	0.00	0.01	0.01	0.01	0.00	0.01	0.01	0.01	0.01	0.01	0.01

Ilmenite

Sample	Dolerite	Dolerite	Dolerite	Dolerite	Dolerite	Dolerite	Dolerite	Dolerite	Dolerite	Dolerite	Dolerite	Dolerite	Dolerite	Dolerite	Dolerite
Comment	**OD1**	**OD2**	**OD3**	**OD4**	**OD5**	**OD6**	**OD7**	**OD8**	**OD9**	**OD10**	**OD11**	**OD12**	**OD13**	**OD14**	**OD15**
SiO_2	0.22	0.20						1.82	0.80				0.31	0.19	
Al_2O_3	0.61	2.02	2.23	2.17	1.76	2.97	1.03	1.16	0.46	2.96	0.32		0.44	0.14	0.14
MgO		0.22	0.27	0.15	0.18			0.67	0.29	0.19			0.20	0.24	0.20
CaO							0.05	0.17	0.15						
TiO_2	33.15	28.10	46.97	23.05	40.10	27.18	36.63	47.28	49.29	32.00	49.24	49.36	49.49	49.40	48.61
MnO	0.54	0.49	0.74	0.42	0.61	0.41	0.55	0.66	0.65	0.46	0.71	0.76	0.73	0.76	0.76
FeO	29.53	24.62	41.01	20.05	35.14	24.03	32.34	42.63	43.92	27.98	43.58	43.63	43.80	43.45	42.61
Fe_2O_3	34.83	44.15	7.14	54.28	21.38	45.54	28.30	4.13	3.83	35.33	4.64	4.76	3.07	4.16	5.83
Total	98.88	99.79	98.36	100.11	99.17	100.13	98.89	98.52	99.39	98.93	98.49	98.49	98.03	98.34	98.15
Formula (3 O apfu)															
Si	0.01	0.01						0.05	0.02				0.01	0.00	0.00
Al	0.02	0.06	0.07	0.07	0.05	0.09	0.03	0.03	0.01	0.09	0.01		0.01	0.00	0.00
Mg	0.00	0.01	0.01	0.01	0.01			0.03	0.01	0.01			0.01	0.01	0.01
Ca							0.00	0.00	0.00						
Ti	0.65	0.54	0.90	0.44	0.77	0.52	0.71	0.90	0.94	0.62	0.95	0.95	0.96	0.95	0.94
Mn	0.01	0.01	0.02	0.01	0.01	0.01	0.01	0.01	0.01	0.01	0.02	0.02	0.02	0.02	0.02
Fe^{3+}	0.68	0.85	0.14	1.05	0.41	0.87	0.55	0.08	0.07	0.68	0.09	0.09	0.06	0.08	0.11
Fe^{2+}	0.64	0.53	0.87	0.43	0.75	0.51	0.70	0.90	0.93	0.60	0.93	0.94	0.94	0.93	0.92

Ilmenite (continued)

Sample	Dolerite	Dolerite	Dolerite	Dolerite	Dolerite
Comment	**OD16**	**OD17**	**OD18**	**OD19**	**OD20**
SiO_2	0.16	0.20			
Al_2O_3	0.27	0.20		5.45	4.07
MgO	0.19			0.37	0.29
CaO		0.04	0.06		
TiO_2	49.58	45.40	38.59	42.48	35.56
MnO	0.76	0.73	0.59	0.70	0.59
FeO	43.69	40.28	34.04	36.84	30.87
Fe_2O_3	4.62	10.21	24.22	12.48	26.87
Total	99.27	97.06	97.50	98.32	98.26
Formula (3 O apfu)					
Si	0.00	0.01			
Al	0.01	0.01		0.16	0.12
Mg	0.01			0.01	0.01
Ca		0.00	0.00		
Ti	0.95	0.89	0.76	0.80	0.68
Mn	0.02	0.02	0.01	0.01	0.01
Fe^{3+}	0.09	0.20	0.48	0.24	0.52
Fe^{2+}	0.93	0.88	0.75	0.77	0.66

Magnetite

Sample	Dolerite	Dolerite	Dolerite	Dolerite	Dolerite	Dolerite	Dolerite	Dolerite
Comment	**UT-1_4**	**UT-1_4**	**UT-1_4**	**UT-1_4**	**UT-1_4**	**UT-1_4**	**UT-1_4**	**UT-1_4**
	OL1	**OL2**	**OL3**	**OL4**	**OL5**	**OL6**	**OL7**	**OL8**
Al_2O_3	1.27	2.82	1.42	1.23	1.05	1.44	8.30	1.75
MgO		0.19					0.25	
TiO_2	8.15	11.99	18.77	10.66	4.89	4.59	2.51	7.83
MnO	0.14	0.21	0.31	0.14				0.12
FeO	38.13	41.56	47.52	40.69	35.57	35.19	34.15	38.06
Fe_2O_3	50.47	41.22	29.06	46.23	57.86	57.59	53.85	50.81
Total	98.17	97.98	97.09	98.94	99.37	98.81	99.06	98.57
Formula on basis on 4 O atoms								
Al	0.06	0.13	0.06	0.06	0.05	0.07	0.36	0.08
Mg		0.01					0.01	
Ti	0.24	0.34	0.55	0.31	0.14	0.13	0.07	0.23
Mn	0.00	0.01	0.01	0.00				0.00
Fe^{3+}	1.47	1.18	0.84	1.33	1.67	1.67	1.50	1.47
Fe^{2+}	1.23	1.33	1.53	1.30	1.14	1.13	1.06	1.22

APPENDIX-4

Methods for Mechanical Tests

Sample Preparation

Preparation of samples for mechanical tests was conducted in Rock Cutting Laboratory at Department of Geology, University of Peshawar, Pakistan and Rock Preparation Laboratory at CSM, University of Exeter. Coring of bulk samples was done in former lab to minimize the weight of samples for shipment to CSM for further testing. Cutting of cylindrical samples to appropriate size as per International Society of Rock Mechanics (ISRM) (2007) recommendations and polishing of cylinder surfaces was done in latter. Cylinder with diameter of 44mm and 32mm were used for mechanical testing. Length to diameter ratio of cylinders was kept in the range of 2 to 2.5 for compressive testing as suggested by ISRM (2007).

The 44mm diameter discs were used for Brazilian tests. Smaller discs were avoided because of size limitations of Brazilian disc yoke. Thickness to diameter ratio of the discs was maintained to 0.5 for Brazilian tests (ISRM, 2007). Size measurement of cylinders was done using digital precision calliper with accuracy of 0.01mm.

Compressive and Tensile Strength Tests

The samples selected for strength testing were free of any kind of visible fracture. Tests were conducted using the MTS servo-controlled hydraulic testing machine at the CSM, University of Exeter. LVDT (Linear Variable Displacement Transformer) was used to record the axial displacement. In addition, an electric resistance 2.54 mm long strain gauges were used for measurement of lateral strain. Care was taken to avoid any feldspar mega-cryst while fixing strain gauges on the samples tested. The uniaxial compressive strength (UCS) of the samples is calculated using following formula:

$$\sigma = F/ \pi r^2$$

Where, σ = UCS

F = Load (N) at the time of failure

r = Radius of cylinder

The Unconfined Tensile Strength (UTS) of samples were measure through Brazilian test (ISRM, 2007). This method measures the tensile strength indirectly by applying load to the sample along its diameter. The results of this procedure is in agreement to ones obtained via direct tensile testing but this procedure is more convenient to execute. The formula used for the calculation of UTS is

$$UTS = 2F/\pi DT$$

Where, F = Load (N) at the time of failure

D = Diameter of disc

T = Thickness of disc

Elastic Modulus

Elastic modulus also known as Young's Modulus after Thomas Young, describe the relationship between stress and strain of a sample tested. It is calculated from the stress-strain curve generated from the data acquired thorough UCS test procedure described above. The software package namely Grapher (version 8.0) was used to calculate the slope of the curve which is more reliable approach than manual graphing procedure.

P-wave Velocity

A pulse generator unit with two transducers (a transmitter and a receiver) with a frequency of 55 kHz was used for determination of ultrasonic P-wave velocities of representative samples of each type of granite tested. The propagation time of waves is noted from the generator screen and divided by the length of sample to calculate the respective velocity.

Schmidt Hardness and Density

Type N Schmidt hammer was used to determine the hardness of granites in the field. Ten readings were taken from each granite surface. The average of top five readings was used for interpretation according to ISRM recommendations.

Density was determined using disc shaped samples obtains for UTS testing. Volume of discs were calculated using digital calliper and a digital balance (0.01g resolution) was used to measure the weight of sample.